Nanostructured Materials as Potential Photocatalysts for Water Treatment

31 December 2018

A thesis submitted in partial fulfilment
of the requirement for the degree of Doctor of Philosophy

Eman Alghamdi

Cardiff University
School of Physics and Astronomy

Abo Hurairah (May Allah be pleased with him) reported: The Massenger of Allah said, “When the son of Adam dies,his deeds come to an end except for three things: ceaseless charity; a knowledge which is beneficial, or a virtuous descendant who pray for him (for the deceased)”.

Dad... Remembering you is easy, I do it every day. Missing you is the heartache that never goes away.

Acknowledgments

It is beyond doubt that completion of this thesis would not have been possible without the advice and valuable guidance of several people whom I would now like to say a special word of thanks.

Foremost, I would like to express my sincere gratitude to my supervisor Dr. Stephen A Lynch for the continuous support of my PhD study and research, for his patience, motivation, enthusiasm, and immense knowledge. His guidance helped me in all the time of research and writing of this thesis. I could not have imagined having a better advisor and mentor for my PhD study. Besides my supervisor, I would like to thank the rest of my supervision team: Prof J Emyr Macdonald and Dr Mark Hannam for their encouragement, insightful comments, and hard questions.

I would also like to express the deepest appreciation to Dr. Chris Hodges, who has shown the attitude and the substance of a genius. Also, his willingness to give his time so generously has been very much appreciated. He definitely provided me with the tools that I needed to choose the right direction and successfully complete my thesis. I thank my colleagues in our research group: Jessica Mabin, Amber Wassell, William Royle, and Dr Ryan Stock for their wonderful collaboration. They supported me greatly and were always willing to help me. I am also very grateful to my friend Katherine Armstrong from the Chemistry department for her continuous support and advice.

I would also like to thank all the faculty members at the School of Physics including Prof Peter A. R. Ade, Prof Wolfgang Langbein, Prof Stephen Fairhurst, Dr Giampaolo Pisano and Mrs Louise Winter for their help and guidance. I am grateful to all staff of Department of Chemistry, including Dr Emma Richards.

I would like to thank my family for their wise counsel, their endless love and unconditional moral support, and to thank my mother in particular. There are not enough words I can say to describe just how important my mom was to me. I may not be able to be like her but she will always be my inspiration. She is the best woman in this world for me. To my children, if I had to choose between loving you and breathing, I would use my last breath to tell you that I love you.

I gratefully acknowledge the Saudi Government for rendering me the sponsorship by trusting me. Special thanks to the former deputy cultural attache in Britain, Dr Mohammed Al-Ahmadi for his continued support to achieve my dreams. Many thanks to Dr Imad Morgan for his important guidance and suggestion.

Thanks to all the above mentioned people for their help and support for me, who are boosting me.

Abstract

This thesis discusses the latest developments in the use of nanostructured materials in water treatment. The method discussed is heterogeneous photocatalysis which uses titanium dioxide to photo-decompose organic compounds. The thesis seeks to determine the effects of the heterogeneous photocatalysis by experimental means. Methylene blue is used as the organic compound, which should be neutralised, and also acts as an indicator due to its blue colour. The objective of the experiment is to determine the optimum conditions which lead to the release of electron-hole pair. The parameters monitored are the temperature of the solution and the wavelength of the UV light. The optimum thickness of the coating of by spin coating and the modifications of titanium oxide that could increase the efficiency of the process are also determined.

Group (VI) or metal transition elements-doped TiO_2 nanoparticles (Cr, Mo, W) were synthesised and utilised as catalyst for the decolorisation of aqueous solution containing methylene blue. FT-IR and UV-vis spectroscopy techniques, X ray diffraction (XRD), scanning electron microscopy (SEM) were used to characterise the samples.

The results indicated that the doped TiO_2 nanoparticles showed higher photocatalytic activity than the pure one.All doped materials display reduced activity compared to their undoped counterparts this suggests the dopant either hinders the electron transfer due to recombination or charge trapping resulting the removal of the active species away from the active sites. P25 is usually considered to be the most active catalyst due to the hetro-junction enabling efficient charge separation. The pure anatase phase is better than pure rutile, due to the relativity surface activity and stability of the respective materials.

Modification of the chemical structure of TiO_2 by Cr, Mo, W doping allows moving the photocatalytic activity of TiO_2 towards visible light.The results indicates that films doped with 0.1% exhibit the highest UV and visible light photocatalytic activity.

Publications

J. Mabin, E. Alghamdi, C. Hodges, S. J. Freakley, and S. A. Lynch,
Monitoring the Photocatalytic Degradation of Water-based Organic Pollutants by FT-IR Spectroscopy in Real-time, Conference Proceedings of the 41st International Conference on Infrared, Millimeter, and Terahertz Waves (IRMMW-THz 2016),
DOI: 10.1109/IRMMW-THz.2016.7758467.

Presentations

E. Alghamdi, C. Hodges, and S. A. Lynch,
"Nanostructured Materials as Potential Photocatalysts for Water Treatment", The Ninth Annual Saudi Student Conference, Birmingham, UK, (13-14 February, 2016).

J. Mabin, E. Alghamdi, C. Hodges, S. Freakley, S. A. Lynch,
"Visible and Infrared Spectroscopy of Photocatalytic Reactions for Water Treatment", PHOTON16 International Conference, Leeds, UK, 5-8 SEP 2016.

J. Mabin, E. Alghamdi, C. Hodges, S. Freakley, S. A. Lynch,
"Monitoring the Photocatalytic Degradation of Water-based Organic Pollutants by FT-IR Spectroscopy in Real-time", 41st International Conference on Infrared, Millimeter, and Terahertz Waves (IRMMW-THz 2016), Copehagen 2016.

List of Figures

List of Tables

Symbols

I	intensity	(W/m^2)
A	Absorbance	(Au)
T	Transmittance	(none)
I	current	(A)
V	voltage	(V)
T	temperature	(K)
t	time	(s)
d	distance, diameter, thickness	(m)
A	area	(m^2)
r	radius	(m)
v	velocity	(m/s)
rpm	rotational speed, frequency	(rev/min)
m	mass	(kg)
C	concentration	(mM)
V	volume	(l)
M	molar mass	(kg/mol)
n	refractive index	(none)
P	power	W (J s^{-1})
wt	weight percent	(%)
$\circ$	degree	(none)
ω	angular frequency	(rad)
ρ	resistivity	(Ωcm)
σ	conductivity	(Ωcm)$^{-1}$
λ	wavelength	(m)
υ	frequency	(Hz)
θ	angle	(rad)

Physical Constants

c_0	speed of light	$2.997\,924\,58 \times 10^{8}\,\mathrm{m\,s^{-1}}$
q	electron charge	$1.6 \times 10^{-19}\,\mathrm{C}$
m_e	electron mass	$9.11 \times 10^{-31}\,\mathrm{kg}$
k	Boltzman's constant	$1.38 \times 10^{-23}\,\mathrm{J\,K^{-1}}$
h	Planck's constant	$6.625 \times 10^{-34}\,\mathrm{J/\,sec}$
eV	electron volt	$1.6 \times 10^{-19}\,\mathrm{J}$
E_g	bandgab of silicon	$1.1\,\mathrm{eV}$ (equivalent to $1.1\,\mathrm{\mu m}$ wavelength light)
ε_s	silicon permittivity	$1.05 \times 10^{-12}\,\mathrm{F\,cm^{-1}}$
$\rho_{at}(Si)$	atomic density of silicon	$5 \times 10^{22}\,\mathrm{atoms/cm^3}$

Abbreviations

MB	**M**ethylene **B**lue
MO	**M**ethyl **O**range
DIW	**D**e-**I**onized **W**ater
PS	**P**oint **S**ource of water pollution
NPS	**N**one-**P**oint **S**ource of water pollution
AOP	**A**dvanced **O**xidation **P**rocesses
RedOx	**R**eduction and **O**xidation reactions.
DBPs	**D**isinfection **B**y **Products**
CCI	**C**ardiff **C**atalysis **I**nstitute
CB	**C**onduction **B**and
VB	**V**alence **B**and
TME	**T**ransition **M**etal **E**lements
UV	**U**ltra-**V**iolet light
IR	**I**nfra**r**ed spectrum
MIR	**M**id **I**nfra**r**ed spectrum
NIR	**N**ear **I**nfra**r**ed spectrum
IPA	**I**so**p**ropyl **A**lcohol
CDA	**C**ompressed **D**ry **A**ir
FFPI	**F**iber optic **F**abry **P**erot **i**nterferometer
SMSI	**S**trong **M**etal-**S**upport **I**nteractions
TAS	**T**transient **A**bsorption **S**pectroscopy
PVC	**P**igment **V**olume **F**raction
DCA	**D**i**c**hloroacetic **a**cid
JCPDS	stands for **J**oint **C**ommittee on **P**owder **D**iffraction **S**tandards.

Contents

Chapter 1

Introduction

1.1 Rationale and Motivation

Over the last few decades environmental pollution and energy consumption has been increasing, as a result of a rapidly growing population and global industrialisation [2]. Consequently, finding novel and eco-friendly methods of cleaning the environment and exploiting clean energy sources has become ever more a necessity [2]. This is especially true for developing nations, where there is a tension between rapid progress and environmental concerns. The central topic of my thesis focuses on nano-structured materials that are tailored to provide affordable and efficient means for cleaning water, and which may also facilitate clean energy production through photocatalytic splitting of water into hydrogen and oxygen [2]. Identifying and synthesising the appropriate nano-materials in large scale are key issues that determine the adoption of nanotechnology solutions to environmental problems and sustainability [3]. My PhD concerns primarily the semiconductor material TiO_2, which is well-known for its photocatalytic properties. The usefulness of TiO_2 is limited by the intrinsic band-gap of the material, which confines the useful window of the solar spectrum to high-energy ultraviolet photons. In this work, I investigate doping of TiO_2 with transition metals, such as chromium or molybdenum to modify (lower) the band-gap to access more of the solar spectrum. The overall aim is to use this novel material for the efficient photocatalytic degradation of pollutants in water (such as petroleum hydrocarbons and chemical dyes). Novel synthesis and characterisation of these materials is discussed in detail, and their effect on the photocatalysis reaction rate is explored.

1.2 Origins of Water Pollution

For some of us, clean water is so plentiful and readily available that we rarely, if ever, pause to consider what life would be like without it. Water covers 70% of the Earth's surface, however, only 0.002% is suitable for human consumption [4]. Notably, the percentage of water suitable for human consumption is set to decrease further due to its pollution by the various pollutants in our environment today. Water pollution is the undesirable alteration in the physical, chemical, or biological properties, making it unsuitable for its intended use [5]. The importance of water in sustaining human life can not be overemphasised. Therefore, its continued contamination will present serious consequences to humans. Research indicates that the possibilities of life existing without water is quite minimal. According to Anne Marie Helmenstine[6], water is essential to life, and the human body is 75% water. A major challenge that humans face when it comes to the utilisation of water is the almost inevitable pollution of this finite resource. When the term ‘water pollution’ is mentioned, it is used to refer to any change in the biological, physical, or chemical composition of water in a manner that it becomes undesirable and unhealthy for utilisation by human or aquatic life [5]. In a broader sense, it can be looked at as the contamination of the various types of water bodies such as rivers, lakes, aquifers, oceans and underground water. The sources of water pollution can be categorised into a point source (PS) and non-point sources (NPS) [7]. A example of PS pollution would be the release of industrial waste from an drain, whereas NPS pollution might describe seepage of agricultural chemicals such as fertilisers into the water table. While PS pollution involves the emission of harmful substances directly into water, non-point sources involve those pollutants that are released due to changes in the environment [7]. Even though a lot of effort has been expended towards controlling PS pollution, NPS pollution is still a major challenge due to the variability, seasonality, and multiplicity of these forms of pollution. The major sources of water pollution are chemical rather than biological in nature. These chemicals exist both in organic and inorganic forms. NPS are the major contributors of chemical pollution in water. Chemical water pollution can further be split into elemental (atomic) or compound (molecular). Notably, toxic heavy metals such as mercury or lead can end up in water from mining, or nitrogen and phosphorus compounds (in the form of nitrate and phosphate fertilisers) are discharged into water bodies through human agricultural activities. An additional (though rarer) type of pollution is by radioactive products, through accidental releases, such as the Chernobyl or Fukushima disasters.

In my thesis, the photocatalytic purification of water is confined to the decomposition of organic chemicals such as benzene derivatives into non-toxic products such as water and CO_2 through oxidation and reduction (RedOx) reactions.

1.3 Water Pollution as a Global Problem

The problem of water pollution is rapidly becoming one of the biggest problems threatening the world today. While past wars have been fought over natural resources such as coal and oil, it is often said that the wars of the future may be fought over access to clean water. Different parts of the world are affected in different ways. In the UK, many lessons were learned during the Industrial Revolution in the 18th and 19th centuries. Consequently most drinking water is relatively unpolluted, and requires little further treatment for consumption. However this is not the case in developing countries. Here the unrelenting drive towards industrial growth driven by economic necessity often outweighs environmental concerns. The infrastructure of these countries is mostly under-developed leading to poor methods of water disposal hence increase in water pollution.

Another issue that has contributed to water depletion is climate change. Climate change contributes to desertification which reduces water catchment areas. This has resulted to overexploitation of underground water leading to its scarcity. In countries such as my own (Saudi Arabia), where most land is desert, there is a shortage of potable water [8]. Such countries often need to capitalise on the short rainy season they experience by constructing rainwater catchment areas. Water treatment plants would be necessary in water catchment areas to make the water potable.

1.4 Limitations of Current Water Treatment

It is important to understand the various stages of water treatment methods. The advantages and disadvantages of the methods that exists are discussed to give an insight on why there is need for the use of nanostructured materials in the purification of water. Some of the disadvantages of the existing methods include high inefficiencies, formation of harmful by-products and inability to neutralize some contaminants.

The most common treatment methods include adsorption, the use of membranes, as well as chemical oxidation and biological methods. The adsorption method involves transferring contaminants to a phase that is different without degrading it [9]. The process is limited by the fact that its lacks of selectivity. The membrane method, uses physical barriers to eliminate contaminants. The method is mostly associated with high energy used for pressure creation to force materials through the membrane [9]. The limitation of this method is that membranes only exclude specific contaminants.

Unnatural substances that humans have contributed to supplying, include organic matter such as sewage and animal fertilisers. For the removal of these substances, filtration techniques can be used, but are somewhat ineffective if the quantities are too high. This can lead to membrane fouling. Thus the whole process has to be continually monitored by testing membrane filtration with backflow and chemical cleaning. A major source of organic matter, as well as bacteria, viruses, and parasites, is sewage. One problem of using surface water is that it is often blended with sewage, allowing these harmful materials to enter the filtration cycle. A surplus of unnatural organic matter within potential drinking water lowers filtration efficiency and increases membrane fouling. So, the membranes need to be constantly cleaned, and this cleaning process can itself result in disinfection by-products (DBPs). In particular, the addition of chlorine to maintain these processes can cause damaging DBPs [10]. In order to determine how to eliminate the DSPs, certain experiments are being conducted to not only identify these products, but to find alternatives to chlorine treatment that proves (a) just as effective in metallic and organic removal, and (b) less apt to form DBPs. One of these tests included inducting two halogenated acetaldehydes (DBPs) into cultured cells to see their effects on DNA. Although the experiment included complex DNA analysis, the results were unambiguous: DBPs are genotoxic and alternative solutions need to be found.

Filtration techniques and membrane technology are often not enough to remove metallic ions from the water. A number of these ions can be very harmful if ingested, the severity of which will be discussed in the next section of this thesis. Not only can the ions be harmful, but certain elements such as Chromium (Cr), Nickel (Ni), and Zinc (Zn) can exist in the form of radionuclides within the water, which on passing through the filtration system can be being potentially dangerous. One proposed method to prevent these metallic ions from entering the drinking water distribution cycle is by using carbon nanoparticle-conjugated polymer nano-composites. In theory, ultrafiltration and water-soluble polymers would be used together in a manner that attaches the ions to these polymers, creating a precipitate that cannot pass through the membrane. This is advantageous because it uses relatively low energy combined with high efficiency in the removal of metal ions. In summary, each method of filtration discussed above are what water treatment plants use to clean drinking water. Utilising the appropriate combination of these techniques under strict inspection is necessary to insure a safe environment and humane public drinking source.

Chemical treatment of water involves breaking down pollutants into by-products that are easier to deal with and exclude [9]. Novel biological methods can also be harnessed. This method exploit organic agents such as plants, algae and bacteria to decompose organic contaminants in water [9]. The limitation of this method is that sludge is often formed is high leading to low inefficiencies. The limitations of these methods along with the constant emergence of new contaminants such as pesticides necessitates a more advanced method of water purification.

1.5 Recent Advances in Water Treatment

In recent years, there have been some promising technological developments amongst the various water treatment technologies that are worth mentioning.

Adsorption is considered an attractive process, since the adsorbent is often cheap and does not require a pre-treatment step before application. However, recent research has shown that electrochemical pre-treatment of certain type of industrial wastewater, can make it more amenable to biological treatment, thus making it more cost effective [11]. In this work, the authors showed improved performance from a carbon-based adsorbent material that preferentially removes chlorinated organic compounds, by electrochemical regeneration over several cycles. Researchers in Canada showed that ferric and limewater treatments were much more effective at removing arsenic by adsorption than the more standard alum water treatment [12].

There have been some advances is the treatment of salt water to make it drinkable that are worth mentioning. Reverse osmosis is the most widely used technology for this application. Al-Rifai *et al.* went further to develop a complementary reverse osmosis method for the removal of pharmaceuticals (such salicylic acid, from aspirin medicines) and endocrine disrupting compounds in a water recycling process [13]. They showed that removal efficiencies of above 97% for most chemicals of concern in a realistic advanced water treatment plant. Öner *et al.* looked at the application of laboratory scale cross-flow flat sheet reverse osmosis method to remove for boron, salt, and silica from geothermal water [14]. Their main finding was that under all operating conditions, salt and silica were rejected effectively by more than 96.5% for all membranes studied.

Disinfecting water containing natural organic matter with chlorine has the potential to create DBPs. This is a problem because some of these DBPs are potentially carcinogenic. Membrane filtration has the potential to replace conventional treatment processes that consist of ozonation, precipitation, coagulation, flocculation, chlorination, and gravel filtration for river water [15]. Stahlwerke Bremen, a major steel company, in cooperation with the Institute of Environmental Process Engineering of the University Bremen and Axiva have now built a large-scale pilot plant for the treatment of water from the River Weser by the combination of direct ultrafiltration and reverse osmosis as a technology demonstrator. Hybrid technologies have also been considered. Fuchs *et al.* demonstrated high anaerobic conversion rates of different types of wastewater were achieved using a membrane bioreactor [16]. Their membrane bioreactor was specifically useful for the treatment of complex wastewater rich in slowly degradable solids, which are often treated insufficiently by other standard anaerobic treatment systems.

An interesting non-traditional method for the elimination of pollutants is to exploit electrochemical technologies. These include direct oxidation, indirect oxidation, and an electrochemical version of Fenton's reaction (electro-Fenton). De Francesco and Costamagna studied the design of electrochemical reactors in depth [17]. They concluded that the most important difference between the various electrochemical processes is the electrode surface, and from this standpoint, direct oxidation would seem to be the most promising route. However, the energy necessary to run these processes (specifically electrochemical abatement) require costs which are higher than with non-electrochemical abatement techniques. Sirés *et al.* reported the electrochemical degradation of β-blockers, which are pharmaceutical pollutants often found at high concentrations in natural waters [18]. They compared anodic oxidation and the electro-Fenton process. While both methods worked, they showed that the electro-Fenton process was more effective in the case of platinum electrodes. They concluded that electro-Fenton is a very effective detoxification method for β-blockers.

One further method worth mentioning is to exploit biological processes. Katsoyiannis *et al.* used microbes to remove manganese and iron [19]. They found that biologically mediated manganese and iron removal followed a first-order reaction rate, presenting a half-life of 3.98 and 0.9 min, respectively. These fast rates of reaction make the treatment method quite economic and environmental friendly, especially because additional use of chemical reagents is not required. Abou-Elela *et al.* developed a method for saline wastewater treatment using a salt-tolerant microorganism [20]. They showed the use of adapted activated sludge only as a microbial culture works efficiently up to 1% salinity, but further increases in salinity causes great deterioration of the system performance.

1.6 Advanced Oxidative Purification Methods

Advanced Oxidation Processes (AOP) potentially offer a solution to the problem of excluding certain types of emerging contaminants. These processes convert organic contaminants into compounds which are not harmful. AOPs mainly harness three processes, which include heterogeneous photocatalysis, photochemical oxidation and chemical oxidation [21]. Of the three methods, the photocatalytic method is the most attractive. The process uses energy from short-wave (ultraviolet) photons to generate reactive hydroxyl radicals, and hence does not require the use of chemicals [21]. The method invariably uses titanium dioxide (TiO_2) in the form of nano-powders, which is a chemically stable and cheap catalyst. Nano-structuring the TiO_2 results in an increased surface area to facilitate more effcient catalytic reaction.

Ever since Fujishima and Honda discovered water-splitting effect of TiO_2, there have been extensive studies on TiO_2 [22]. TiO_2 has many advantages as a photocatalyst, such as chemical stability, inert nature, non-toxicity, and cost effectiveness, resulting in one of the most commonly used photocatalysts in the environmental and energy related fields. However, pure TiO_2 is not conventionally used in water treatment due to the dispersed nature of the catalytic nanoparticles in the water and the need for UV illumination. In addition, the major disadvantage of TiO_2 is its relatively wide band gap necessitating light wavelengths below 400 nm for electron and hole separation. This is important because researchers are interested in exploiting solar radiation as the source of photons. At this point, it is worth considering what percentage of the sun's radiation is useful for this application? NASA produced a detailed technical report which models the solar spectrum for a broad wavelength band and over a wide range of atmospheric conditions [23]. I have used this information to calculate the percentage of useful photons reaching ground level. The data plotted in figure 1.1 compares the extra-terrestrial solar irradiance with the attenuated solar irradiance at ground level. NASA define the atmospheric turbidity by an attenuation coefficient c_2 according to the equation,

$$c_2 = \beta\lambda^{-\alpha} \quad , \tag{1.1}$$

where 'clear conditions' are defined by $\alpha = 1.3$ and $\beta = 0.04$. By integrating the area underneath the blue curve, which describes the solar irradiance passing through the atmosphere (air mass = 1), we can estimate the percentage of useful photons for photocatalysis (the solid purple area). For the longest (lower) wavelength limit, I have assumed the TiO_2 phase of smallest band gap (rutile) with $E_g = 3.05$ eV. This

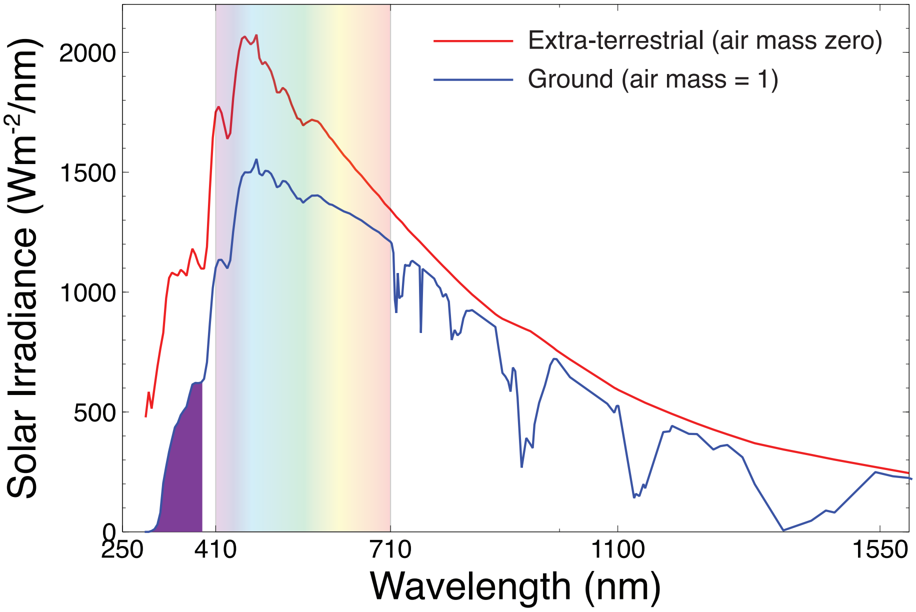

Figure 1.1: Solar Irradiance as a function of wavelength plotted using the NASA data retrieved from [23]. The red curve shows the extra-terrestrial irradiance (above the earth's atmosphere), and the blue curve shows the solar irradiance after passing through the atmosphere (of air mass = 1). I have plotted the ideal conditions, which NASA describe as 'clear conditions'. These conditions assume standard temperature and pressure, and correspond to water vapour 20 mm, ozone 3.4 mm, and turbidity conditions described by coefficients $\alpha = 1.3$ and $\beta = 0.04$. The shaded region (in dark purple) corresponds to photons with a wavelength shorter than 387 nm.

corresponds to $\lambda = 387$ nm. Dividing this area by the total area under this curve (up to $\lambda = 4045$ nm) gives the percentage of useful photons, which is $\approx 3.5\%$. This small percentage makes a very strong argument for exploring strategies to lower the band gap of TiO_2 and thereby use more of the solar spectrum.

Researchers have developed two strategies to expand its light absorption range. The first one is by incorporating an organic dye as a photo sensitiser; the second is by 'doping' TiO_2 with metallic/nonmetallic elements [24]. The second method has been perfected by the Cardiff Catalysis Institute (CCI) and was studied as part of a collaboration during my PhD. 'Doping' introduces either occupied orbitals (which leads to negative doping) or unoccupied orbitals (which leads to positive doping) in the band gap area of the semiconductor, thereby reducing the band gap. In the past, TiO_2 has been doped with various metals like Fe, Pd, Pt, Cr, and rare-earth metals causing a large shift in its absorbance band, moving into the visible region . It has been observed that there is an optimal value or level for doping TiO_2 which in many cases is between 3-7 wt% in order to reach maximum efficiency of the catalyst. Although doping with novel metals like Pt exhibited high photocatalytic activity by reducing the recombination of photo-created electron-hole pairs, its high cost and indefinite sustainability have led researchers to use other potential dopants. Transition metals like copper are available at low cost. There have been few investigations concerning the doping of titania with copper resulting in enhanced photocatalytic activity, hydrogen generation and carbon dioxide reduction. Researchers have shown that a modification to the optical properties of TiO_2 was brought about by the copper-doped TiO_2 nano particles, enabling the composite material to show activity in the UV-visible region of solar radiation, enhancing the degradation of organic pollutants several times faster than bare TiO_2 [25]. However, the photocatalytic nanoparticles combined to form aggregates which become attractive sites for the photo-generated electrons and holes, leading to recombination reactions and rapid loss in active sites, which ultimately hindered photocatalysis [26].

1.7 Quantifying Photocatalysis by Experiment

Chemists routinely use dispersed nano-powder TiO_2 to perform photocatalytic reactions. However, to understand how modifying TiO_2 can be used to improve the photocatalytic degradation of organic pollutants in water, we are presented with several experimental challenges. A major problem is that small amounts of the reacting solution have to be constantly removed and tested for the concentration of the reactants. This means that the reaction rate is measured from a few discrete points. It is clear that a method needs to found to continuously monitor the reaction rate. This was one of the first experimental parts of my PhD research. I designed and built an experiment with a flow cell with optical windows to facilitate continuous optical monitoring of the concentration of the test pollutant dye as the photocatalytic reaction progresses.

1.8 Aim and Objectives

The overall aims of this research was to study the photocatalytic properties of TiO_2 films for the application in water purification. It helps to break this further down into a number shorter-term aims. These are summarised here.

- To design and build a repeatable experiment to allow the activity of the TiO_2 photocatalyst to be monitored over time in a quantifiable way.
- To find a repeatable method for fixing the TiO_2 nanoparticles thus avoiding a dispersed nanoparticle mixture (spin-coating).
- To find an accurate method to quantify the amount of photocatalyst material (the nano-film thickness) used in each experiment.
- To understand the parameters governing the reaction rates for pristine TiO_2 nanoparticle films, including any background decomposition rate of the test pollutant dye.
- To understand the factors affecting the activity of the nanoparticle photocatalyst over time (catalyst poisoning, and in particular the effect of chlorine ions).
- To synthesise pure TiO_2 nanoparticles and understand the role of crystal structure in photocatalysis (Anatase vs Rutile).
- To synthesise modified TiO_2 nanoparticles with the aim of reducing the band gap to access more of the available solar spectrum.
- To characterise this modified TiO_2 material and quantify the incorporation of the rare-earth atoms (using XRD, XPS, and Raman).
- To understand the effect of incorporating different rare-earths on the band-gap of TiO_2 (UV-Vis).
- To produce a modified TiO_2 photocatalyst with a smaller band gap and compare its photocatalytic activity against the pristine TiO_2 (demonstrate photocatalysis for violet, blue, and green light, rather than just UV light).

1.9 Thesis Outline

Chapter 1 (this chapter) introduces the research topic. In this chapter I have discussed the overarching rationale behind this work and what I hoped to achieve. Chapter 2 looks at the background science. This subject matter crosses many disciplines, but I try to make the connection with semiconductor physics, since TiO_2 is considered to be a wide band-gap semiconductor. This topic provides a way in to understanding how doping with transition metals can affect the optical properties of the material. The connection is then made to photocatalysis, where we see that the optically generated electron-hole pair facilitates the RedOx reactions at the surface. Chapter 3 deals with production and characterisation of the photocatalytic thin films. There is a general introduction to thin-film production, before I concentrate on the details of spin-coating. A big part of this chapter discusses the challenges measuring the thickness of the films. Chapter 4 describes the experimental test-rig that was used to evaluate the photocatalytic reaction rates. All aspects behind the design are explored. This was important because the test-rig was the foundation for all further research performed during the rest of my PhD. Chapter 5 discusses the poisoning effect of chloride ions on the photocatalytic action of TiO_2. Chapter 6 explores whether modifying the TiO_2 through doping with transition elements can have any beneficial effects. Much of this chapter concerns the many and varied material characterisation techniques used to study the incorporation of the transition metal atoms into the TiO_2 crystal lattice. The final part of the chapter deals with the effect on photocatalytic rate and response to longer wavelengths. The thesis concludes with a short final chapter and some thoughts on future research directions.

Chapter 2

Background Science

2.1 Introduction and Overview

This chapter deals with some of the background science required to understand the science behind my PhD project. Because photocatalysis falls in the interface between physics and chemistry, it is necessary to make the connection to both subjects. A catalyst is a material that facilitates a chemical reaction to proceed at increased rate. It usually achieves this by lowering the activation energy for the reaction. The catalyst itself is not consumed during the reaction. A photocatalyst requires photons to activate the catalytic material, in this case TiO_2. Chemists have known about the photocatalytic properties of TiO_2 for a long time. However, it is through understanding the physics of crystalline TiO_2 that we can understand why it is such a good photocatalyst. Physicists know crystalline TiO_2 as a wide-band gap semiconductor. Like all other semiconductors, the electrical properties change when the semiconductor is exposed to light of sufficiently short wavelength. A short wavelength photon may have enough energy to excite electron-hole pairs in the semiconductor, if the energy is larger than the band gap of the material. These free electrons and holes can then contribute to conduction. It is these free electrons and holes that facilitate the catalysis at the surface of the TiO_2, by interacting with the surrounding aqueous environment. The photocatalysis effect is greatly enhanced if the surface area of the TiO_2 is maximised. Nanostructured TiO_2 has a larger surface to volume ratio, and so nano-powdered TiO_2 is preferred for this application. So, in this chapter, I will introduce some basic semiconductor concepts before moving to the photo-chemistry of TiO_2. It is necessary to do this because the final chapter of my thesis deals with doping TiO_2 nano-powder films. The rationale behind doing this is that it lowers the band gap energy of the material, so that longer wave photons can achieve the same effect of generating electron-hole pairs. This has the consequence that more of the solar spectrum can be harnessed to achieve the photocatalytic effect.

2.2 Connection with Semiconductor Physics

2.2.1 Semiconductor Basics

Semiconductor materials have electrical properties somewhere between metals and insulators. The semiconductor properties arise because of the band structure of the solid-state material. When two atoms form a stable chemical bond, the overall potential energy is lowered. As the atoms move closer together, the degeneracy of the atomic orbitals is lifted, and bonding and anti-bonding orbitals form. The bonding orbital energy is lowered and the anti-bonding orbital energy is raised, as is shown in the left of figure 2.1. Because there are many similar bonding and anti-bonding orbitals, they must form bands. This explains the origin of the conduction and valence bands. There is a forbidden electronic energy range between the conduction band and valence band, which is known as the band gap (E_g). The properties of the material depend on the size of this band gap, as shown in figure 2.2. In the case of a metal, E_g is either very small or doesn't exist. So, electrons are free to move into the conduction band. For an insulator E_g is very large. There is not enough thermal energy at room temperature to excite electrons across the band gap into the conduction band. A semiconductor is somewhere between these two extreme cases. E_g is small enough so that some electrons are excited into the conduction band where they can contribute to conduction. Our photocatalyst TiO_2 is what is known in physics as a wide band-gap semiconductor. The TiO_2 band gap E_g is not large enough to be a true insulator, but it is still large enough that it requires a high-energy UV photon to excite an electron into the conduction band.

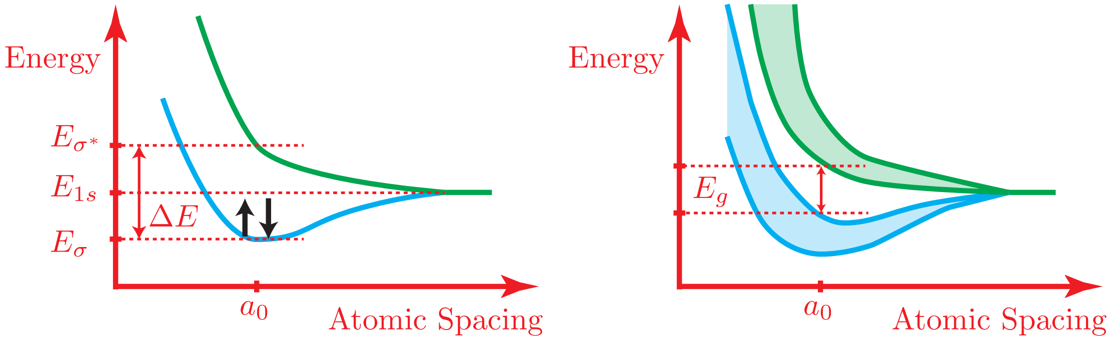

Figure 2.1: Left: Energy of bonding and anti-bonding orbital as a function of atomic spacing. As the atoms in the bond move closer together, the orbital degeneracy is lifted so that the bonding orbital energy is lowered and the anti-bonding orbital energy is raised. Right: Because there are many similar bonding and anti-bonding orbitals, they must form bands. This explains the origin of the conduction and valence bands.

The best-known semiconductor is probably silicon because it is found in nearly every modern electronic device. Silicon is a member of group-IV of the periodic

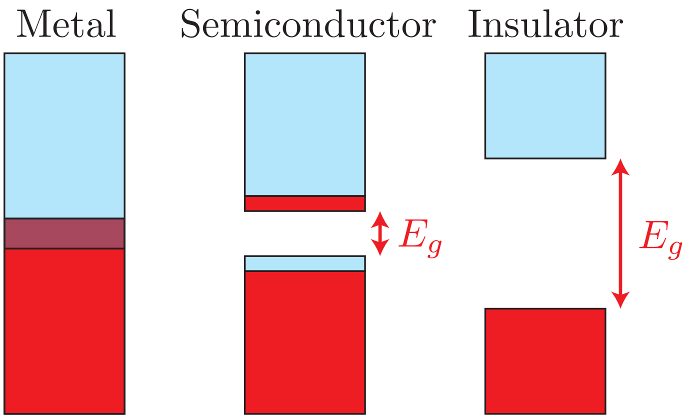

Figure 2.2: Simplistic picture showing the difference between metals semiconductors and insulators. For a metal the energy of the bonding and anti-bonding orbitals overlaps, so electrons are free to move. In an insulator the separation between and the conduction and valence band gap is very large. There are no electrons in the conduction band and so the material is an insulator. The semiconductor is in between. The band gap is small enough that electrons can hop across into the conduction band.

table, as shown in figure 2.3. Along with germanium these two materials are the only elemental semiconductors [27]. Elements to the left-hand side of the periodic table are generally metallic while elements to the right-hand side of the periodic table are generally non-metallic. More complicated semiconductors are formed from chemical compounds, for example when elements from group-III bond with elements in group-V (such as GaAs).

2.2.2 Semiconductor Doping (and Band Gap Shrinking)

A dopant is an extra element that is added to the semiconductor which changes its electrical properties [29]. There are two types of dopants, n-type (where there is an excess of electrons) and p-type (where there is a deficiency of electrons, and consequently an excess of holes). The detailed physics of doping is complicated particularly in non-elemental semiconductors such as GaAs (or TiO_2). It is easiest to understand what happens for the simplest and most common semiconductor (silicon). Silicon is an elemental semiconductor. Each silicon atom bonds to four other silicon atoms. All the valence electrons are used up in the bonding. If an atom from group-III or group-V (the periodic table columns to either side) replaces one of the silicon atoms then the local electronic configuration changes. For a group-V atom (such as phosphorus) there is an extra loosely bound electron that is not directly involved in the bonding. This electron sits at an energy level just below the conduction band. It takes very little energy to excite this electron into the conduction band and so there are many more of these extra electrons in the conduction band at room temperature. This is highlighted in figure 2.4a. The contra situation happens if a group-III atom is added

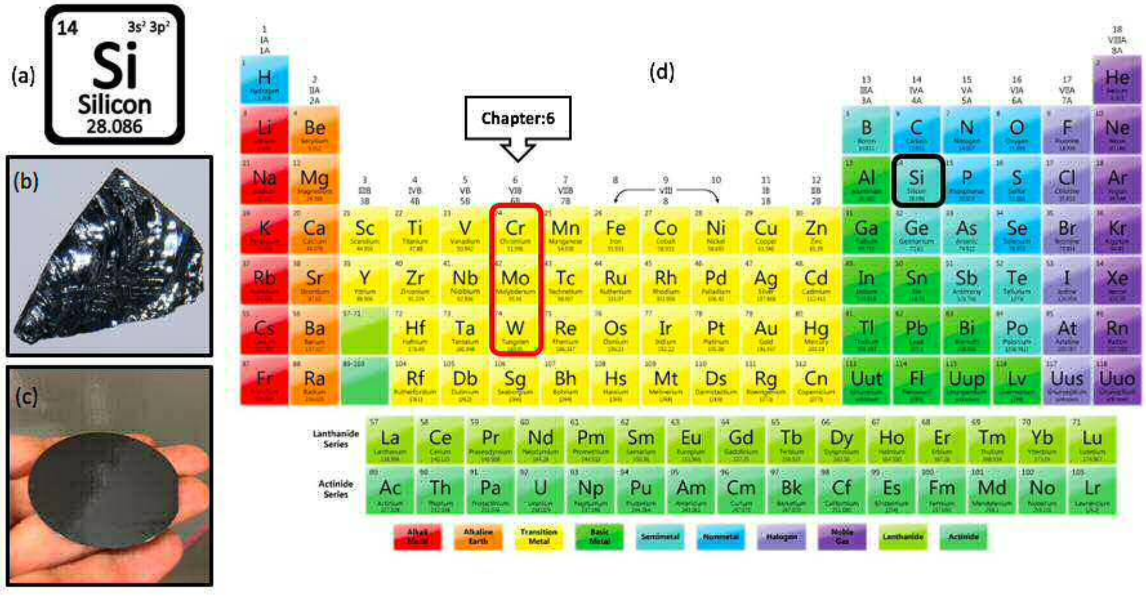

Figure 2.3: (a)Electron configuration of silicon element, (b) ultra pure silicon chunks, (c)a silicon wafer, (d) the periodic table showing the place of Si element and group(VI) [28]

to silicon. There is now a deficiency of bonding electrons, or in other words a hole. In this situation the top of the valence band is full of holes which can move around an also contribute to conduction. This is highlighted in figure 2.4b.

Another consequence of doping is that the electrons associated with doping sit at energy levels just below the conduction band (in the case of donors) and just above the valence band (in the case of acceptors). In both cases this has the effect of effectively of shrinking the band gap [30]. It is important to stress that the spacing between the conduction band and the valence band is still the same, but there are now extra levels just below the conduction band and just above the valence band so that a longer wavelength photon which otherwise would not have enough energy to excite an electron into the conduction band could still excite an electron into these levels (and the same for holes).

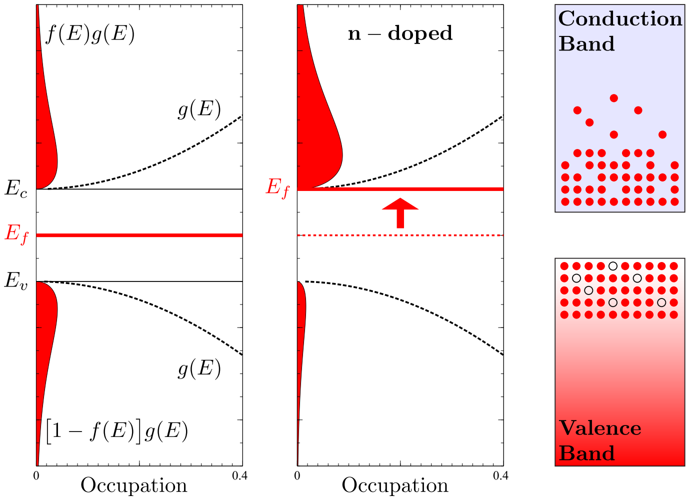

(a) The addition to silicon of a group-V element (such as phosphorus) provides an extra loosely bound electron that is not involved in bonding. So, the population of electrons in the conduction band is much larger than for the un-doped extrinsic semiconductor material. The Fermi-level is close to the conduction band.

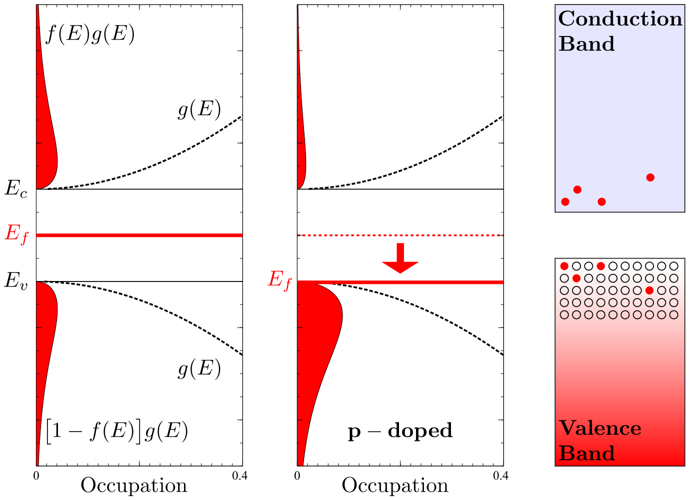

(b) The addition to silicon of a group-III element (such as boron) provides a deficiency of electrons (or holes). So, the population of holes in the valence band is much larger than for the un-doped extrinsic semiconductor material. The Fermi level is close to the valance band.

Figure 2.4: Effect of p- and n-type doping on the Fermi level in semiconductors. (Sourced from Cardiff Physics PX2236 'Introduction to Condensed Matter Physics' course notes - Dr Stephen A. Lynch.)

2.3 Semiconductor Photocatalysts

It has long been known that many oxide semiconductors (such as TiO_2) show practical performance as photocatalysts in water disinfection and detoxification. Semiconductors can act as photocatalysts for light-induced RedOx processes due to their electronic structure, which is characterised by a filled valence band (VB) and an empty conduction band (CB) with a suitable gap between them. A semiconductor photocatalytic material absorbs light with photon energies that are the same or greater than the band gap, $hv \geqslant E_g$, creating an electron in the conduction band and a hole in the valence band of the semiconductor [2]. The physical statement for this reaction is:

$$TiO_2 + hv \rightarrow e^-_{cb} + h^+_{vb} \tag{2.1}$$

If the photocatalytic material is nano-structured then the electron and hole can easily make their way to the surface where they then interact with the surrounding environment. The connection between the energy E of the photon and the wavelength λ for the best outflow of electrons from the surface of the photocatalyst, can be found by substituting the equation connecting the wavelength λ and photon's frequency v of light with the Planck formula,

$$v = c/\lambda \tag{2.2}$$

$$E = hv \tag{2.3}$$

where h is the Planck constant and c is the speed of light in vacuum. As h and c are both well-known physical constants, the photon energy changes with direct relation to wavelength λ.

$$E = hc/\lambda \tag{2.4}$$

When the charge separation of the electron and hole happens, the charge carriers can then interact in several different ways. The first possibility is that the hole and electron recombine with each other before reaching surface of the material. The second possibility is that they recombine at the interface between the TiO_2 surface and the liquid thereby neutralising each other. Another possibility is that hole combines with water molecules leading to oxidation reaction. The last possibility is the combination of the electron with oxygen in water to form a reduction reaction [27].

The hole can break up a water molecule producing a highly reactive OH^-hydroxyl radical. This in turn can oxidise organic chemicals dissolved in the water, producing carbon dioxide and water. The electron can react with any dissolved oxygen molecules in the water to leave a highly reactive activated O_2^- radical which can in turn facilitate reduction reactions in the water [2]. Semiconductor photocatalysts have been utilised to break up natural and inorganic contaminants, for example, alkanes, aliphatic alcohols, aliphatic carboxylic acids, alkenes, phenols, sweet-smelling carboxylic acids, colours, PCB's, basic aromatics, halogenated alkanes and alkenes, surfactants, and pesticides and in addition for the reduction reaction of metals (e.g., Pt^{4+}, Au^{3+}, Rh^{3+}, Cr^{vi}) from water at surfaces [2]. Atomic oxygen adsorbed on the surface of

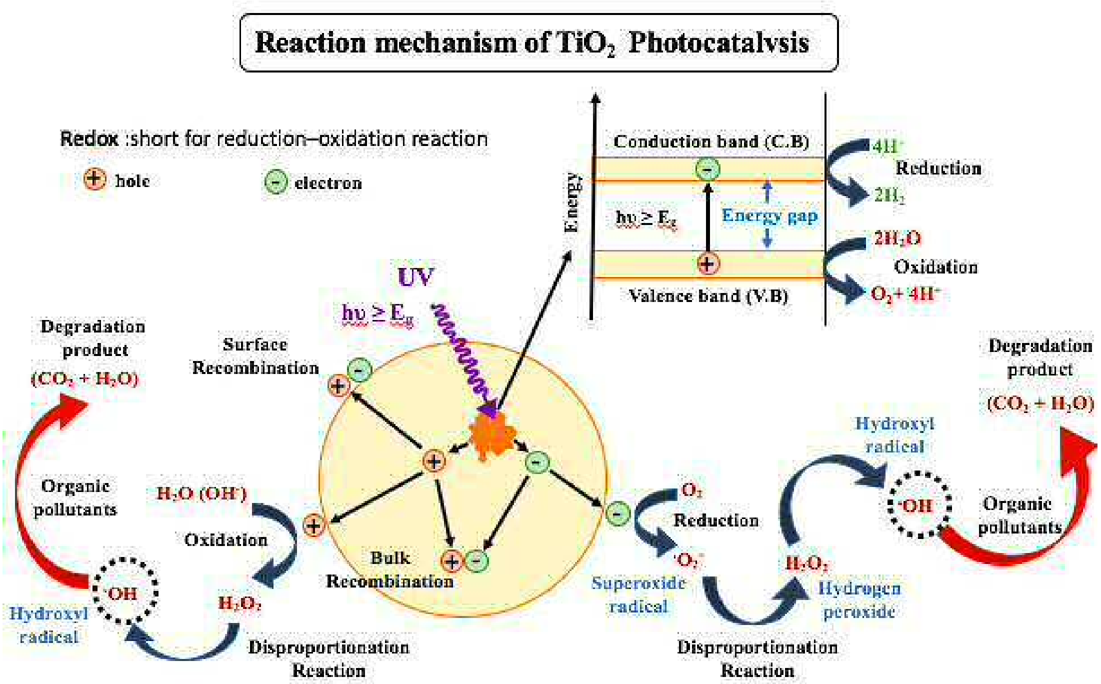

Figure 2.5: The diagram shows the four possibilities of the electron and hole formed by the photo catalyst.

the photocatalyst is released by charge exchange of electrons produced from band gap excitation of the semiconductor photocatalyst [2]. The activated O_2^- oxygen species are the essential radicals which facilitate these reactions [27].

2.4 Types of Photocatalytic Reactions

Photocatalysis is a combination of two Greek words. Photo which implies light, and catalysis which means to decompose [31]. Photocatalysis is, therefore, a term used to refer to the rate of the chemical reaction or the initiation of chemical reactions under the influence of ultra-violate radiation, infrared or visible light. Its action is required in the chemical transformation of reacting partners. A catalyst is used but in very small quantity since the activation energy required to start the reaction is minimal. For simplicity, there are two types of catalysts that can be used. Heterogeneous catalysts are distinguished from homogeneous catalysts by the different phases present during reaction. Homogeneous catalysts are present in the same phase as reactants and products, usually liquid, while heterogeneous catalysts are present in a different phase, usually solid [32]. The main advantage of using a heterogeneous catalyst is the relative ease of catalyst separation from the product stream that aids in the creation of continuous chemical processes. Additionally, heterogeneous catalysts are typically more tolerant of extreme operating conditions than their homogeneous analogues.

2.4.1 Homogeneous Photocatalysts

In homogeneous photocatalysis reactions, both the reactants and the catalyst are in the same phase. Most homogeneous photocatalytic reactions happen in the liquid phase. There is a good example, of such a homogeneous reaction that is particularly relevant to water treatment. Fenton's reagent is a solution of hydrogen peroxide with ferrous iron (Fe^{2+} ions) as a catalyst, and it has historically been used to decompose organic compounds dissolved in water. The oxidation process produces OH^- radicals and Fe^{3+} which are either transient (very short-lived) or non-toxic substances. Exposing the reaction to UV light reduces the $Fe^{3+}+$ to Fe^{2+} hence regenerating the catalyst. The equations for the reactions are given by:

$$Fe^{2+} + H_2O_2 \rightarrow Fe^{3+} + OH^- + OH \tag{2.5}$$

$$Fe^{3+} + H_2O + hv(< 450nm) \rightarrow Fe^{2+} + OH^- + H^- \tag{2.6}$$

The process has been in use since the 1960s for the treatment of wastewater because it is an environmental friendly method that can be used on a large scale [33]. The method can also be used in the treatment of chemicals that are used as pesticides hence is a reliable method. The efficiency of the method is also high compared to the heterogeneous method. The only limitation was maintaining the stoichiometric levels of the catalyst. However, it was later discovered that UV light (either natural or artificial) could be used to regenerate the catalysts as explained by the equations above.

2.4.2 Heterogeneous Photocatalysts

Heterogeneous chemical reactions involve reactants which are in different phases. The most familiar everyday example of a heterogeneous catalysis reaction is the decomposition of exhaust gases from car engines using a catalytic converter. Typically, toxic gases like carbon monoxide are converted into CO_2 and oxides of nitrogen are reduced back to diatomic N_2 gas. The catalyst usually takes the form of a ceramic filter that has been impregnated with noble metals such as platinum or palladium. The catalysts are activated at high temperature. As the gases are forced through, the toxic emissions are either oxidised or reduced to safer gases. Heterogeneous photocatalysis reactions are also now commonly harnessed to clean water. In particular, semiconductor photocatalysts are used to chemically convert contaminants to non-harmful by-products. The semiconductor most commonly used is TiO_2, although others such as ZnO, WO_3 and CdS can also be used. TiO_2 is most commonly used because it is photostable and cheaply available. This research field is particularly active. One of the biggest challenges is to use a larger portion of the solar spectrum. The band gap of TiO_2 is 3.2 eV (which corresponds to a wavelength of 387 nm). This means that only UV photons are useful for generating electron-hole pairs. For example, recent research published in the literature shows for the first time that a visible light activated self-supporting CuO-TiO_2 nanomats can achieve a degradation level of 97% for methylene blue aqueous solutions [34]. The electrochemical behavior of CuO-TiO_2 nano-fibrous materials were studied using cyclic voltammetry (CV) in 0.1M KOH solution in the range of -1 to 1V. The cyclic voltammetry curve of the pure TiO_2 Nano-fibrous show no obvious oxidation or reduction peaks. The difference in the current values on the edge of the curves may be due to photocurrent from pure TiO_2 nano-fibrous mats upon light illumination. The RedOx reaction here involves transition between Cu and Cu(I) oxide and similar behaviour has been reported for transition metals in alkali solutions. Cu(II) oxide only formed in solution from the slow dehydration of Cu (OH). During the CV measurement, the whole cycle was completed with approximately 1min therefore CuO is not expected to form. The peak potential shifted to more anodic and cathodic directions under light illumination.

2.5 Titanium dioxide (TiO_2)

Titanium dioxide is the most commonly used photocatalyst, and it is also the main subject of my PhD research. It is most usually encountered as a white powder. There are multiple practical applications of titanium dioxide (TiO_2) such as in drugs, food, catalysts and among others whereby it is used as a desiccant, reactive mediator or brightener. For example, TiO_2 is often used to make white paint. Relevant to this discussion, TiO_2 is used in photocatalysis since it is highly hydrophilic, insoluble in water, cheap and it is supported by multiple substrates. However, TiO_2 has a low efficiency under visible light. As discussed earlier in section 2.4.2, its large band gap means that the useful excitation wavelength falls in the UV region. Through RedOx reactions, TiO_2 can easily oxidize organic and inorganic substrates in the air. This unique combination of characteristics, when combined with lack of toxicity and low cost make it an ideal catalyst, as discussed by Seghetti [35].

Titanium dioxide is a polymorphic material with three allotropic forms, namely anatase, rutile, and brookite [36]. These crystal structures are shown in figure 2.6, with the crystal lattice parameters listed in table 2.1. The physiochemical properties of the three phases are different from each other and are related closely to the synthetic conditions. Anatase is the one that is most thermodynamically stable when the size is less than 11 nm. The brookite stable phase is between 11nm and 35 nm. Rutile is most stable when all the sizes are larger than 35nm. Anatase is considered to be more active than rutile phase as a photocatalyst. This is because it has higher crystallinity which offers fewer defects enabling it to act as a recombination site between holes and photo-generated electrons.

2.5.1 More on Anatase and Rutile Phases

Anatase and rutile are two metastable forms of titanium dioxide, which differ in properties, structure, and applications. Rutile is found in nature as a reddish mineral:

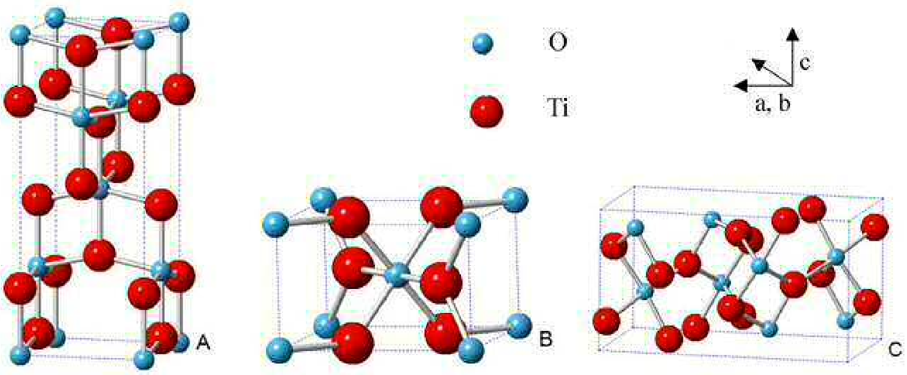

Figure 2.6: (a) Anatase, (b)Rutile, and (c) Brookite.

Crystal phase	**Lattice parameter**		
	a(A°)	b(A°)	c(A°)
Anatase	3.7842	3.7842	9.5146
Rutile	4.5937	4.5937	2.9581
Brookite	9.16	5.43	5.13

Table 2.1: The crystal phases of TiO_2 and their lattice parameters [37]

hard, and chemically inert, with high refractive index. The heating of anatase to 915 °C forms a brownish or yellowish rutile. The conductivity and photocatalytic characteristics of anatase are higher than that of rutile. Anatase has a higher band gap of 3.2 eV as compared to 3.0 eV for rutile, as shown in figure 2.7. The higher crystalline structure of anatase promotes the transference of free electrons in the presence of vacancies in the conduction band. In rutile, this is not the case because it's structure is more disordered. The distance between Ti and Ti in the anatase is much wider than that of rutile. Also, the Ti and O distances are shorter in anatase as compared to rutile, which leads to alterations in mass density as well as variation in electronic configuration. The rutile has much higher localisation of the 3d state and a narrow 3d band. Structurally, the oxygen's 2p band and titanium 3d hybridisation is distinct in both the structures. This allows for easier photo-conduction of electrons in anatase, which spans over a wide range of energy as well.

The anatase crystal system is tetragonal. It exists as one of the five forms of titanium dioxide that are found freely in nature. The hardness of this mineral is 5.5 to 6 on Mohs scale. The main polymorphs of anatase are brookite, TiO_2, akaogiite, and TiO_2(II). The specific gravity of anatase is 3.79-3.97 g/cm^3. The lustre of anatase is metallic or adamantine. This mineral occurs in various colours. Anatase appears to be transparent when it is of light colour and translucent when it is of deep colour. The common impurities of anatase are Fe, Sn, Nb, and V.

Rutile has a molecular weight of 79.88 u. This mineral is commonly found under igneous rocks where there is high temperatures and high pressure. This mineral has the biggest refractive indices at wavelengths that are visible. It also shows a large birefringence and a dispersion that is very high. This mineral is very useful in the manufacturing of some optical elements. In its natural form, it can contain iron up to 10%. It can also contain tantalum and niobium at levels considered larger than trace amounts. Rutile as the polymorph of TiO_2 that is most stable at all temperatures. The process of transforming anatase and brookite to rutile is an irreversible process. While rutile can be found in plutonic igneous rocks, anatase and brookite can be found in an igneous environment as products of autogenic alteration when the plutonic rocks are cooled.

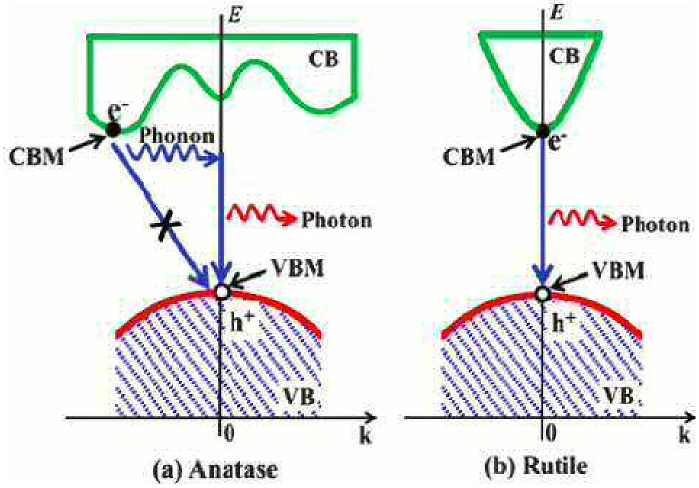

Figure 2.7: (a) Anatase: the band gap of the anatase phase is slightly larger than the rutile phase (3.2 eV as compared to 3.0 eV). However, another important difference is the indirect nature of the band gap. This means that the minimum of the conduction band (CB) does not occur at the same value of *k* as the maximum of the valence band (VB). In addition to the photon, an extra phonon is required to conserve momentum, for a transition between the bands. (b) Rutile: unlike the the anatase phase, the band gap is direct. The minimum of the conduction band matches the maximum of the valence band and only a photon is required to make a transition across the band gap (taken from [38]).

(a) Anatase: The band gap of the Anatase phase is slightly larger than the rutile phase (3.2 eV as compared to 3.0 eV). However another important difference is the indirect nature of the band gap. This means that the minimum of the conduction band does not occur at the same value of *k*. In addition to the photon, and extra phonon is required to conserve momentum. (b) Rutile: unlike the the anatase phase the band gap is direct. The minimum of the conduction band matches the maximum of the valence band and only a photon is required to make a transition across the band gap.

2.5.2 Nano-powder TiO_2 (Degussa P-25)

The photocatalytic reactions take place at the surface of the TiO_2, and so the surface-to-volume ratio is of critical importance in the efficiency of the photocatalyst. Hence powdered TiO_2 is preferred. There are many different types of TiO_2 powder available, but one particular product stands out. In this research field, the commercial product “Degussa” (or “Evonic”) P-25 is known to have by far the highest efficiency. P-25 is a mixture of anatase and rutile TiO_2, in the ratio of 3:1. The final product is produced in the form of an “aeroxide”, which has a particularly high surface area [39]. It is not well-understood why this mixture of anatase and rutile produces the optimum results, however, according to Choi and Ryu[40], various studies have shown that a mixture 80% anatase and 20% rutile is the most active phase. P25 is certainly better than either the pure anatase and rutile phases of TiO_2. The so-called aeroxide powder is manufactured through a process called flame hydrolysis [41]. Currently, many studies have been conducted to improve the photocatalytic efficiency of P25 which include noble metal deposition and doping of metals or non-metal ions. When doped ions are introduced, there if the formation of the energy level of doping between the valence bands and conduction of P25.

Between anatase and rutile, the former is more photocatalyticly active. However, this difference cannot be explained by a clear consensus. The only known difference results from the transport of bulk excitons to the surface. An evaluation of the photocatalytic activity as a function of TiO_2 film thickness is made when high quality epitaxial TiO_2 films of the two polymorphs are utilised. The activity for anatase would increase for films for up to 5nm thick. Rutile films reach an activity of 2.5 nm films which is their maximum. This is important in showing that charge carriers excited deeper in bulk contributes to the surface reaction in anatase than in rutile. Understanding why anatase is better than rutile is important in understanding how they both influence P25. Bickley *et al.* [42] proposed a synergetic effect between rutile and anatase in Degussa P-25 in 1991. Comparison of pure titanium dioxide samples with various Rutile to Anatase samples with identical properties forms the basis of this study. There is a clear synergetic effect within a range of rutile to anatase ratios that are well-defined. A film of 40% rutile and 60% anatase showed optimal performance in these experiments, with a 50% improved activity compared with a pure anatase. This was demonstrated through using the photocatalytic oxidation of methylene gas.

The photocatalytic activity of P-25 is enhanced by the photocatalytic activities of both Anatase and Rutile. The TiO_2 which has nanoparticles has always been considered as a catalyst for the photodegradation of compounds which are organic because of their chemical properties and their physical which is unique. The photocatalytic performance of Titanium dioxide is greatly determined by its crystalline, stability of their phase, the particles crystal phase, size, and their surface chemical properties which relies on their synthetic route.

2.6 Reactions at the Surface of TiO$_2$.

Heterogeneous photocatalysis works by using light energy to activate catalysis which initiate a chemical reaction at the surface of water causing a RedOx reaction which reduces oxygen and oxidizes organic contaminants [2]. The photocatalysis process is divided into five steps as follows:

- The first step involves the transfer of reactants from a bulk phase to the catalyst surface [2].
- The second step is the adsorption of reactants.
- The third phase involves the photocatalytic reaction. The processes involved in this step includes photon absorption by the catalyst, formation of electrons and holes and charges generated by photons are transferred to the surface of the catalyst to induce reaction.
- The fourth step is product desorption.
- The last step is the transfer of the products from the surface to the fluid [27].

2.6.1 Radical Formation from Electron-Hole Pairs

The third step involves the absorption of light by a catalyst (which is usually a semiconductor). A semiconductor photocatalytic material absorbs light with photon energies that are the same or greater than the band gap, $hv \geqslant E_g$, creating an electron in the conduction band e^-_{cb} and a hole in the valence band h^+_{vb} of the semiconductor [2]. The reduction process is represented by the following equations:

$$TiO_2 + hv \rightarrow e^-_{cb} + h^+_{vb} \tag{2.7}$$

The electron acceptor produces super-oxide anion radicals, according to equation,

$$e^-_{cb} + O_2 \rightarrow {}^{\bullet}O_2^- \tag{2.8}$$

Positive holes are trapped by surface hydroxyl groups forming reactive hydroxyl radicals.

$$h^+_{vb} + OH^- \rightarrow {}^{\bullet}OH \tag{2.9}$$

The ${}^{\bullet}O_2^-$ formed in the reduction process is protonated to a hydroperoxyl radical $\mathrm{HO}_2^{\bullet}$ (or ${}^{\bullet}HOO$ in the equations here). The hydroperoxyl radical formed reacts with the electron-hole pair to produce hydrogen peroxide. The following equations represent the formation of hydrogen peroxide:

$${}^{\bullet}O_2^- + H^+ \rightarrow {}^{\bullet}HOO \tag{2.10}$$

$$2{}^{\bullet}HOO \rightarrow H_2O_2 + O_2 \tag{2.11}$$

$$H_2O_2 + {}^{\bullet}O_2^- \rightarrow {}^{\bullet}OH + O_2 + OH^- \tag{2.12}$$

2.6.2 The role of dissolved oxygen

TiO_2 mediated photocatalysis can act via two different routes (as shown in figure 2.5). The main photocatalytic degradation route is through the generation of hydroxyl radicals by the photo-generated holes at the surface of the nanoparticles. Another photocatalytic reaction route is through the generation of superoxide radicals by photo generated electrons. This reaction pathway depends critically on the concentration of dissolved oxygen in the aqueous dye medium. All my experiments were performed in closed (but not airtight) reaction vessels. This was to minimise water loss through evaporation, which would affect the concentration of the dye. Consequently, I believe that the concentration of oxygen was always constant throughout our experiments, especially since the water in the reaction vessel was constantly mixing through circulation. I did consider designing bespoke dissolved oxygen experiments, but this would have required building an airtight reaction vessel where the concentration of oxygen could be controlled. There was not time for this during my PhD, but this is certainly a promising route for future investigations.

2.6.3 Decomposition of the Organics

There are several ways in which organic contaminants can be destroyed through RedOx processes. The $^{\bullet}OH$ formed causes photodegradation of organic contaminants by the following equation

$$R + {}^{\bullet}OH \rightarrow R^{'\bullet} + H_2O \tag{2.13}$$

Hydrogen ions also cause photodegradation of the contaminants by the following equation:

$$R + h^{+} \rightarrow R^{+\bullet} \rightarrow degradation \tag{2.14}$$

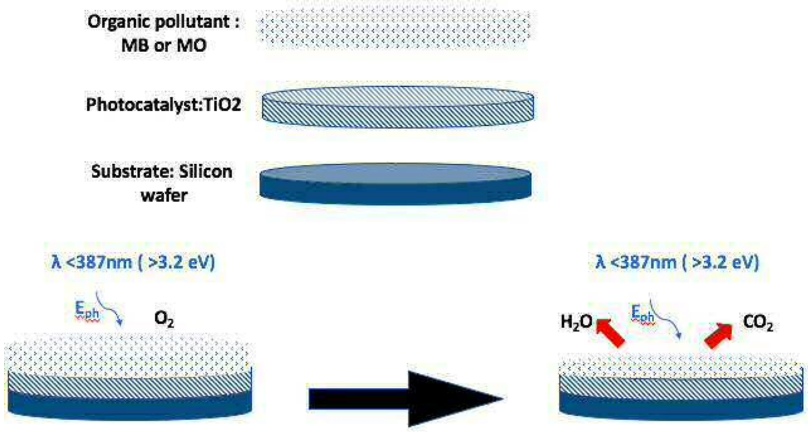

Figure 2.8: The photooxidation of an organic pollutant on a photocatalyst surface

2.7 Test Pollutants (Organic Dyes)

Many of the organic pollutants that people might want to remove from water are toxic (benzene compounds are carcinogenic and dioxins are thought to be mutagenic). Researchers typically want to minimise exposure to these chemicals, and so we need a safer approach to study the photocatalytic degradation of these toxic chemicals. To get around this problem we exploit safer organic dyes which contain many of the chemical structures that we might want to destroy (such as benzene rings). The experiments in this thesis uses methylene blue (MB) and methyl orange (MO) to represent organic pollutant that should be decomposed by photocatalyst process.

Methylene blue is a green crystal that turns blue when mixed with water. The chemical formula for MB is given by :

$$C_{16}H_{18}ClN_3S \tag{2.15}$$

The molecular structure of the compound is given by the figure below. The blue colour formed by the solution of water and methylene blue also acts as an indicator of the experiment. The change in colour of the solution from blue to clear will indicate that methylene blue has been decomposed.

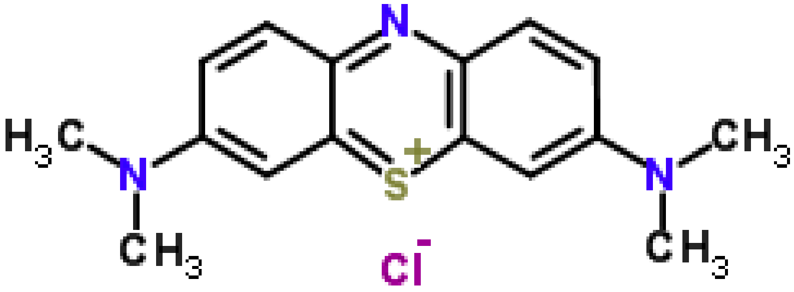

Figure 2.9: Methlyne blue molecular structure

Methyl orange is a pH indicator frequently used in titrations because of its clear and distinct colour change. Because it changes colour at the pH of a midstrength acid, it is usually used in titrations for acids. The chemical formula for MO is given by:

$$C_{14}H_{14}N_3NaO_3S \tag{2.16}$$

The molecular structure of the compound is given by the figure below. These two non-toxic dyes can be compared in structure to some known problem pesticides. For example, there is an important family of pesticides known as the pyrethroids. They

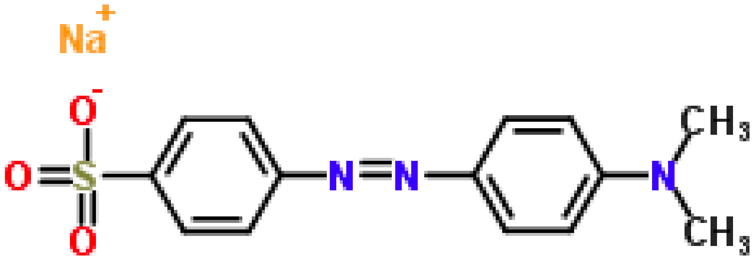

Figure 2.10: Methyl orange molecular structure

are commonly found in residential insecticides, for ant control, home lawn, garden and landscape care, as well as in structural pest control products. Common pyrethroid active ingredients in home use products include bifenthrin, cypermethrin, permethrin, and cyfluthrin. Pyrethroids attach to soil particles and are washed into waterways on sediment. They are particularly toxic to fish and invertebrates.

Another class of exceedingly toxic pesticides (which are now banned) are the organophosphates diazinon and chlorpyrifos. They are nerve poisons and act by inhibiting important enzymes in the nervous system in animals.

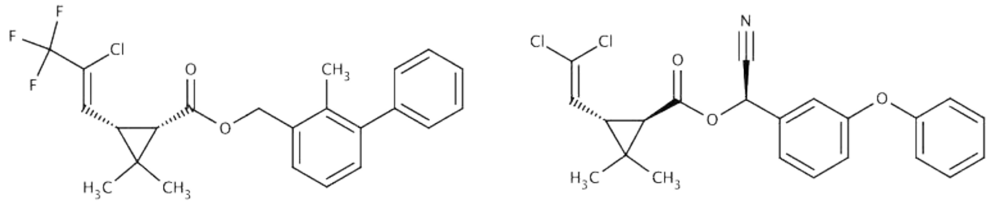

(a) Bifenthrin (b) Cypermethrin

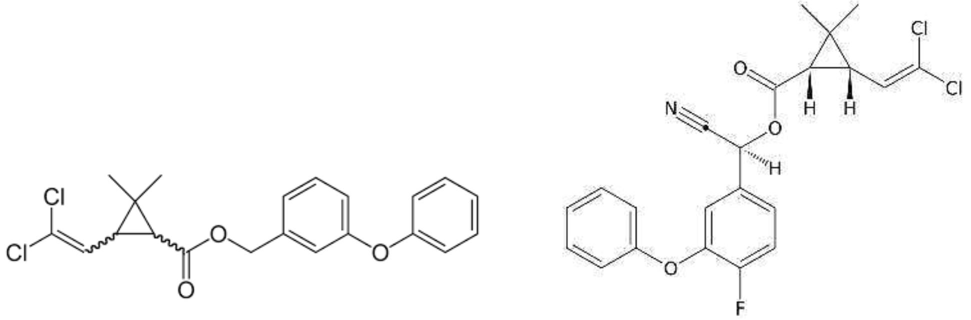

(c) Permethrin (d) Cyfluthrin

Figure 2.11: Common problem pesticides from the pyrethroid family.

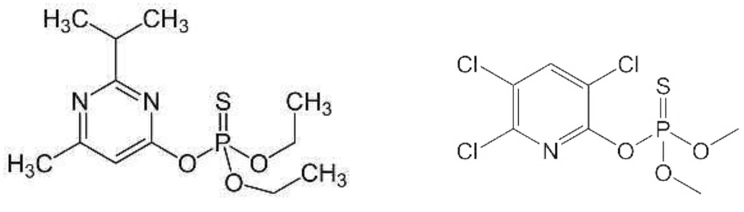

(a) Diazinon (b) Chlorpyrifos

Figure 2.12: Two now-banned organophosphate pesticides.

2.7.1 MB degradation

The full degradation pathway for MB is quite complicated. It has been discussed in considerable depth in [43], and the reactions described below have been taken from this reference.

The initial step of MB degradation is the the cleavage of the bonds of the [C-S^+=C] functional group, according to,

$$R - S^+ = R + OH^\circ \rightarrow R - S(=O) - R + H^+ \tag{2.17}$$

The electrophilic attack of OH° on the free doublet of heteroatom S, makes its oxidation state pass from 2 to 0. However, the passage from C-S+= C to C-S(=O)-C requires the conservation of the double bond conjugation, which induces the opening of the central aromatic ring containing both heteroatoms, S and N. The sulfoxide group can undergo a second attack by an OH° radical producing the sulfone radical (not-detected) and causes the definitive dissociation of the two benzenic rings.

$$NH_2 - C_6H_3(R) - S(=O) - C_6H_4 - R + OH^\circ \rightarrow NH_2 - C_6H_3(R) - SO_2 + C_6H_5 - R \tag{2.18}$$

and/or

$$NH_2 - C_6H_3(R) - S(=O) - C_6H_4 - R + OH^\circ \rightarrow NH_2 - C_6H_4 - (R) + SO_2 - C_6H_4 - R \tag{2.19}$$

The sulfone can be attacked itself by a third OH° radical for giving a sulfonic acid[43].

$$SO_2 - C_6H_4 - R + OH^\circ \rightarrow R - C_6H_4 - SO_3H \tag{2.20}$$

The final release of SO_4^{2-} ions can be attributed to a fourth attack by OH°.

$$R - C_6H_4 - SO_3H + OH^\circ \rightarrow R - SO_4^{2-} + 2H^+ \tag{2.21}$$

The radical R-$C_6H_4^\circ$ can subsequently react either with OH° giving a phenolic compound or with a H° radical. Concerning the mineralization of the three nitrogen-containing groups in MB molecule, two cases have to be examined. First, the central imino-group undergoes a N=C double bond cleavage induced by the cleavage of the double bond of the -S+= group in para position in the central aromatic ring. The saturation of the two amino bonds is obtained by H° radicals mentioned above, yielding a substituted aniline. As previously observed, the amino group can be substituted by an OH° radical forming the corresponding phenol and releasing a NH_2° radical which generates ammonia and ammonium ions, estimated to be primary products.

$$R - C_6H_4 - NH_2 + OH^\circ \rightarrow R - C_6H_4 - OH + NH_2^\circ \tag{2.22}$$

$$NH_2^\circ + H^\circ \rightarrow NH_3 \tag{2.23}$$

$$NH_3 + H^+ \rightarrow NH_4^+ \tag{2.24}$$

The other two symmetrical dimethyl-phenyl-amino groups undergo a progressive degrading oxidation of one methyl group by an attack by OH° radical producing an alcohol (not detected), then an aldehyde, which is spontaneously oxidized into acid, which decarboxylates into CO_2 through the photo-Kolbe reaction.

$$R - C_6H_4 - N(CH_3)_2 + OH^\circ \rightarrow R - C_6H_4 - N(CH_3) - CH_2^\circ + H_2O \tag{2.25}$$

$$R - C_6H_4 - N(CH_3) - CH_2^\circ + OH^\circ \rightarrow R - C_6H_4 - N(CH_3) - CH_2OH \tag{2.26}$$

$$R - C_6H_4 - N(CH_3) - CH_2OH + OH^\circ \rightarrow R - C_6H_4 - N(CH_3) - CH^\circ - OH + H_2O \tag{2.27}$$

$$\begin{aligned} R - C_6H_4 - N(CH_3) - CH^\circ - OH + OH^\circ &\rightarrow R - C_6H_4 - N(CH_3) - CH(OH)_2 \\ &\rightarrow R - C_6H_4 - N(CH_3) - CHO + H_2O \end{aligned} \tag{2.28}$$

$$R - C_6H_4 - N(CH_3) - CHO + OH^\circ \rightarrow R - C_6H_4 - N(CH_3) - C^\circ = O + H_2O \tag{2.29}$$

$$R - C_6H_4 - N(CH_3) - C^\circ = O + OH^\circ \rightarrow R - C_6H_4 - N(CH_3) + COOH \tag{2.30}$$

$$R - C_6H_4 - N(CH_3) - COOH + h^+ \rightarrow R - C_6H_4 - N^\circ - CH_3 + H^+ \tag{2.31}$$

Subsequently, the phenyl-methyl-amine radical is degraded, probably by successive attacks by OH^- radicals. The aromatic ring will undergo hydroxylations producing phenolic metabolites, hydroxyhydroquinone being the last aromatic compound detected before the ring opening. The amino group can form ammonium ions as developed above, which are slowly oxidized into nitrate or can be directly oxidized into hydroxylamine leading also to nitrate. Many other hydroxylated intermediates have certainly been formed but they were difficult to detect because of their poor extractability owing to their hydrophilic character [43].

When the dye is broken down and the color disappears, we could assume that other organic substances and micro-organisms have also been broken down and the water is now safe to drink. It is non-toxic and the doses people can withstand have been well-researched. By the time that methylene blue is broken down, other organic substances and micro-organisms have also been broken down. Methylene blue would also support the destruction of micro-organisms in its own right. It absorbs red light and generates free radicals which attack micro-organisms. A greater proportion of the visible spectrum could be used and more hydroxyl free radicals generated which attack micro-organisms [44].

2.8 Doping of TiO_2 Semiconductor Nano-particles

A key aspect of this PhD research was to explore whether TiO_2 could be modified to access more of the solar spectrum. This was achieved by doping. For simple elemental semiconductors such as silicon, substitutional doping is most effectively achieved by replacing a silicon atom with a similar sized atom with a different electronic configuration, i.e. from group-III (such as boron) or group-V (such as phosphorus). In the case of TiO_2 it is sensible to achieve doping by substituting nearby elements from the periodic table grouping, i.e. other transition metals. I opted to dope TiO_2 with transition metal elements (TME) to try to change (lower) the band gap. TiO_2 on its own has a relatively wide band gap, necessitating light wavelengths below 387 nm for electron and hole separation. It is worth noting that the content of UV light is approximately 3-5%, which limits the applicability of photocatalysis using solar light [45]. More recent studies investigate the detailed impact of chemical and physical properties of (TME) nanoparticles, such as the dependence of gel fil refractive indices on the said materials. Researchers are also working on other methods to expand the light absorption range of TiO_2: incorporating an organic dye as a photo-sensitiser, and doping using non-metallic elements. Thus, numerous research has been directed at augmenting the photocatalytic activity of TiO_2 towards the visible spectrum. It is true to say that appropriate modifications of the mentioned material can induce desired activity.

The photocatalytic process is influenced by several factors beginning with the mass of the photocatalyst, which is directly proportional to the said reaction up to a specific point where there is a full absorption of photons. The preceding activity is also affected by the wavelength of irradiation and temperature. Notably, the photocatalytic reaction is optimal between 20 °C and 80 °C [45]. Photocatalytic reactions are also proportional to the radiant flux up to a specific value that is dependent on experimental conditions. As such, the photocatalytic reaction is affected primarily by charge creation and recombination, light parameters and absorption, as well as surface reactivity [46]. One of the main results in my thesis is that doping TiO_2 with transition metal elements nanoparticles significantly augments the ability of TiO_2 to treat water.

2.8.1 Properties of Transition Metal Elements

The transition metal elements are the elements that have partially filled d-orbitals. Transition metals usually form complexes that are vibrantly coloured. The elements in block d in the periodic table are divided into four transition series in the periodic table. The transition elements have some important physical and chemical properties. Their densities are high and they are mechanically strong. Both their boiling and melting points are very high. They form paramagnetic compounds. Their oxidation states are variable. They usually form coloured compounds and ions. The compounds formed from these elements tend to have high catalytic activities. The complexes formed from these elements are very stable.

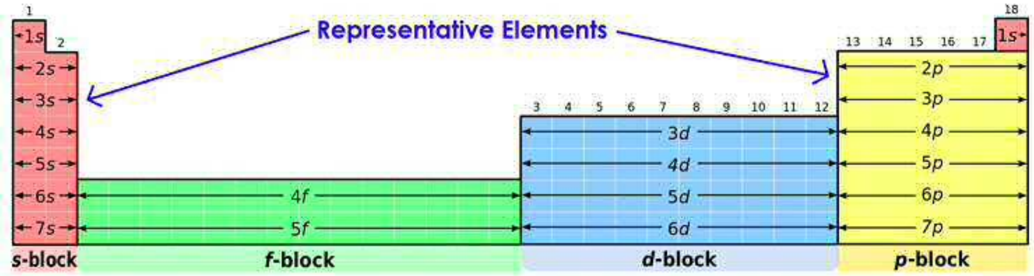

Figure 2.13: The diagram represents the representative elements. The transition elements are found in the d-block.

[47]

An examination of the chemical properties of these elements shows that these elements are much denser than the elements in the s block. Along the first period, the elements increase in density from scandium (Sc) to copper (Cu). Their density trend is as a result of a small and irregular decrease in their radii which is comprised of an increase in the relative atomic mass. Compared with the main group elements, the melting points and the fusion molar enthalpies of these metals are high. This is because of metallic bonding in these metals that is very strong which is caused by delocalization of electrons facilitated by the presence of both s and d electrons [48]. These metals can form compounds that have a wide range states of oxidation. When we move from left to right across the periodic table, the common oxidation states number increases at first to a maximum toward the middle of the table then starts to decrease. For scandium and manganese elements which are on the first half of the first transition series, the highest oxidation state corresponds to the loss of all their electrons both in d and s orbitals of their valence shells [49]. The highest oxidation states are scandium (Sc), vanadium (V), and titanium (Ti) which are the most stable. As one continues through the series, it is not possible to remove the valence electrons from the metals. The atoms of the transition elements in the first row have a similar electronic configuration. Starting from scandium, there is the gradual filling of the orbitals that are 3d across the series. At chromium and copper, the filling is not regular and the acquisition of an electron from the 4s shell results as the population of the 3d orbitals increases. These metals show a wide range of chemical behaviours. Some of these transition metals are powerful reducing agents while others have very low reactivity [50].

2.9 Comparing Pristine & Doped Semiconductors

In pristine conditions, a P-N semiconductor has equal numbers of positive vacancies or holes in the p region and an equivalent number of negative electrons in the n region. This condition leads to the generation of a depletion barrier that does not allow the passage of electrons or holes across the border. In the second state, the conduction band and the valence band have some doped entities inside them, which has increased the level of energy in the area in between. The transference of electrons from CB to VB is equal to the rate of transfer of holes from VB to CB, which renders the overall state of the semiconductor in equilibrium. Lastly, the band gap is narrowed by the increase of doped regions in the VB, and consequent decrease of the depletion barrier energy required for jumping of holes from VB to CB.

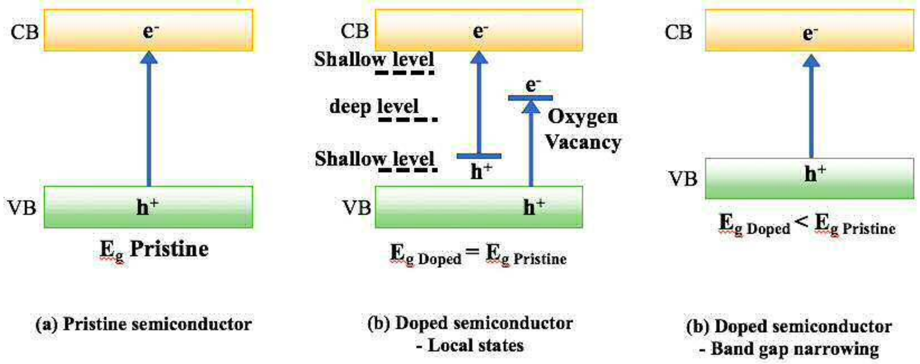

(a) Pristine semiconductor

(b) Doped semiconductor - Local states

(b) Doped semiconductor - Band gap narrowing

Figure 2.14: The diagram shows (a) the pristine semiconductors, (b) doped semiconductors and local states, and (c) doped semiconductors with band gap narrowing

2.9.1 Engineering the Band Gap of TiO_2

Normally TiO_2 is un-doped, i.e. it does not have any impurity elements with a different number of valence electrons that act as donors or acceptors, which would lead to shrinking of the large intrinsic band gap. Normally a quantum (photon) of 3.2 eV is required to make a transition between the conduction and valence bands for the anatase phase (3.06 eV for rutile). Substitution doping using other transition elements is possible in the crystal. If transition elements different from tungsten are used, the substituted atoms may be different in size and displace the atoms of the titanium dioxide. This may decrease the energy required for transference of electrons to the conduction band to below the 3.06 eV band gap of the rutile phase. Another possibility is interstitial doping. Atoms whose size is very different from tungsten may lie at interstitial points within the TiO_2 crystal structure. This allows easier movement of energy and charge carrying, and consequently decreases the energy barrier required for the electron to move into the conduction band.

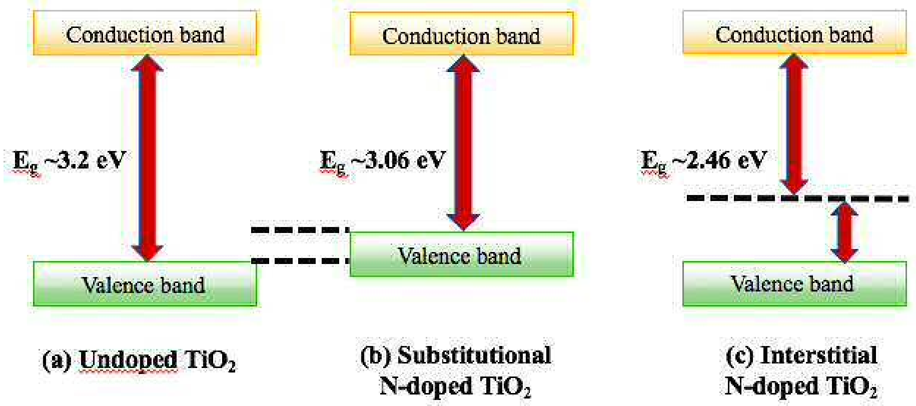

Figure 2.15: The diagram shows (a) undoped TiO_2, (b) substitutional N-doped doped TiO_2 ,(c) interstitial N-doped TiO_2

2.10 Conclusions

I have gathered all of the relevant background science together in this chapter. It is clear that the research topic crosses many different disciplines within material science. While some the aspects of involving the photocatalysis are clearly in the chemistry domain, I wanted to make a strong connection to physics of the base photocatalytic material, (TiO_2). TiO_2 is a wide band gap semiconductor, and its photocatalytic properties arise precisely because it is a semiconductor. It is through the interaction of light in generating electrons and holes, that the catalysis process is facilitated. The limitations of the base TiO_2 material come about because of its wide band gap, which restricts the amount of the solar spectrum that can be usefully accessed. One of the main aims of my PhD research was to explore how the TiO_2 band-gap could be modified through doping. This aspect of material property modification lies in the physics world.

Chapter 3

Nano-Films for Photocatalysis Experiments

3.1 Introduction and Overview

Many possible avenues exist for undertaking photocatalysis research, and the research direction is often dictated by some of the early decisions. While it is common to perform catalysis experiments in Cardiff Chemistry by adding the TiO_2 powder directly to the reaction mixture, this makes optical monitoring of the reaction rate more difficult. I decided earlier to fix the photocatalyst on a wafer. Spin-coating became the chosen method of preparing the photocatalytic nano-films. However, an immediate question arose regarding how to find a reproducible quantifiable way to estimate the amount of photocatalytic material used during each reaction (in other words the nano-film thickness). This proved much more challenging than I originally envisaged, and unsuccessful methods were tried before I finally hit on a solution. All the contact methods tried ultimately failed because of the low adhesion of the films to the substrate. Optical methods also failed, mostly due to scattering resulting from random size of the nano-particle agglomeration in the film. I also tried to measure the mass of the films directly, and while this provided a rough estimation, the experimental error was too large to make this a practical method. This nano-film characterisation problem continued throughout the course of my PhD research until I finally hit on a technique which worked. I found a method to encapsulate the nano-films and measure the thickness directly through mechanical sectioning. This chapter describes the manufacture of the nano-films used throughout this research for photocatalysis and the methods used to characterise the nano-films.

3.2 Slurry vs Fixed-Bed Systems

Various methods of treatment in photocatalytic processes have been implemented since the 1990's [51]. Two methods are worth some further discussion. The first of these methods is to form a suspension of granular or powder form of the catalyst in water, a process known as the slurry method. This method has obvious advantages in terms of simplicity. The slurry system has an advantage of presenting a higher surface-to-liquid interface area, enabling a higher efficiency generation of reactive oxygen species as well as direct interaction with the pollutant elements in the water. However, the slurry method also presents an obvious disadvantage. The catalyst is thoroughly mixed through the liquid. From a practical standpoint, this would entail the eventual separation of catalyst from the water. Another practical problem is that the slurry mixture is optically opaque (it bears a close resemblance to milk) and this precludes any sort of optically facilitated monitoring of the ongoing reaction. The other immediately obvious method is to fix the catalyst on some sort of substrate or scaffold. This is essentially what is done in the catalytic convertor of a car exhaust. In our system, this method is referred to as fixed bed photocatalysis. While this method mitigates the problems just discussed regarding slurry systems, it does bring with it new additional problems. Fixing the photocatalyst is far from trivial. Photocatalyst adhesion over the long-term may also be a problem depending on the fixing method used. We chose the latter of these two methods primarily because we wanted to study the photocatalytic reaction rate in real-time using optical monitoring.

3.3 An Overview of Thin-film Deposition

Thin-film deposition is the technology that, as the name suggests, involves the application of an extremely thin material film to a substrate so as to be crusted-over, or to form deposited coatings to produce layers. There are both chemical and physical processes involved in this technology. The various methods are summarised on the tree-diagram in figure 3.1 over the page. It is worth spending a little time briefly discussing pros and cons of the various processes.

3.3.1 Physical Coating Processes

Evaporation

Evaporation methods are largely applied in the production of thin layers. Many materials can be evaporated and, in case the process takes place in a vacuum system, then it will be under much reduced temperatures, thereby reducing the volume of impurities in the developing. Evaporation in a vacuum involves the use of vapour form to aid the evaporant as well as to produce the heat necessary for the process, while permitting the evaporant's charge to rise to a temperature that is enough to yield the preferred vapour pressure. Different forms of evaporation include...

- **Ion plating:** Ion plating is a type of vacuum deposition. It applies the substrates simultaneous or episodic bombardment, and releases the film by very

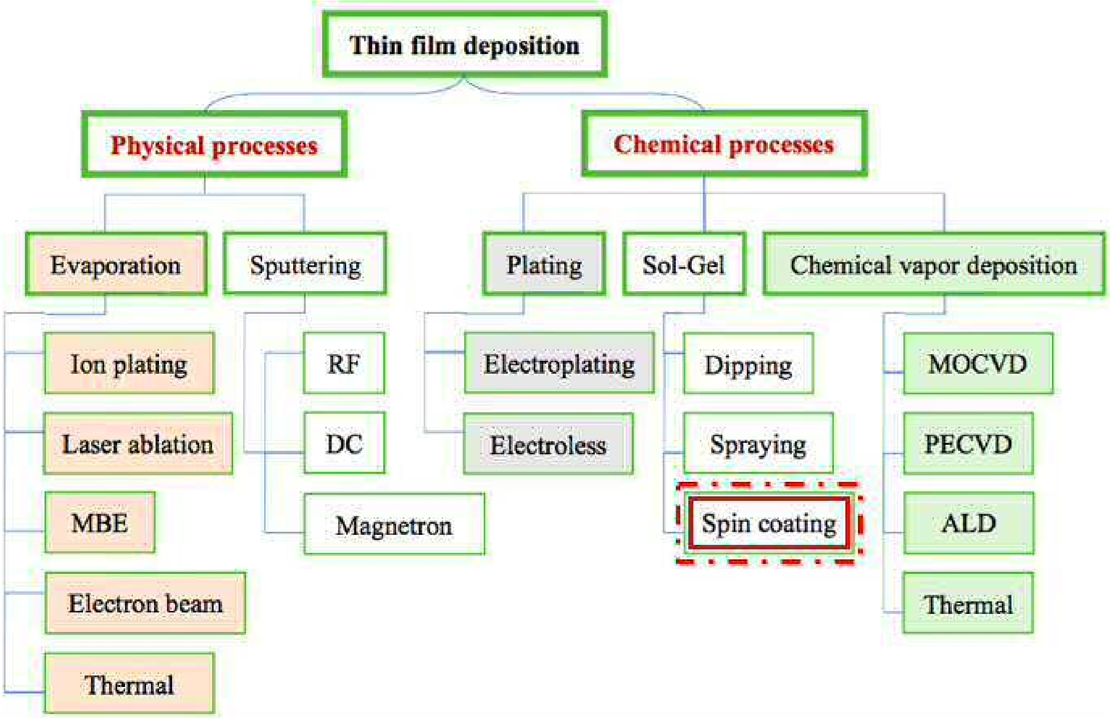

Figure 3.1: Illustration the film deposition process

small-sized active bits. During the process of ion plating, the energy, stability as well as the mass of the shelling species together with the ratio of the bits to depositing particles are essential processing factors [52]. The material which is supposed to be deposited is vaporised through evaporation. However, sometimes spluttering can also be used to vaporise it.

- **Laser ablation:** This process removes a specific material from a particular surface by applying a laser beam to it. At small laser flux, the particular material gets heated by the laser energy, making it either sublime or evaporate. When the laser flux becomes high, the material gets transformed in to a plasma. Normally, this process involves the removal of a material by use of a pulsed laser, although one can still use a continuous wave laser beam with sufficient laser intensity.

- **Molecular Beam Epitaxy:** In the MBE process, the material may be evaporated or sublimated from effusion cells, hence producing beams which are formed on the heated sample. It is mostly used for the deposition of single crystals.

- **Electron beam:** This is a type of deposition where the targeted anode is shelled with an electron beam produced by a tungsten wire which has been a charged in high vacuum. The beam makes atoms in the anode change into the vaporous stage. The atoms are subsequently precipitated into solid form, forming a coat on everything that is inside the vacuum chamber with a slim layer of the material of the anode.

- **Thermal Evaporation:** This is a common vapour deposition technique, probably the simplest. It normally applies a resistive source of heat to evaporate a solid element inside a vacuum to produce a thin film. The heating occurs inside vacuum chamber till vapour pressure is formed. The material then coats the vacuum chamber, assisted by thermal energy and forms a coat on the substrate.

Sputtering

Sputtering takes place when a gas plasma is applied on a particular substrate in extremely small particles. The effect of the particles activates a collision effect, which makes most of them to pass through the substrate, coating the whole substrate surface. Different forms of spluttering include...

- **Ratio frequency (RF) Sputtering:** This is the method used in interchanging the electrical potential in the vacuum setting so as to keep the charge from increasing on particular types of sputtering materials, which can periodically lead to arcing into the plasma that discharges drips, leading to quality control problems on the thin films, or sometimes total interruption.
- **Direct current (DC) Sputtering:** This is a cheap and simple deposition technique which involves the coating material being shelled with ionised gas particles, hence sputtering atoms into the plasma. When the atoms condense, they get deposited on the substrate in very thin films.
- **Magnetron Sputtering:** This is a vapour deposition technique where the plasma is formed and the ions in the plasma, which are positively charged, are fast-tracked by an electrical field overlaid on the substrate, which in this case is negatively charged.

3.3.2 Chemical processes

Plating

This process involves the immersing of a substrate into a chemical bath, usually made up of a mixture of water and metal salts meant to be deposed. The metal salts apply on the substrate uniformly, forming a thicker film the more the substrate if immersed. There are two types of plating:

- **Electroplating:** This is a specialised plating method which applies electricity. When the substrate is connected to a powered anode, the metal elements present in the liquid start forming a film on the substrate surface through oxidation. Various metals coat at different speeds and amount. However, a higher charge means that the coating will be thicker.

- **Electroless Plating:** This a non-galvanic technique of plating where numerous concurrent reactions are applied in an aqueous solution. The difference between this and electroplating is the fact that it does not use external electric power.

Sol-gel

Sol-gel is a means of creating solid materials from tiny molecules. It is mainly applied for metal oxide fabrication. The types of sol-get processes include:

- **Dip coating (Dipping):** This is an industrial coating method which is applied, for instance, in the production of bulky goods like coated fabrics or condoms and dedicated coatings especially in the biomedical industry.
- **Spray Coating (Spraying):** This is the industrial coating method used for car painting, it is also the same method applied by spray artists who use cans. The ink used is atomised at the spout of the spray can, hence producing a constant droplet stream [53].
- **Spin Coating:** This was the method used during my research, and I will expand on it further later on.

Chemical Vapour Deposition

This is a material fusion technique where the components of the vapor stage react together to create a solid film on the surface. It does not involve any liquid bath; the substrate put in a chamber that is under pressure and filled with organometallic gas. Examples include:

- **Metal Organic Chemical Vapour Deposition (MOCVD)**: This is a technology applied in the deposition of extremely thin atom layers onto a semiconductor wafer (these are very thin disks, typically a fraction of 1 mm thick, usually made of silicon.)
- **Plasma Enhanced Chemical Vapour Deposition (PECVD)**: This is a deposition technique applied in the deposition of very slim films through vaporisation (solid to liquid). During this process, various chemical processes and reactions are applied.
- **Atomic Layer Deposition (ALD)**: This is a thin-film deposition method that is dependent on the chronological application of a gas period chemical procedure. It can be considered a sub-branch of chemical vapour deposition.
- **Thermal Deposition**: This refers to a synthesis technique involving the substrate being heated between 600 °C and 800 °C and then exposed to the reactants, which decompose to form a deposit.

3.4 Preparation of TiO_2 Photocatalytic Films

As discussed, there exist various film coating methods, including spin coating and sol-gel dip coating. In the case of sol-gel dip coating method, the TiO_2 catalyst is immobilised on discs of a particular substrate, for example a stainless steel mesh and flat plates. Then, the substrate is dipped horizontally onto the catalyst, thereby creating a photo-reactive surface, through which the wastewater will flow. In this research, the spin coating method was preferred because it enables the quick formation of the very uniform film, whose thickness falls in the sub-micrometer range.

3.4.1 Spin Coating of Thin-films

Spin coating refers to a method of depositing an even film on a flat substrate. A device called a spin coater is used. In this process, small quantities of the coating material are deposited at the centre of the substrate, after which, slow to fast spinning is conducted. As such, the coating material is distributed on the surface by centrifugal force, the spinning disk causes the liquid to be forced towards the edge, as shown in figure 3.2. If conducted properly a thin layer of the coating material to result. Here, the rotation speed is one parameter that controls the thickness of the film. Coatings will normally be thicker for slow spin speeds, and thinner for faster spin speeds. The viscosity of the solvent containing the material is another parameter which can be used to control the coating thickness. The solvent is usually a volatile liquid, which will evaporate as the rotation is conducted. Another reason for opting for the spin coating method is because it is highly repeatable and can be well-controlled. The variation between thin-films is negligible because there is less time for the solvent to evaporate during spinning and the ramp time is not of critical concern, given that the substrate quickly reaches the desired spinning speed of 3000 rpm before any drying takes place [54]. However, a low spinning speed does not always yield a complete

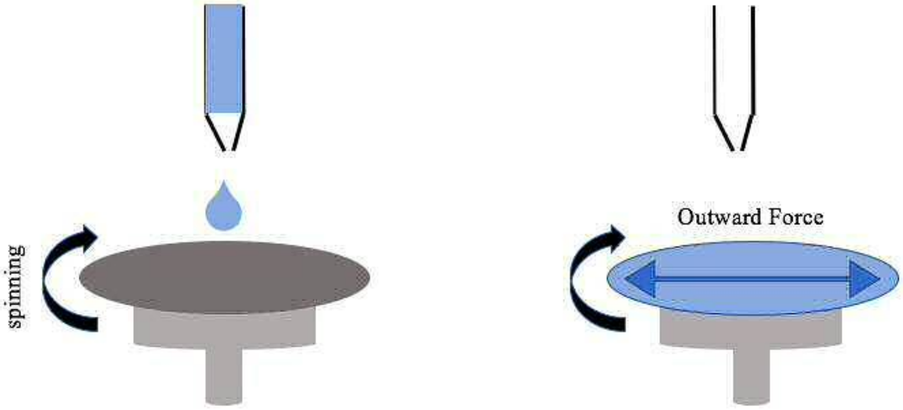

Figure 3.2: Illustration of the spin coating process

substrate coverage or when a very viscous solution is used because the centrifugal force will not be sufficient to spread the film sufficiently. The method is summarised graphically in figure 3.3.

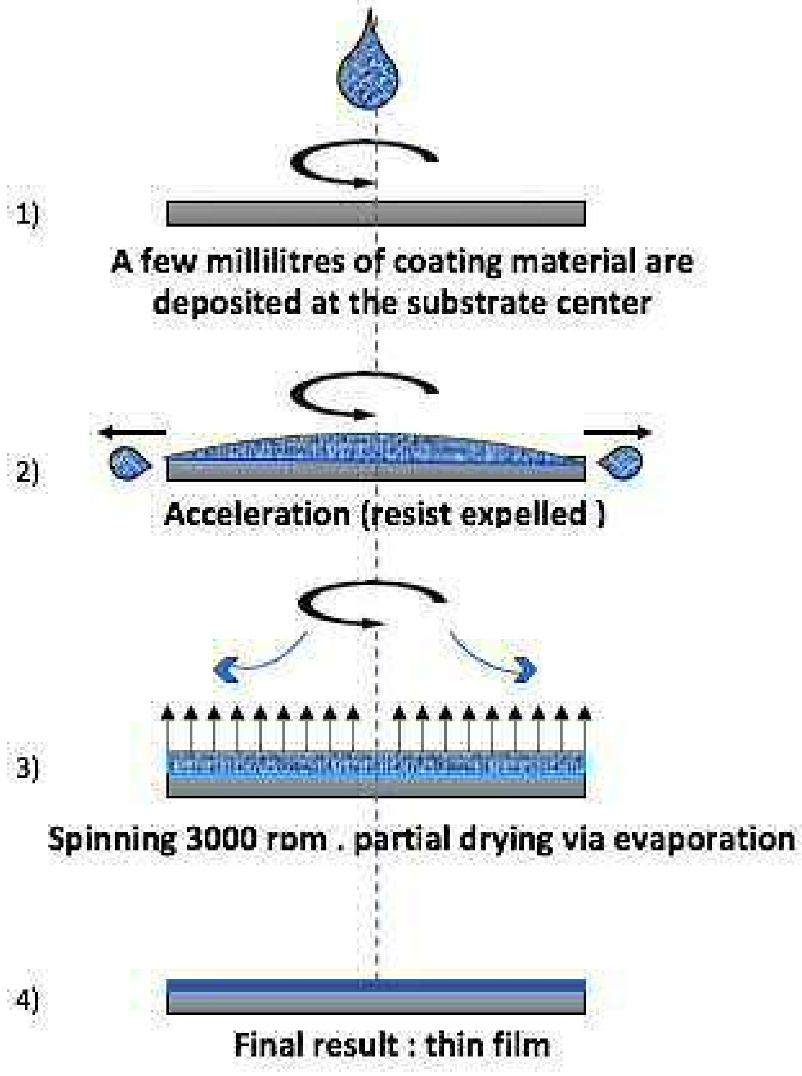

Figure 3.3: The spin coating process

TiO_2 Spin Coating Recipe

The spin coating liquid recipe was adapted from earlier work [55]. For all of the experiments involving un-modified TiO_2, the recipe used was

- 800 mg of titanium dioxide (Degussa P-25)
- 250 μl Triton X-100

- 8 ml of IPA (Isopropyl alcohol - $CH_3CHOHCH_3$)

A small amount of triton X-100 surfactant is added to help wet the substrate and obtain good coverage. A suspension is created through agitation in an ultrasonic bath. Compressed Dry Air (CDA) gas, a spin coater with vacuum chuck, and a hot plate, were used in the preparation and stabilisation of the thin-film on the substrate. An example of the result is shown in figure 3.4.

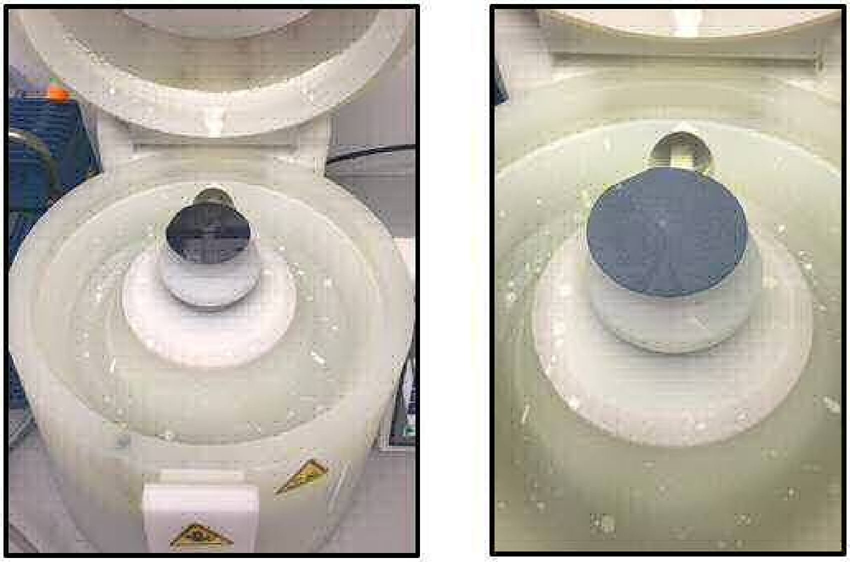

Figure 3.4: (a) A silicon wafer before spin coating (left), and after spin coating with titania (right)

3.4.2 Choice of TiO_2 Support (Substrate)

There are different materials that have been examined to support the TiO_2 to facilitate experiments on the pollutant photo-degradation of in contaminated water. Restrictions can be applied where there is a necessity for transparent or opaque substrates. Practically, the best photocatalyst support has to conform to various conditions. Ideally the support will maintain total adhesion with the TiO_2 photocatalyst and there should be no de-lamination (peeling) of the film. Silicon wafers are a good choice, since they are very pure (and also very clean) [56] and they can be sourced cheaply.

3.4.3 The TiO_2 Suspension

The coating method entailed obtaining 250 μl of Triton x-100 surfactant, which was pipetted into a test tube. This was mixed with 800 mg of Degussa P-25 TiO_2 powder suspended in 8 ml of IPA. The suspension is then agitated in an ultrasonic bath. The suspension is not stable over time, and subsequently separates into two phases (a clear liquid at the top, and a thick TiO_2 liquid near the bottom). The first step in the preparation entailed spinning the TiO_2 which had settled at the bottom of the test tube. It was mandatory to obtain the viscous TiO_2 immediately after settling at the base of the test tube because as evaporation occurs, the titanium dioxide suspension quickly hardens. A pipette was used to transfer 10 mg of solution onto the wafer substrate at a constant angular velocity on the chuck. Then, the chuck was spun for one minute at a spin speed of 3000 rpm. After this step the coated substrate was removed and heated for about 60 minutes at a temperature of 450 °C on a hotplate. This drives off any remaining solvent or Triton-X residue. Notably, selecting a temperature of 450 °C was because this is the ideal annealing temperature for the sub-microstructural transformation of the film [54]. Steps involved in this process are illustrated as shown in the figures below.

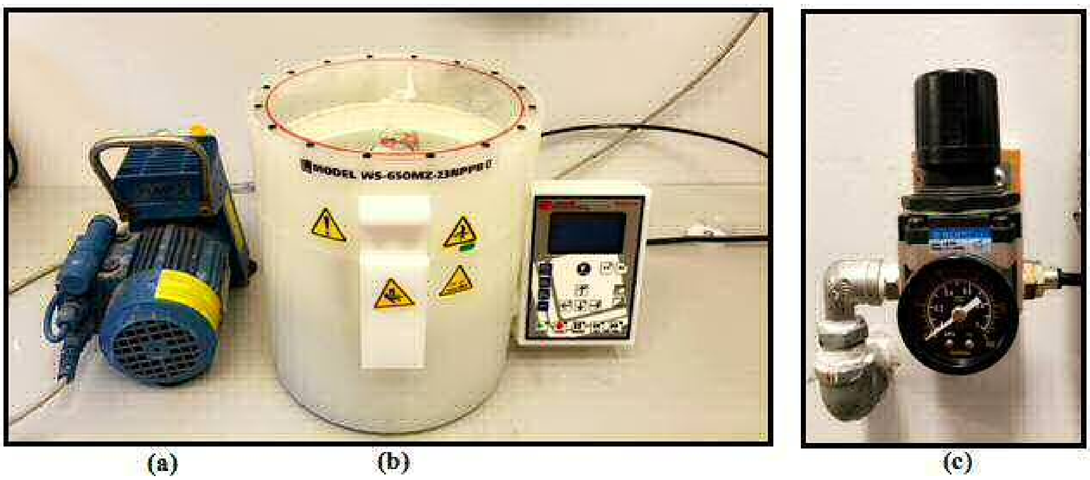

Figure 3.5: (a)The vacuum pump, (b) the spin coater, and (c) CDA gas valve.

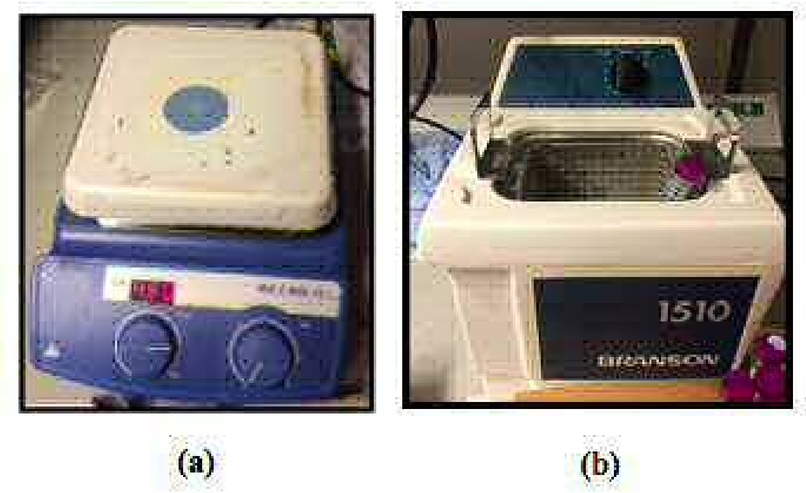

Figure 3.6: (a) Wafer being heated at a temperature of 450 °C to one hour (b) the test tube of suspension was spinning in the ultrasonic bath

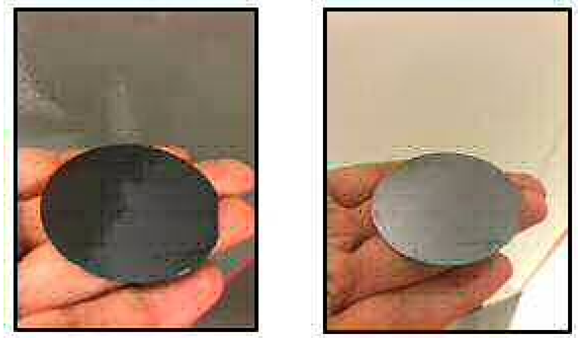

Figure 3.7: The silicon wafer before (left) and after (right) coating with TiO_2 nanoparticles

3.5 Evaluating Spin Coating Film Thickness

One of the reasons for choosing spin-coating is the consistent repeatability of the technique. The thickness of the film formed after the spin coating is dependent on various factors: they include the concentration of the TiO_2 in the coating liquid and the viscosity. Also, the thickness will depend on evaporation rate of the solvent [57]. Notably, the rate of solvent evaporation is in turn dependent on the vapour pressure, the viscosity of the solvent, and temperature of the surroundings. Also, the range of spin speeds will determine the film thickness. In the range of 1000 rpm and above, a uniform film can be achieved, where the maximum speed in most spin coating machines can reach up to 8000 rpm. Specialty coaters exist that can attain speeds of higher than 12000 rpm [57]. All things remaining constant, the thickness of the coating layer should be completely repeatable.

Knowing the thickness of the film is a different matter, and this proved to be one of the biggest experimental challenges during my PhD studies. Measuring the thickness of a spin coating is important because the thickness of a film may affect the efficiency of removal of the pollutants. Here, methods of measuring the thickness include surface profilometry and ellipsometry and interferometry. We tried the usual methods available to us at Cardiff, along with a few additional experimental techniques of our own design. These techniques included the use of a micrometer, AFM, SFM, SEM, and ellipsometry and the colour technique, as well as the Fabry-Perot interferometry. I now discuss these techniques: why we hoped they would work, and why they ultimately failed? Finally, I discuss our solution to this measurement problem at the end of the chapter.

3.5.1 Micrometer Gauges

Micrometers gauges have been used in many areas. This method entails contacting the two edges of a specimen to be measured and finding the span between the two edges. The difference between these two edges is the thickness or length measured. The accuracy attainable is up to 0.001 mm [58]. However, the use of a micrometer requires contact both sides of a workpiece, meaning that there must be tightening. In the case of the TiO_2 film, this process would damage the film. Also the accuracy obtainable is quite course (comparable to the thickness of the film). Thus this method was initially rejected. However, we came up with another way to use a micrometer to measure wafer thickness. For this purpose, six coated wafers were taken and arranged in a stack such that a bare silicon wafer was at either end of the sandwich. The configuration was in the form of (wcwccw) where w represents the wafer and c represents the coating. Measuring the entire stack would provide an approximate measure of the coating thickness by taking the average of all six thicknesses if C1, C2 ..C6 are the individual thicknesses then the average thickness will be calculated as C [59]. The first step towards measurement was to clean the wafers and obtain their weights. This was followed by individual measurement of wafer thicknesses using

Figure 3.8: The thickness of a clean silicon wafer without any coating

Figure 3.9: The different thicknesses of coated silicon wafer with TiO_2 nanoparticles

the micrometer. In order to improve the accuracy of measurement, each wafer was measured at five different locations, one at the center and another four at the four edges. Care was taken to ascertain that the five measurements yielded five numbers close to each other, even being identical if possible. The wafers were then stacked and the same micrometer was used to obtain the stack thickness. Once again, care was taken to ascertain that the number obtained was as close as possible to the sum of the individual thicknesses of the wafers. The measurements were taken at five location as before (one at the center and four edges) [60]. Let the measurements be denoted by W1,W2 .. W6, then their average thickness is W. In that case the average coating thickness, as obtained through mechanical means, is (C-W)/6.

3.5.2 Mass Difference

The difference between the mass of the substrate before and after the spin coating process can also be applied in determining the film thickness. Here, it would entail finding the area of the film, density of the material and then applying the formulation of the resultant film as a disc. As such, the calculation of thickness could be ,

$$t = m/Ad \ , \tag{3.1}$$

where t is the coating thickness, m is the mass deposit, A is the wafer area and d is the density. Notably, the density, which is the intrinsic parameter relating the TiO_2

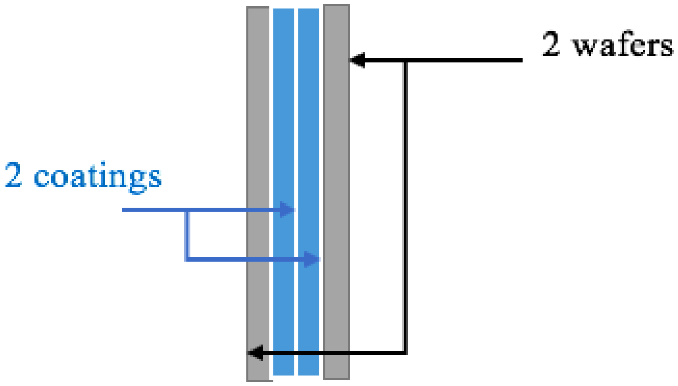

Figure 3.10: Illustration of a stack of two wafers with coating

Figure 3.11: Thickness measurement of a stack of two wafers with coating

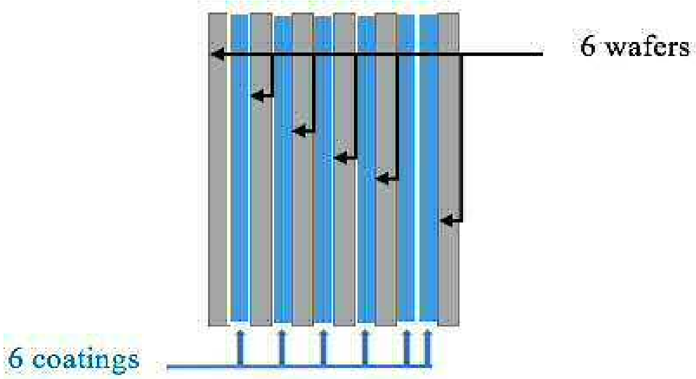

Figure 3.12: Illustration of a big stack of six wafers with coating

Figure 3.13: Thickness measurement of a big stack of six wafers with coating

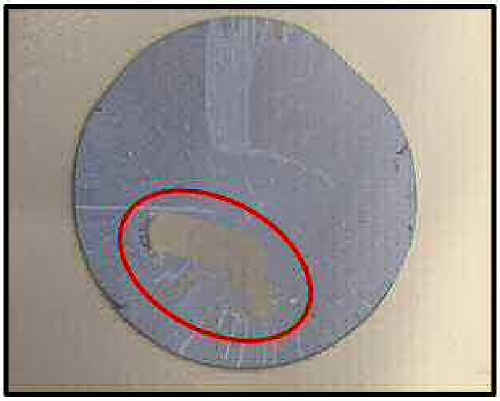

Figure 3.14: Damage that happens to the TiO_2 film by using the micrometer

film and the initial viscous titanium oxide solution prepared, is not a constant. This is because the hydration levels differ as well as the variation in the evaporating constituents. As such, the calculation based on the equation above assumes homogeneity of the film as well as uniformity of the film. These are two assumptions that will significantly affect the results, given the heterogeneous and mesoporous surface nature of the film surface [61]. Also, the measurement of mass will require a measuring device that attains sub-milligram resolution. These is not available, thus the measurement method is not a viable option. As such, this measurement method was reject as well.

3.5.3 Stylus Profilometry (Dektak)

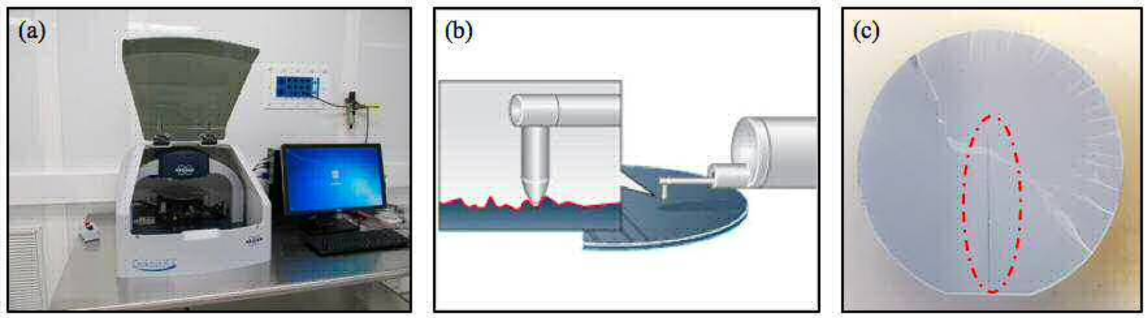

Figure 3.15: (a) The Stylus profilometry machine,(b) illustration of how the tip stylus works,and (c)wafer were scratched due to measuring the thickness by stylus profilometry

Dektak is a diamond-tip stylus profilometer that contacts the sample. It maintains a constant stylus force as the sample stage moves the sample being measured under the stylus tip. The tip will, therefore, trace a profile of the surface, providing a topographic view of the sample. As such, the lateral and height dimensions of the sample are measured, including the roughness of the surface. Dektak was tried using conditions of minimum stylus downward force. However this still resulted in “snow-plowing”, where the TiO_2 material collected in front of the stylus tip. I concluded that this method is not suitable for this research because the tip damages the TiO_2 film as it is dragged along the surface.

3.5.4 Atomic force microscopy (AFM) or Scanning force microscopy (SFM)

This method entails a scanning probe, which will move over the surface, creating a surface probe of the surface using a mechanical probe. The electronic command has piezoelectric elements that facilitate tiny and accurate motion during scanning. As such, the surface profile is measured to sub-micrometer scale, reaching the nanoscale.

However, like Dektak profilometry, the moving mechanical probe removes the TiO_2 wafer. Thus this method was rejected in this research.

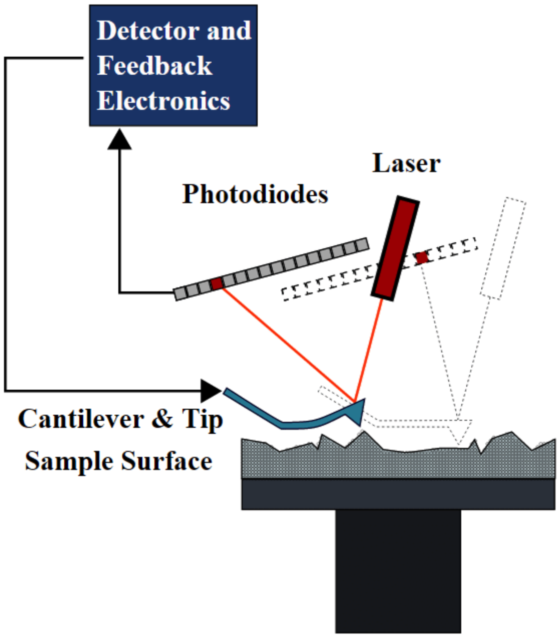

Figure 3.16: Atomic force microscopy
[62]

3.5.5 Scanning Electron Microscopy

Scanning electron microscopy (SEM) uses a focused beam of electrons that scans the surface of the sample being measured. The topography is measured based on the nature of signals received after the electrons emitted by SEM interact with the surface thereof. The convergence of the signals forms an image, which depicts the characteristic of the surface being measured. The resolution attained is high, up to 1 nanometer. The image can provide a cross-sectional analysis (for example including a scratched trench). While this method initially showed promise it did not in the end give the best results. The SEM approach clearly showed the nanostructure of the film from the edge of the wafer, and a thickness measurement could be extracted. However, it is well-known that their are edge effects from the spin coating technique. To get a true estimation of the thickness across the entire wafer, we would need to take a cross-section. One possibility to achieve this would be to make a scratch and view the coating at angle close to edge-on. However, we did not manage to achieve this. Also, the fore-shortening as a result of the viewing angle would need to be accounted for.

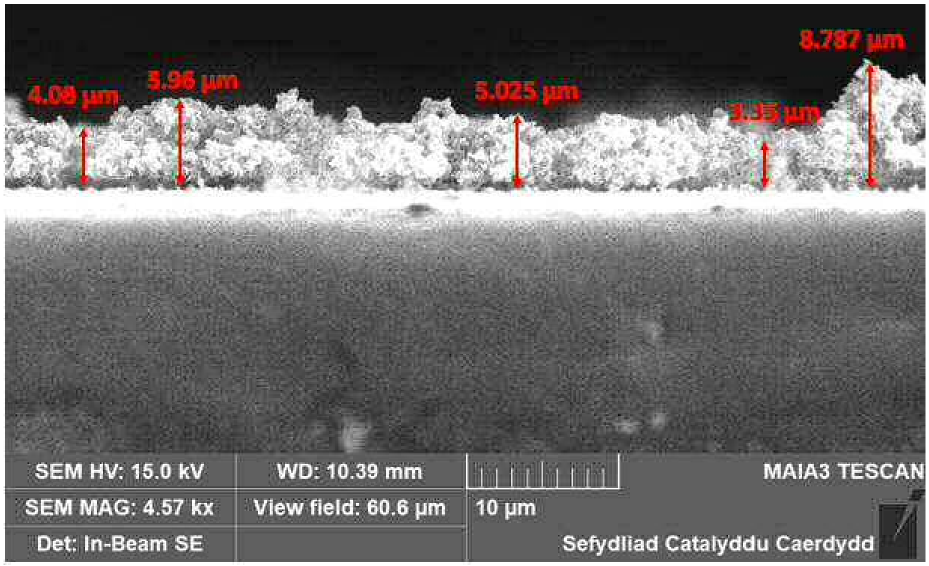

Figure 3.17: (SEM) micrograph of TiO_2 nanoparticles at ×4570 magnification.

3.5.6 Ellipsometry and Spectral Ellipsometry

Ellipsometry entails measuring of dielectric properties of a thin film, based on complex refractive index measurements. Here, the change of polarization upon reflection or transmission of light passing through the sample is compared to a model, after which the properties of the measured surface are derived [61]. As such, this method allows characterization of the thin film, where the composition, thickness and roughness of the surface is measured. This method entails interaction with the surface being measured. A schematic representation of this method is shown in the figure below. Correlation between film thickness and the film index causes some limitations in applying ellipsometry to analyze sub-10-nanometer thick films. However, a comparative study by [51] shows that this method is superior to the reflectometry based methods when applied in the analysis of films whose thickness is lower than 25 nanometer. Another limitation exists because single wavelength ellipsometer is used because there are multiple thicknesses on the film, which may satisfy the thin film equation, thus causing a periodicity problem [51]. The calculation of thickness of the film, based on the thin film equation (from [63]):

$$\rho = \tan{(\Psi)} e^{i.\Delta} = \frac{R_p}{R_s} = \frac{\frac{r_{p01}+r_{p12}e^{-i2\beta}}{1+r_{p01}r_{p12}e^{-i2\beta}}}{\frac{r_{s01}+r_{s12}e^{-i2\beta}}{1+r_{s01}r_{s12}e^{-i2\beta}}} \tag{3.2}$$

$$\beta = 2\pi \frac{d}{\lambda} n_1 \cos{(\theta_1)} \tag{3.3}$$

In spectral ellipsometry, the main difference is that the source is not mono-chromatic. So extra(better) information can be acquired. The first step entails measuring the

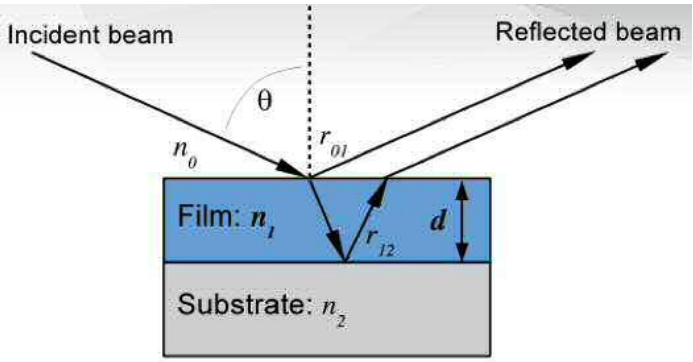

Figure 3.18: A diagrammatic illustration of ellipsometry

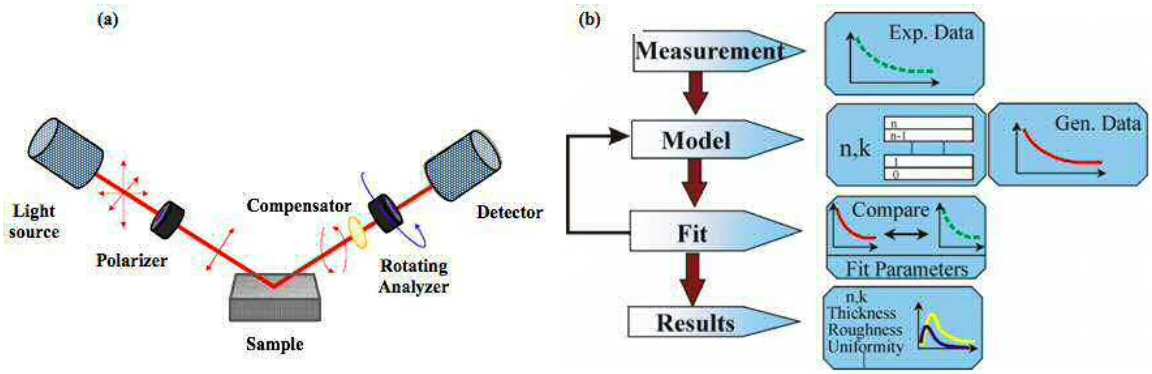

Figure 3.19: (a) Schematic setup of an ellipsometry experiment ,(b) flowchart showing the process of spectral ellipsometry process [64].

sample dimensions followed by creating a model of the sample. Then, Fresnel's equations are applied to describe the thickness and optical constants of the sample are calculated [51]. Then, a comparison of the calculated data and set experimental data is done, and upon harmonisation, the experimental data points can be plotted, and the characteristics of the model are identified. Here, regression analyses are applied, where the estimation is based on linearisation of the plotted data points, using the statistical methods, such as finding the means squared error, a process that is repeated until the least error is attained, meaning that the best accuracy is achieved at the point thereof. It is important to note that this method is desirable because it has unique sensitivity to changes in the optical response of incident ratios, which interact with the samples surface [51]. Here, a plot of the ellipsometer will show the change in polarisation against distance, as the points recorded on the profile of the sample being measured. Here, the change in polarisation is based on the amplitude ratio and phase difference measured. This method requires modelling of the data, to find the specific thickness and crystallinity. Here, the thin film coating equation needs to be applied.

To apply the thin-film coating equation, the film thickness is measured through ellipsometry, where the spin speed is adjusted experimentally to achieve the highest possible accuracy of the data appoints. The maximum film thickness that can be produced will depend on the maximum concentration of the dissolved material in a solvent. As such, a high solubility material such as TiO_2 shall have a concentration of up to 100 milligram/milliliter, thus attaining a thickness of less than 1 micrometer [51]. Low solubility substances whose concentration is about 5mg/ml will attain a thickness of about 20 nm. Notably, the thickness of the film is almost linearly dependent on the concentration of the material in the solvent, but increased concentration will cause an increase in viscosity, which in turn shifts the linearity of the concentration-thickness relationship. Another factor affecting linearity is the rate of evaporation of the solvent. As such, some spin coating machines will have a cap that limits the rate of evaporation, thus maintaining a lower viscosity that enables yielding of a thinner layer. The relationship between thickness and spin speed is an inverse square relationship:

$$t \propto 1/\sqrt{w} \tag{3.4}$$

Here, t is the film thickness, w is the angular velocity. As such, the spinning speed emerges to be 4 times the unit thickness. The spinning curve can be illustrated as shown in the figure: 3.20. A close observation shows that spectral ellipsometry offers unique sensitivity to the changing optical response of incident ration. However, the need to model the results to find the specific thickness is an evident limitation. This creates the need to get the data points and fit the modelled data, meaning that additional steps shall be involved. However, this method leads to substantial scattering, meaning that it is not the perfect method to be applied in this research. As such, this method was eventually rejected.

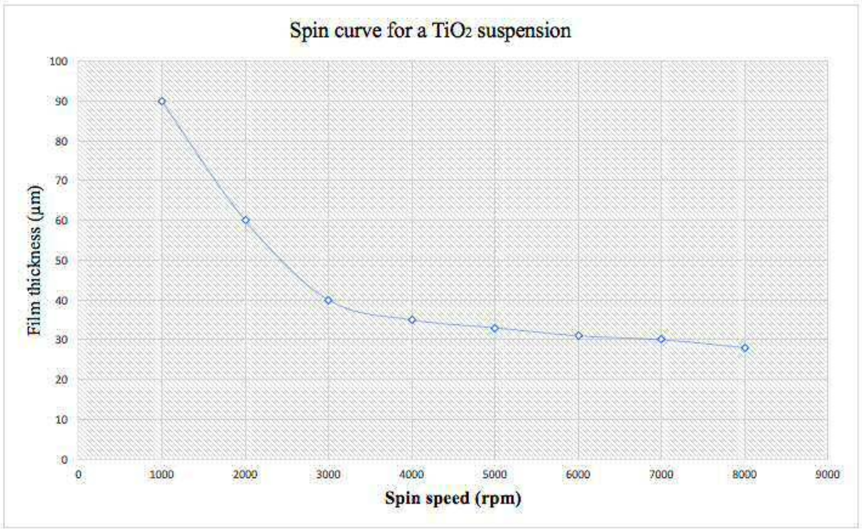

Figure 3.20: typical plot of a thickness of film vs. spin speed.

3.5.7 Colour Technique

This technique is often used by geologists to estimate the thickness of prepared thin sample sections (in the few 10s of micron range). The colour technique can also be applied in measuring the thickness of transparent films with a different refractive index from that of the substrate. This method is applicable in determination of oxide and nitride films, where the wafers are either silicon or other polymers with different refractive indices. Here, the method is quick but entails staining. After spin coating, the film is held under a white light source, and the colour of the film is observed. Then, spectrophotometers are applied to estimate the wavelength of the light that constructively interferes with the film, given that there is a colour difference between the substrate and the film, meaning that the interference level depicts the thickness of the film. Here, it is mandatory to know the refractive index of the coating and the substrate, from which interference equations are applied. This method offers an estimate of the thickness, but the accuracy falls below the attainable accuracy using ellipsometry. Given that ellipsometry itself has significant margin or error, it would be imprudent to apply this method in measurement and characterisation of the TiO_2 film in this research. Also, this method is not applicable to this study because the film is not transparent. Thus, it was rejected based on these two limitations.

3.5.8 Fabry-Perot Fringe Technique

The Fabry-Perot fringes method applies the principle of internal reflection, thus measuring of refractive index is the foundation of the characterisation process. A Fabry-Perot interferometer consists of two partially reflecting surfaces, which are aligned in such a way that many waves emanating from a single incident light can interfere.

Then, the resulting interference patterns are applied in the analysis of spectral characteristics, such as the thickness of thin films. Addition of the contribution of each pattern of transmitted waves enables finding of the total transmitted field. Here, it is mandatory to know the relative phases of the waveforms and the amplitudes. They are calculated based on the Fabry-Perot equation [65]. In this method, the phase difference δ and amplitude are calculated based on the equations:

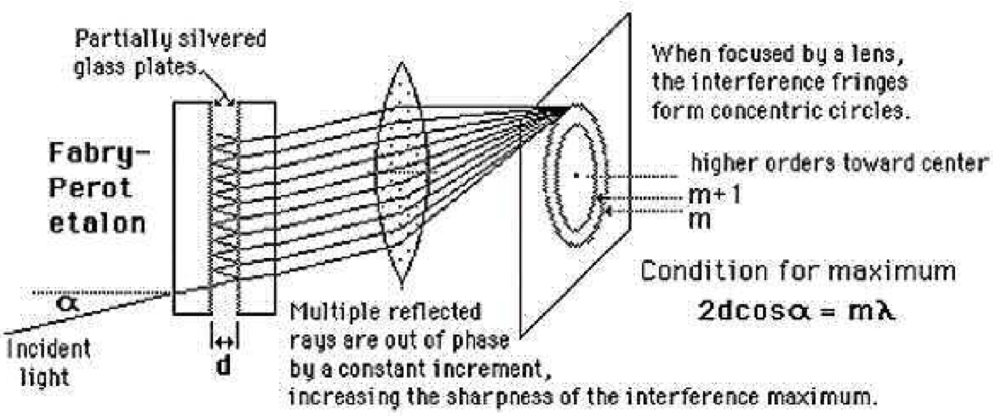

Figure 3.21: The parts and principle of the Fabry Perot interferometer [1]

$$2\delta = 2\pi \times \frac{2ndcos\theta}{\lambda} = \frac{4\pi ndcos\theta}{\lambda} = \frac{\omega 2ndcos\theta}{c} \quad , \tag{3.5}$$

where n is the refractive index of the TiO_2 / air, d is its thickness, and θ is the angle of incidence. It is assumed that both sides of the reflecting surfaces are identical and thus, amplitude is, therefore, calculated as:

$$\frac{I_R}{I_{inc}} = R \tag{3.6}$$

R is a fraction of the intensity of the incident light from a source (c). The total transmittance is given by the equation:

$$I_T = \frac{I_0}{1 + Fsin^2\delta} \quad , \tag{3.7}$$

where F is the coefficient of finesse. There is a need to include the Finesse F because it represents the resolution of the Fabry-Perot instrument used [66]. F describes the maximum number of resolvable peaks which can be inserted in the cavity, with an interval of π, meaning that it is a function of the distance between the surfaces. It is important also to note that the impact of its inclusion helps to find the range in which the phase shift can be found, given that the shifts are fundamentally used to find the thickness of the layers thereof.

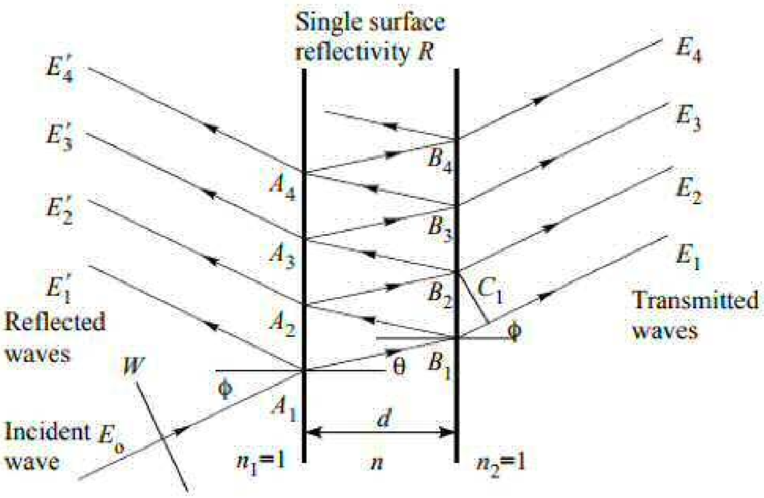

Figure 3.22: This illustrates the multiple beam interference that is created when Fabry Perot interferometry is applied on either single or multi-layered film. It is noted that both reflection and transmission are represented

In this research, a fiberoptic Fabry-Perot interferometer (FFPI) was proposed for use based on its advantages over the other forms. Notably, FFPI depicts high sensitivity, small temperature cross-sensitivity, good linear response and the components have a small overall size. Most importantly, the interference is linearly proportional to the optical length, which is defined as the product of micro-cavity length and the n of the filling medium [65]. Unfortunately, this method was also not successful. Although there were a number of wafers whose mass has been measured before and after coating with titania and the wavelength-dependent refractive indices of Si wafer and TiO_2 suspension were known, the signal spectra was not clear in the range 1000-3500 cm^{-1} and was not easy to record.

3.5.9 FTIR Spectroscopy

In order to conduct FTIR spectroscopy, the top-of-the-line research model Bruker VERTEX80V FTIR was used, since it allows high resolution infrared spectrometry. The first step was to eliminate disturbance due to moisture in the atmosphere and for this the optics were evacuated. The instrument has two infrared detectors, one at liquid nitrogen temperature and another at room temperature. The following options were also available: liquid flow cell with provision for operating at 250 °C; Pike^{TM}gas flow cell; and rapid and step scans for quick in-situ measurements. In addition, optical components can be attached for investigating additional portions of the spectrum such as far- and mid-IR down to the UV wavelength band. The optical components are pre-aligned, which facilitates maintenance and changes in range.

Figure 3.23: FTIR machine

The instrument was also used to obtain UV spectra of Methylene Blue and Methyl Orange. The IR band has wavenumber range 9000-25000 cm^{-1} and the MIR band can be used for determining the chemical composition of a sample [67]. Fourier transform infrared spectroscopy is often used in sample characterisation, because it allows identification of each of the specific molecular bond family of the sample. Mid-infrared spectroscopy is used in vibration spectroscopy to identify the constituents based on how the molecules interact with the MIR portion of the spectrum. On the other hand, if the sample has a large number of constituents or has a complicated chemical formula then the vibrational signature can be investigated using NIR spectroscopy which uses vibrational overtones and combinations [68]. In fact NIR is widely used for quickly obtaining spatial, chemical, structural and functional information from single samples and uses a specialised camera for each pixel of the sample to create creating 3-D hyper-spectral image consisting of both spatially resolved spectra and wavelength dependent images.

In order to obtain the wafer thicknesses, FTIR was used in this research. The Fabry-Perot interferometer was used to obtain spectra of the six wafers. The wafers from the first part had been stored unused for this purpose. The wafer was placed in the middle of the sample compartment, as shown in figure 3.24, and was positioned between the detector on the left and the laser beam on the right. It can be observed that the cavity has accurately parallel reflecting surfaces in order to improve the accuracy of the line width measurements [69]. The obtained spectra were compared with those obtained in the earlier parts.

3.5.10 Encapsulation and Sectioning Method

This was the method that finally produced usable results. It involves first encapsulating the coated wafer in hard resin and then sectioning vertically through the wafer.

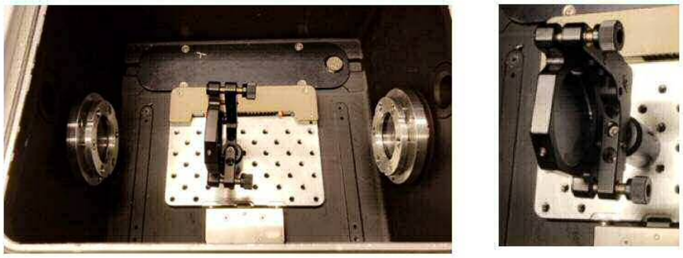

Figure 3.24: FTIR was used to obtain spectra of the six wafers

For this job we used the Struers Secotom-50 diamond saw, available in our lab. The Secotom-50 is a precision cut-off machine that has an adjustable cutting surface and a variable speed. The positioning of the cut-off wheel is motorised, while feed speed is controlled electronically with provision for automatic feeding. The machine is used in this case to cut the wafer precisely to facilitate the measurement of the coating thickness using a microscope. After layering the silicon wafer with TiO_2 nanoparticles, a few drops of methylene blue solution were introduced on the top surface of the coated silicon wafer, to highlight the TiO_2 layer. Notably, this was only done on the half side of the wafer area no 1, 2. Afterward, the remaining half, area no. 2, 4, was covered with glue, after which the wafer was set in a template and closed precisely as can be seen in fig: 3.26. Thereafter, the machine was programmed, and the template was placed on the appropriate area on the said device. After the machining action, the cuts were employed to measure the thickness by microscope, and some photos were taken. Finally, the Adobe Photoshop program was employed to determine the thickness of the coating and the wafer in pixels. This pixel count was compared against a calibrated ruler length in mm, as shown in figure 3.28.

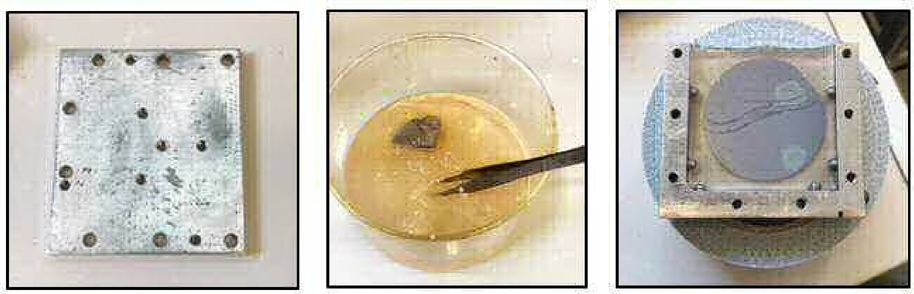

Figure 3.25: Preparation of the template solution

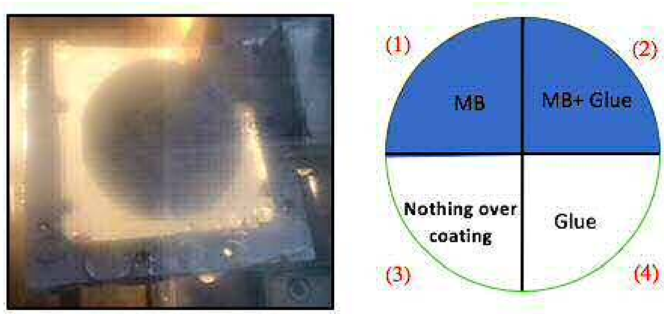

Figure 3.26: Left: The template was ready and placed on the Struers holder. Right: This illustrates the parts of the wafer that were used.

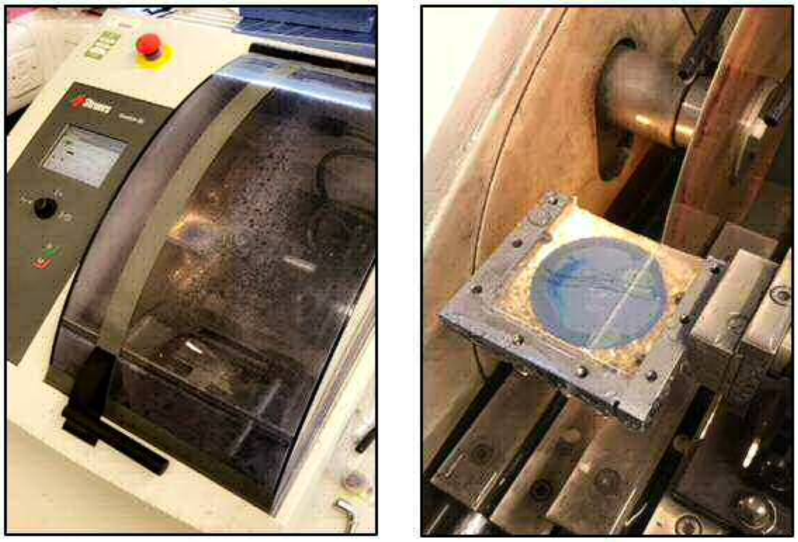

(a)

(b)

Figure 3.27: (a) Stuers Secotom-50 cut-off machine, and (b) the wheel starting to cut the wafer, to be ready to measure the thicknesses later.

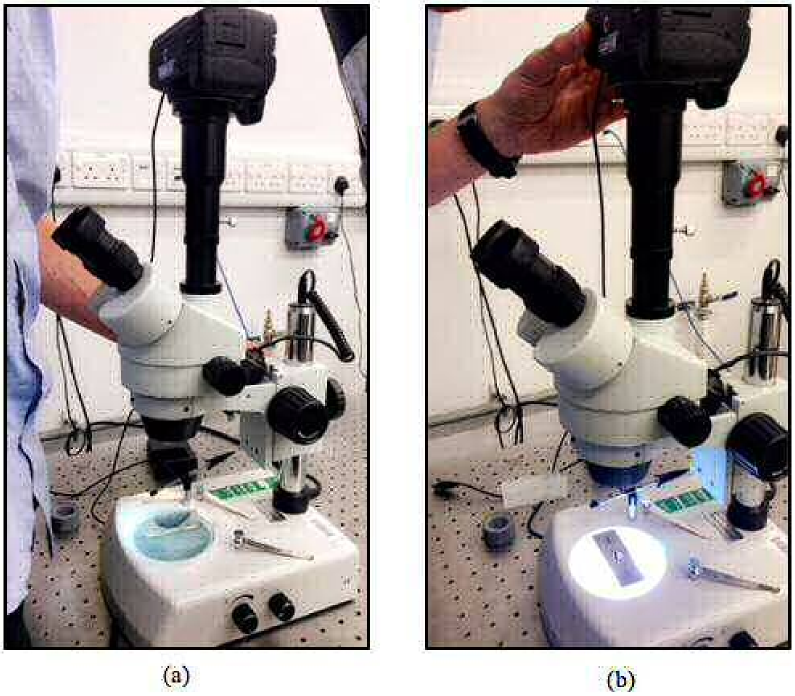

Figure 3.28: Photos of (a) wafer thicknesses, and (b) calibration ruler for comparison were taken by optical transmission microscope.

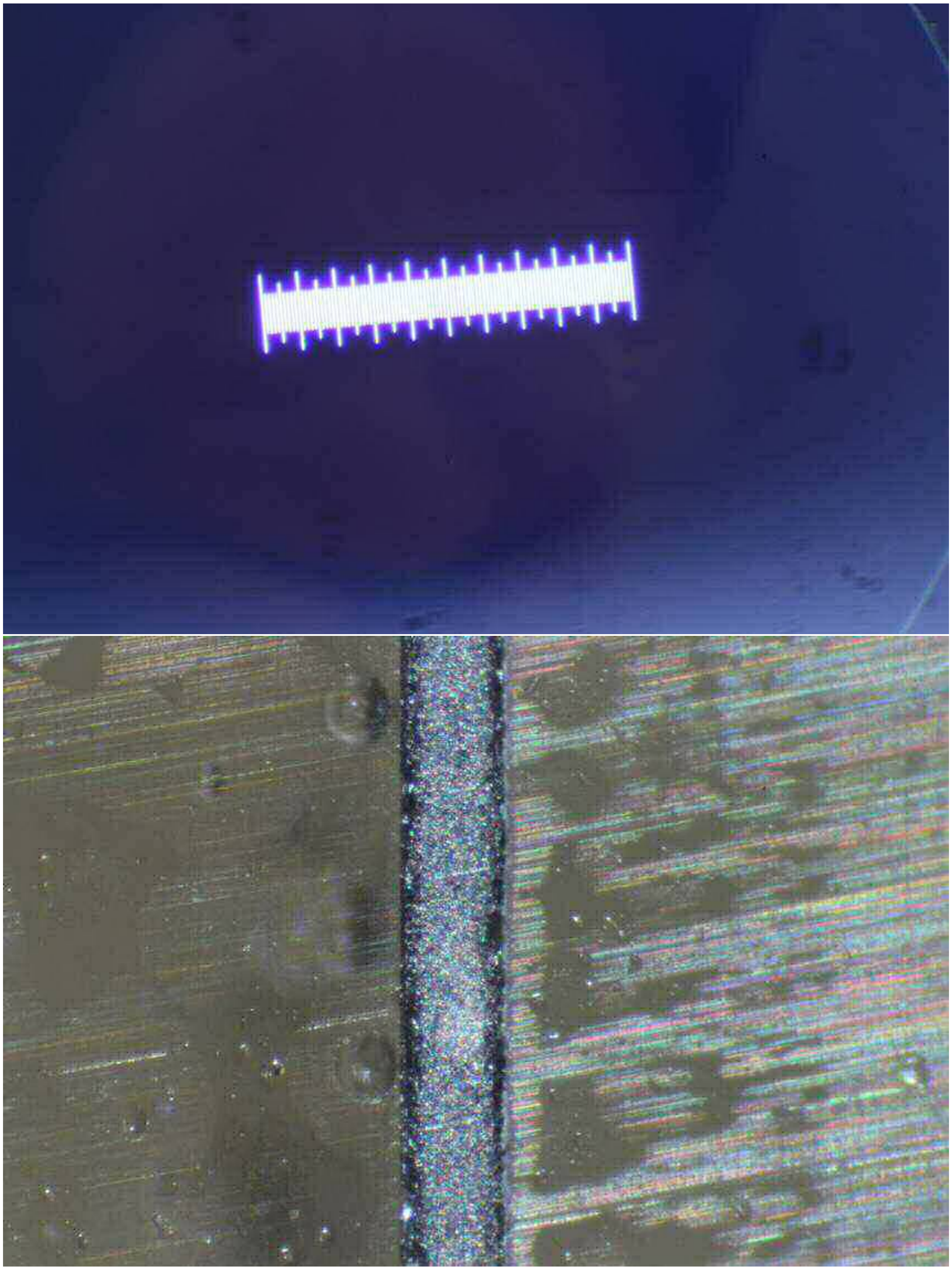

Figure 3.29: Top: The calibration ruler with 1mm length. Bottom: Wafer cut with 34 μm coating thickness and 275μm Si wafer thickness. The edges of the silicon wafer manifest themselves in this photo as two dark vertical parallel lines. An additional thin white-grey layer can be seen to the right of the righthand dark line. This is the TiO_2 layer.

Table 3.1: Sample output script showing the calculation of the wafer and TiO_2 thin-film thickness.

Label	Mean	Std Dev	Min	Max	Angle	Thickness
wafer	129.625	23.766	68.859	173.422	-90.000	0.275
wafer	127.898	33.759	47.924	177.543	-90.000	0.271
wafer	131.902	29.361	59.443	167.409	-91.548	0.275
wafer	132.334	25.178	85.124	171.430	-90.000	0.275
wafer	131.317	36.102	52.231	206.301	-90.000	0.271
TiO_2	114.308	28.192	78.516	143.272	90.000	0.025
TiO_2	81.777	31.677	49.025	118.569	90.000	0.025
TiO_2	99.333	19.018	68.193	116.363	-90.000	0.042
TiO_2	135.893	26.872	99.143	167.621	-90.000	0.030
TiO_2	97.989	19.111	72.456	116.087	90.000	0.034
TiO_2	105.362	19.044	80.482	125.185	90.000	0.034
TiO_2	121.902	33.377	62.781	153.882	90.000	0.038
TiO_2	109.603	23.777	72.255	135.882	90.000	0.042
TiO_2	108.751	29.959	58.372	146.795	90.000	0.042
TiO_2	126.603	31.375	71.3.49	154.764	90.000	0.034

3.6 Conclusion

There exist various methods of characterising thickness and nature of the surface of the TiO_2 thin films after spin coating. However, suitability of the method will depend on the impact of the method on the nature of thin film surface. If the interaction causes damage to that surface, the method is rejected. Another factor for consideration is the accuracy of the results obtained. Here, it is notable that the methods applied have different accuracy, with ellipsometry and interferometry attaining the highest accuracies (in theory). Also, the experimental setup and the complexity of the process needs to be considered. This consideration led to the rejection of the colour technique, and the late rejection of ellipsometry, in favour of interferometry, specifically Fabry-Perot interferometry. It can, therefore, be deduced that method offers the most accurate results, with the least amount of time. However, various *a priori* assumptions have to be made, and their effect on the accuracy needs to be considered as well. First, it has been assumed that the profile of the layers attains uniformity during deposition. This assumption has then been catered for by determination of the average packing fraction, which has also assumed uniformity. Thus, it can be identified that there still exists significant errors in this formulation and the models subsequently developed are subject to inaccuracies. In the end, the

Fabry-Perot method was also rejected in this research.

In the end, two methods showed promise, although neither method resulted in a perfect solution. The SEM approach clearly showed the nanostructure of the film from the edge of the wafer, and a thickness measurement could be extracted. However, it is well-known that their are edge effects from the spin coating technique. To get a true estimation of the thickness across the entire wafer, we would need to take a cross-section. One possibility to achieve this would be to make a scratch and view the coating at angle close to edge-on. However, we did not manage to achieve this. Also, the fore-shortening as a result of the viewing angle would need to be accounted for. The optical method (with encapsulation) also produced repeatable quantifiable estimations of the TiO_2 layer thickness. It also had the advantage of measuring the thickness variation across the wafer. However, this method does also have some inherent disadvantages. It is a destructive method (the wafers are useless for photo catalysis experiments after), and there is a very high overhead. It takes time to set the wafer in resin and perform the sectioning. Measuring the thickness from optical microscope images is also time consuming, although this part of the process could eventually be automated with the correct image analysis software. However, in the end, the desired result was achieved. A method to check the layer thickness was found. Assuming the repeatability of the spin-coating method, this test needs only be performed occasionally as a sanity check.

While the SEM images, do give some impression about the surface morphology, they do not give us quantifiable method to compare samples. For this we would have to use something like AFM (Atomic force microscopy). However, we have already seen problem with this technique (snow-plowing) when used for thickness evaluation. Hopefully in the future work we will find an ideal and easy method to do that properly.

Chapter 4

Experimental Determination of Photocatalytic Reaction Rates

4.1 Introduction and Rationale

The overriding aim of this research was to investigate whether material modifications to the intrinsic TiO_2 photocatalyst could improve performance, and specifically to access more of the available solar spectrum. The intrinsic band gap of TiO_2 is 3.2 eV, which means that only photons with wavelength shorter than 379 nm can create the electron-hole pairs necessary to facilitate the photocatalytic reactions. However, before attempting to modify the TiO_2, it is necessary to find a way to ascertain the effect of any changes. While we can exploit various characterisation techniques to study the material properties, it is ultimately the effect on the photocatalytic properties that are most interesting. Furthermore, there are two questions to look at here: can we improve the photocatalytic reaction rate, and can we access a broader range of photon wavelengths? Both questions are in some ways linked.

The photocatalytic effects of TiO_2 are activated using UV light. Here, UV light offers enough photon energy to overcomes the band gap of TiO_2. As such, electrons from the valence band are moved to the conduction band, leading to diffusing of holes and electrons, generated through the photocatalysis process [70]. Here, these electrons and holes generate highly reactive species in the water that chemically break down the pollutants as shown in figure 4.1. It is important to note that the properties of TiO_2 will affect the work function. As such, the evaluation of change in work function can represent the photocatalytic reactions of the TiO_2 [65]. The photocatalytic reactions can, therefore, be utilised in the analysis of TiO_2. Here, the possibility of visible characterisation forms a foundation for fine-tuning the surface properties of TiO_2 to various applications, including mineralization of contaminants in wastewater [70].

A good starting point is to develop an experimental setup to directly measure the photocatalytic reaction rate. Many of the techniques already used by chemists to achieve this are labour intensive and time-consuming. They usually involve removing

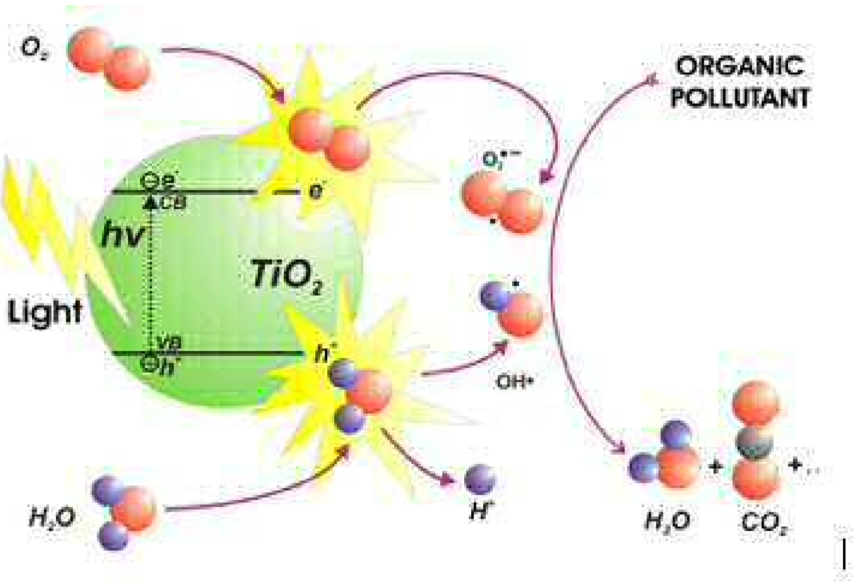

Figure 4.1: Schematic diagram showing the interaction of the electron and hole at the surface of the TiO_2 with the surrounding aqueous medium after above band gap excitation.

[71]

a small amount of the reaction liquid and testing for the concentration of the reactants and products. This only provides a snap-shot picture of what is going on at a single point in time. I developed a real-time monitoring technique which could be used to follow the reaction pathway throughout from beginning to end. Since both the test pollutants are organic dyes, we can harness real-time spectroscopy to monitor and colour changes during as photocatalytic reaction progresses. Specifically, in the case of methylene blue (MB), and methyl orange (MO), the intense colour of the dye should degrade as either organic compound is broken down into simpler molecular compounds. The experimental setup we finally settled on combines a photo-reactor with an optical flow-cell. The photo-reactor part allows the photon flux activating the photocatalysis to be controlled. The photon source can be changed to study the effects of changing the illuminating wavelength. The flow-cell allows the concentration of the organic dye to be monitored optically through measuring the transmission through the cell at a wavelength matched to the peak absorption of the dye. Thus, the monitoring optoelectronics will change depending on the colour of the dye. I will discuss this setup now.

4.2 Experimental Design Criteria

The photocatalytic reaction rate experiment is the foundation for all the experimental studies in this work. It is the workhorse that produced the key results in chapters 5 and 6. The experimental setup was based on a previous design described elsewhere[55] with two main criteria in mind...

- The setup should continuously monitor the colour change of an organic dye (over several hours) in an automated way.
- The setup should allow the properties of the illuminating photon flux on photocatalyst to be controlled both in intensity and wavelength.

4.2.1 Description of the Experimental Setup

A schematic overview of the experimental setup is shown in figure 4.2, and the functionality is described below.

The Liquid Flow Circuit

The main flow circuit (shown in blue) in the centre contains three key elements, the flow-cell (FC), the reactor vessel, and the recirculating pump (P). All three elements were connected with 6 mm internal diameter hose to form a circuit.

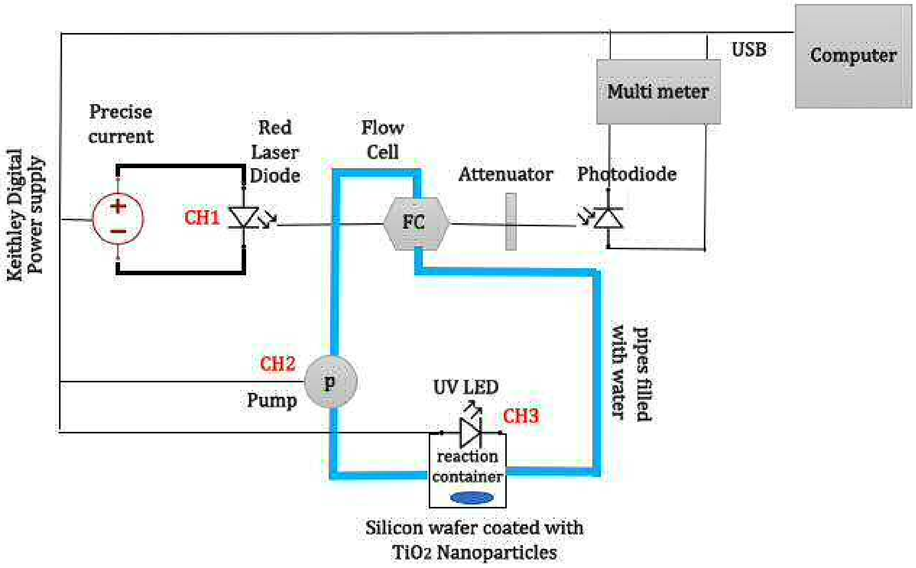

Figure 4.2: Experimental set up, to measure the photocatalytic decomposition rate of a test pollutant in the presence of TiO_2 nanoparticles fixed to a silicon wafer.

- The flow-cell was designed in-house and a schematic is shown in figure 4.3. The flow-cell was manufactured from three pieces of aluminium: the central unit, and two identical retaining rings/disks. The retaining rings holds two 12.5 mm diameter CaF_2 windows in place. A watertight seal was made with rubber o-rings. CaF_2 was chosen for the window material because it is transparent in the visible, and insoluble in water. It was also cheaper then glass. Two hose barbs were fitted to the threaded holes in the central unit.

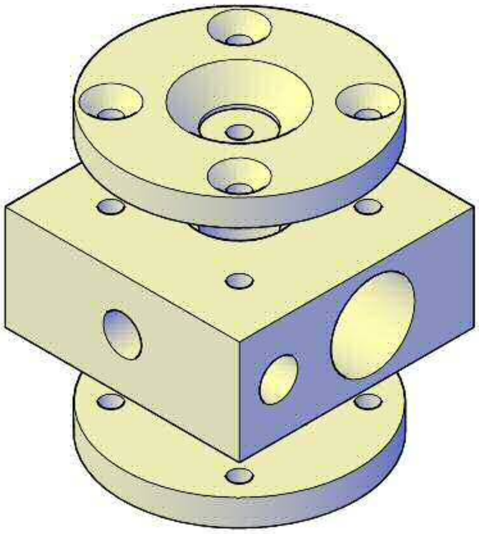

Figure 4.3: AutoCAD design for the flowcell.

- The reaction vessel was also a bespoke item. It consisted of a glass beaker with two glass hose barbs located towards the bottom and off-centre to encourage mixing. It was ordered from a bespoke glass blowing company called GPE Scientific Ltd.
- The micro-pump was sourced from RS Online (part number 702-6872). The pumping speed was controlled by the bias voltage over a range 3-12 V. This allowed a free flow rate of up to 2800 ml per minute. I typically used much lower free flow rates than this to avoid disturbing the wafer in the reaction beaker.

The Photon Source

The second aspect of the experimental setup was the photon source to drive the photocatalytic reaction. For this we initially chose a high-power UV LED. The UV LED was sourced from DigiKey Electronics UK. The original manufacturer was LED ENGIN and the part number was LZ1-10UV00. The LED is an ultraviolet (UV) emitter centred at 365 nm. It requires a bias voltage of 4.1V and draws a current of 1A. The configuration is a “star array”. The LED delivers up 1200 mW flux output at 2.7 W power dissipation, with an emission angle of 70°. Since the LED generates a lot of heat under normal operation, it was attached to a heat-sink. Both the micropump, and the UV-LED were powered by a Keithley 2230-30-1 Triple Chanel DC Power Supply. The third channel was used to power the monitor laser diode.

Figure 4.4: Micropump.

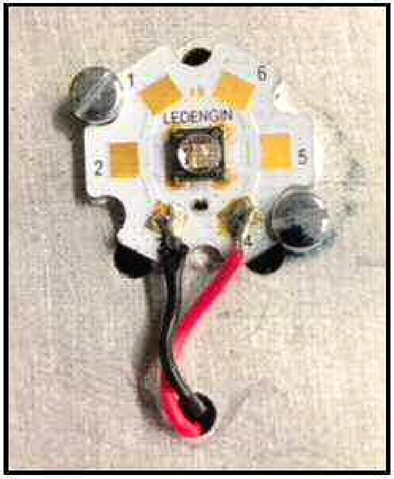

Figure 4.5: LED ENGIN LZ1-10UV00 UVA LED with emission centred on 365 nm.

Optoelectronic Monitoring

The monitoring was achieved by measuring the change in intensity of a light source which was directed through the optical windows of the flow-cell. The monitor photon source was chosen to match the peak optical absorption of the test organic dye (see section 4.2.2). The monitor photodiode was a Thorlabs variable gain Si photodiode (part number PDA100A2), with a BNC output. The output was directed to a computer-controlled Keithley 2100 6.5 Digit Digital Multimeter (DMM).

4.2.2 Choice of Monitor Laser Diode

Clearly both MB and MO have very different optical characteristics. MB is dark blue in solution, while MO is bright orange. In order to the best select laser diode source for monitoring the dye absorption, I first attempted to perform an FTIR transmission measurement to understand the visible absorption. The sample was placed inside the flow cell in the sample compartment of the FTIR as shown in figure 4.6. The difference between the two dyes is obvious in these two photos. This was a useful measurement, but since the shortest wavelength response of the FTIR visible detector is around 400 nm, the absorption in the UV region is missing from the spectrum. Instead I present here a plot of calibrated transmission data recorded elsewhere using a dedicated UV-vis spectrometer, figure 4.7. The MB calibrated data was downloaded from [72], while the MO data was downloaded from [73]. I have normalised both curves for molar concentration.

Figure 4.6: 0.01 mMol of each solution MB (left),and MO (right) in the Bruker Vertex 80V FTIR to identify and analyse the absorbance spectra of both of them

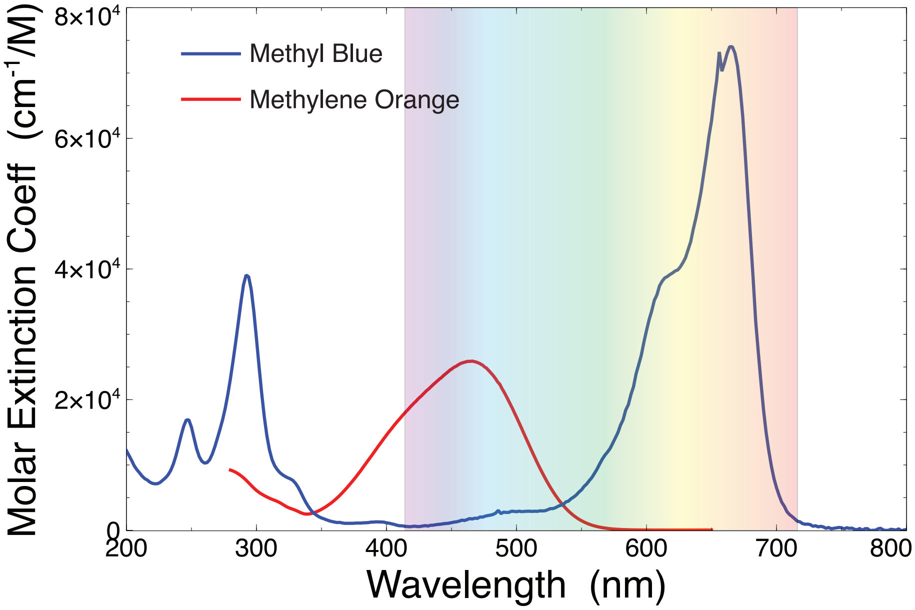

Figure 4.7: Calibrated molar extinction spectra using the data from [72] and [73], showing the relevant UV and visible absorption features of the two dyes. The plot shows why we chose the different wavelengths for the monitor light sources.

The MB transmission spectrum shows a peak absorption centred in the red between 600-700 nm. It is also interesting to note the UV absorption feature centred at 300 nm because it highlights that the solution is transparent to the longer wave UV photons ($\lambda = 375$ nm) necessary for photo excitation of the TiO_2. For MB experiments I chose a standard red laser diode (of the kind often found in laser pointers) with emission wavelength $\lambda = 630$ nm, close to the centre of this absorption band. The MO spectrum shows a maximum absorption between 400-500 nm. For the MO experiments, it was difficult to find a cost-effective low-power (eye-safe) laser diode operating at a wavelength range matching the peak MO absorption. Most available cheap blue laser diodes are designed for Blu-ray players, and have optical output powers > 80 mW, which would place them in the Class 3B category. Consequently, I chose to use a generic blue LED with emission broadly centred at $\lambda = 450$ nm.The two monitor light sources are shown in figure 4.8.

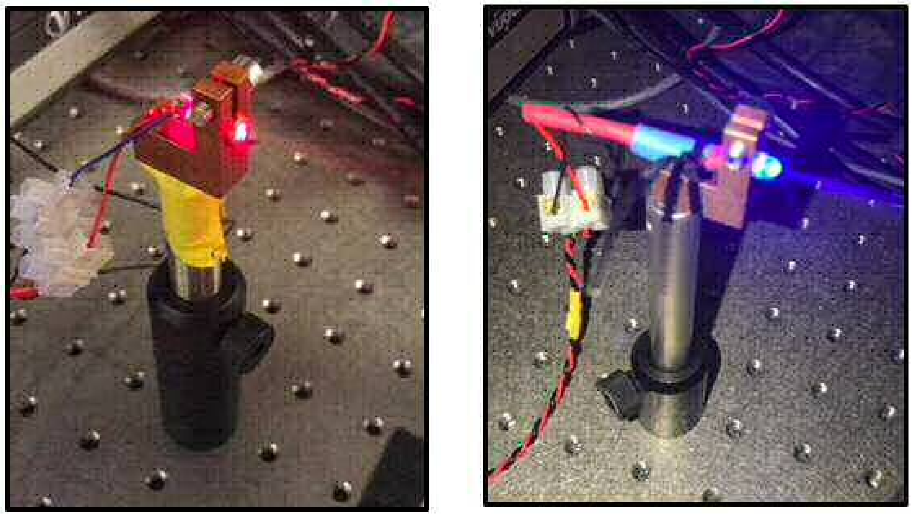

Figure 4.8: Red laser used in MB set up vs the blue LED that used in MO experiments.

4.3 Experimental Protocol

A typical time to run the experiment through to completion was several hours. This was the time taken for the colour of the dye to completely disappear, so that it was necessary to automate the experiment. Throughout this time, the voltage on the Thorlabs photodiode was recorded by the computer controlled Keithley DMM. The computer control was realised via some Python code (See relevant Appendix). The frequency interval of the readings could be set, although typically I recorded readings every five minutes. The data file contained a list of photodiode voltages and time stamps. The format of the data file was 3-column ASCII, where the first column was a datapoint identifier (n), followed by the time stamp (t) in the second column, and the photodiode voltage (v) in the third column. These readings were recorded that could enable plotting of graphs for later analysis. The entire experimental protocol is illustrated in the flow chart shown over in figure 4.9.

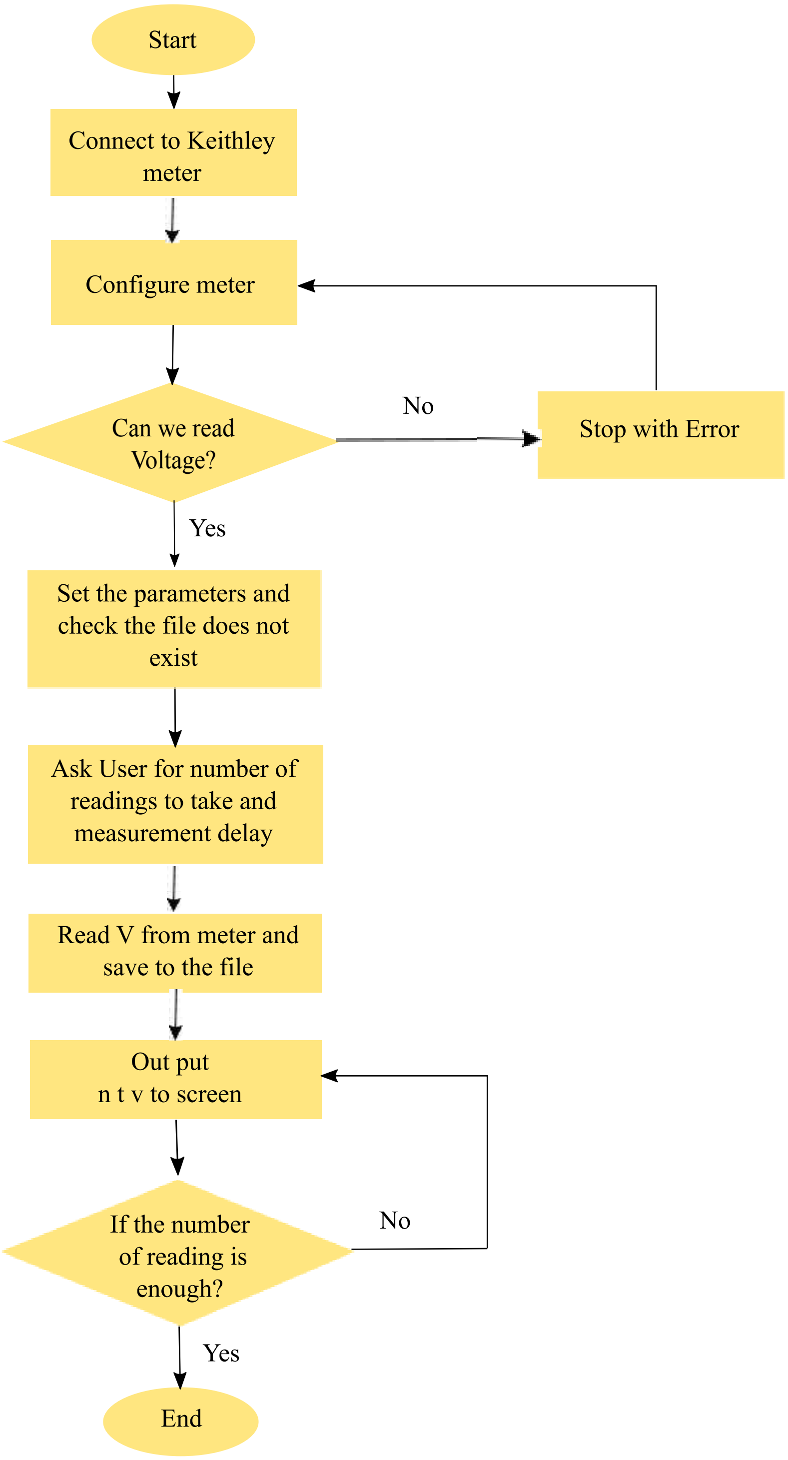

Figure 4.9: Flowchart showing the experimental protocol used in the photocatalytic absorbance voltage test experiments.

4.4 Standard Dye Solutions

In order that experiments can be compared, the dye solutions needed to be standardised. This means that the concentration (molar concentration) needs to be known. Different solutes may have different molecular masses and so I used the following equation to work out the molarity of the solution.

$$Mass(mg) = Concentration(mM) \times Volume(ml) \times MolarMass(g/mol) \tag{4.1}$$

where the in both cases, MO and MB, the standard solution preperation was conducted step wise as described below.

4.4.1 Methyl Orange (MO) Standard Solution

Methyl Orange (MO) was obtained from Sigma-Aldrich and dissolved in de-ionised (DI) water, where concentrations of 1 mM of MO were set. Here mixing 163.665 mg of MO in 500 ml of de-ionised water was done and based on the known molar mass of MO is 327.33 g/mol, the concentration of 1 mM was achieved. The next step entailed adding 2 ml of the MO solution into the reactor containing DI water. Here, the photodiode signal was monitored in real-time during this process. It was observed that a homogeneous mixture was produced on a timescale of seconds. Notably, this timescale was negligible when compared to the rate, and constant timeframes of any of the reactions were studied. For these experiments, the blue LED was biased 4.7 V and drew 18 mA current. The photodiode output was 5.8 V when illuminated by blue LED. The pump and UV LED were set at 3.49 V and 800 mA respectively.

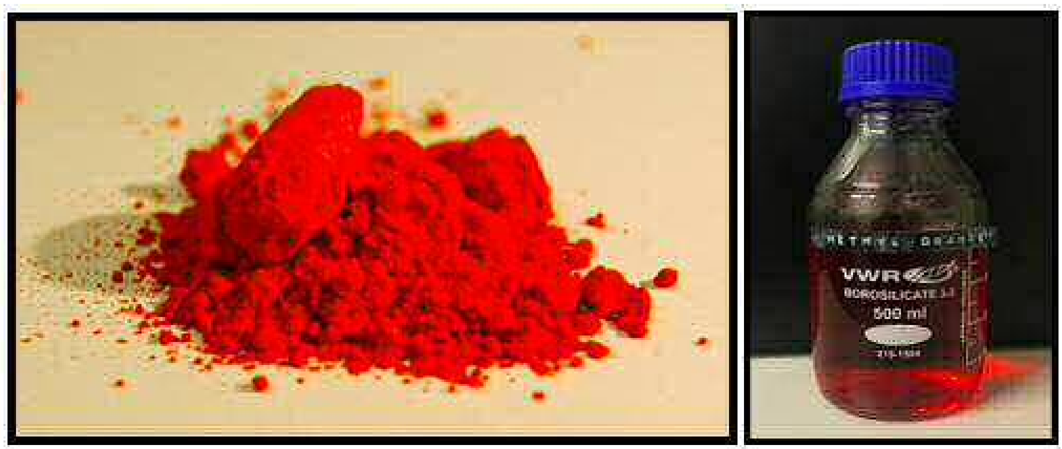

Figure 4.10: Methyl orange powder and 1mMol/l MO solution

4.4.2 Methylene Blue (MB) Standard Solution

Methylene blue (MB) was also prepared for use in this test. This compound consists of a dark green crystalline powder, which upon dissolving in de-ionised (DI) water, a deep blue solution is obtained. Here mixing 159.925 mg of MB in 500 ml of de-ionised water was done, to get a concentration of the 1 mM solution of MB, given the molar mass of MB is 319.851 g/mol. The MB experimental conditions were set, such that the photodiode output was 7.8 V when illuminated by laser, In CH1, the laser rating was 12 mA. Here, the pump bias voltage was set at 3.49 V. Finally, the bias current of the UV LED was set to draw 800 mA.

Figure 4.11: Crystalline methylene blue and 1 mMol/l MB solution

4.5 Preparation of Photocatalyst Thin-film

For these test experiments we used commercial TiO_2 powder. The reagent used was Evonic (Degussa) P25 TiO_2 "aeroxide" powder. This photocatalyst comprises a 20% rutile and 80 % anatase TiO_2 mixture. The suspension for coating was prepared in the standard way described fully in section 3.4.1. In short, a suspension of 800 mg of P25 TiO_2 in 8 ml of isopropyl alcohol (IPA) was made then 250 μl of Triton X100 surfactant was added. The reasons leading to the choice of IPA include the bigger molecule size and has less severe toxicity than methanol (pure ethanol is too expensive because of the duty). The choice of triton X100 was based on the relatively high ethylene oxide units, and the non-ionic surfactant properties, making it a highly hydrophilic aromatic carbon (Triton X-100 ($C_{14}H_{22}O(C_2H_4O)_n$). The three components of the suspension are shown in Figure 4.12

Figure 4.12: (a) Isopropyl alcohol (IPA), (b) Triton x-100 surfactant (c) TiO_2 P25 powder

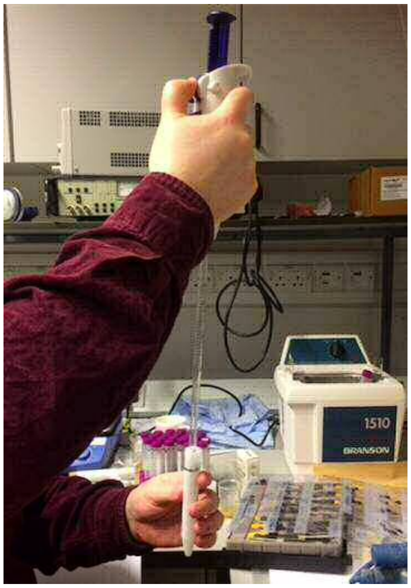

Figure 4.13: A pipette is used to add 8*ml* of IPA to 800 *mg* TiO_2 powder, a step preceding the addition of Triton x-100 surfactant of the 250 μl.

4.6 Data Analysis

4.6.1 Background

According to Khaydarov [74], a fundamental definition of a solution is an ionic mixture of a solute and a solvent, to form a homogenous liquid, where the ionic ratio of the two determines the concentration at a particular time of reaction. Here, different methods can be used to determine the concentration of a solution [74]. In our experiment, we used transmittance to determine the concentration of the solution. In the case of photocatalytic reactions, monitoring can entail various methodologies, depending on the suitability and the level of details expected from the observations. One of the other methods commonly used is the measurement is a decrease of the weight of reactants, a method that is popular in photocatalytic reactions that lead to loss of the control mass. Van Driel [70] applied this method in quantifying the photodegradation of TiO_2 photocatalyst on alkyd paint films (an alkyd is a polyester modified by the addition of fatty acids and other components, often used in paints where some elasticity is desired after drying). Here, this method is applicable because CO_2 is formed and the pigment volume fraction (PVC) causes measurable variation, with a significant loss of 35%in control mass (CM) . However, for us, monitoring the photo-degradation of the dye colour allows greater accuracy, because it is a function that can be monitored accurately based on photo-transmittance quantification.

The equations applied include the absorbance equation and Beer-Lambert law. The Beer-Lambert law was applied to determine concentration through transmittance. The law states that the concentration of a substance is directly proportional to its absorbance [74].

4.6.2 Determining the Absorbance

The absorbance method involves placing the solution in the path of a ray of light with known intensity and wavelength. The intensity of light changes as it passes through the solution because the solution absorbs the light. The light that passes through it is directed to a detector which measures its intensity. The equation of the intensity of light is given by:

$$I_0 = I_a + I_b \ , \tag{4.2}$$

where, I_0 = the initial intensity of light,I_a = the intensity of light that is absorbed by the solution and I_b = the intensity of light that passes through to the detector.
Absorbance is a function of the molecular concentration of the solution. Here, the number of molecules in the solution and the rate of absorbance as a proportionality. This law can be represented by a linear equation, known as the Beer-Lambert equation as indicated by [74].

$$A = \epsilon d C \ . \tag{4.3}$$

Here, A = Absorbance, ϵ= Molar absorptivity given by litre/mol.cm, d = Path length of the cuvette containing the sample (cm) and C = Concentration of the solution given in moles/litre.

4.6.3 Determining the Transmittance

Transmittance is the relationship between the intensity of light that passes through the solution and the initial intensity of the light and is given by the following equation:

$$T = \frac{I}{I_0} \tag{4.4}$$

Where, T = transmittance, I = intensity of the light that passes through the solution and I_0= intensity of light incident to the solution. Notably, transmittance can also be expressed as a percentage based on the equation:

$$T\% = \left(\frac{I}{I_0}\right) \times 100\% \tag{4.5}$$

4.6.4 Absorbance/Transmittance Relationship

The absorbance and transmittance are related according to the following equations:

$$A = log_{10}\left(\frac{1}{T}\right) \tag{4.6}$$

$$A = log_{10}\left(\frac{100}{T\%}\right) = 2 - log_{10}T[\%] \tag{4.7}$$

The logarithmic relationship above allows the use of curve-fitting tools to find the time (β), which is the characteristic time for the reaction. Plotting the absorbance as a function of time allows us watch the dye is degrading in the presence of the photocatalyst. Re-plotting the data on a semi-logarithmic graph reveals a straight line. The reaction rate constant is obtained from the slope of this line. The time constant represents the characteristic time for the total decay to drop 36.8%. In this case, the equation for the delay model becomes:

$$A = A_0 e^{-\beta t} \tag{4.8}$$

Where t= reaction time, A = the matter that decays after time t, and -β = rate of decay. It, therefore, emerges that the equation can be re-written as:

$$e^{-\beta t} = A/A_0 \tag{4.9}$$

$$A/A_0 = 1/e \tag{4.10}$$

Replacing time (t) with constant time gives:

$$e^{-\beta t} = 1/e \tag{4.11}$$

Simplifying the equation gives:

$$t = 1/\beta \tag{4.12}$$

4.7 Real Data Example

Figure 4.14 shows a typical experimentally measured photocatalytic decay trace. The first plot (a) shows the raw data (voltage plotted as a function of time). The decay curve follows a standard path. In the beginning, the concentration of the dye is maximum and so the transmission of the flow-cell is minimum. As the photocatalytic reaction progresses, the concentration (and hence the colour) of the dye degrades. The flow-cell becomes more transparent and the voltage on the photodiode increases because more light from the monitor laser diode reaches it. The voltage signal on the photodiode continues to grow as the dye clears until it eventually saturates (here at a value of about 7 volts). At this point the solution is completely transparent. This voltage saturation value is important because it allows the absolute transmission to be calculated, according to equation 4.4. In (b), I have used this saturation value to normalise the transmission. From the transmission it is now possible to calculate the

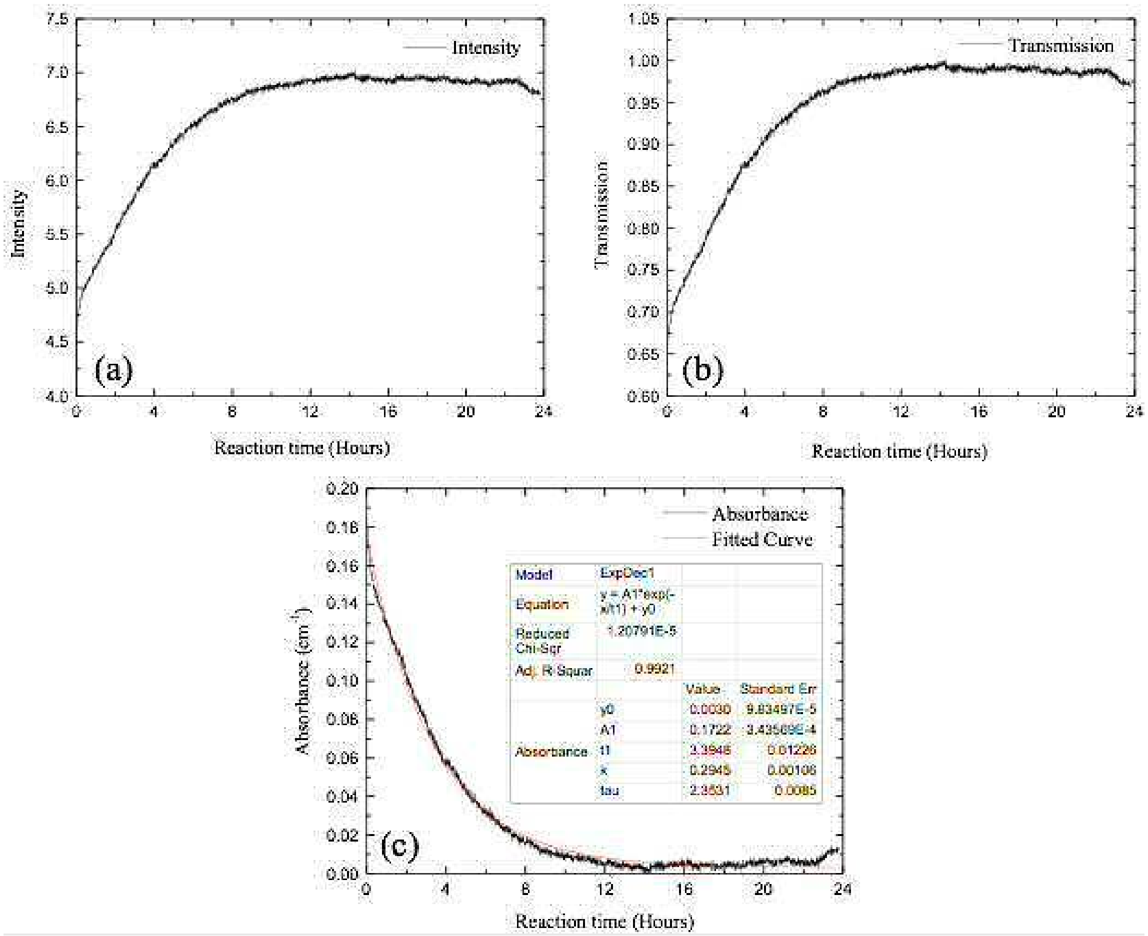

Model	ExpDec1		
Equation	y = A1*exp(-x/t1) + y0		
Reduced Chi-Sqr	1.20791E-5		
Adj. R-Squar	0.9921		
		Value	Standard Err
Absorbance	y0	0.0030	9.83497E-5
	A1	0.1722	2.43569E-4
	t1	2.3946	0.01226
	k	0.2945	0.00106
	tau	2.3531	0.0085

Figure 4.14: (a) Photodiode voltage plotted against time. (b) Transmission as a function of time. (c) Absorbance as a function of time.

absorbance using equation 4.7. This is plotted in (c). From a plot of absorbance as a function of time, I can fit an exponential decay (as shown in the insert) and extract the characteristic time constant for the photocatalytic decay reaction. For this data set the time constant “t1” was approximately 3.4 hours.

4.8 Conclusions

In this chapter I have described in detail the experimental setup that was used throughout this work. The photocatalytic reaction rate measurement experiment is the foundation for all the experimental studies in this work. It allows real-time monitoring to follow the reaction pathway throughout from beginning to end. With this experiment, I can characterise and quantify the performance of a photocatalyst in a precisely repeatable way. The experimental tool allows me to compare the performance of new photocatalysts.

Chapter 5

Photocatalytst Poisoning by Chloride (Cl^-) Ions

5.1 Introduction to the Problem

During my studies, I observed a behaviour inconsistent with the definition of a catalyst. Catalysts by definition lower the activation energy of a reaction, causing the reaction rate to increase, but they should never be consumed during the reaction. Only the reactants are consumed to form the reaction products. After running many experiments I noticed that the photocatalytic rate appeared to slow for methylene blue (MB) reactions if the photocatalyst wafer was not renewed. This lead me to add a new experimental protocol which was followed throughout: the photocatalytic reaction is always studied with a newly prepared TiO_2 film. Various theories were put forward to explain this behaviour but none of them were convincing. I worried that over time the photocatalyst was being slowly washed away during the reaction. However, by chance I discovered that the photocatalytic reaction rate for methyl orange (MO) did not appear to change no matter how many times I reused the wafer. This was a puzzle. Why should the methylene blue reaction eventually stop working while the methyl orange reaction rate remained constant with time? What is different about methylene blue? A clue to the answer can be found by looking again at the molecular structure of both organic dyes. The molecular structures of MB and MO are shown in figure 5.1. Both molecules contain similar atoms and chemical bonds, although there are some important differences. MB is a salt, containing an organic cation and a chloride anion, while for MO (also a salt) the organic part of the molecule is the anion and the cation is a sodium ion. Is this important? I set out to understand this puzzle through a careful set of experiments.

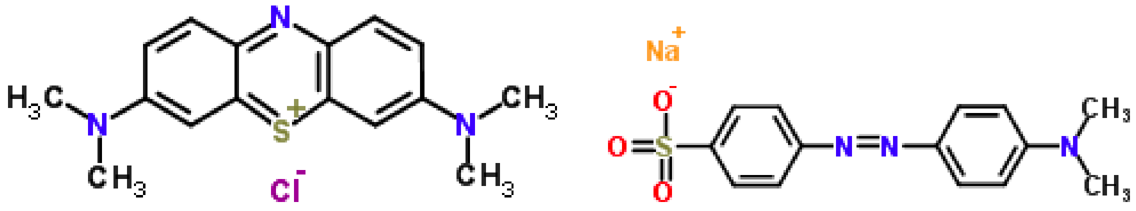

Figure 5.1: Left: the molecular structure of methylene blue. Right: The molecular structure of methyl orange.

5.2 Background Theory

The ability of dyes to lose their colour upon photocatalytic activity forms the pillar for this analysis. It is important to note that the dye solutions can either be UV-stable or photocatalytically active, wherein no discolouration is observed. In order to understand the photocatalytic action of TiO_2, in conjunction with the variables that affect the nature of the activity, it is necessary to consider the representation of the reactions as charge exchange, which can be represented as shown in the following equations [75].

$$TiO_2 + UV - Light \rightarrow e^- + hole^+ \tag{5.1}$$

$$e^- + hole^+ \rightarrow TiO_2 + heat \tag{5.2}$$

$$alternatively, hole^+ + OH^- \rightarrow OH^* + e^- + O_2 \rightarrow O_2^- \tag{5.3}$$

$$R^* + organic\, material \rightarrow intermediates \rightarrow CO_2 + H_2O \tag{5.4}$$

The above charge exchange changes are subject to various sequential steps, meaning that if one step is prevented or slowed down, the photocatalytic action can either be stopped or slowed down. The implication is that Cl^-, being strong anions, will have an impact on various changes, since they can affect the concentration of the ions in the control volume. Notably, the concentration and pH are important factors that affect the photocatalytic action [75]. The objective of this chapter is to identify the impact of chloride ions, to deduce a workable foundation of deriving the most appropriate procedure of preparation during TiO_2 waste water treatment.

5.3 Source of Chloride Ions

The chloride ion is a negatively charged ion formed when chlorine gains an electron or when one of its compounds is dissolved in a polar solvent ($Cl + e^- \rightarrow Cl^-$).The diagram below shows how chloride ion is formed. The main source of chlorine and chlorine-based compounds in the wastewater and water bodies include the use of water softener in water treatments (using sodium chloride), mineral deposits, water chlorination, and agricultural wastes containing chloride ions. These waste products breakdown once in water to release chloride ions. For instance, the sodium chloride in water softener breaks down to give sodium ions and chloride ions. The chloride ions may also be from degradation of dichloroacetic acid (DCA) found in wastewater ($CHCl_2COOH$).

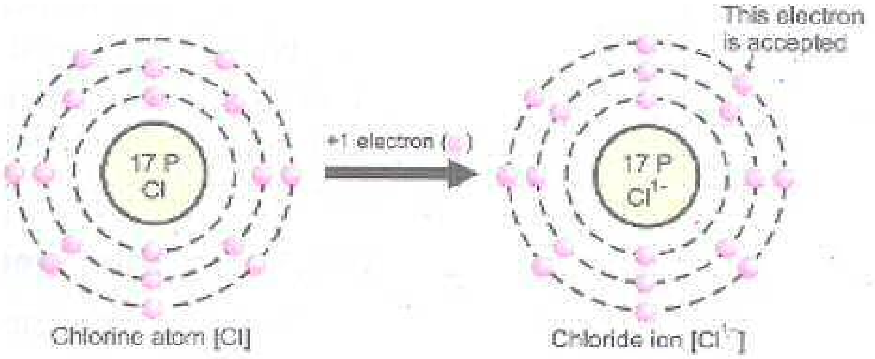

Figure 5.2: Formation of Chloride Ions
[76]

$$CHCl_2 + O_2 \rightarrow 2CO_2 + H^+ + 2Cl \tag{5.5}$$

The chloride ions inhibit the photocatalytic activity of a system containing TiO$_2$. The inhibition is done through two different mechanisms. The first one is competitive adsorption of inorganic ions on the TiO$_2$ active surface which blocks adsorption sites for the target molecules [77]. The other mechanism is a possible scavenging effect of the adsorbed inorganic ions which consume photo-generated holes and, therefore, decrease the efficiency of the photo-catalytic process [78]. Additionally, Zalazer [79] pointed out that the most significant oxidative step in photocatalytic oxidation process is the direct attack of the photo-generated hole.

The chloride ions also have an impact on the pH of the solution. The rate of degradation is expected to increase with an increase in the pH. This is because, in such a medium, the hydroxyl radicals increase at the surface of the titanium dioxide by trapping photo-induced holes. Experiments by Dhanya [80] show that the absorbance rate of methyl orange dye at a maximum wavelength in different pH indicates that rate of decolourisation increased with a decrease in the pH. The efficiency of decolourisation was observed to be highest in acidic regions and lowest in basic regions.

A similar experiment by Afarani [81] indicated that low pH led to the formation of HO_2, which consequently led to decrease in the concentration of the OH^- ions. For that reason, the impact of chloride ions in this experiment was completely reduced using methyl orange instead of methylene blue. This is because methylene blue works best in basic conditions, and therefore its degradation would otherwise be further inhibited by the acidic condition created by the chloride ions. The figure below 5.3 shows the effect of pH on the rate of dye decolourisation.

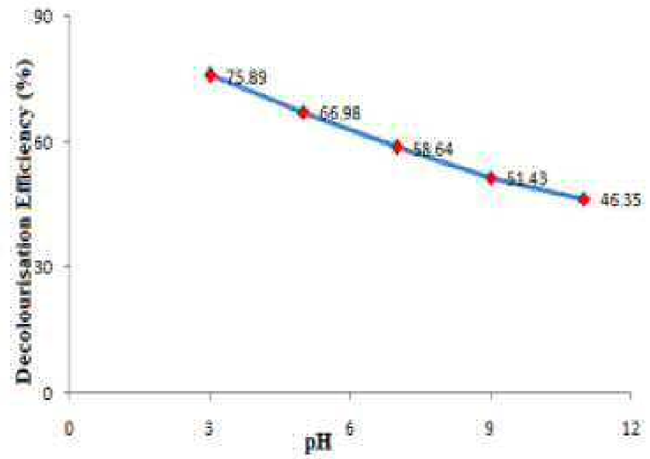

Figure 5.3: Effect of pH on the Rate of Dye Decolorization [82]

The chloride ions also add to the overall concentration of the ions. A study by [80] shows that increased concentration of chloride ions increases the effectiveness of photocatalytic degradation. As such, although the chloride ions have an inhibiting characteristic, they can also help in speeding up the rate at which the dyes in effluent water is broken down to less harmful compounds such as hydrochloric acid. However, this is subject to the amount of the anion present and the concentration of the dye and the catalyst used for the process.

5.4 Experimental Protocols for Chloride Ion Tests

A volume of 150 ml of de-ionised water was used to provide enough water to circulate and provide an environment for the reaction. A suitable concentration for observation of the reaction path and the change in the intensity of light transmitted through the flow cell was chosen. In this case of MO, 2ml of 1 mMol/L MO solution was used. Once the MO was added to the circuit, the UV LED has to reach the wafer for the reaction to take place, an electron-hole pair are created, and two important reactions take place, an oxidation and reduction reaction [75]. These reactions aid in the process of organic pollutant degradation. One variable was changed between the 4 different runs, the de-ionised water (DW). The wafer used for this run was freshly spun. Before the next run, the digital multimeter was calibrated, and we made sure that the laser and detector were in the same line, the pump still worked to circulate the water through the pipes. Then the whole system was flushed with clean water to ensure that the next run was efficient.

5.5 Testing The Impact of Chloride Ions on Reaction rates in Methylene blue (MB) and Methyl Orange (MO)

5.5.1 The Reaction Rates for Methylene Blue (MB)

Equipment set up

A study of the impact of chloride ions on the photocatalysis of MB by the TiO_2 requires a setup of experimental conditions that compare the rate of absorbance, in the presence, and in the absence of the chloride (Cl^-) ions. In each experiment, the UVA LED pump and laser were turned off, and the system drained. Then, it was filled with DI water which was allowed to circulate for 10 minutes. The water was then changed and allowed to circulate for 10 minutes again. This was followed by having the lid replaced, and the laser turned on. Then, the voltage on the photodiode was measured before mixing water with methylene blue or methyl orange. However, it is notable that the current chosen regardless of the magnitude has to be constant throughout the experiment. The UVA LED is fed with a relatively high bias current of 800 mA to increase the UV photon flux to get acquire data quickly. This bias current was kept constant across all runs. The next step entailed turning on the laser diode in the case of methylene blue or blue LED for methyl orange. Once the laser diode, for MB or LED for MO, turned on, it was ready to measure the signal through the DI water. Here, the system was filled with DI water to a certain point then MB or MO was added and the mixture will placed in the beaker. Logging was then started and the specific readings taken, noting the time. Here, an experiment set up entailed changing either water or wafer or both each time and observing the variation in the absorbance. This process entailed experiments conducted in three tests namely experiments 1, 2, and 3 (below).

Experiment 1: Same Wafer, Changing the Water

In this experiment, the silicon wafer was set up and reaction runs performed 4 times. Each time, the water was changed and repeating the steps above draining and filling the apparatus with DI water was done 4 times. Notably, the same silicon wafer was retained during the 4 runs, despite the water being changed.

Experiment 2: Different Wafers, Same Water

This experiment was conducted in a similar procedure as described above. However, four silicon wafers were used, without repeated use of a silicon wafer. This implies that one silicon wafer was used in each run. Here, a change of wafers was done by removing them from the beaker and replacing with a new one, but retaining the water. In correspondence with the test above, this test was repeated four times. Thus the readings were recorded for the four reaction runs.

Experiment 3: Same Wafer, Same Water

In this test, the same silicon wafer and the same water were used for all the 4 runs. Each time it was ascertained that everything was settled and the system was working, before commencing the run. This test was repeated thrice to get the mean and standard deviation.

5.5.2 The Reaction Rates in Methyl Orange (MO)

The test process was conducted in a similar way to that described in section 5.5.1. It is important to note the variation of equipment set up, where in this case, a blue LED with peak emission between 400-500 nm was used, instead of a red laser diode with $\lambda = 500$ nm. The procedures were repeated, but this time, methylene blue was replaced with methyl orange (MO) and the results compared with that in section 5.5.1. The data recorded was filled in the forms presented in the appendix. Here, the start time, end time, some wafers below each of the set experimental parameters and the changes made were analysed. The reaction time and the file name, as well as voltage reading before and after the adding the organic dyes, was recorded.

5.6 Results and Discussion

5.6.1 Dye Containing Chloride Ions (MB)

This experiment used MB. The tests conducted varied in the number of runs and the number of wafers. Here, the reaction rates in experiment 1, 2, and 3 were observed and then used to plot the absorbance curves. The curves help to show the variations in the case where chloride ions are present and when they are absent. The results are presented as shown in the graphs below .

Experiment 1: Same Wafer, Changing the Water (4 Reaction Runs)

The reaction has finished after 24 hours and the water was completely clean. The decay reaction time was different in all four runs as can be see in the table 5.1. It was particularly short in the first run (a) with a characteristic decay time of 2.57 hours. In the second run (b), the decay reaction time was a factor of 3 longer than the first run, at 6.07 hours. The exponential fit was a good match the reaction curve since (Adj R-square) was nearly 0.99. In the third run (c), the curve after 23 hours increased and that could be due to people entering the lab towards the end of the experiment and changing environmental conditions. The fourth graph (d) was difficult to fit and gave a large error. This reaction run gave a decay time of 20 ± 0.34 hours. It was much longer than all previous runs. The error was large here and the fit was not good. The wafer was not fresh and the photocatalytic material was barely left on the silicon wafer. This shows that there is something going wrong with the experiment, perhaps a stability problem with the laser intensity, photo diode reading, or a significant change in room temperature.

Experiments	**Absorbance Decay Time (hrs)**
First run	2.57 ± 0.01
Second run	6.07 ± 0.01
Third run	7.96 ± 0.03
Fourth run	20 ± 0.34

Table 5.1: The decay time of absorption for four runs in the same wafer with changing water using MB solution (i.e. changing the entire liquid but keeping the same photocatalytic film for all 4 reaction runs).

As can be seen from the graphs however, the absorbance behaves according to a exponential decay within the first ten hours. The experiment was run for 24 hours, and by then the water was completely clean. The decay time was varied from one run to another in this experiment. After all runs, it was clear that proper amount of MB solution and fresh catalyst would make the reaction faster. It is evident that the first characteristic reaction rate was the shortest and the fourth characteristic reaction was the longest, after which the photocatalyst has become tired.

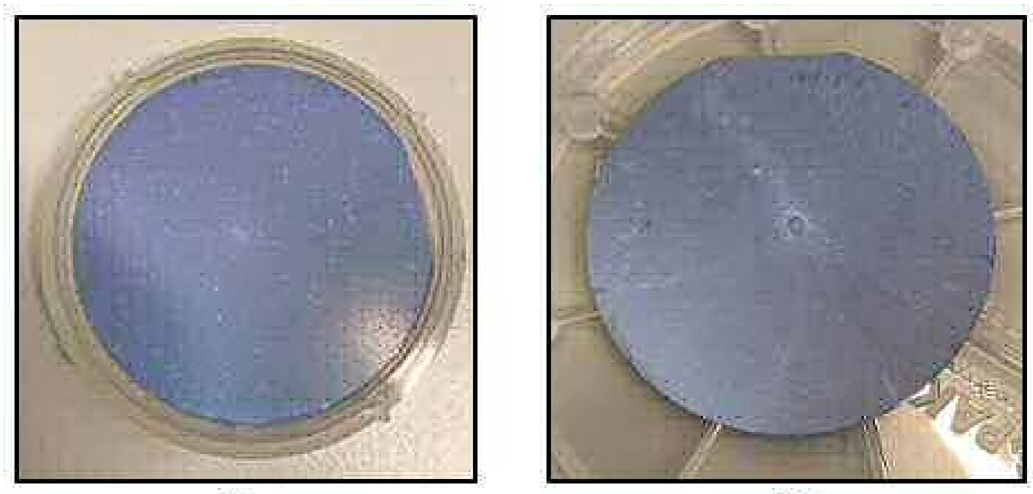

(a) (b)

Figure 5.4: (a) and (b) shows the wafer before and after all four reaction runs.

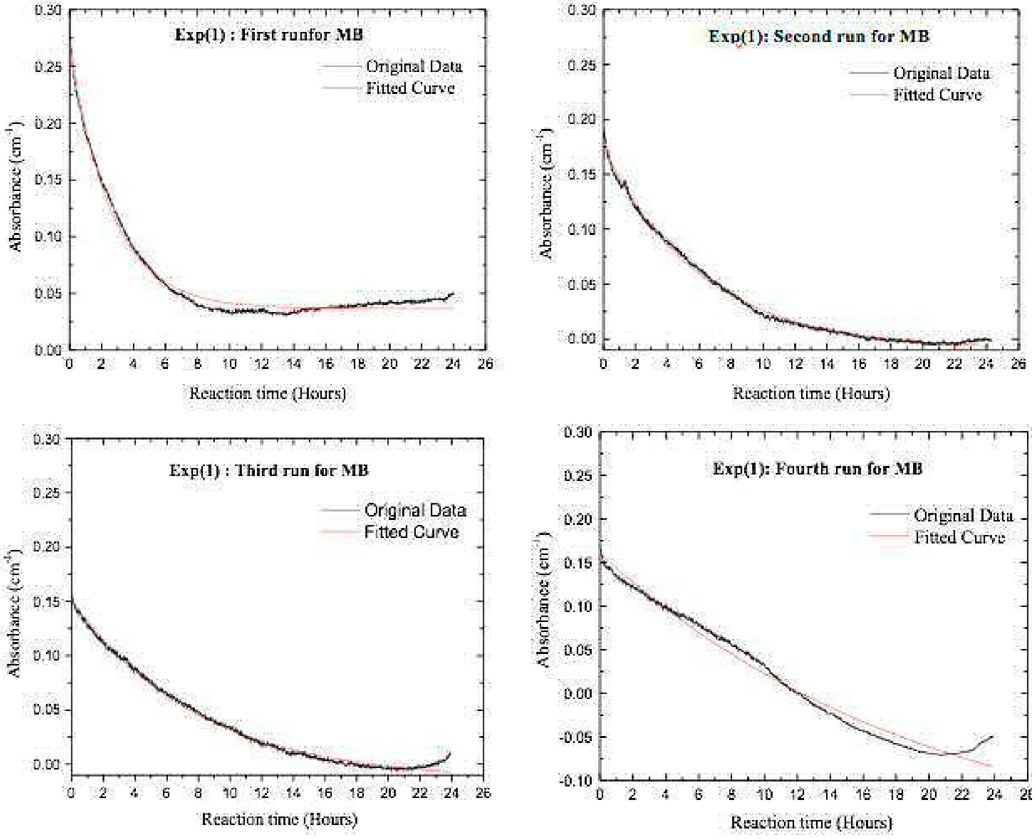

Figure 5.5: (a), (b), (c), and (d) represent the first, second, third, and fourth run respectively for the same silicon wafer with changing water each reaction run in MB solution.

Experiment 2: Using 4 Wafers in the Same Water (4 Reaction Runs)

The decay reaction time was different in all four runs as can be seen in table 5.2. The (Adj R-square) was nearly 0.99 in all, so the exponential fit was matching the reaction curve.The experiment was run for 24 hours, until the water was completely clean.

Experiments	**Absorbance decay time(hrs)**
First run	3.39 ± 0.02
Second run	6.82 ± 0.03
Third run	9.36 ± 0.01
Fourth run	10.41 ± 0.01

Table 5.2: The decay time of absorption for four runs in different wafers with the same water using MB solution

The results of experiment 2 are slightly similar to the runs conducted with same wafer in experiment 1. It shows that the fourth run is slower than the first run. It was much longer than all previous runs. Absorbance time for the first run reached the earliest time. The decay reaction time of the second run was longer than the first run and the third run was longer than the second. This observation shows that each wafer run contributed to the photocatalysis, and the combined action is recognisable as the number of wafers increase. The result confirms that the photocatalysis action on MB is a result of the wafers used (as shown in experiment 1) and that repeated action causes a decrease in the reaction rate.

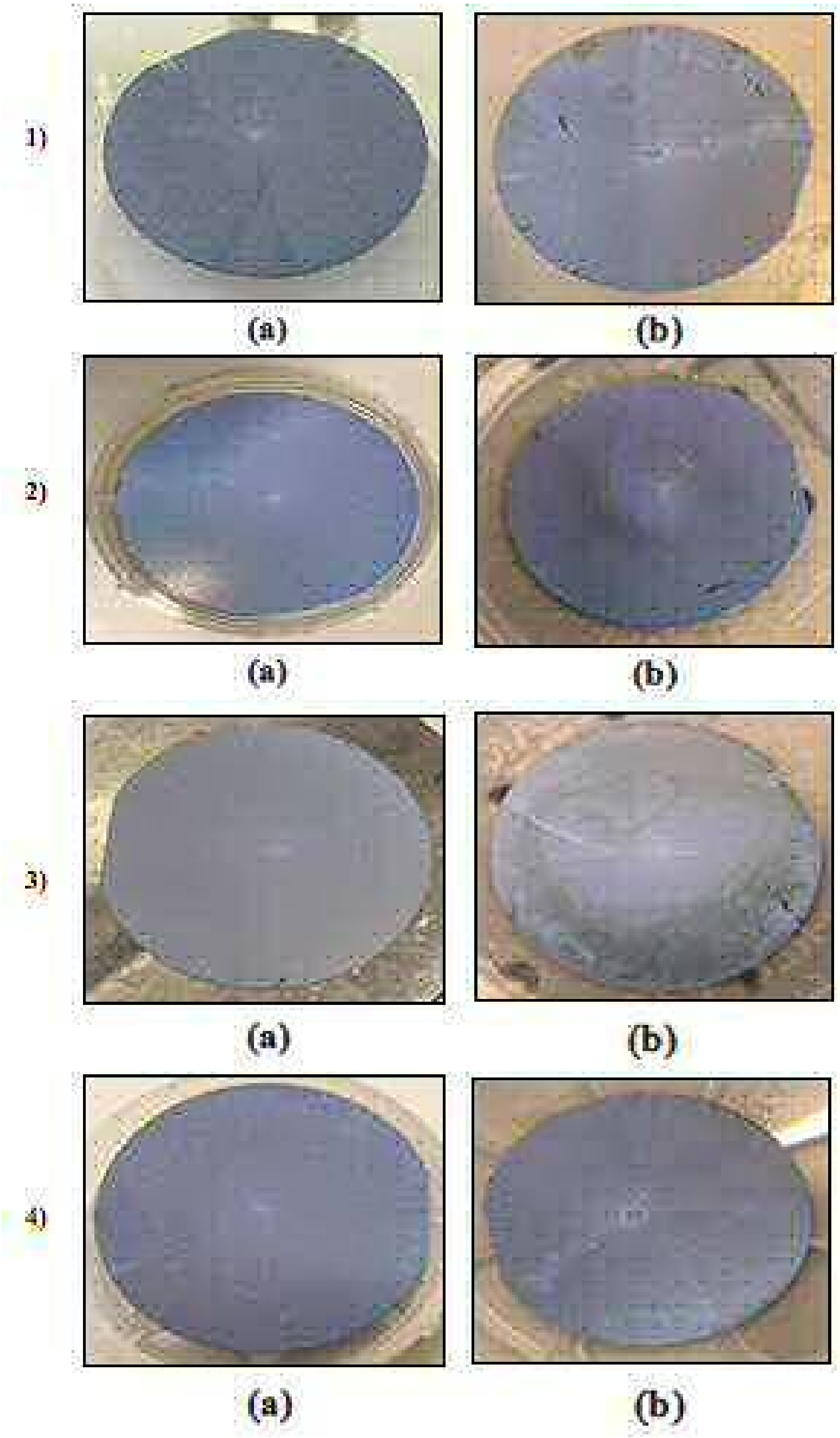

Figure 5.6: (a) and (b) shows the wafer before and after all four runs, (1), (2), (3), and(4) represent the first, second ,third, and fourth run.

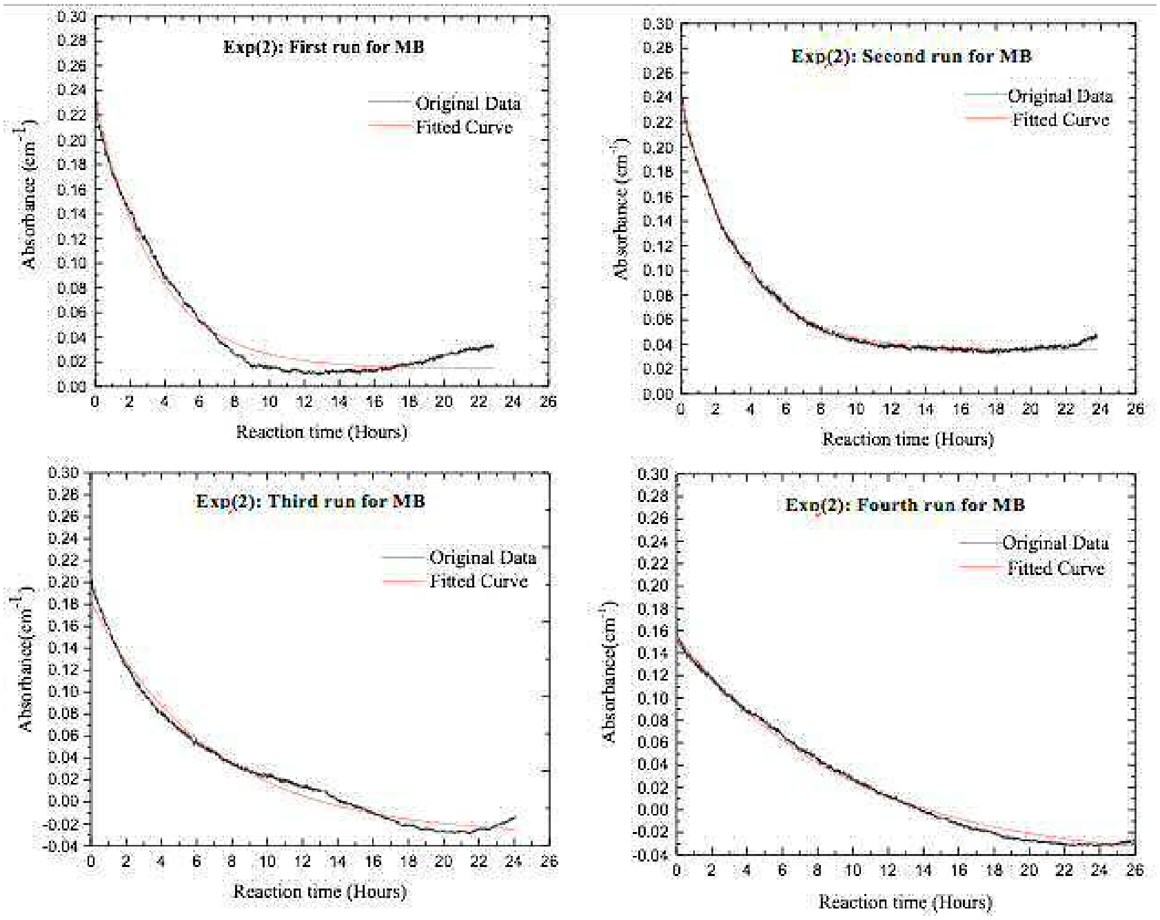

Figure 5.7: (a), (b), (c), and (d) represent the first, second, third, and fourth reaction run respectively for four different silicon wafers in the same water using MB solution.

Experiment 3: Using Same Wafer, Same Water (4 reaction runs)

The experiment was run for 24 hours and the water was completely clean. The decay reaction time was different in all four runs as can be see in the table 5.3. It was short in the first run (a) and long in the fourth run (d). The exponential fit matched the reaction curve of the graph perfectly since (Adj R-square) was nearly 0.99. In the second run (c), the curve after 15 hours was fluctuating a bit (probably due to changing the room temperature) or some stability problems with either the laser or the UV LED. In this experiment, we used the same wafer and water for all four runs and the catalysts was barely left on the silicon wafer. Each photocatalytic reaction runs typically for about 24 hours. This is usually enough time for the colour of the dye to clear completely from the water.

Experiments	**Absorbance decay time(hrs)**
First run	3.39 ± 0.01
Second run	8.38 ± 0.04
Third run	9.81 ± 0.05
Fourth run	10.52 ± 0.05

Table 5.3: The decay time of absorption for four runs in same wafer and same water using MB solution.

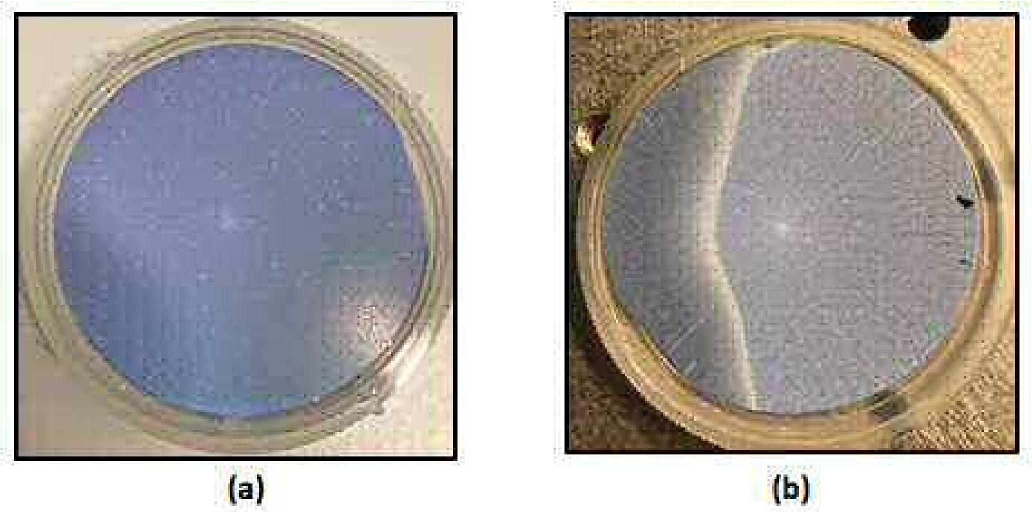

Figure 5.8: (a) and (b) shows the wafer before and after all four runs

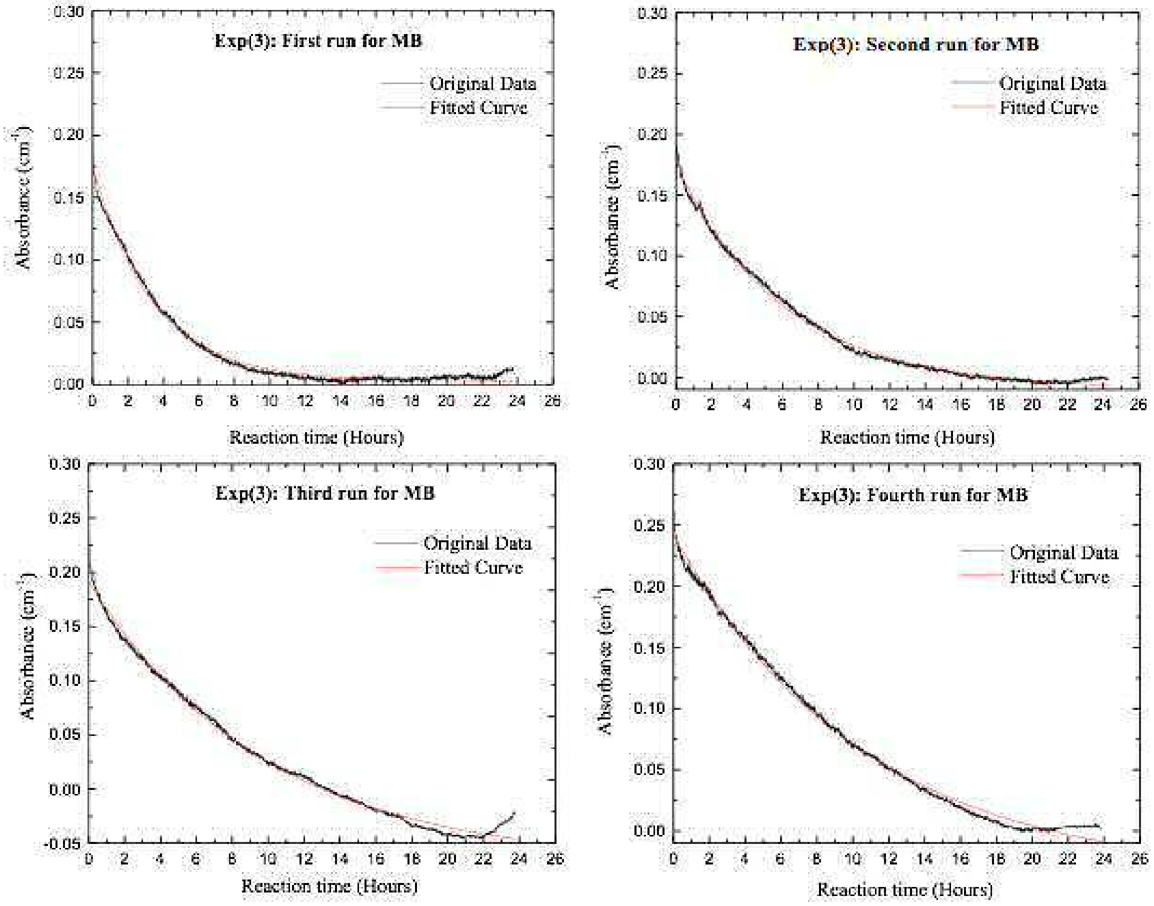

Figure 5.9: (a),(b),(c) and (d) represent the first ,second,third and fourth run respectively for the same silicon wafer and same water using MB solution

5.6.2 Dye Containing No Chlorine Ions (MO)

Experiment 1: Using Same Wafer, Changing Water (4 Reaction Runs)

The figure 5.10 shows the results obtained when the tests were conducted with no chlorine, for the case of methyl orange dye (MO). Here, the scratch that can be seen before the run which was made due to human error when removing it from the hot plate. The white spot on the wafer could be water staining when it was removed from the reservoir, then after it was left out to dry. The wafer colour became a bit lighter after running, and that implies that the MO dye has degenerated after the exposure to the wafer. This observation shall recur in all the observations.

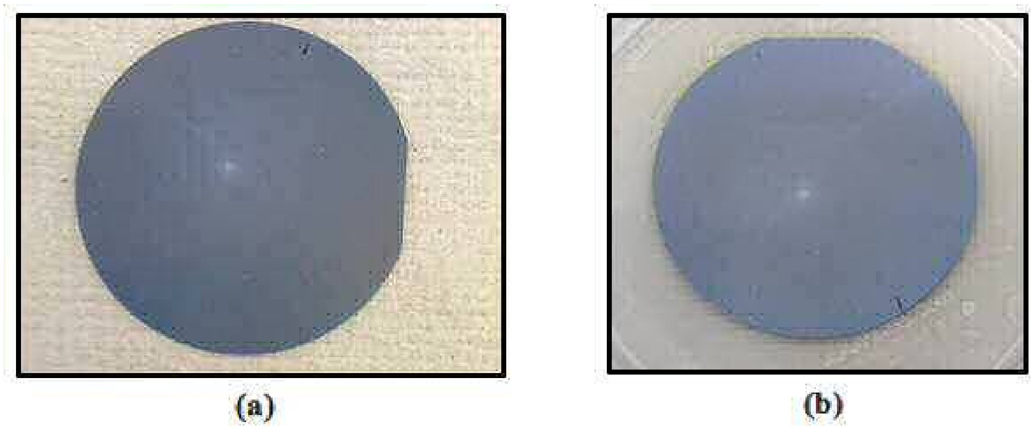
(a) (b)

Figure 5.10: (a) and (b) shows the wafer before and after all four runs.

The absorbance data was plotted in Origin, to determine the decay time. Analyzing data using linear fit, followed by an exponential fit and logarithmic scale was conducted, to find the coefficient of the exponential fit. The exponential represents the reaction rate constant β , and from the linear fit, we can get the gradient of the graph which is τ (the reciprocal of β). In this case, the time taken for the concentration of the dye to decrease by $1/e$ is the reaction time.

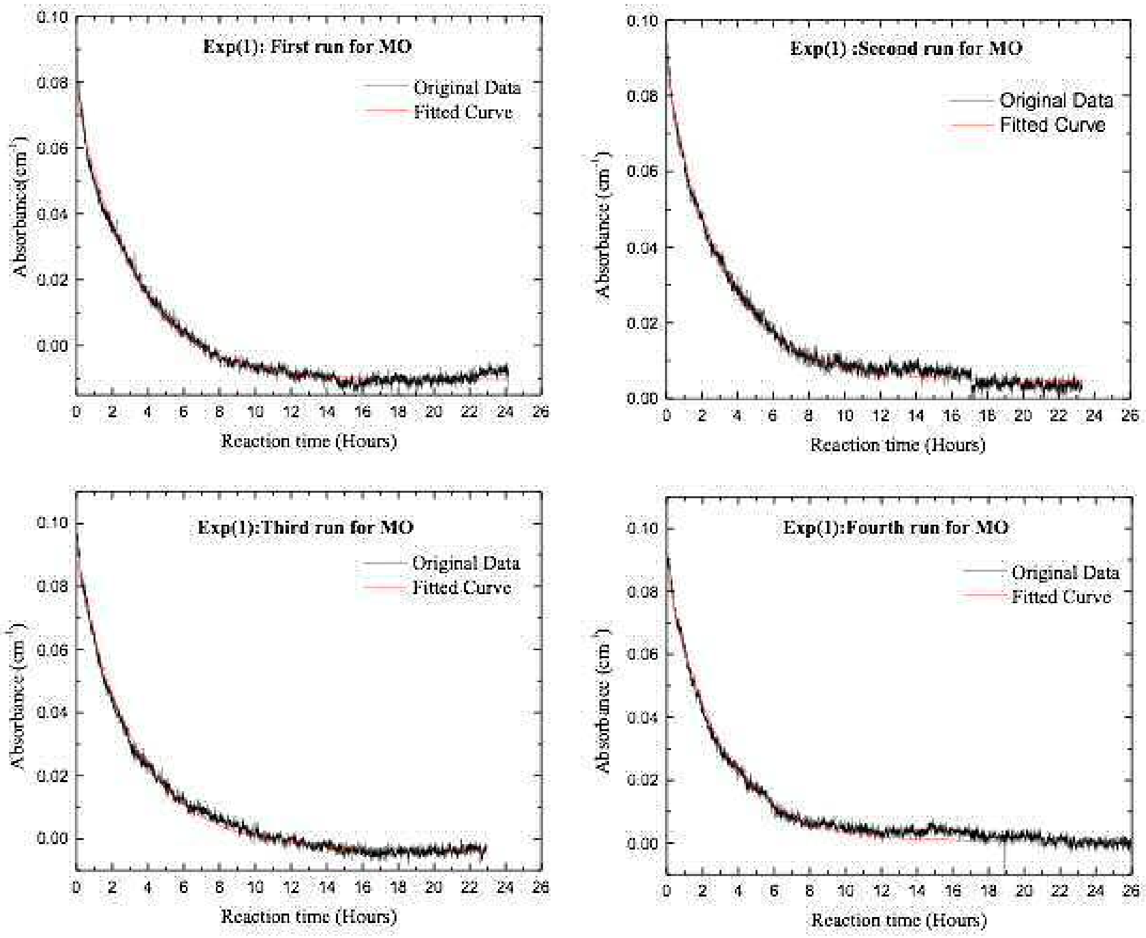

Figure 5.11: (a), (b), (c), and (d) represent the first, second, third, and fourth run respectively for the same silicon wafer with changing water each reaction run in MO solution.

It can be observed that the last experiment was running for two days, which led to plotting for 50 hours. Here, the decay time 2.97 ± 0.01 hours for absorption. The reaction was monitored over a day, and the results were plotted using Origin. The reaction was finished, and the water was completely clear at the end of the test. The experiment was run for 24 hours, this run gave a decay time as can be seen in the table 5.4 for the first, second, third and fourth run respectively. The error within this result was ±0.01 hours. The value of this error is small because the exponential fit was matching the curve of the graph to perfection. The drop in the curve represents the fast reaction curve that can be seen between 0 -10 hours, and after that it becomes relatively constant, implying that the rate of degradation has reduced, due to a reduced concentration of the organic dye molecules.

Experiments	**Absorbance decay time(hrs)**
First run	3.30 ± 0.01
Second run	3.23 ± 0.01
Third run	3.26 ± 0.01
Fourth run	2.97 ± 0.01

Table 5.4: The decay time of absorption for four runs in the same wafer with changing water using MO solution.

Experiment 2: Using Different Wafers, Same Water (4 Reaction Runs)

In this experiment, the variable that was changed between the four different runs was the wafer, four fresh silicon wafers coated with TiO_2 nanoparticles were used. The wafer used for this run was freshly spun. Before the next run and the digital multimeter was calibrated, the laser and detector in the same line, the pump still work to circulate the water during the pipes. We keep the same water in the whole system until finishing four runs. The experiment was run for 24 hours .when the reaction was finished, the water was completely clear. The decay time for each run was recorded in the table 5.5. The error within this result was ±0.01 hours. The value of this error is small because the exponential fit was matching the curve of the graph to perfection. The absorbance goes downward from left to right represents the fast reaction curve that can be seen between 0 -10 hours, and after that it has declined.

Experiments	**Absorbance decay time(hrs)**
First run	3.02 ± 0.01
Second run	3.08 ± 0.01
Third run	3.01 ± 0.01
Fourth run	3.27 ± 0.01

Table 5.5: The decay time of absorption for four runs in different wafers in the same water using MO solution

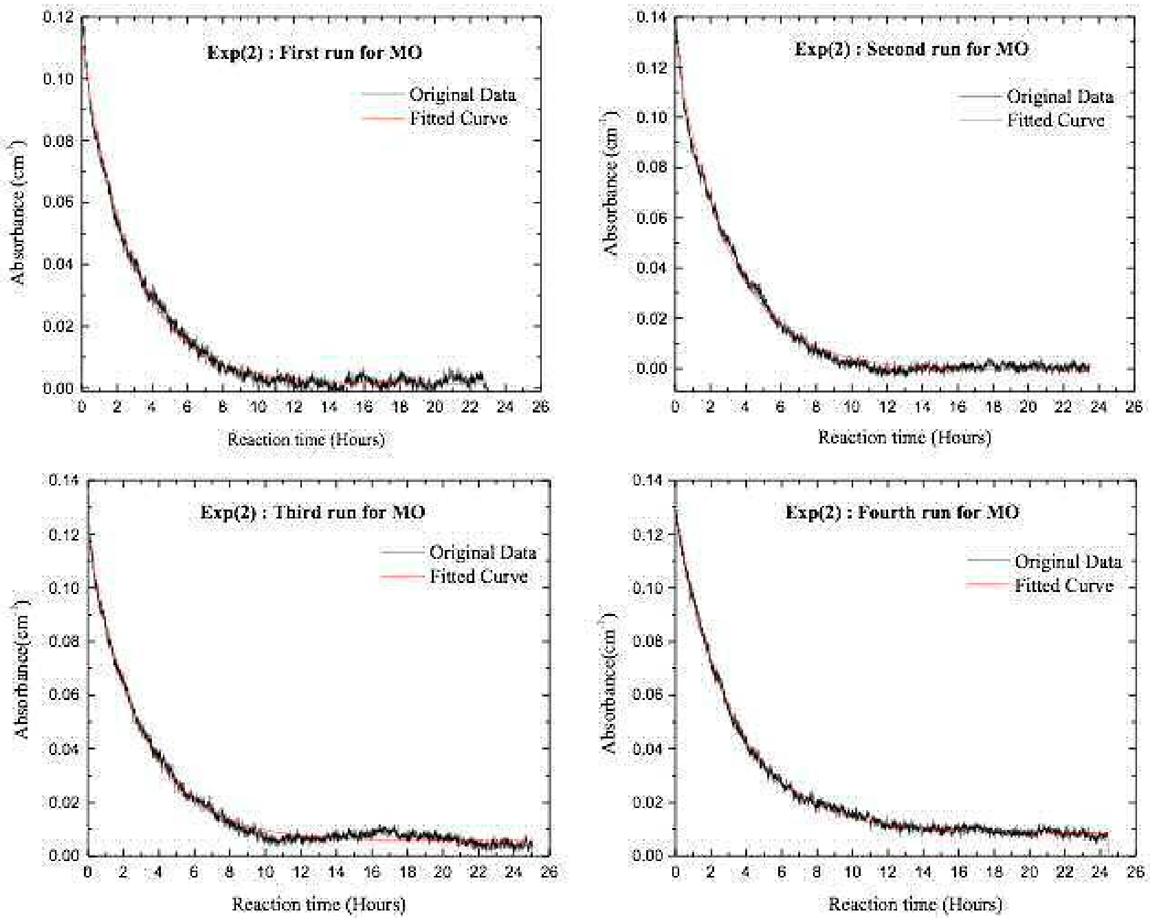

Figure 5.12: (a), (b), (c) and (d) represent the first, second, third, and fourth run respectively for four different silicon wafers in the same water using MO solution.

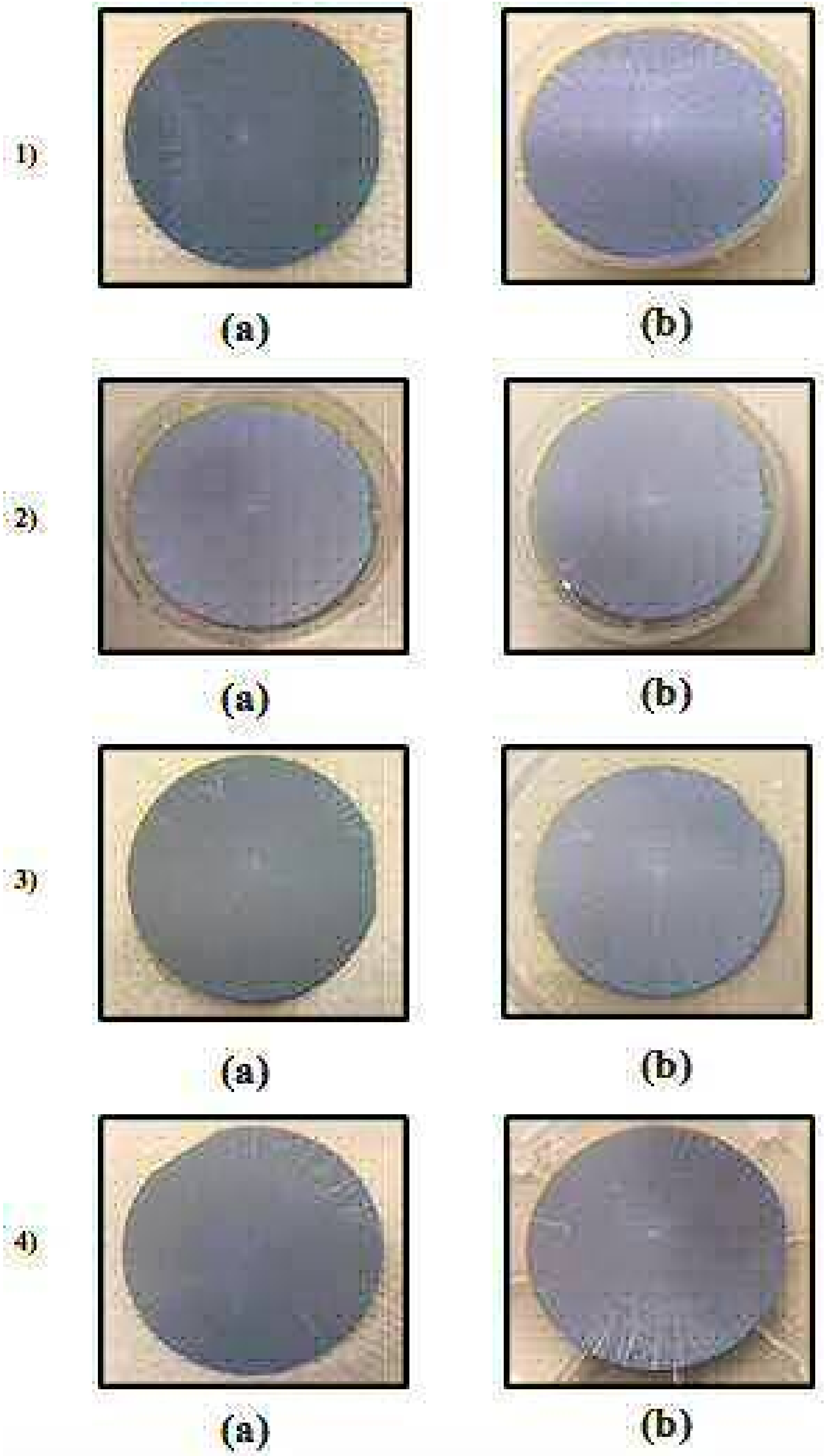

Figure 5.13: (a) and (b) shows the wafer before and after all four runs respectively.

Experiment 3: Using Same Wafer, Same Water (4 Reaction Runs)

Here, there were two options that include keeping the wafer and the water without changing in all the four runs or change both wafer and water in each run. However, I preferred doing that without change any of them thus same water, and the same wafer was used. The experiment was run for 24 hours. This runs gave a decay time as shown in the plots 5.14. The error within this result was ±0.01 hours and the reaction rates are collated in table 5.6. The reaction was finished after running for 24 hours. The water was clear. The absorbance decay time for each run was recorded in the table 5.6. Since the exponential fit was matching the curve of the graph, the error within this result was very small ±0.01 hours. The absorbance decreased exponentially from left to right . The curve was dropping between 0 -10 hours and after that it declined steadily then became constant.

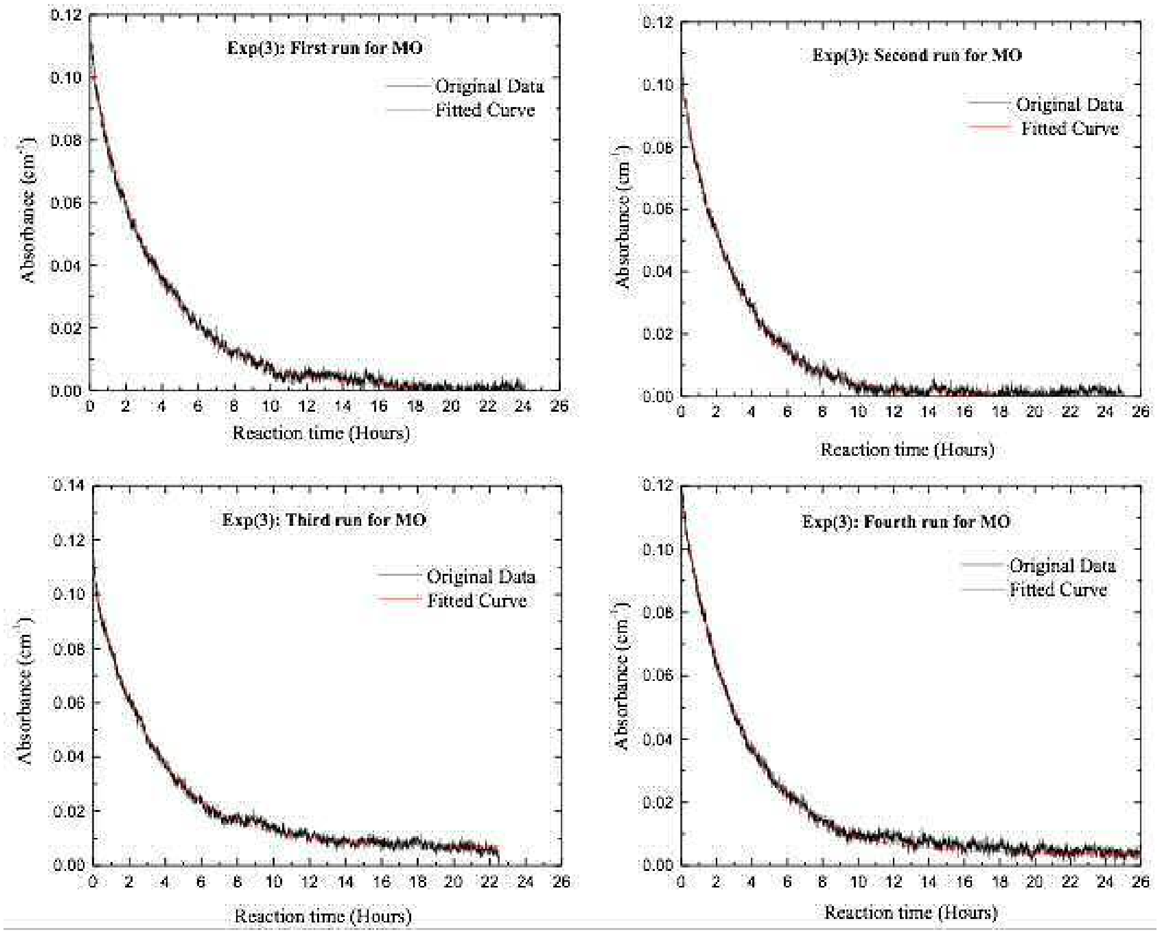

Figure 5.14: (a), (b), (c) and (d) represent the first, second, third, and fourth run respectively for the same silicon wafer and same water using MO solution.

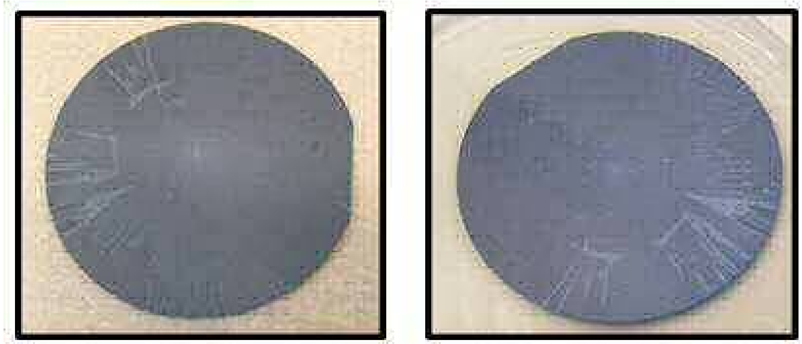

(a) (b)

Figure 5.15:]
(a) and (b) shows the wafer before and after all four reaction runs.

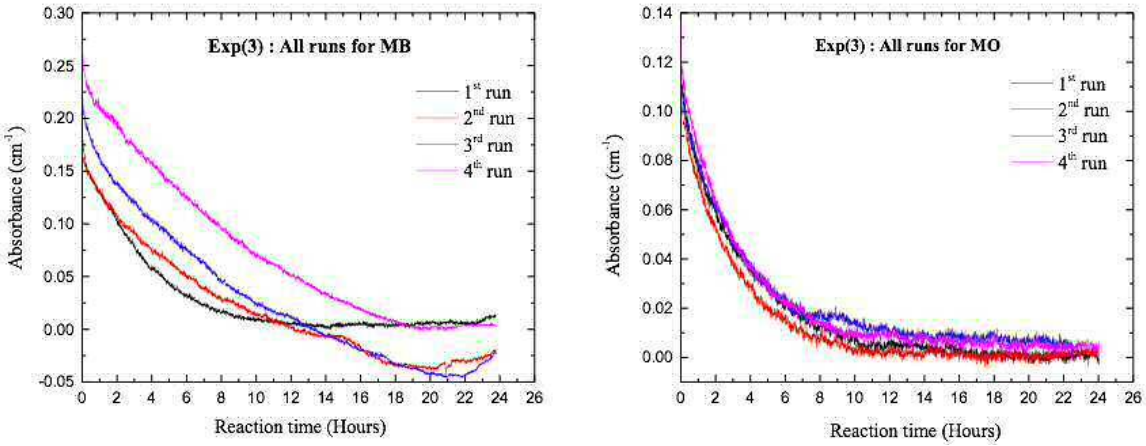

Figure 5.16: Combined plot of the four runs in MB and MO

Experiments	**Absorbance decay time(hrs)**
First run	3.63 ± 0.01
Second run	3.04 ± 0.01
Third run	3.41 ± 0.01
Fourth run	3.38 ± 0.01

Table 5.6: The decay time of absorption for four runs in same wafer and same water using MO solution

5.7 Adding Chloride Ions to Methyl Orange

There was one further experiment to perform as a sanity check. What is the effect of artificially introducing chloride ions to methyl orange? I tried to mimic the concentration of chloride ions that would naturally occur in a comparable concentration of methylene blue. A specific amount of NaCl was added to methyl orange solution. To achieve this a simple calculation is performed.

5.7.1 MB Chloride Ion Calculation

The concentration of MB that been used in the system was 1.37×10^{-4} moles/L. The number of moles of MB can be calculated from this equation:

$$n(Moles) = M(moles/L) \times V(L) \tag{5.6}$$

In this experiment, we added 2 ml of MB solution to 100ml of deionised water. Then the number of moles can be calculated by this equation:

$$M = 1.37 \times 10^{-4} \times \frac{2}{1000} \tag{5.7}$$

$$M = 2.74 \times 10^{-7}(moles/L) \tag{5.8}$$

For every 1 mole of MB, there will be 1 mole of Cl^- ions.

$$Moles\,of\,Cl^- = M \times V = \frac{mass(g)}{m_r} \tag{5.9}$$

$$8.5 \times 10^{-4}(moles/L) = \frac{mass}{35.45(g/mol)} \tag{5.10}$$

$$mass = 8.5 \times 10^{-4}(moles/L) * 35.45 = 0.031875g \tag{5.11}$$

5.8 Chloride Poisoned MO Results

It is clear from the four reaction runs shown in figure 5.17, that the reaction rate is slowed down (just like what naturally happens for MB).

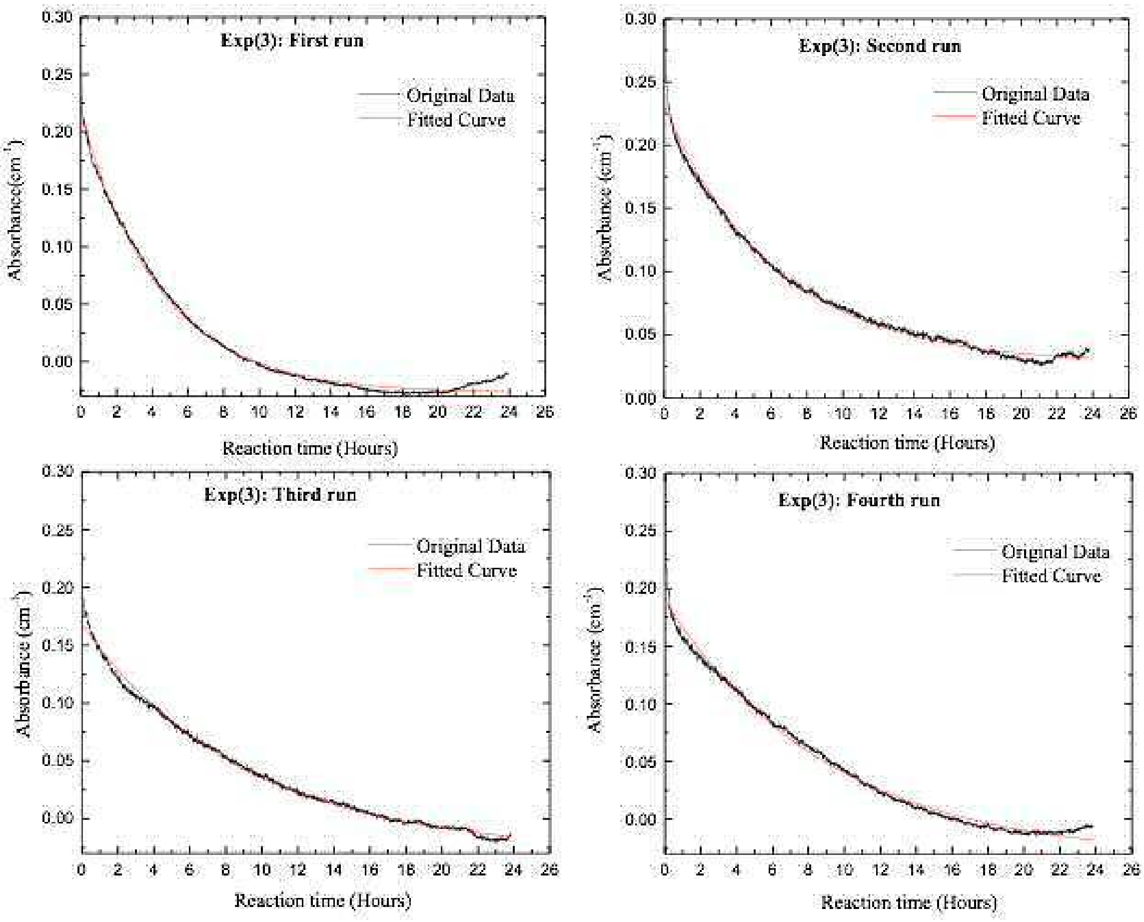

Figure 5.17: MO solution with chloride ions

5.9 Effect of Sodium Ions

While my experiments assess the effect of adding chloride anions, I cannot explicitly rule out some effects of the sodium cations. However methyl orange is a sodium salt, so sodium cations are always present. A further set of experiments (future work) might resolve this issue. The experiments could be repeated with comparable molar concentrations of LiCl, KCl, and NH_4Cl to check whether changing the cation had any effect on poisoning effect in methyl orange.

5.10 Summary

The aim of conducting the tests using MB and MO is to test the hypothesis that there is a significant poisoning of the TiO_2 photocatalyst by chlorine ions. MB has chloride ions but MO dos not. Both dyes are discoloured by the photocatalytic action of TiO_2. Our experiments show that Cl^- ions have an impact with MB. This was established by testing the photocatalytic reaction rates for both dyes, under the same conditions. This analysis is based on a comprehensive set of experimental variations (Experiments 1, 2, and 3), performed for both MB and MO dyes. The results obtained in the experiments conducted in this chapter highlight distinctive characteristics of MB and MO, in regard to photocatalytic reaction rate.

The rate of photocatalytic action shows how extraordinarily active is the TiO_2 nanostructured layer. The comparison between, MB and MO shows the impact of Cl^- on the photocatalytic properties of TiO_2. The results obtained using MO do not have a significant change, for experiment 1, 2, and 3. On the other hand, the photocatalytic reaction rate varies considerably for experiment 1, 2 and 3 in the case of MB. This can be interpreted in terms of the poisoning properties, meaning that MO does not poison the TiO_2 catalyst, but MB does. These results show that there is a significant impact of Cl^- ions in the reaction. Thus, the outcome shows that that MB contains the ions that causes the poisoning, which reduces the photocatalytic action. The results support the chloride poisoning hypothesis, showing that when the TiO_2 is used in treatment of waste water, presence of Cl^-should be considered.

Chapter 6

Modified TiO_2 Photocatalysts

6.1 Introduction

We have seen in previous chapters that TiO_2 is very effective at destroying organic pollutants when it is illuminated with UV light. This is because of the inherently large band-gap of 3.0-3.2 eV in the intrinsic material. Thus, the longest wavelength photon that can create the electron-hole pairs necessary to facilitate photocatalysis is $\lambda =$ 378 nm. This only corresponds to between 3-5% of the photons in the solar spectrum. There are many more available photons with wavelengths crossing the visible solar spectrum. In order to access these longer wavelength photons, the energy gap in TiO_2 needs to be red-shifted to lower energies. There have been a several approaches tried. The world-leading Cardiff Catalysis Institute (CCI) have successfully pioneered the technology of impregnating TiO_2 with precious metal nanoparticles such as gold and paladium to enhance the photocatalytic properties [83]. I also previously mentioned the work of Lee *et al.* [84], who demonstrated 97% degradation of MB dye under visible light within 3 hours, which was 9 times better than TiO_2 (P25) under similar conditions.

In this chapter I will concentrate on my efforts to redshift the intrinsic band-gap of TiO_2 through incorporating transition metals in the TiO_2 crystal matrix. If transition elements from period (row) below tungsten are used, the substituted atoms are bigger in size and displace the atoms of the titanium dioxide. This should decrease the energy required for transference of electrons to the conduction band, consequently red-shifting the intrinsic band-gap, as depicted in figure 6.1. For transition metals drawn from periods two or three below titanium, the atomic radii are larger and so the atoms need to be incorporated into the crystal lattice interstitially rather than substitutionally. This should affect the intrinsic band-gap differently.

I am eternally grateful to Dr Emma Richards and Kate Armstrong of the Cardiff School of Chemistry, who helped me with the synthesis and characterisation of these new doped TiO_2 compounds.

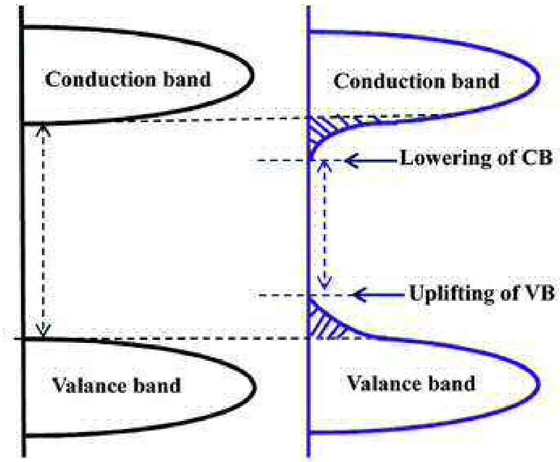

Figure 6.1: The dopants able to narrow the band gap and push the absorption wavelength into the visible region.

6.1.1 Metallic-doping of TiO_2

When Titanium dioxide is doped with metallic/nonmetallic elements, it should become a more effective photocatalyst for the purification of air and water. It also becomes effective for self-cleaning surfaces. It can also be used as an antibacterial agent as a result of its strong oxidation activity and super hydrophilicity. It also shows high chemical stability and super hydrophilicity when it is under the UV light whose energy exceeds the band gap of 3.2 eV in the crystalline phase of anatase. The development of photocatalysts that shows high reactivity under visible light should allow access to the main parts of the solar spectrum, even when the interior lighting are under poor illumination.

Metallic transition elements (MTE) or Group VI doping is a common method to improve the catalytic activity of TiO_2-based materials (highlighted in the Periodic Table shown in figure 6.2). This is due to the dopants ability to narrow the band gap and push the absorption wavelength into the visible region which increases the photonic efficiency. The presences of dopants can also play a role in either the charge separation or the charge recombination which also influences the material's ability to act as a photocatalyst. The transition metals used for this work are chromium (Cr), from the same period (row) as Ti, molybdenum (Mo) for the period below Ti, and tungsten (W) from the period two below Ti. There is one further element in the column, Seaborgium (Sg). However, this element is significantly different from the other transition elements, and I did not use it in my research experiments. It is one of the new family of artificial elements with atomic number larger than the last naturally occurring element, Uranium (U). Sg is highly unstable, radioactive, and it has only one stable isotope, Sg-271 with a half-life of about 2.4 minutes. I chose W, Cr, and Mo, since they can be easily inserted into the lattice and electronic structure

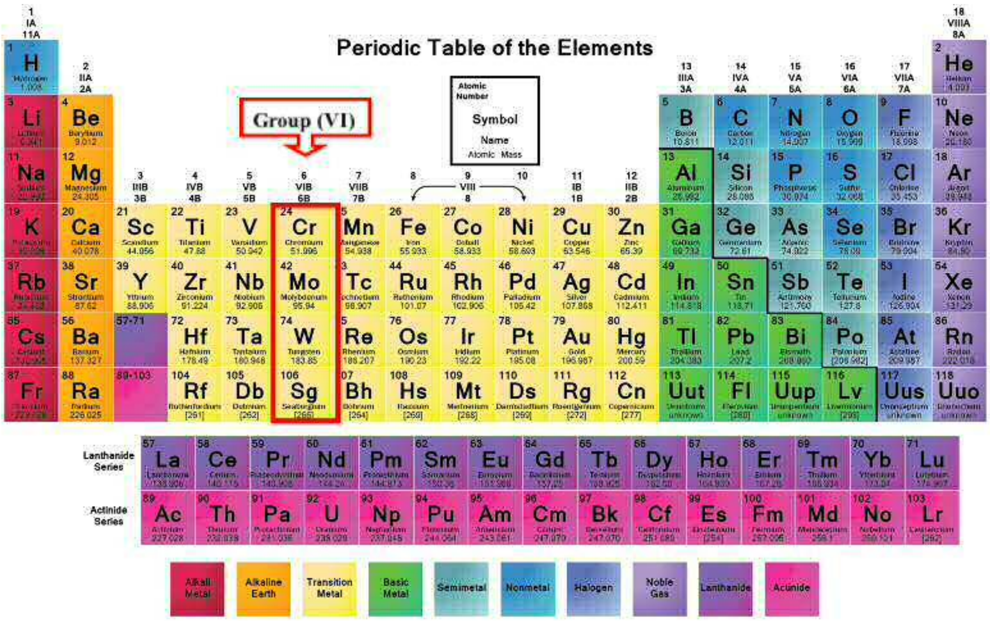

Figure 6.2: The periodic table

Element Name	**Atomic number**	**Oxidation states**	**Electronic configuration**
Chromium (Cr)	24	$+2, +3, +6$	$Cr : [Ar]3d^5 4S^1$
Molybdenum (Mo)	42	$+4, +5, +6$	$Mo : [Kr]4d^5 5S^1$
Tungsten (W)	74	$+4, +5, +6$	$W : [Xe]4f^{14} 5d^4 6S^2$

Table 6.1: Oxidation states of Cr, Mo and W

because of their size and they, are abundant on the earth. These metals also have a high tendency to dope TiO_2. Mo has 11 isotopes, a melting point of 2610 °C, and a boiling point of 4825 ◦C. It has a density of 10.2 g/cm^3 at 20 °C. This element is commonly used as an alloying agent. It is used to harden and toughen steels. It is used as a catalyst, an for electrodes in plasmas. Cr has six isotopes. It has a melting and a boiling point of 1907 °C and 2672 °C respectively. It has a density of 7.19 g/cm^3 at 20 °C. This element is used as an alloy in the steel industry. It is also used in metallurgy for corrosion resistance and to have a finish that is shiny. This element is also used in the manufacturing of a magnetic tape. It is also used as a catalyst in leather tanning and dyes. Tungsten has an atomic number of 74. It has ten isotopes. It has a melting and a boiling point of 3410 °C and 5660 °C respectively. It has a density of 19.3 g/cm^3 at 20 °C. It is used in the incandescent bulb as a filament. It is also used as an alloy. It is also used in LCD and microchip technology.

6.2 Experimental details

To study the effect of doping TiO_2 with metallic nanoparticles on the reaction rate, the experiment was divided into three parts. First, I prepared the pure anatase and rutile suspensions for spin coating, and the effect of both of them on the reaction rates under the UV lights was to be studied. Second, I prepared transition metal doped TiO_2 (both anatase and rutile phases) for spin coating, and I studied the effect of both of them under UV lights as well. Thirdly, I did the same step as step 2 but under the longer wavelengths required for each doped materials. I then compared the three ways together to choose the best one in the photocatalytic reaction rates.

6.2.1 Chemical Reagents Used

All the chemicals used in the present work were utilised without further purification. The materials used are: Titanium (IV) iso-propoxide $Ti[OCH(CH_3)_2]_4$ ($\geqslant$97%), the dopant precursor: Tungstic acid H_2WO_4, Chromium(VI) nitrate $Cr(NO_3)_6$, Molybdenum(V) pentachloride $MoCl_5$, all sourced from (Sigma Aldrich). Anhydrous ethanol and de-ionised water were used throughout all the experiment.

6.2.2 Synthesis of Pure TiO_2 Suspensions

Pure TiO_2 suspension were prepared using a sol-gel method. In the synthesis of pure anatase and rutile suspension for spin coating, I added 10 ml of titanium iso-propoxide $Ti[OCH(CH_3)_2]_4$ in a 10 ml of anhydrous ethanol in a round bottom flask and dissolved it using graduated cylinders to measure the volume of liquids. I stirred the solution using a magnetic stirrer bar. I added 5 ml of deionised water about 18 $M\Omega$ dropwise to the solution using a separating funeral for consistent drops. Upon adding of water, a white precipitate was instantly formed which redissolved upon further stirring. A lid covered the solution in the round bottom flask and stirred overnight producing the suspension for spin coating in the next day after 24 good hours. The process of spin coating has been explained in detail in the fourth chapter of my thesis. After coating the wafers with thin film of TiO_2 nanoparticles, the wafers were calcined for one hour to different temperatures for the different phases: 400 °C for anatase, and 800°C for rutile .

6.2.3 Synthesis of pure anatase and rutile powder

I had also prepared pure anatase and rutile nanoparticles in powder form. I did the same previous steps to the end (as described in section 6.2.2) to get the final suspension. The following day, the precipitate was filtered and washed. The apparatus consisted of a Buchner funnel which is a white ceramic funnel on top of a filter vac which is a red rubber donut and then underneath that is the filter flask which is like an Erlenmeyer flask with the exception that it has an arm which can be attached

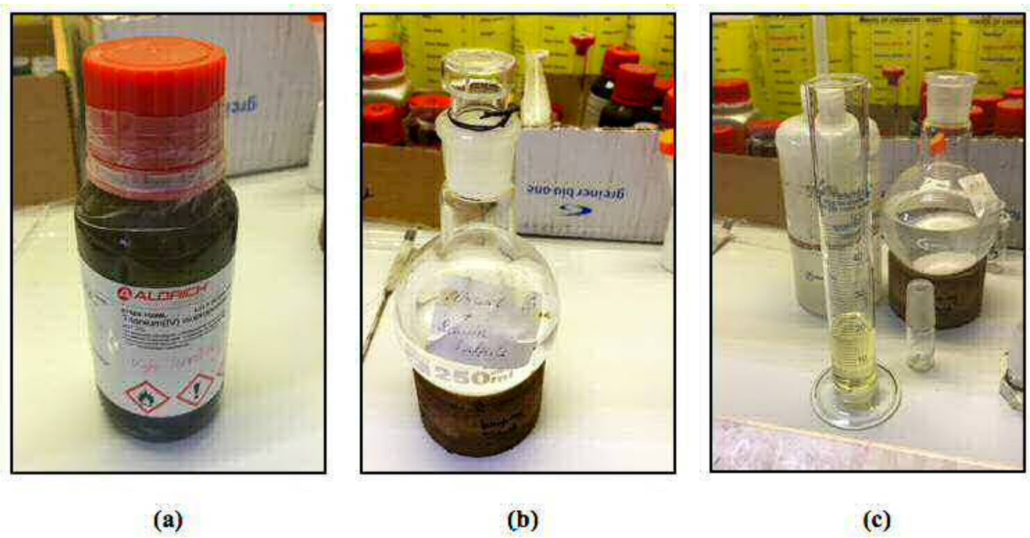
(a) (b) (c)

Figure 6.3: (a) Titanium iso-propoxide, (b) Anhydrous ethanol, (c) Graduated cylinders to measure the volume of liquids

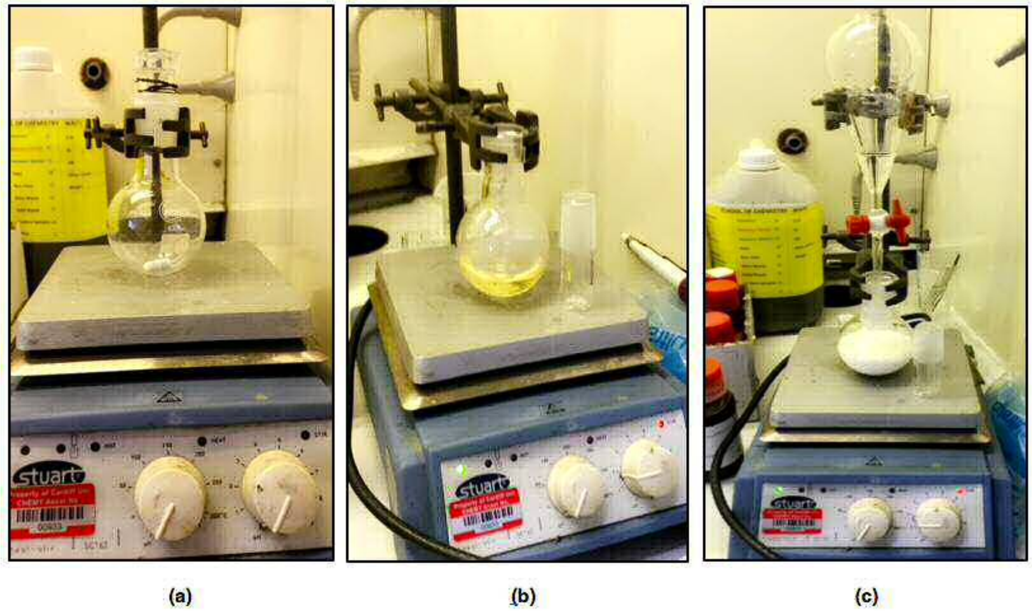
(a) (b) (c)

Figure 6.4: (a) The magnetic stirrer bar, (b) Mixture of titanium iso-propoxide and anhydrous ethanol in the magnetic stirrer bar, (c) Deionised water drop-wise to the solution using a separating funnel.

with a rubber tube to the vacuum machine. I placed a fitter matching of diameter into the Buchner funnel and to get my filter paper to stick to the funnel I put a little water onto the filter paper and turn on the vacuum machine. By pressing down on the funnel I could make an excellent seal so that it draws the liquid through the filter paper and then I could put my mixture of solid and liquid into the filter paper and begin the process of separation. Later, I took the precipitate and put it in aluminium paper inside the oven to dry it under the temperature of 65 °C to 70 °C. The precipitate was dried overnight for a period of complete 24 hours. The sample was ground and calcined to different temperatures for the different phases. For anatase, it was 400 °C for 4 hours and 800°C for rutile for 4 hours. The sample was then ground post-calcination. It is important to note that this could be scaled up or down according and the product would not be impacted.

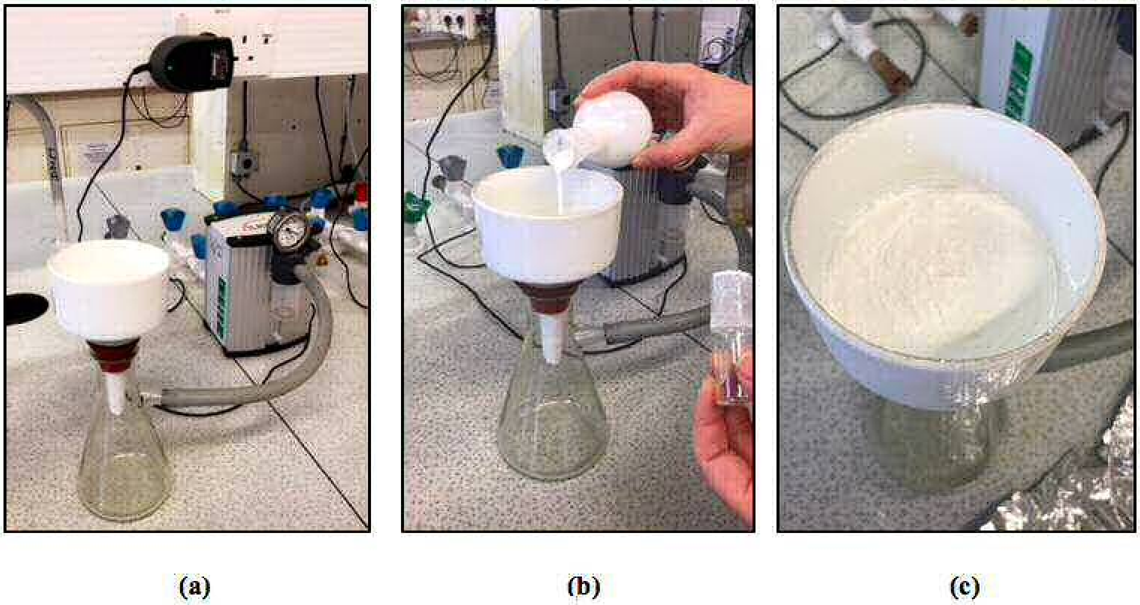

Figure 6.5: (a) The Buchner funnel with a proper filter paper inside it. (b) The precipitate was filtered. (c) The precipitate after washed with drops of deionised water.

Figure 6.6: The precipitate in aluminium paper inside the oven to dry

Figure 6.7: The upper image shows the shape of precipitate after drying it under 65 -70 degree while the bottom image shows the sample being grounded to become fine powder

(a) (b) (c)

Figure 6.8: The sample was calcined to different temperatures for the different phases (a) The oven with the stick (b) The tube is tight inside the oven (c) Slot to insert the sample and push it inside with the stick

Figure 6.9: Although the mass of each of the three materials P25, Anatase and Rutile are the same 800 mg the size of each one in the test tube is different because of its different density

6.2.4 Synthesis of Metal-doped TiO_2 Suspensions

For the synthesis of metal-doped TiO_2 suspension for spin coating, Titanium isopropoxide (10 ml, $\geqslant$97%, Sigma Aldrich) was dissolved in anhydrous ethanol about 10 ml. After thorough mixing of the solution, deionized water of 5 ml, 18 MΩ was added slowly to the solution. The resulting white precipitate was redissolved upon further stirring. The desired amount of the dopant precursor (tungstic acid for W-TiO_2, Chromium nitrate for Cr-TiO_2 and molybdenum pentachloride for Mo-TiO_2) (Sigma Aldrich) in deionized water (5 ml, 18 MΩ) was then added producing the suspension for spin coating. The wafers were calcined at 400 °C or 800 °C to produce the Anatase and Rutile phases respectively. It is important to note that we can change the doping concentration by adjusting the amount of dopant added from masses calculation which will be explained in the following paragraph.

Figure 6.10: Rutile on the silicon wafer was calcined at 800 °C

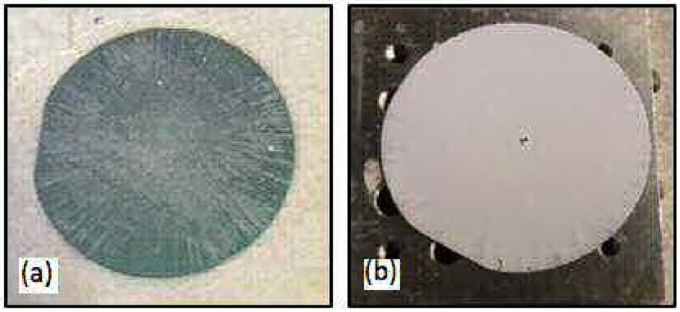

Figure 6.11: (a)The coating was not perfect even after putting the suspension in ultrasonic bath , still granules and gave a bad coverage by using pure anatase powder, (b) perfect coating by using the stirred overnight suspension.

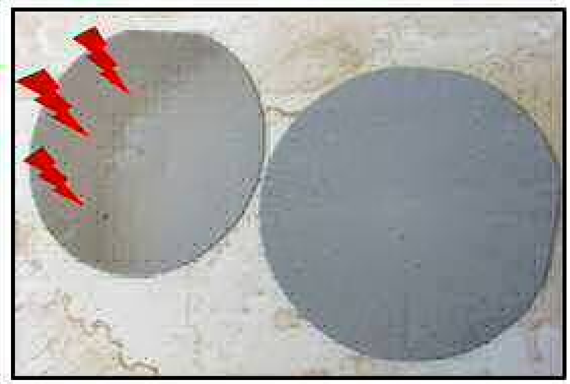

Figure 6.12: After coating the Si wafers with TiO$_2$ nanoparticles, It is important to be heated directly on a hot plate at 400 °C to get a good coverage like the wafer on the right. If the surface of the hot plate was not flat, then the wafers will burn like the one on the left.

6.2.5 Calculation of Desired Mass of the Dopants

To calculate the mass percent or weight percent of a solution, we must divide the mass of solute by the mass of the solution and then multiply by 100 to change it into percent. wt% means weight percent which is sometimes written as w/w.

Cr-doping - 0.1 wt %

$$0.1\% = \left(\frac{1Cr\,atom}{1Cr\,atom + 999\,Ti\,atoms}\right) \tag{6.1}$$

$$0.1\% = \left(\frac{1mol\,Cr}{1mol\,Cr + 999\,mol\,Ti}\right) \tag{6.2}$$

$$Density(g/ml) \times Vol(ml) = mass(g) \tag{6.3}$$

$$Density\,of\,Ti\,precusor(0.96) \times volume\,used(20) = (19.2)g\,of\,Ti\,used \tag{6.4}$$

$$\left(\frac{mass}{Mr(Ti\,precusor)}\right) = moles \tag{6.5}$$

$$\left(\frac{19.2(g)}{284.2(gmol^{-1})}\right) = 0.06756\,(moles) \tag{6.6}$$

$$Mol\,Cr = \left(\frac{0.06756}{(999\,mol\,Ti/mol\,Cr}\right) = \left(\frac{0.06756}{999}\right) = 0.00006763mol\,Cr \tag{6.7}$$

$$= 6.763 \times 10^{-5} mol\,Cr \tag{6.8}$$

$$moles \times Mr = mass \tag{6.9}$$

$$6.763 \times 10^{-5} \times 238.01 = 0.0161g\,of\,Cr(NO3)6\,in\,20ml\,of\,TTIP \tag{6.10}$$

Mo-doping - 0.1 wt %

$$0.1\% = \left(\frac{1 Mo\, atom}{1 Mo\, atom + 999\, Ti\, atoms}\right) \tag{6.11}$$

$$0.1\% = \left(\frac{1 mol\, Mo}{1 mol\, Mo + 999\, mol\, Ti}\right) \tag{6.12}$$

$$Density(g/ml) \times Vol(ml) = mass(g) \tag{6.13}$$

$$Density\, of\, Ti\, precusor(0.96) \times volume\, used(20) = (19.2) g\, of\, Ti\, used \tag{6.14}$$

$$\left(\frac{mass}{Mr(Ti\, precusor)}\right) = moles \tag{6.15}$$

$$\left(\frac{19.2(g)}{284.2(gmol^{-1})}\right) = 0.06756\, (moles) \tag{6.16}$$

$$Mol\, Mo = \left(\frac{0.06756}{(999\, mol\, Ti/mol\, Mo}\right) = \left(\frac{0.06756}{999}\right) = 0.00006763 mol\, Mo \tag{6.17}$$

$$= 6.763 \times 10^{-5} mol\, Mo \tag{6.18}$$

$$moles \times Mr = mass \tag{6.19}$$

$$6.763 \times 10^{-5} \times 196.01 = 0.0133 g\, of\, MoCl_5\, in\, 20 ml\, of\, TTIP \tag{6.20}$$

W-doping - 0.1 wt %

$$0.1\% = \left(\frac{1W\, atom}{1W\, atom + 999\, Ti\, atoms}\right) \tag{6.21}$$

$$0.1\% = \left(\frac{1mol\, W}{1mol\, W + 999\, mol\, Ti}\right) \tag{6.22}$$

$$Density(g/ml) \times Vol(ml) = mass(g) \tag{6.23}$$

$$Density\, of\, Ti\, precusor(0.96) \times volume\, used(20) = (19.2)g\, of\, Ti\, used \tag{6.24}$$

$$\left(\frac{mass}{Mr(Ti\, precusor)}\right) = moles \tag{6.25}$$

$$\left(\frac{19.2(g)}{284.2(gmol^{-1})}\right) = 0.06756\, (moles) \tag{6.26}$$

$$Mol\, W = \left(\frac{0.06756}{(999\, mol\, Ti/mol\, W}\right) = \left(\frac{0.06756}{999}\right) = 0.00006763mol\, W \tag{6.27}$$

$$= 6.763 \times 10^{-5} mol\, W \tag{6.28}$$

$$moles \times Mr = mass \tag{6.29}$$

$$6.763 * 10^{-5} \times 249.85 = 0.0169g\, of\, H_2WO_6\, in\, 20ml\, of\, TTIP \tag{6.30}$$

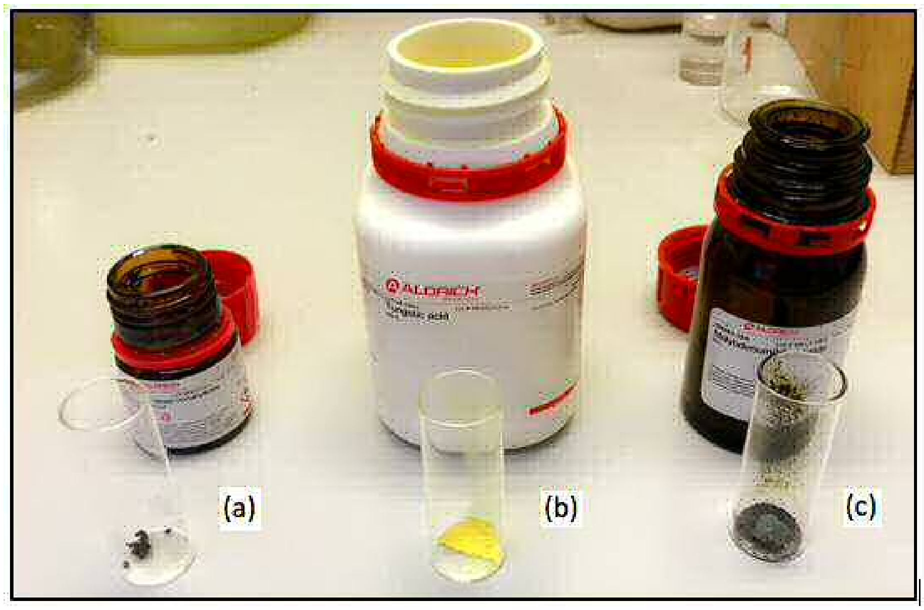

Figure 6.13: Desired mass of the dopants : (a) 0.0161g of Chromium (VI) nitrate Cr(NO3)6, (b) 0.0169g of Tungstic acid H_2WO_4, and (c) 0.0133 g of Molybdenum (V) pentachloride $MoCl_5$.

6.2.6 Photocatalysis Experiments - Setup and Calibration

The experimental setup is the same as that used in chapter 4, with some modifications. The calibration process is done to measure the variations accurately. The red laser diode channel 1 (CH1) is fed with a current of 12 mA. The current must be kept constant for each experiment. The micro pump channel 2(CH2) use 3.5V. The visible light source channel 3 (CH3) were varied depending on the type of wafer used in the experiment. If the CH3 was (LED 420 nm) for W-TiO_2 experiment, then it fed with a current of 720 mA and voltage 5V. For (LED 455nm) that used in Mo-TiO_2 experiment , then it fed with a current of 600 mA and 6V. In Cr-TiO_2 wafer, (LED 525 nm) were used and fed with 600 mA and 3V. Each of them were mounted onto an aluminium lid placed above the glass reaction with distance of 10 cm between them. All these changes to the third channel I made after finishing the experiment using ultraviolet light UVA (LED 365 nm). Three different experiments are carried out: first with the metal doped TiO_2, and second with un-doped TiO_2 (anatase phase),and finally with methylene blue only (blank). The photocatalytic reaction rates of these experiments were evaluated by measuring the time of degradation of MB. The initial concentration of the solution of MB was 1mMol.

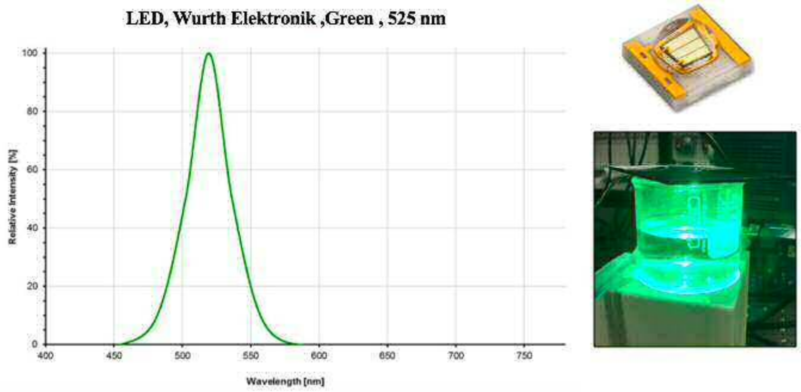

Figure 6.14: LED 525 nm used with catalyst Cr-TiO_2 [85]

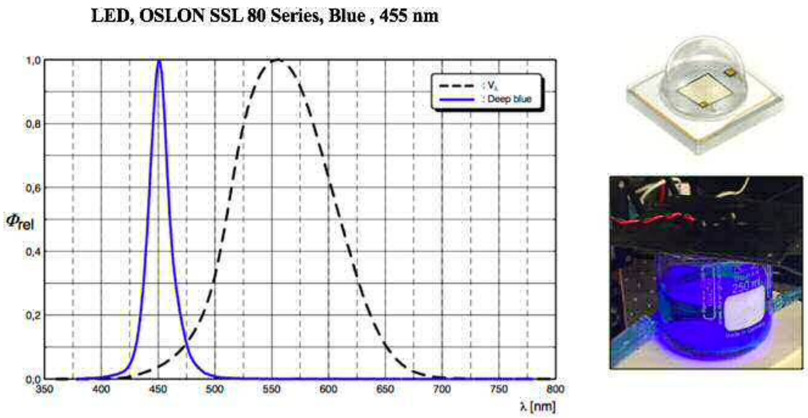

Figure 6.15: LED 455 nm used with catalyst Mo-TiO_2 [86]

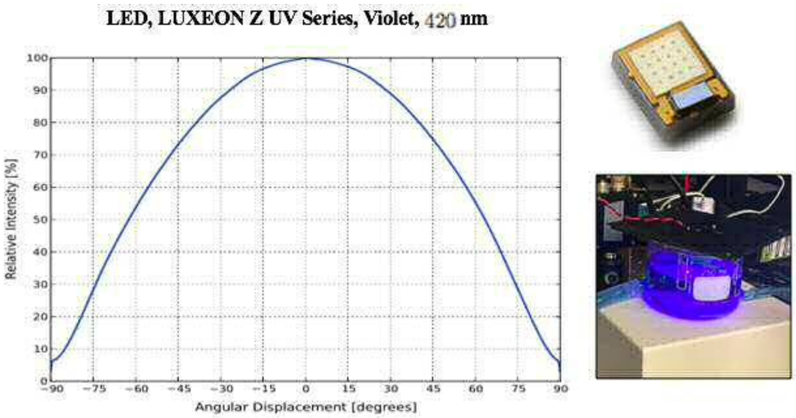

Figure 6.16: LED 420 nm used with catalyst W-TiO_2 [87]

	Visible Light LEDs		
Feature	**LED** 525 **nm** [85]	**LED** 455 **nm** [86]	**LED** 420 **nm** [87]
Color	Green	Deep blue	Violet
E(eV)	2.362	2.725	2.952
E_{ph}(J)	$3.779 * 10^{-19}$	$4.360 * 10^{-19}$	$4.723 * 10^{-19}$
Radiant flux (J/m^2)	$1.864 * 10^{-16}$	$2.151 * 10^{-16}$	$2.330 * 10^{-16}$
Voltage	6.0 V	6.0 V	5.0 V
Current	600 mA	600 mA	720 mA
Catalyst used	Cr-TiO_2	Mo-TiO_2	W-TiO_2

Table 6.2: LED lighting

6.3 pH measurement

Monitoring the pH of drinking water is an important process in ensuring the safety of water. Environmental agencies in different countries recommend the pH of drinking water from municipal suppliers to range between 6 and 8.5. Within this pH range, water is not too alkaline or too acidic to affect human health negatively. Moreover, a pH level of below 6 (acidic) facilitates the dissolution of some heavy metals which makes the water toxic and unfit for human consumption [88]. Similarly, if water has a pH that is too high (above 8.5), it may not have health risks but it has aesthetic problems that are associated with being hard. The aesthetic issues of hard water include bitter flavour, scale formation, and low heat efficiency when heating (Islam et al). Therefore, I undertook the relevant procedure of checking the water pH during the experiment. Using the MB and catalyst, I ran de-ionised water to obtain the results as summarised in Table 6.3.

Type of water	**pH level**
Deionized water	7.5 ± 0.01
Deionized water +MB	$8.2 - 8.3 \pm 0.01$
Catalyst+Deionized water + MB	7.3 ± 0.01
After run	$7.6 - 7.5 \pm 0.01$

Table 6.3: The pH measurement for water during the photocatalytic activity

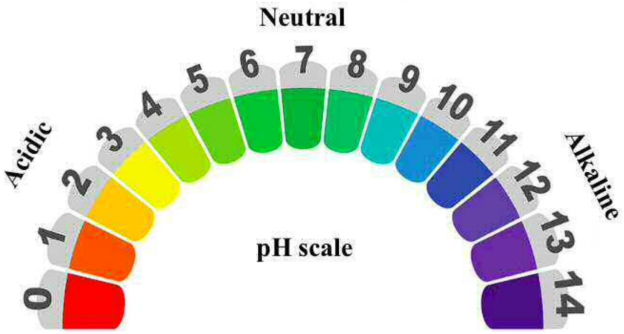

Figure 6.17: pH level for different type of water

Figure 6.18: The portable electronic pH measurement unit and pH paper

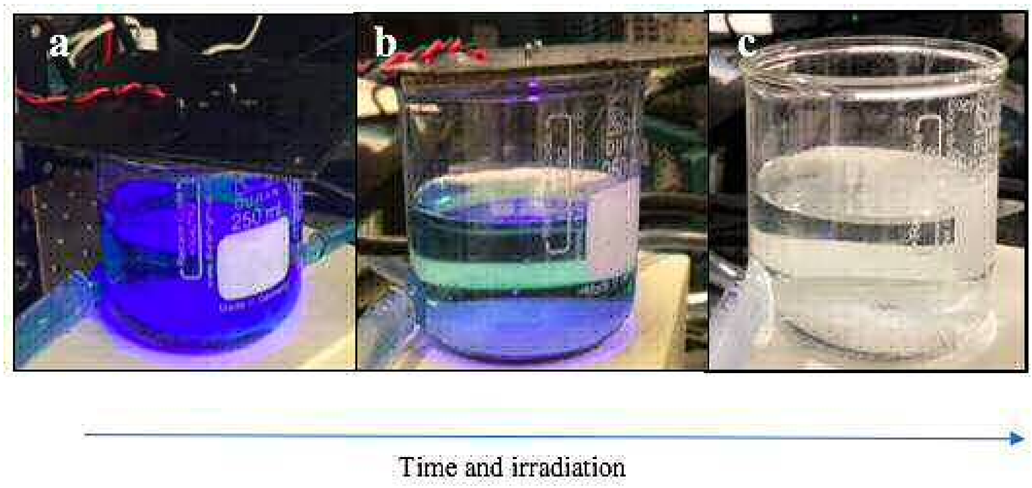

Figure 6.19: The stages in which the water passes to purify it from impurities by using fresh catalyst and UVA LED (a) contaminated water with MB,(b) water is bale and not quite pure,and (c) pure water after run the experiment

General	**Type of Test**	**Instrument(s) Used**
Materials characterization	Absorbance measurements and band gap energy determination	UV-Vis spectroscopy
	Morphology	SEM
	Surface elemental composition	XPS
	Crystal phase	XRD , Raman

Table 6.4: Common characterization and experimental methods

6.4 Characterisation methods

6.4.1 Optical Measurement of TiO_2 and Metal-TiO_2

A UV-Vis-NIR spectrophotometer was used for molecular spectroscopy analysis.The Cary 5000 is a high-performance UV-Vis-NIR spectrophotometer with good photometric performance in the 175-3300 nm range Fig: 6.20. It collects the absorbance of certain samples when exposed to energy at UV and visible wavelength, this can help to identify certain elements, chemical bonds and so forth. Optical measurement can determine whether the band gap is direct or not. The absorption spectrum of direct band gap materials should be able to more clearly distinguish intrinsic absorption band and absorption edge, the change is relatively slow, but that for indirect band gap materials is steep. In order to determine the band gap (E_g) of Cr-TiO_2, Mo-TiO_2 and W-TiO_2, tauc plots were constructed by plotting the graph between $(ah\upsilon)^{(1/n)}$ versus photon energy ($h\upsilon$), where a is the optical absorption coefficient, which can be calculated from absorbance A, and thickness of the sample t using the formula :

$$a = \frac{2.303A}{t} \tag{6.31}$$

($h\upsilon$) can be calculated form wavelength using the equation: ($h\upsilon = 1240/\text{wavelength}$); The power factor n takes the values of (0.5, 2, 1.5, and 3) for allowed direct, allowed indirect, forbidden direct and forbidden indirect transitions. Extrapolation of the straight line cutting the x-axis gave the values of indirect band gaps.

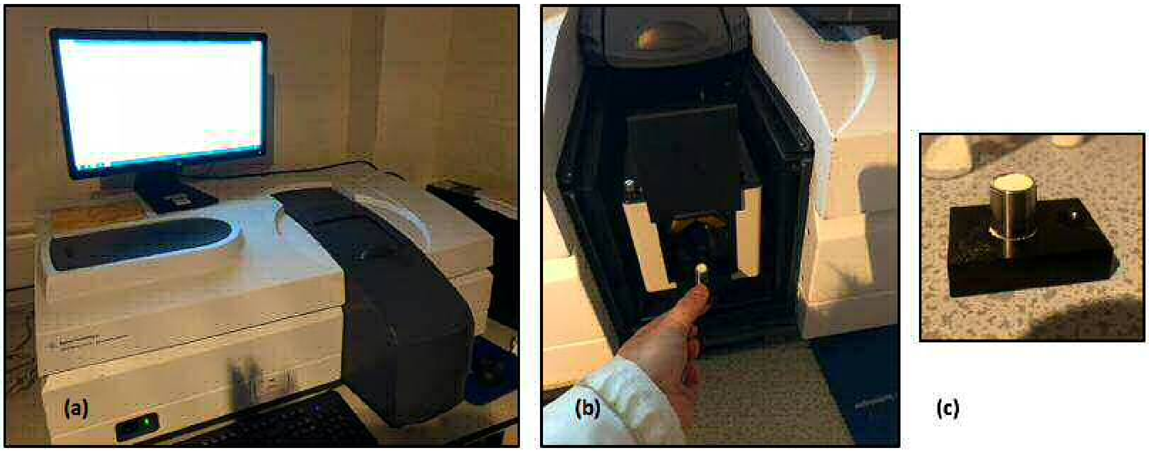

Figure 6.20: (a)UV-Vis-NIR spectrophotometer ,(b) The proper sampling accessory is loaded in the box, and (c) The sample to be tested.

Fig:6.22 shows the optical absorbance spectra for pure anatase. It shows a strong absorption below 400 nm. The UV-visible studies of 0.1% Cr,Mo and W doped TiO_2 also displayed a shift of the absorption spectra towards visible. The band gap was reduced in doped TiO_2 compared to 3.06 eV for pure anatase. The values of 2.94 eV, 2.75 eV and 2.69 eV were indirect band gaps of Cr-TiO_2, Mo-TiO_2 and W-TiO_2 respectively. The band gap narrowing is attributed to the defect generation and oxygen vacancies for m-TiO_2.

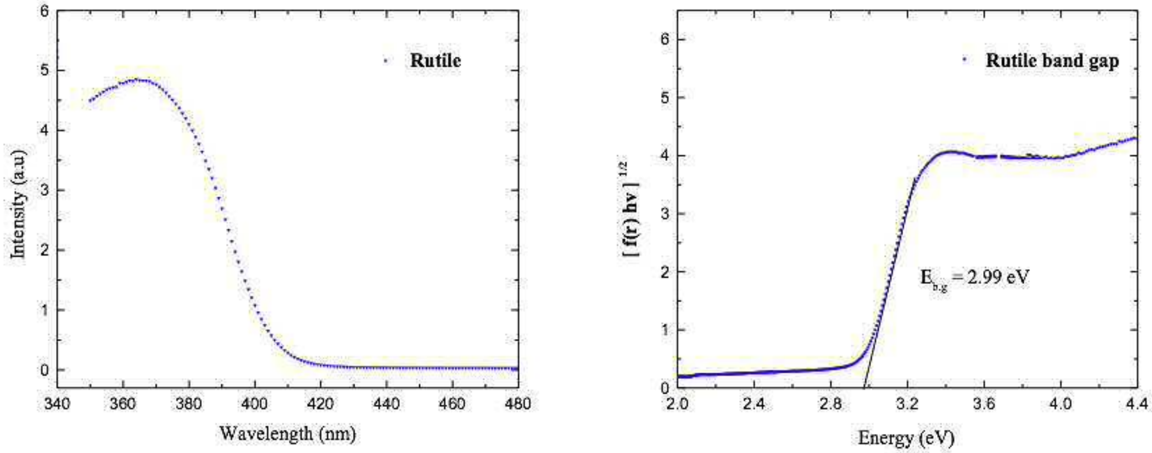

Figure 6.21: Absorption spectra of pure rutile (left), indirect tauc plot demonstrating the band gap of pure rutile(right)

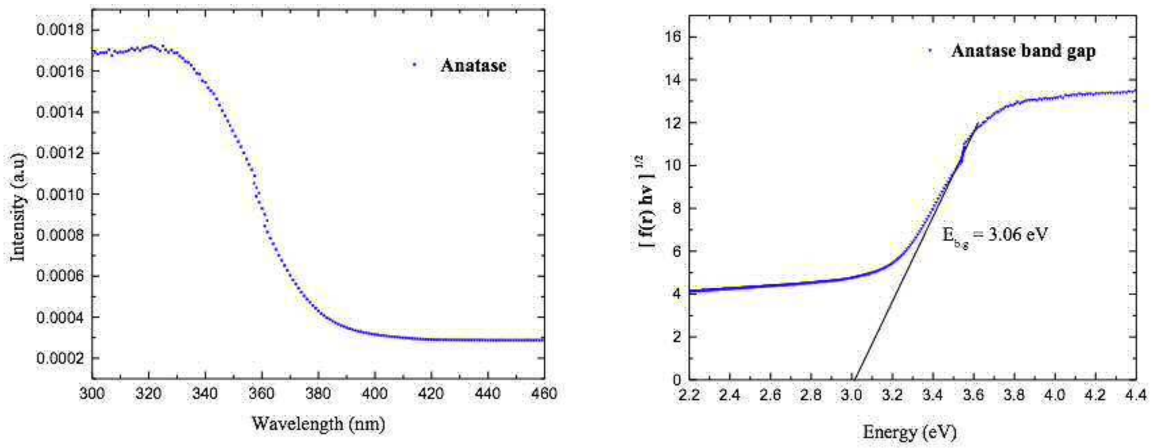

Figure 6.22: Absorption spectra of pure anatase (left), indirect tauc plot demonstrating the band gap of pure anatase (right)

Catalyst	**Experimental band gap**	**Literature band gap**
Anatase	3.06 eV	3.2 eV [89]
Rutile	2.99 eV	3.02 eV [89]
Cr-TiO_2	2.94 eV	2.95 eV [90]
Mo-TiO_2	2.75 eV	2.73 eV [91]
W-TiO_2	2.69 eV	2.9 eV [92]

Table 6.5: The experimental and literature values of band gap for pure anatase, rutile and doped TiO_2 with chromium, molybdenum and tungsten.

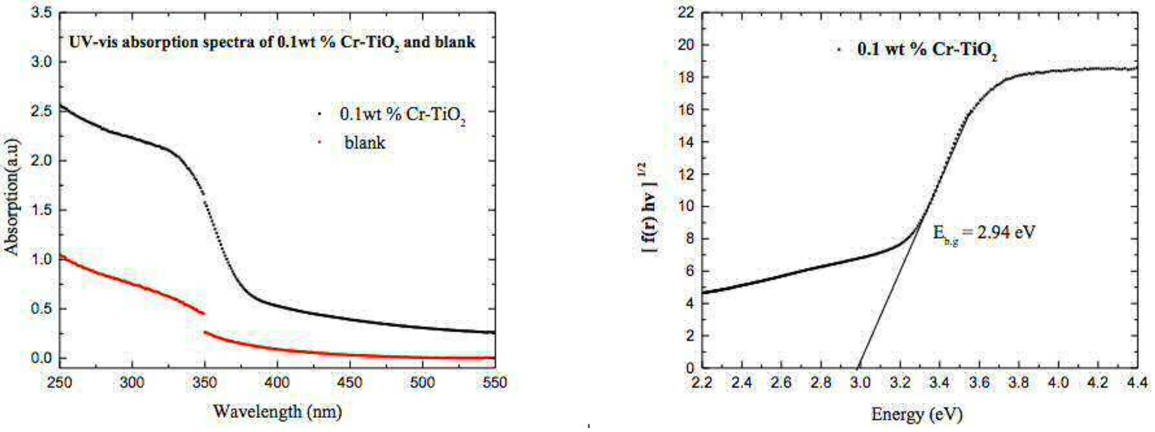

Figure 6.23: Solid state UV for blank and Cr-TiO_2 0.1 wt %

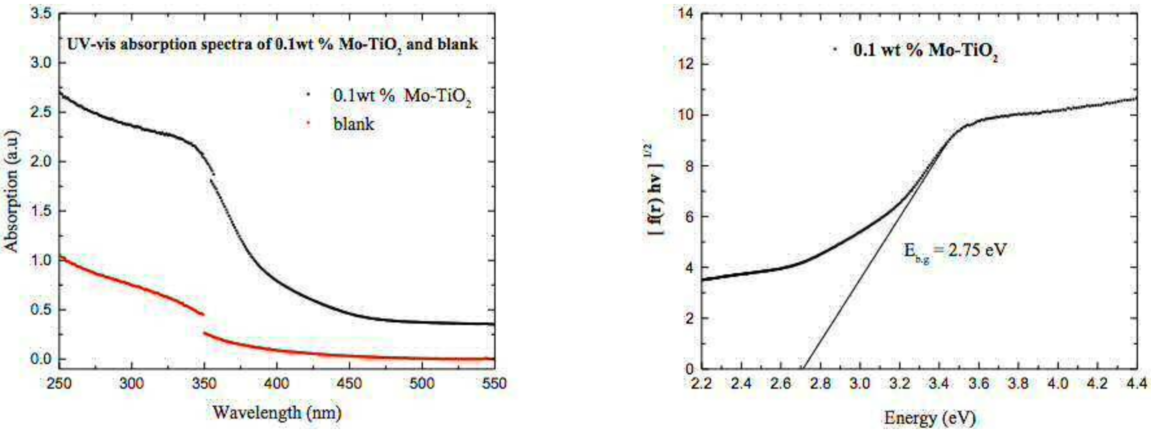

Figure 6.24: Solid state UV for blank and Mo-TiO_2 0.1 wt %

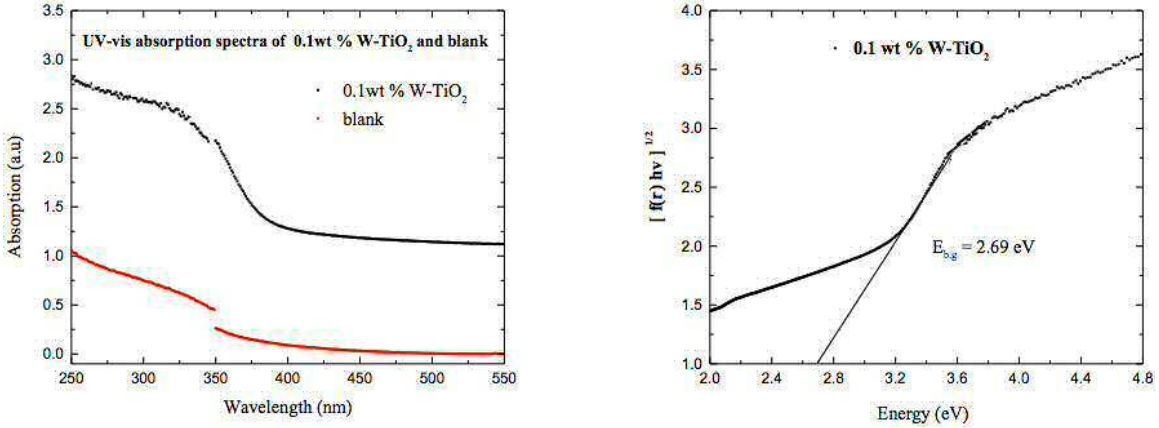

Figure 6.25: Solid state UV for blank and W-TiO_2 0.1 wt %

6.4.2 SEM Analysis of Coated Wafers

Scanning electron microscopy (SEM) was used to examine the morphology and dimension of different samples for silicon wafers coated with pure and doped TiO_2 nanoparticles. It is called a Tescan MAIA3 field-emission-gun scanning electron microscope (FEG-SEM). It is operated at 15 KV and imaging was done using the secondary electron detector. Samples were mounted on aluminium stubs using adhesive carbon discs as shown in figure 6.26. From figure 6.31, it can be seen that the shape of the prepared pure TiO_2 photocatalyst looks like spherical structures with diameter range between (20-40μm). After doping with Cr, Mo and W, the morphologies look more like aggregated plates. The aggregation in the particles increased with Tungsten more than Molybdenum and Chromium. The particle size increases with diameter between 40-50μm in W-TiO_2, 25-30μm in Mo-TiO_2 and 15-25μm in Cr-TiO_2 .

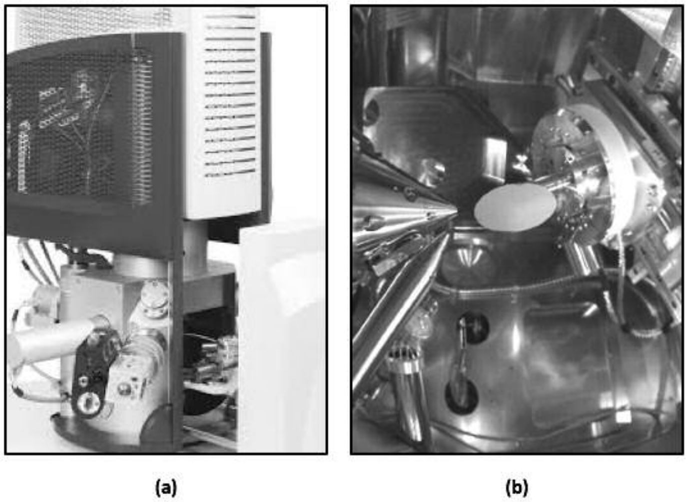
(a)
(b)

Figure 6.26: (a)The MAIA3 is an ultra-high resolution SEM with excellent imaging capabilities in the whole range of beam energies, (b) Silicon wafer during scanning

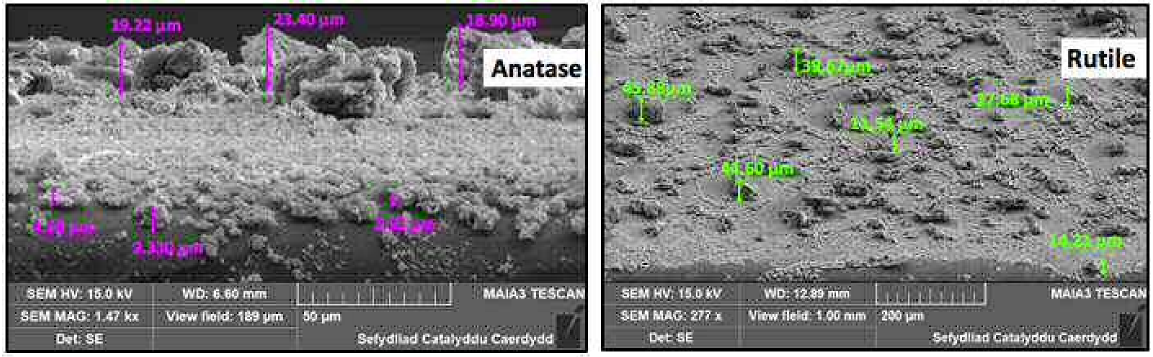

Figure 6.27: SEM for pure anatase and rutile phases

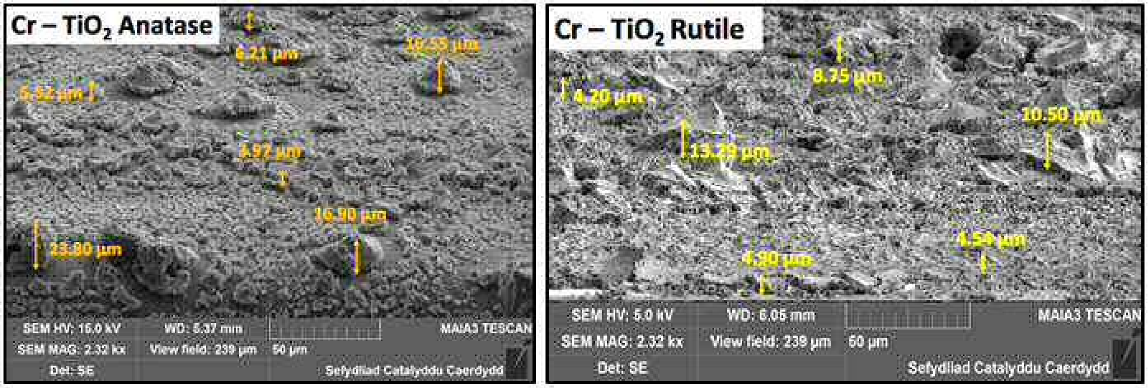

Figure 6.28: SEM for anatase and rutile doped with Chromium nanoparticles

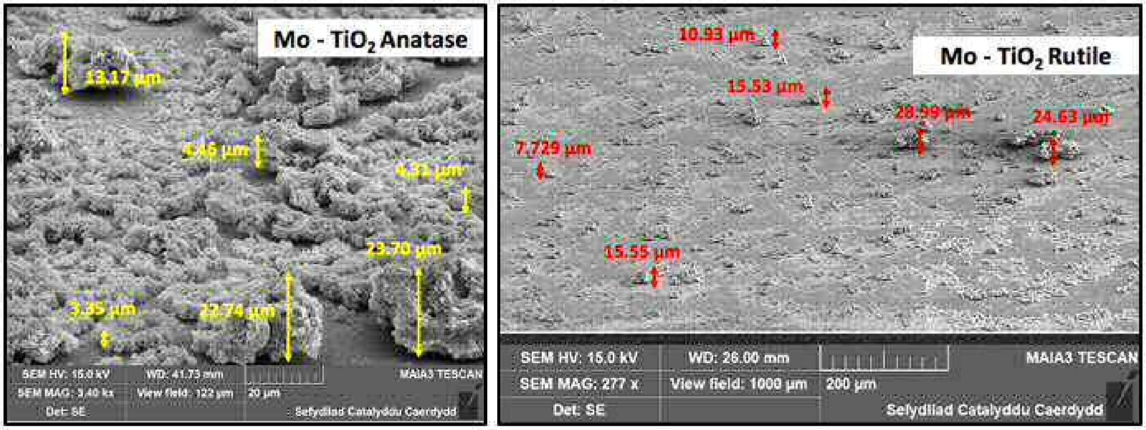

Figure 6.29: SEM for anatase and rutile doped with Molybdenum nanoparticles

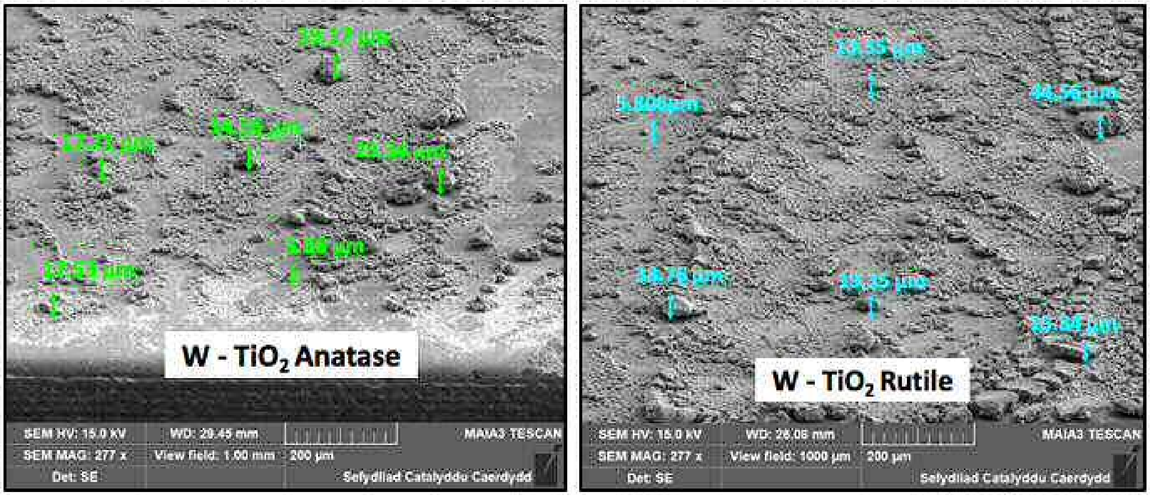

Figure 6.30: SEM for anatase and rutile doped with Tungsten nanoparticles

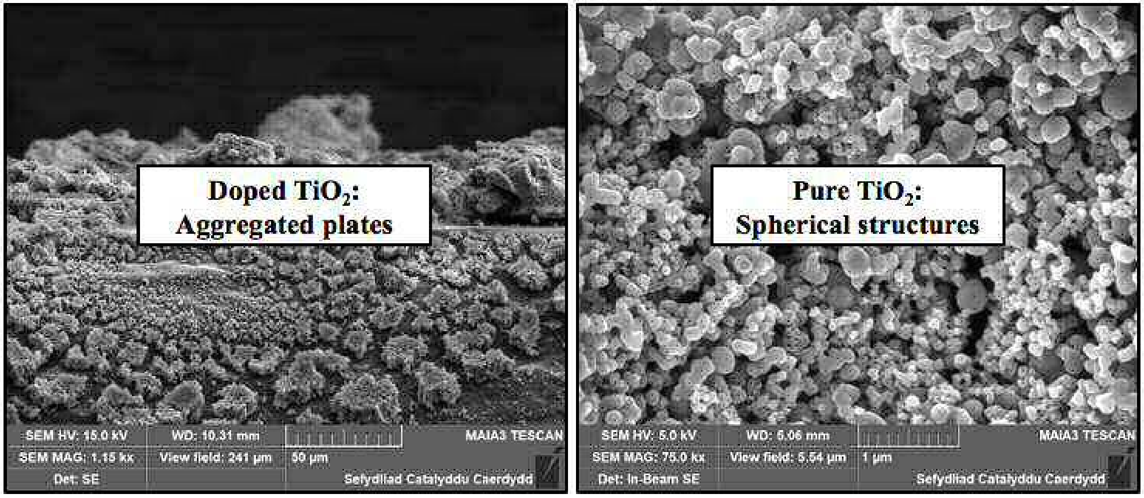

Figure 6.31: The SEM morphologies of the nanocrystalline pure and doped TiO_2

6.4.3 XPS

X-ray photoelectron spectroscopy (XPS), and also known as ESCA (electron spectroscopy for chemical analysis.It was performed on a Thermo Fisher Scientific Kα^+ spectrometer. Samples were analysed using a micro-focused monochromatic Al x-ray source (72 W) over an area of approximately 400 microns. Data was recorded at pass energies of 150 eV for survey scans and 40 eV for high resolution scan with 1eV and 0.1 eV step sizes respectively. Charge neutralisation of the sample was achieved using a combination of both low energy electrons and argon ions. Data analysis was performed in CasaXPS (v 2.3.19 dev1.1k) using Scofield cross sections and an energy dependence of -0.6. XPS instruments consist of an x-ray source, an energy analyser, an electron detector, and instrumentation for data acquisition. X-ray photoelectron spectroscopy measurements were carried out to examine the valence states of Cr, Mo and W elements doped into TiO$_2$. Chemical shifts, or changes in the binding energy of core electrons, can result due to a change in the chemical environment of the core electrons, such as : a change in the nearest neighbour, the oxidation state, compound, or crystal structure. XPS allows for these shifts to be readily measured, which is one of the technique's most important capabilities. The s orbitals are not spin-orbit splitting, it is a singlet in XPS. The other orbitals p, d and f are spin-orbit splitting, they are doublets in XPS.

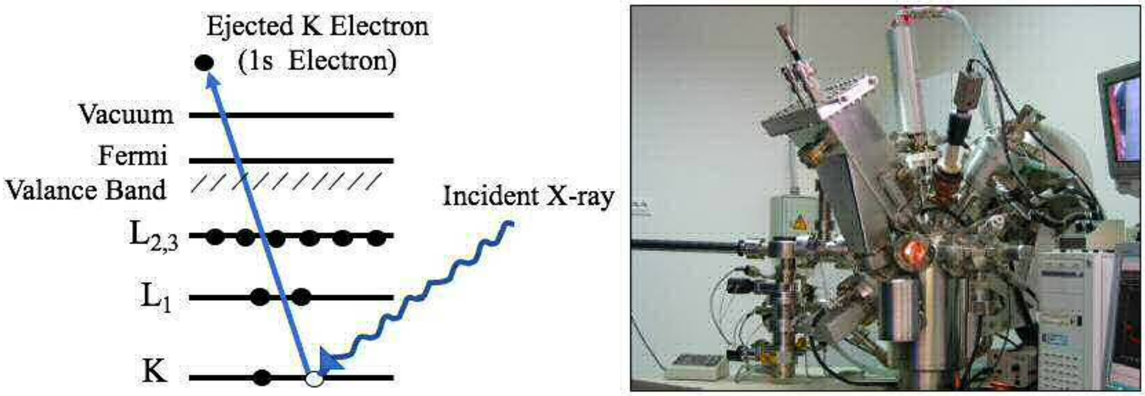

Figure 6.32: XPS working mechanism (Left), Maker: Thermo Fisher Scientific (Model: K-Alpha, Monochromated high-performance XPS spectrometer) (Right).

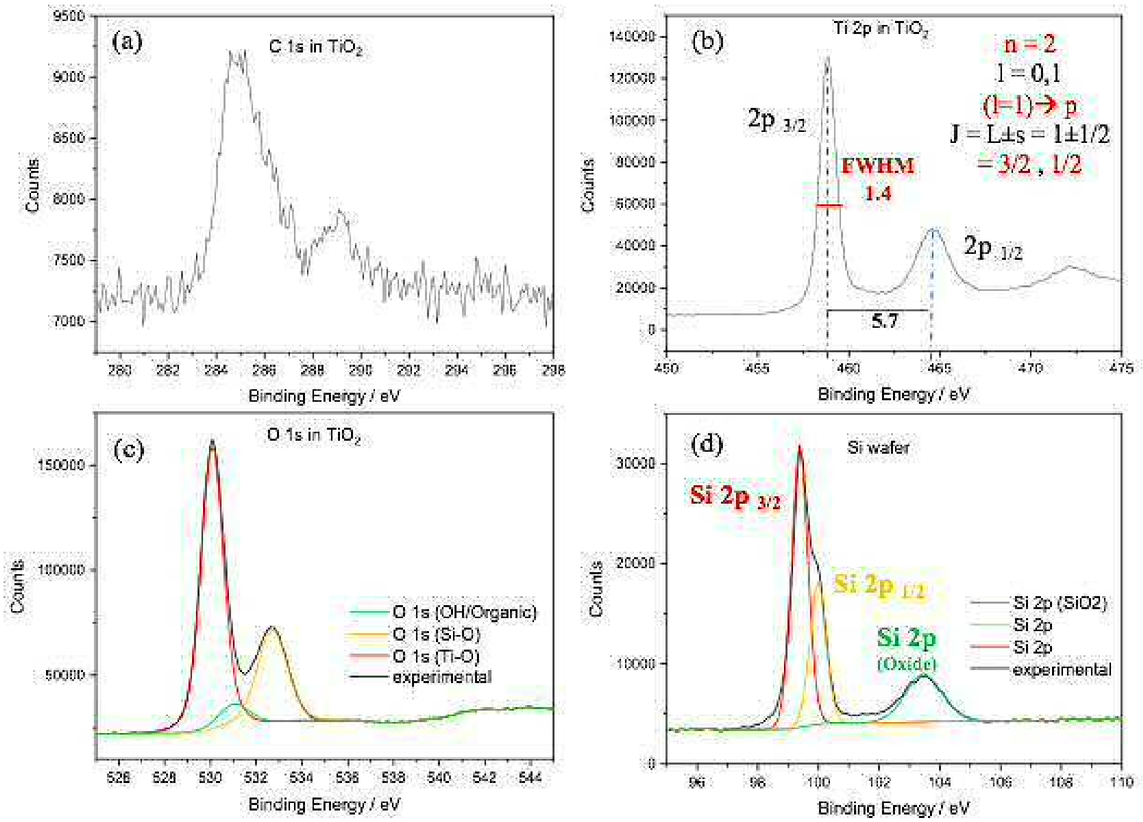

Figure 6.33: XPS for silicon wafer coated with TiO_2, (a) Residual C from the synthesis preparation but the counts are very low (b) Ti $2p_{3/2}$ and Ti $2p_{1/2}$ confirms the presence of Ti^{4+} species in TiO_2 lattice, (c) The O 1s, O^{2-} in TiO_2 lattice and adsorbed oxygen, (d) Si wafer.

Ti 2p		**O 1s**	
Peaks	B.E./eV	Peaks	B.E./eV
1	458.3	1	529.9
2	464.0	2	531.1
		3	532.5

Table 6.6: Deconvolution of Ti 2p and O 1s signals in TiO_2 lattice

The O1s binding energy for different compounds falls within a very narrow range figure 6.33-c. The O1s spectra is not straightforward and it tend to be broad, with multiple overlapping components.It has three contributions at 529.9 , 531.1 and 532.5 eV after peak modelling.The peak at 529.9 eV for all samples is due to O^{2-} ion in the TiO_2 lattice [93], and that peak could be associated to lattice oxygen (Ti-O) in TiO_2 which can be seen in Figure 6.33 in red colour, and the other peak at 532.5 in yellow colour could be represented the (Si-O), the signal at 531.1 eV could be ascribed to surface hydroxyl groups (OH) that represented by green colour. The hydroxyl groups are beneficial for oxidation reactions, because they act as adsorption sites of organic compounds and traps of photo-generated holes producing hydroxyl radicals, which directly attack the organic matter during the reactions of photo-degradation. The XPS spectrum of Si in region 2p, showed a peak at 99.4 eV. The overlapping of Si 2p$_{3/2}$ at 99 eV and Si 2p$_{1/2}$ at 100 eV component, giving asymmetric peak shape. Si 2p(oxide) peak located at 103.5 eV as shown in figure 6.33-d in green colour, while Si 2p$_{3/2}$ came in red colour, and yellow for Si 2p$_{1/2}$.

The doping process moved absorption threshold of TiO$_2$ into visible spectrum range. I have examined three areas of the XPS spectrum of samples: the Ti 2p region between 455 and 470 eV, the O 1s region between 525 and 535 eV, the Cr 2p region in Cr-TiO$_2$ between 570eV and 590 eV, and also the Mo 4p and 3d region for Mo-TiO$_2$ between 30-50 eV and 220-240 eV respectively, finally, the W 4f and 4d region for W-TiO$_2$ between 30-45 eV and 240-270 eV respectively.

The XPS in the Ti 2p region of pure titania is compared with the spectra taken for the Cr, Mo and W doped samples.The Ti $2p_{1/2}$ and Ti $2p_{3/2}$ spin-orbital splitting photoelectrons for all samples are located at binding energies of 464.4 and 458.0 eV, respectively, as can be seen in figures 6.33, 6.34, 6.35, and 6.37. The XPS spectra of O 1s electronic state for doping TiO_2 with Cr, Mo and W that are shown in figures 6.34, 6.35, and 6.37 have two contributions at 530.1 eV and 532.3 eV .The first peak was shown in red colour at 530.1 eV could be ascribed O^{2-} ions within lattice TiO_2, while the other peak in yellow could be associated to (Si-O) at 532.3 eV. After peak fitting, the overall convolved peak shape was represented by black colour.

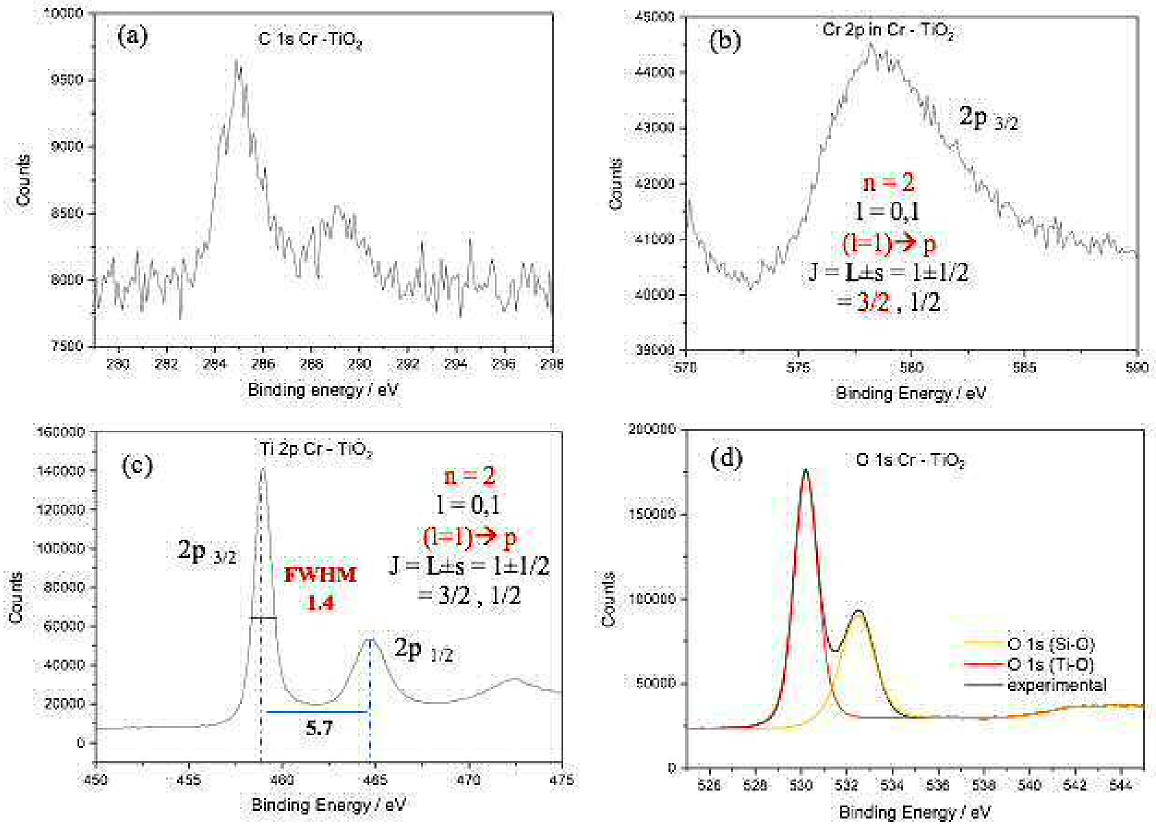

Figure 6.34: XPS for Cr doped into TiO_2 (a) Residual C 1s from the synthesis prep but the counts are very low, (b) The XPS spectrum of Cr doped into TiO_2 in region (2p), (c) Ti $2p_{3/2}$ and Ti $2p_{1/2}$ confirms the presence of Ti^{4+} species in TiO_2 lattice, (d)The O 1s, O^{2-} in TiO_2 lattice and adsorbed oxygen.

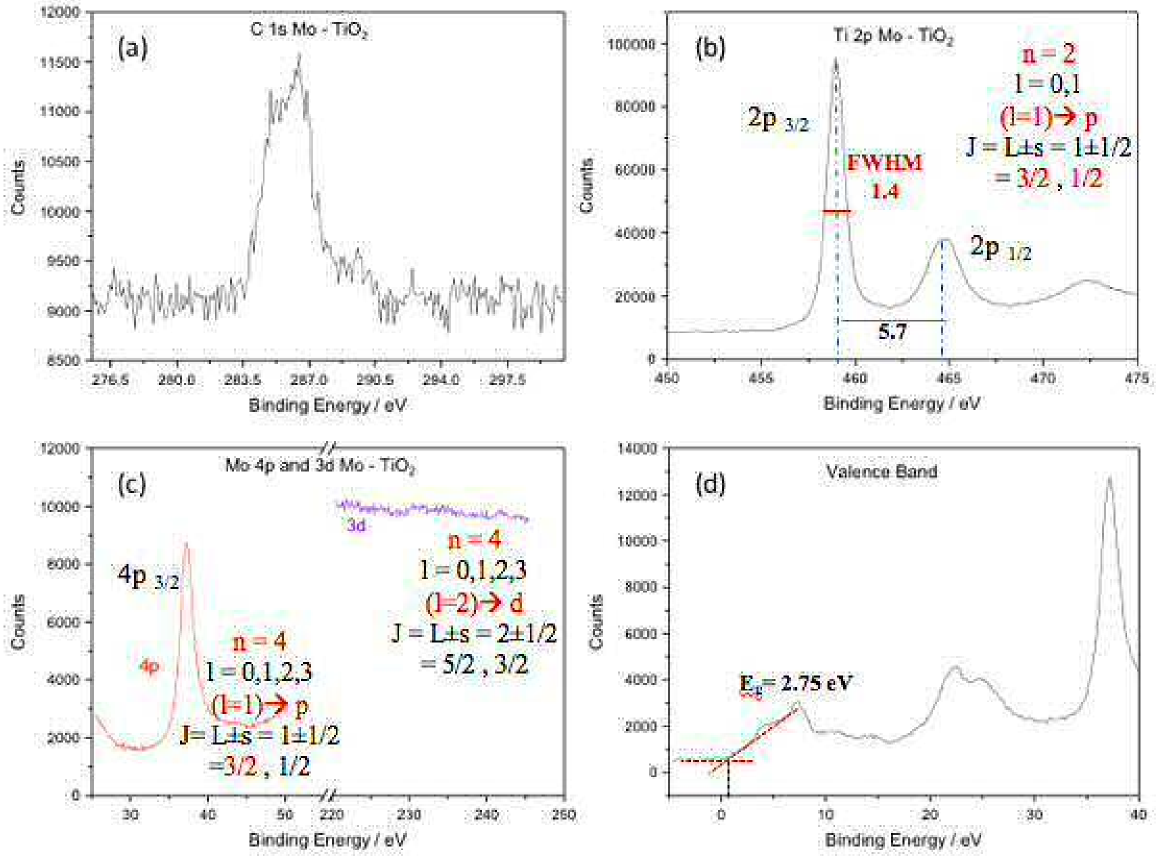

Figure 6.35: XPS for Mo doped into TiO_2 (a) Residual C 1s from the synthesis prep but the counts are very low, (b) Ti $2p_{3/2}$ and Ti $2p_{1/2}$ confirms the presence of Ti^{4+} species in TiO_2 lattice, (c) Mo $4p_{3/2}$ and Mo 3d confirm the presence of Mo^{6+} and Mo^{5+}, (d) The valence band of Mo-TiO_2.

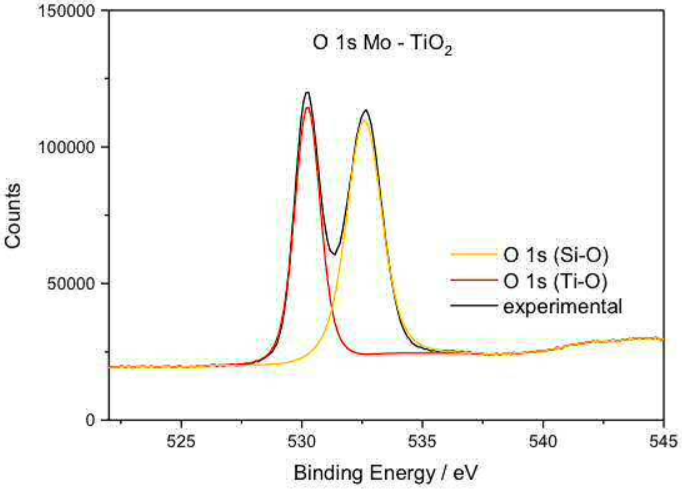

Figure 6.36: XPS for O 1s Mo doped into TiO_2.

Figure 6.37(c), shows the XPS spectra in the W 4f and 4d regions of the sample W-TiO_2. A peak at about 35.9 eV corresponding to W $4f_{7/2}$ state in the forms W^{5+} ,W^{6+}species. The XPS spectra for Mo-TiO_2 in the Mo 4p and 3d regions fig :6.35(c), shows a peak at about 37 eV corresponding to Mo $4p_{3/2}$ state in the forms Mo^{5+} ,Mo^{6+}species. the presence of W^{5+} and W^{6+} ions in the samples implies the existence of oxygen vacancies due to the incorporation of dopant cations. XPS shows the influence of the dopants (shift in Ti) and gives an indication on the oxidation state of the species present.The Cr 2p XPS for Cr-TiO_2 fig: 6.34 (b), shows no significant reactivity for Cr^{3+}, and active for O2 evolution under wavelength 365nm and the formation of Cr^{6+} was very week and shift to Ti peaks [94].

The creation of oxygen vacancies in the doped samples reduces negative charge in the crystal system which is balanced by the conversion of Ti^{4+} to Ti^{3+}. These changes clearly point out that W, Mo and Cr are successfully doped in TiO_2.

It seems that these energies are not affected by doping with these ions. Although, due to the low concentration of these doped materials, the shift of Ti 2p peaks could have been below the detection limit. No Ti^{3+} species were observed in XPS. The absence of peak broadening of Ti $2p_{3/2}$ signals may also indicate the presence of Ti^{4+} species only , and good crystallisation for all samples. All previous figures show the O 1s core level spectra of pure and doped TiO_2. In all spectra at higher binding energy a shoulder is observed, which can be attributed to the surface hydroxyl groups of chemisorbed water molecules on the titania or this is the way in which presence of metal ions influences the TiO_2 matrix.

The residual C 1s peak was found in all spectra of samples with very low counts, at around 284.6 eV due to carbon impurities, which probably came from the background of XPS test or the residual precursors[95].

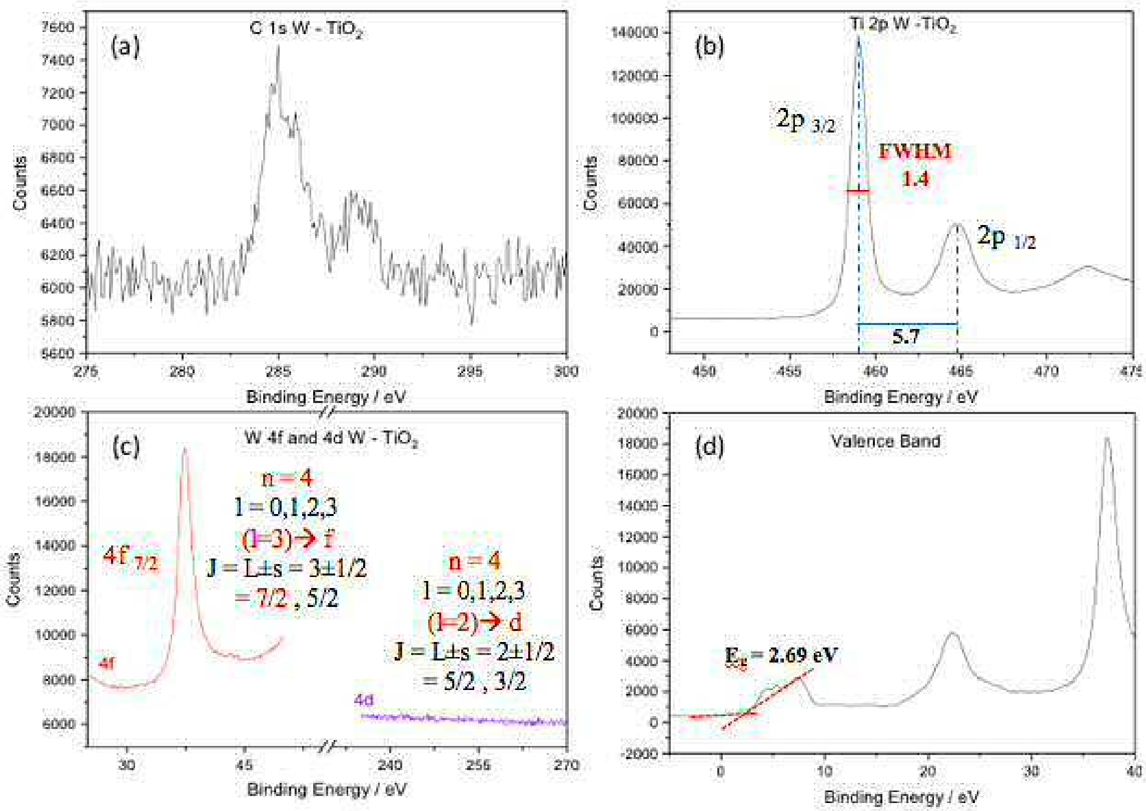

Figure 6.37: XPS for W doped into TiO_2 (a) Residual C 1s from the synthesis prep but the counts are very low, (b) Ti $2p_{3/2}$ and Ti $2p_{1/2}$ confirms the presence of Ti^{4+} species in TiO_2 lattice, (c) W $4f_{7/2}$ and W 4d confirm the presence of Mo^{6+} and Mo^{5+}, (d) The valence band of W-TiO_2.

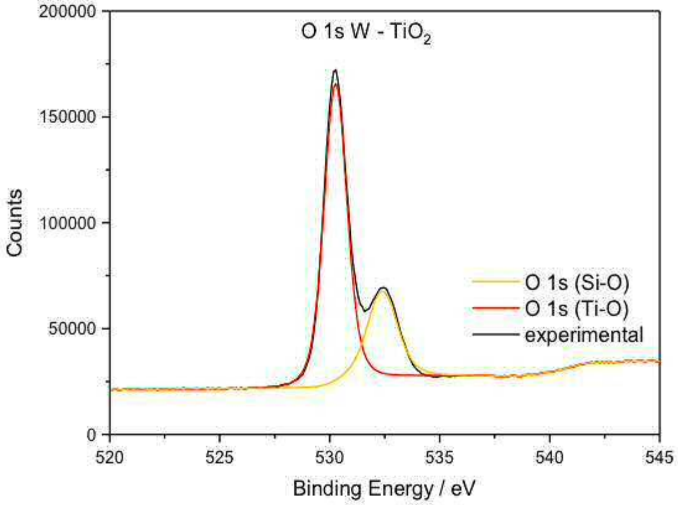

Figure 6.38: XPS for O 1s W doped into TiO_2.

Figure 6.39-a, shows the general spectrum obtained and the assignation of the peaks found for TiO_2 nanoparticles. TiO_2 has symmetric peaks shapes. Ti 2p peak has significantly split spin-orbit components with splitting value of 5.7 eV as can be seen in fig:(6.33-b). The full width half-maximum (FWHM) for each spin-orbit component is the same,or similar but for Ti 2p the Ti $2p_{1/2}$ component is much broader and shorter than the Ti $2p_{3/2}$ peak due to Coster-Kronig effect, wherein post-ionisation. Ti $2p_{1/2}$ state is very short lived compared to Ti $2p_{3/2}$ state fig:(6.33-b). For undoped TiO_2 the Ti $2p_{3/2}$ and Ti $2p_{1/2}$ peaks were located at 458.3 and 464.0 eV respectively, this result is relatively approach with the literature values [95],and the FWHM of Ti $2p_{3/2}$ signals was about 1.4 eV for all samples which confirms the presence of Ti^{4+} in TiO_2 lattice and also confirms the presence of oxygen vacancies.

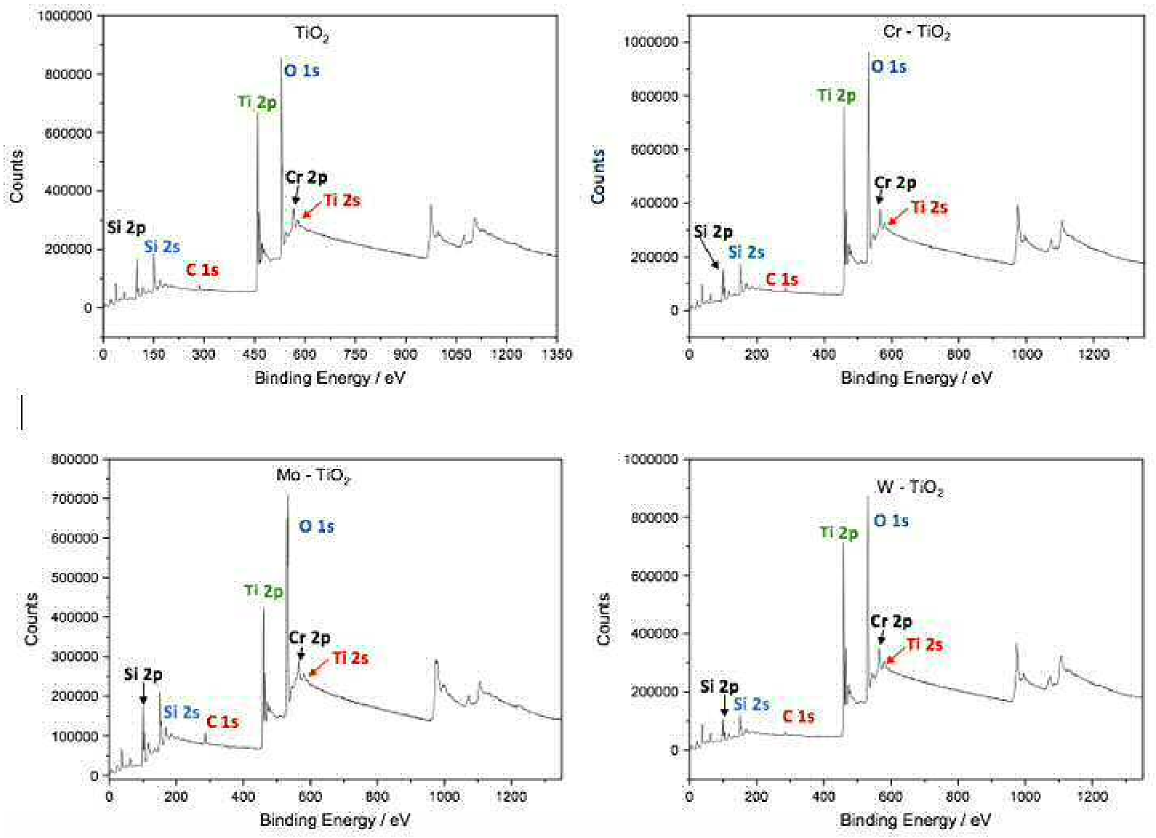

Figure 6.39: Binding energy tells elements by wide scan for Pure TiO_2 and doped into TiO_2.

6.4.4 XRD

X-ray diffraction is an analytical characterisation technique employed to identify crystalline phases that may be present in the material. It also provides information on structural properties such as defect structures, grain size and different phases. The XRD X'Pert pro (serial number DY2739) was applied on different samples at room temperature in the range 2θ: 5 to 80 ° using K_α radiation ($\lambda = 1.54$ A°), and 40 mA to determine any phase changes as a result of doping. It is an expert powder diffractometer set up to do X-ray diffraction applications on both powder and solid materials, shown in figure 6.40. The monochromatic X-ray is generated by an X-ray source. The primary X-ray hits the lead screen to filter of the scattered race and to concentrate the X-ray beam. The concentrated X-ray beam with wavelength (λ) that hits the crystalline solid at angle (θ) which scatters the x-ray to a specific pattern correlating to the crystalline structure. The detectors collects the scattered pattern

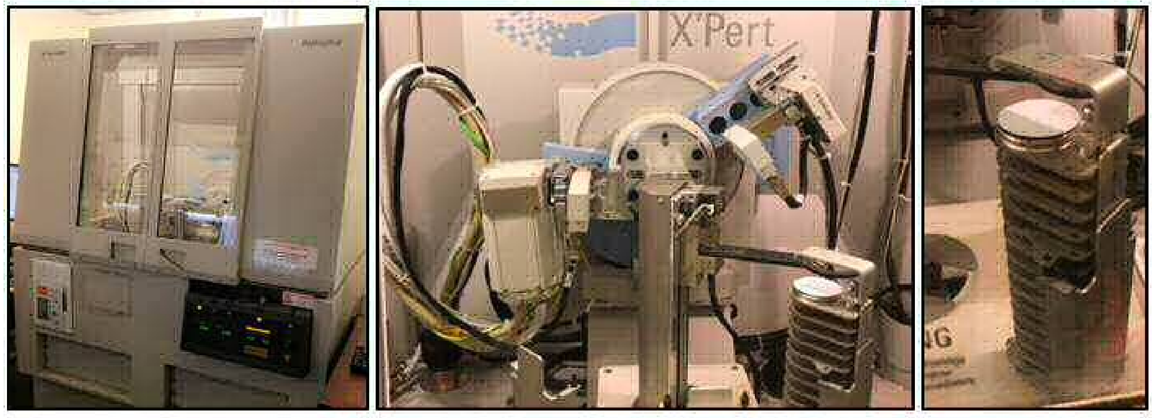

(a) (b) (c)

Figure 6.40: (a) XRD room, (b)The doping wafer was taken by the XRD arm for 30 minutes X-ray diffraction, (c) the holder that saves the wafer with 15 loading positions.

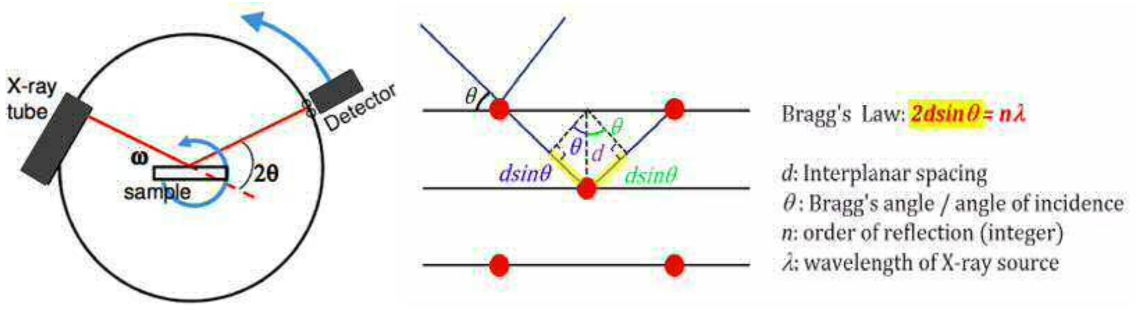

Figure 6.41: X-ray diffraction and Bragg's law

on a photographic plate. The incident x-ray reflects on different plans by an integer n when it strikes lattice of atoms. The incident x-rays that stretch the second array of lattice has travel extra distance d and the diffraction rays has to travel extra distance again $2d$ when it comes out of the plan. The observer sees the superposition of all the waves coming out. No peak is observed unless the condition for constructive interference is precisely met:

$$n\lambda = 2dsine\theta \tag{6.32}$$

When the Bragg's law is satisfied, reflected beams are in phase and interfere constructively. Specular reflections can occur only at these angles. Plotting the angular positions and intensities of the resultant diffracted peaks produces a characteristic pattern. Where different phases are present, the diffraction trace represents the sum of the individual patterns. Figure 6.40 shows that the coated wafer mounted on the front of a crystalline silicon zero background. The sample specimen is then put on the sample holder. Put the sample holder into one of 15 position magazine tray system.The system set up to begin and the beam current is adjusted. Different programs can be set up in the absolute scale. The starting angle, angle step size, tamper step scale, speed etc. can be optimised to achieve best results. Generally smaller step size and longer scanning time gives better results. The sample arm takes the sample from sample holder and put it on the platform.The detector angle is changed to collect the reflected x-ray different diffracted angles. The data is being collected by the detector and the signature pics start to show.

Figures 6.42, 6.44, and 6.43, show the XRD diffraction patterns for pure TiO_2 (anatase and rutile phases) and doped TiO_2 with Cr, Mo and W, calcined at temperatures of 800 °C and 450 °C. It is noticeable from these figures that there are various peaks of 2θ for Cr, Mo and W doped TiO_2, and that the observation was for anatase phase only. The anatase peak was represented by red star while rutile came in a pink colour and the silicon wafer was represented by black star. The anatase phase belongs to space group D_{4h}^{19}-$I4_1$/amd, while rutile phase is in D_{4h}^{14}-$P4_2$/mnm space group. The various peaks occurs at 25°, 38°, 48° ,54° and 63°for Cr, Mo and W doped TiO_2. The corresponding planes are (101), (004), (200), (105), and (118).

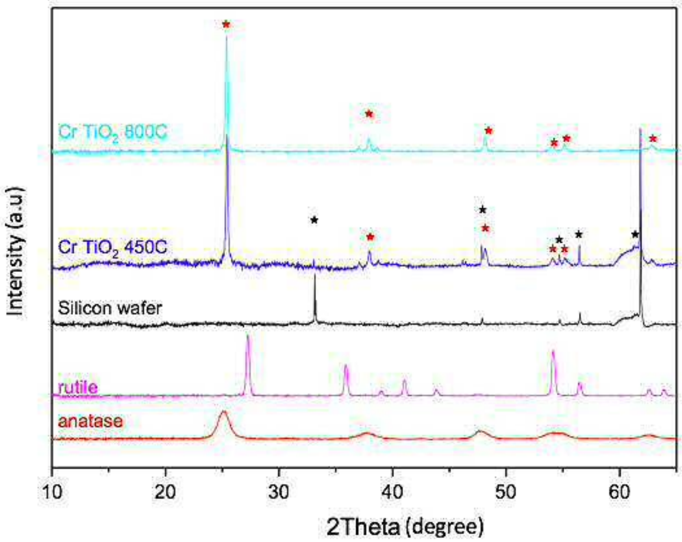

Figure 6.42: X-Ray diffraction pattern for Cr doped TiO_2 on Si substrate.

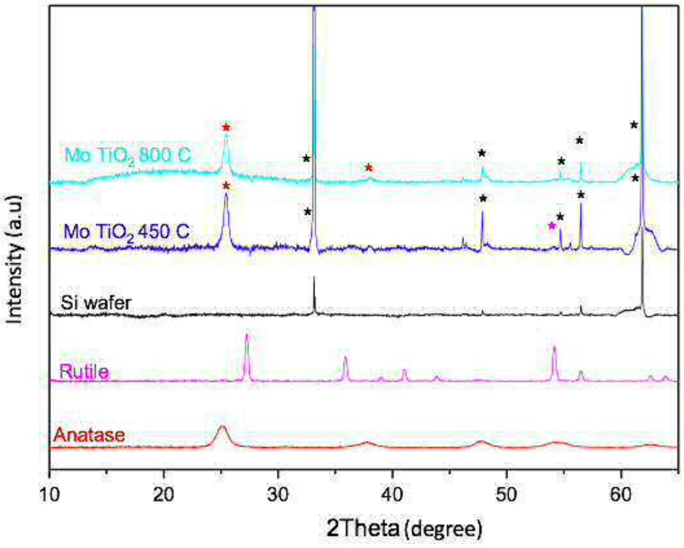

Figure 6.43: X-Ray diffraction pattern for Mo doped TiO_2 on Si substrate.

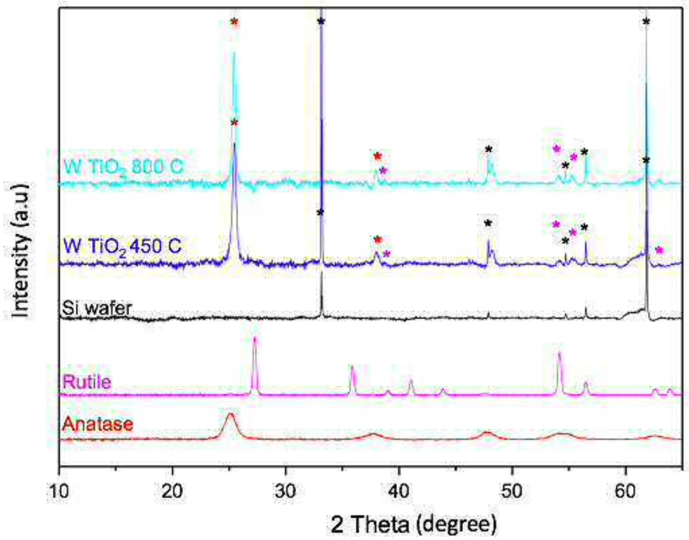

Figure 6.44: X-Ray diffraction pattern for W doped TiO_2 on Si substrate.

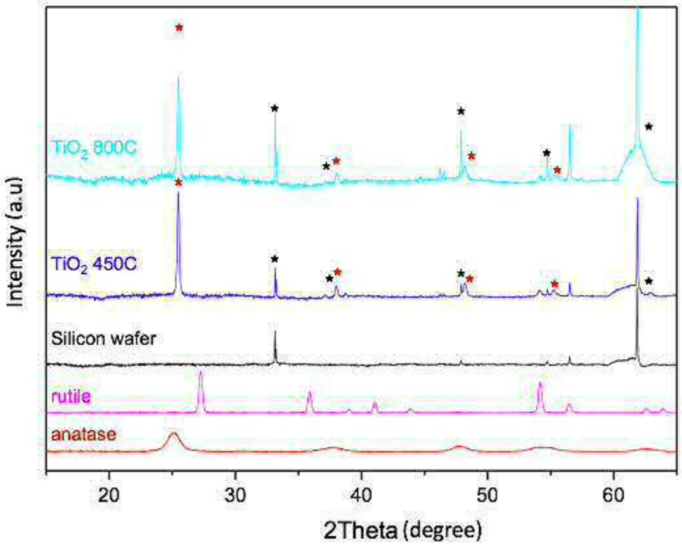

Figure 6.45: X-Ray diffraction pattern for Anatase and Rutile on Si substrate.

The diffraction pattern of pure anatase and rutile powder are illustrated on the respective plots figures 6.46, and tables 6.7, 6.8. The stated occurrence of peaks confirms that there is an anatase structure in the Cr-TiO_2, Mo-TiO_2 and W-TiO_2 [96]. The peaks are in tandem with the standard spectrum specification in JCPDS number 84-1286 and 88-1175.

$2\ \theta$	phase
25	(101)
37	(103)
38	(004)
39	(112)
48	(200)
54	(105)
55	(211)
63	(118)
69	(116)
71	(220)
75	(215)

Table 6.7: Diffraction pattern for Anatase

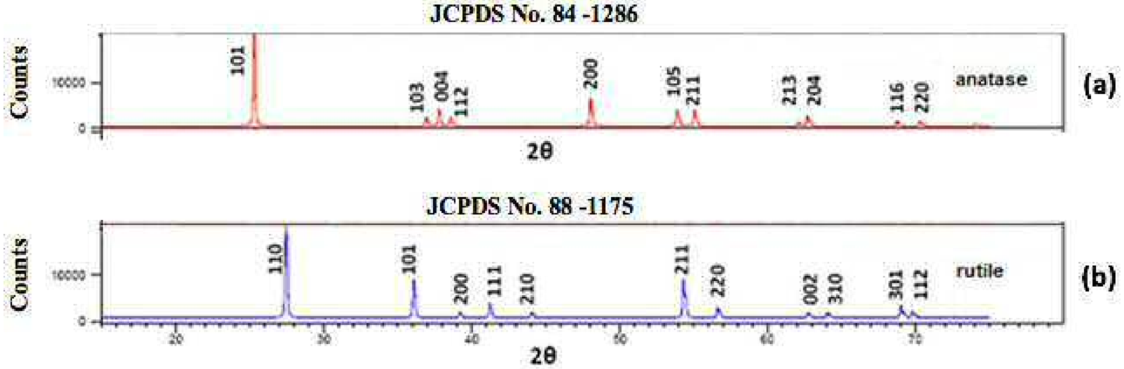

Figure 6.46: Diffraction pattern of both (a) anatase and, (b) rutile powders were compared with reference to JCPDS database

From the intensity of the diffraction peaks, it can be confirmed that the nanoparticles are crystalline [97]. Furthermore, it can be seen from the graphs that the peaks for Mo Calcined at 800 °C and 450 °C are widely spaced. This implies incomplete crystallization as a result of the presence of an amorphous component, and therefore, the Mo-TiO_2 and W-TiO_2 are made up of a polycrystalline with an irregular shape. It is also deducible from the XRD diffraction diagram that an increase in the calcined temperature from 450 °C to 800 °C does result in the change in the anatase phase.

$2\ \theta$	phase
27	(110)
36	(101)
39	(200)
41	(111)
44	(210)
55	(211)
57.5	(220)
63	(002)
65	(310)
70	(301)
71	(112)

Table 6.8: Diffraction pattern for Rutile

Even so, there is a small improvement in the crystallinity of the TiO_2 as depicted by a slight change in the broadness of the peaks [98].

The weight percentage (0.1 wt%) of W doped into TiO_2 show a small shift in the characteristic peaks of TiO_2 as given in figure :(6.44) which might be due to the difference in the ionic radii between W^{6+} (0.60 A) and Ti^{4+} (0.605A) for the six-fold coordination ,thereby inducing some changes in the lattice parameters. The lattice parameters of these samples were calculated using the procedures described elsewhere from the XRD patterns. The strong diffraction peaks indicate the good crystallinity of the material. The particle size of crystals can be estimated by using the Paul Scherrer equation.

$$D_{XRD} = \frac{K\lambda}{\beta cos\theta} \ , \tag{6.33}$$

where λ is the X-ray wavelength, β is the line broadening at half maximum intensity. θ is the Bragg's angle, K is a dimensionless shape factor with a typical value of about 0.9.

In catalysis studies, the morphology of substances is of paramount importance since it can influence surface reactions greatly. In this regard, polymorphs are substances having similar compositions and varying crystal structures. As suggested by their name, polymorphs can have drastically different morphologies depending on the crystal phase, such as anatase and rutile phases of titania. Types of crystal phases, their growths, shapes and faces are characteristics of polymorphs. Polymorphs generally have highly specific physical and chemical properties that enable their specific thermodynamic behaviours and stabilities. Equivalent crystal phases may be different depending upon conditions under which each phase is developed, despite their shapes and forms being identical.

Differences in morphologies are displayed in X-ray diffraction (XRD) charts. Along-side structural and and analytical applications, XRD is also used for studying fundamental polymer properties, such as crystallinity, crystallite size, orientation, phase changes and melting points [99]. XRD used for characterisation of polymorphs shows identical peak positions due to their identical chemical compositions. Intensities of peaks, however, are different depending upon the peak area calculated for each crystal phase, which depends on the growth of the phase.

Qualitatively, the extent of crystallinity can be estimated from the number and sharpness of the diffraction maxima. High temperature X-ray techniques have been applied to studies of polymer melting behaviour, and to the determination of crystallinity as a function of temperature. The melting point is determined by observing the temperature of disappearance of the crystalline diffraction peaks. Crystallinity can be determined at temperatures below the melting point. Some polymers undergo fundamental changes in crystalline structure which may have profound effects on physical properties. X-ray methods are particularly well adapted to studies of these phase changes.

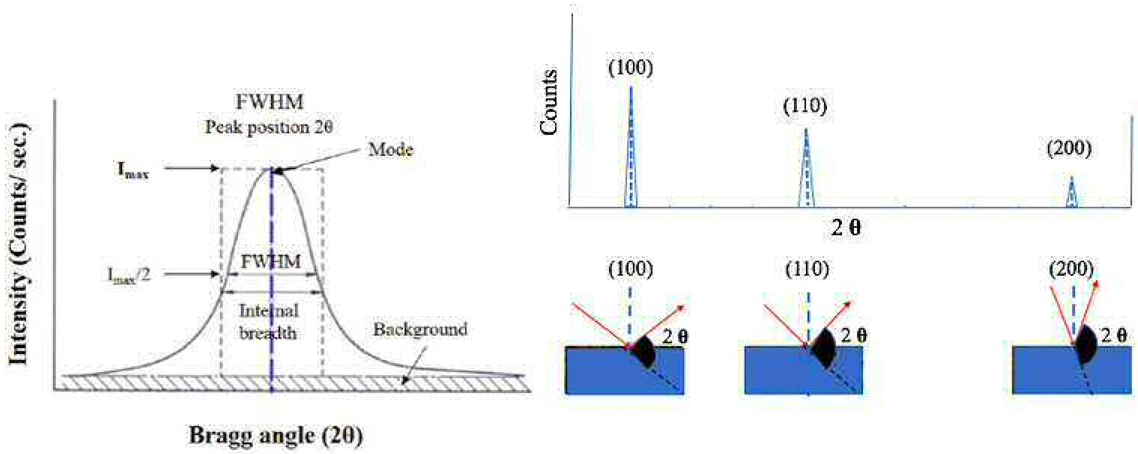

Figure 6.47: For every set of planes, there will be a small percentage of crystallites that are properly oriented to diffract (the plane perpendicular bisects the incedent and diffracted beams). Basic assumptions of powder diffraction are that for every set of planes there is an equal number of crystallites that will diffract and that there is a statistically relevant number of crystallites, not just one or two.

The samples of Cr-doped TiO$_2$ nanoparticles show a variation in the intensity of diffraction peaks with a small shift indicating a slight expansion of the unit cell volume with reduction in the crystallite size. Such expansion of the unit cell volume is quite feasible due to a small difference between ionic radii of the dopant (Cr) and the host titanium-ions. The ionic radii of both Cr^{6+} and Ti^{4+} ions are 61.5 and 60.5 pm which are close to each other therefore, Cr^{6+} ion can enter the lattice sites of Ti^{4+} via substitutional doping. As a result, the periodicity of the lattice gets disturbed and affects the crystal growth which reduces the crystallite size [100]. The metal content, temperature and particle size are crucial to the anatase phase stability and to the transformation anatase-to-rutile. In the presence of chromium with different content, the anatase phase remains stable at 800°C. Chromium ions incorporated in TiO_2 anatase phase delay the transformation to rutile and preserve smaller crystallite sizes thus inducing better catalytic activities. The stability of anatase phase is favored with excess of Cr content and the crystallite size is less than 30 nm. The rutile phase is absent after treatment at 400-500°C and decreases with increase of chromium content [101].

Mo^{6+} ion is doped into the TiO_2 lattice. XRD analysis shows no change in crystal structure except a slight variation in crystallite size and elongation along the c-axis with increase in the concentration of the dopant [102]. The average anatase crystallite size were determined by Scherer formula ($D = k\lambda/\beta\cos\theta$, where D= Crystallite size, k = share factor, λ = wavelength, θ = diffraction angle, β = Full width at half maximum) and it is found to be 26.3 nm for TiO_2 sample. The data obtained from the Scherer equation shows a slight increase in crystallite size with increase in Mo content [102]. Further a change in lattice parameter corresponding to the elongation of the c-axis is also observed. The dopant can enter the TiO_2 lattice either interstitially or it can act as substitutional impurity. Mo is in +6 oxidation state and Ti is in +4 oxidation state. The ionic radius of Mo^{6+} is 0.062 nm and that of Ti^{4+} is 0.0605 nm. Due to the similarity in the ionic radii of Mo^{6+} and Mo^{4+} (0.068), they can replace Ti^{4+} in the lattice. It can be observed that unit cell parameter along c-axis and the crystallite size keep increasing with dopant concentration up to the dispersion capacity. This linearity confirms the fact that the Mo is incorporated as substitutional dopant [102].

Leghari *et al.* and other works [103] reported that tungsten ions doped in TiO_2 can replace titanium ions to form new W-O-Ti bonds. Considering the decrease in the unit cell volume and parameters a and c of both anatase and rutile phases, it is likely that the tungsten ions replaced the titanium ions here, thus making a new WOx-TiO_2 solid solution based on the fact that W^{6+} (0.6 A) has a smaller ionic radius than Ti^{4+} (0.605 A) [103].

6.4.5 Raman Spectroscopy

Raman spectroscopy techniques were used to identify molecules and provide a structural fingerprint of them by observing the vibrational and rotational modes of non-doped TiO_2 and doped TiO_2 with the different elements Cr, Mo, and W, on a silicon wafer substrate. Because Raman spectroscopy is a scattering process, samples of any size or shape can be examined. Very small amounts of material can be studied down to microscopic levels ($\approx 1\mu$m). The system allows spectra to be obtained from different depths within the sample and its X-Y stage also facilitates automated mapping of samples. The Raman system with confocal microscope contains a 514 nm 25mW argon laser, and a 785 nm 300mW diode laser. The microscope contains 5x, 20x, 50x and 100x dry objectives, as well as a 50x and a 100x oil immersion objective, figure 6.48.

The sample was placed on the microscope slide which is inserted into the closed room on the monitoring stage. Visualisation of the surface of the sample was realised using the (WIRE2 spectral acquisition wizard) software. First, select 20x objective. Then use the joy stick and the stage wheel to adjust the position of sample and focusing on it and checking at the same time on the computer screen. Then choose the acquisition parameter; the grating 2400 /mm,1% laser power, 5 second exposure time and accumulations of 10 times. Running the background first and then the sample itself either powder phase or coating on wafers to eliminate the background from our spectra and get better results. Figure 6.49 shows the Raman spectra results

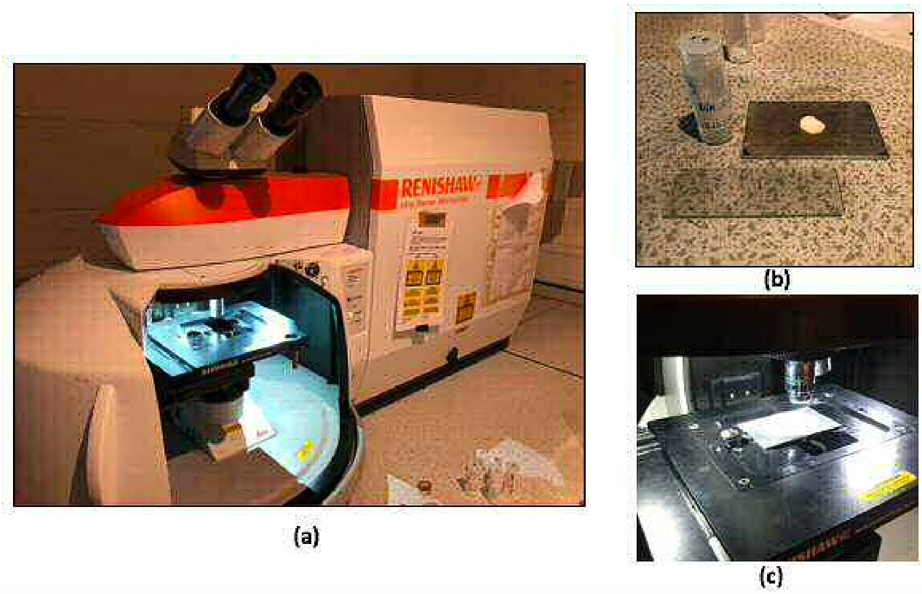

Figure 6.48: (a) Renishaw InVia Reflex Raman Spectrometer, (b) The sample (powder) to be examined, and (c) Coated wafer.

of $Cr\text{-}TiO_2$, $W\text{-}TiO_2$, and $Mo\text{-}TiO_2$; reference spectrum for both anatase and rutile.

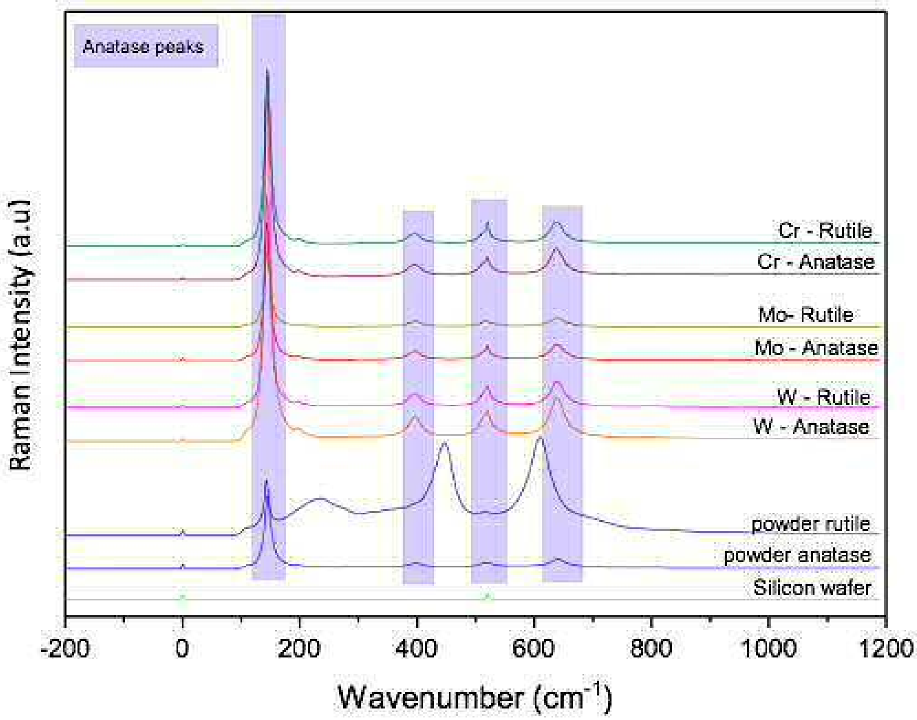

Figure 6.49: Raman spectra for wafers with different coating

From the figure, it is evident that all the doped samples exhibited anatase TiO_2 peaks only, implying that the diffractions are attributed to anatase only. The corresponding planes are illustrated on the respective plots. It is also deducible from figure 6.49 that the Raman band tends to move towards the low wavenumber and intensity decreases with an increase in the size of the nanoparticles. Cr-TiO_2, W-TiO_2, and Mo-TiO_2 have varied peaks implying varied Raman intensity among doped-TiO_2 particles.

According to Scepanovic et al [104], the intensity can be affected by various factors that include particle size non-homogeneity, phonon confinement, anharmonic effects, and nonstoichiometry.[104] in their study further states that it is not able to determine the contribution of each of the stated factors to the change in peak position. As I earlier commented, the Raman spectrum indicates that the diffraction is attributed to anatase only. This is due to the fact that for a doped material, the peaks correspond to the major component only, and in this case, the major component is anatase hence a confirmation of effective doping of TiO_2 with W, Cr and Mo. This is unlike in oxides of similar W, Cr and Mo, where the peaks correspond to the respective elements. Another distinguishing feature between the doped-TiO_2 and other material containing W, Cr and Mo such as nanoparticles and oxides is that, such compounds are multiphase solids and thus, their diffraction patterns has peaks that corresponds to more than 1 crystalline solid [105],[106].

Raman spectroscopy showed the crystal phases of TiO_2 samples. Table 6.9 shows that the anatase TiO_2 spectra have six Raman active fundamentals in the vibrational spectrum: three E_g modes centred around 145.9, 198.5, and 638.9 cm^{-1}, two B_{1g} modes at 398.8 and 515.5 cm^{-1}, and one A_{1g} mode at 515.5 cm^{-1}. Figure 6.50 shows the wafer calcined at 1000 °C, for 1 hour on the normal furnace we've been using, and another wafer at 800 °C for 4 hours again in our normal furnace. I have then taken powders and heated them in another furnace in the chemistry department to 800 °C for 1 hour and 800 °C for 4hours. Our normal furnace shows anatase for all the samples whereas the new furnace shows rutile for both samples.

Wavenumber (cm^{-1})	Assignment
145.9	Anatase E_g
198.5	Anatase E_g
243.7	Anatase B_{1g}
319.9	Brookite B_{2g}
362.	Brookite B_{1g}
398.8	Anatase B_{1g}
515.5	Anatase A_{1g} $/B_{1g}$
638.9	Anatase E_g

Table 6.9: Raman spectrum of TiO_2 nanoparticles

The Raman spectra of the pure TiO_2 showed peaks at 141, 397, 516 and 639 cm^{-1} and agree with the results of Ohsaka et al[107]. For 0.1 wt % of W-TiO_2, the band position was slightly shifted as shown in Fig:(6.49).The high intensity peak at 141 cm^{-1} is consistent with the Ti-Ti covalent interactions (2.96 A; 0.29 valence units). The Ti-O bands at 516 and 639 cm^{-1} yield the calculated Ti-O bond lengths of 1.98 and 1.90 A while the O-O interactions occurs at 397 cm^{-1} [108].The chemical bonds with W^{6+} are stronger than those with the W^{5+} and W^{4+}, therefore the Raman peaks for W^{6+} and W^{6+} appear at higher wavenumbers.

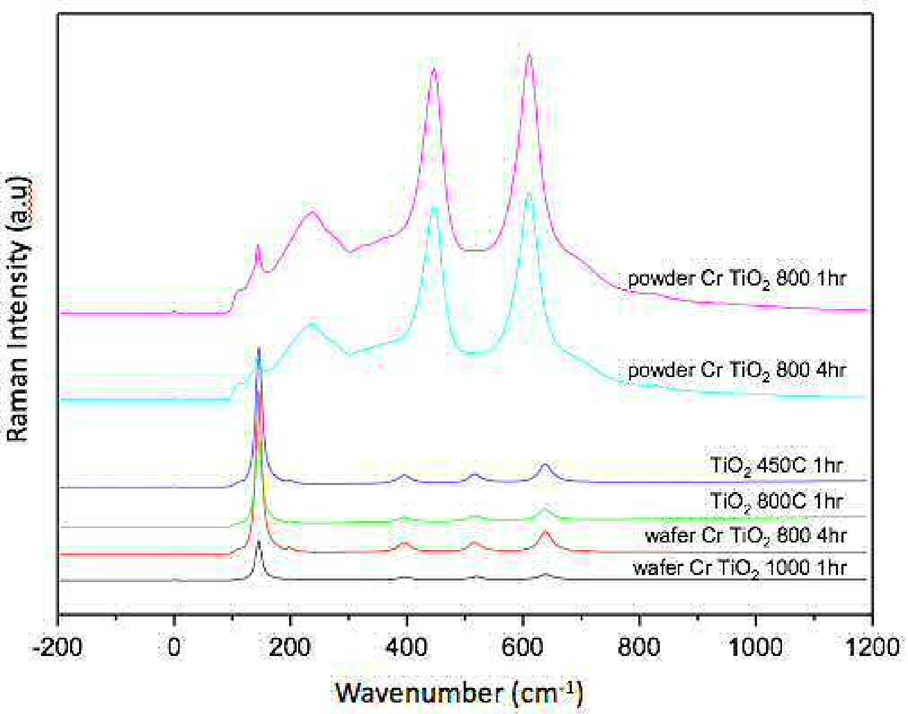

Figure 6.50: Raman spectra for Cr doped into TiO_2 at different temperatures

6.5 Photocatalysis Results and Discussion

6.5.1 Methylene Blue as a RedOx Agent and Photosensitiser

Before measuring the reaction rates in the presence of the photocatalyst, I performed a control calibration using just methylene blue and no photocatalysis. Methylene blue is known to decompose slowly under UV illumination. This is especially important since some of the reaction rates proceeded very slowly and it was important to be to discriminate between the natural decomposition under UV illumination. The decay profile indicates a first order decay process.

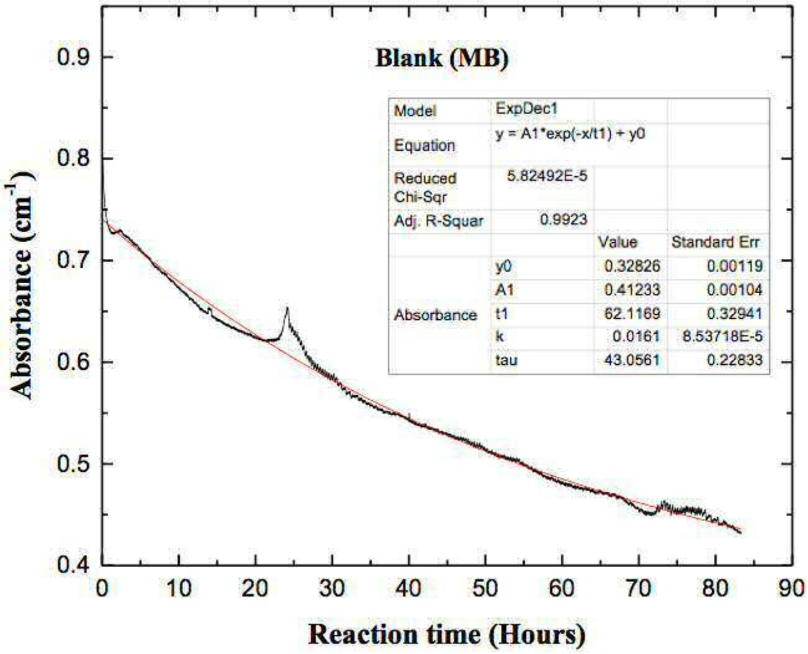

Figure 6.51: A control experiments using no wafer and with UVA illumination was undertaken.

$$[MB]_t = [MB]_0 \exp(-kt) \tag{6.34}$$

where k is the reaction decay constant or rate constant and it is the slope of the exponential curve. t is the time required for a methylene blue molecule to decay to a fraction of the initial number equal to 1/e, where e. τ is the time required for decaying MB molecules to fall to half of its initial value and it is the result of the multiplication of t by $\ln 2$, which is $\approx$(0.693)t. The MB was considered as an effective self-cleaning surface, which can degraded in the water without any catalysts. It took a long time but it still worked. MB is a single oxygen photo-sensitiser. The active species of MB itself could oxidise substrates that were unaffected by oxygen in its normal energy state. Oxygen is more oxidising in its singlet excited state and is therefore significantly more electrophilic, reacting rapidly with unsaturated carbon-carbon bonds.

Methylene blue has an absorbance of between 550 and 700 nm. It was used in the experiment due to its strong photosensitising properties. In other words, its three states of excitation make it a strong sensitiser of oxygen. Apart from being an efficient sensitiser of oxygen in its singlet state, methylene blue can also be oxidised thus consuming the oxygen species [109]. This means that a reaction involving methylene blue may not necessarily produce singlet oxygen. Rather, the oxygen species could be quenched thus resulting in photo-degradation or photo-bleaching. The latter occurs when dyes are degraded by singlet oxygen and the former refers to the reaction between a given material and the singlet oxygen [110].

The production of free oxygen species through photo-sensitisation is controllable. The method requires three key elements: an efficient photo-sensitiser (such as methylene blue), oxygen, and light of wavelength 365 nm. The excitation process involves the transfer of one photon to convert the oxygen from its ground state to its excited singlet form (S_n). Once the S_n state undergoes relaxation, the sensitiser attains a lower state of excitation, S_1. Due to intersystem crossing, there is a possibility of forming T_1 which is the triplet state of the sensitiser. This triplet form has a longer lifetime, which is calculated in milliseconds (ms) in contrast to the shorter lifetime of the singlet state; calculated in nanoseconds (ns) [111].

One of the mechanisms of intersystem crossing involves the abstraction of hydrogen atoms. In other words, free radicals are generated through electron transfer between a substrate and the excited form of the sensitiser. The free radicals are susceptible to a reaction with oxygen, which converts the oxygen species to one active state or the other. An example of such is the superoxide anion. The second mechanism is where a collision between the triplet oxygen and the excited sensitiser results in the production of singlet oxygen. In this case, there is a transfer of energy [111].

So far, a lot of research has been conducted to investigate how wastewater treatment processes can be made more efficient by oxidation reactions involving photosensitised oxygen. However, more work needs to be done on the production of singlet oxygen from semiconductors that have been photoexcited (examples include ZnO and TiO_2). Yamamoto et al [112] used these semiconductors in a photooxidation process involving methyl oleate to demonstrate their potential to produce photosensitised oxygen in its singlet form.

6.5.2 Comparison with Anatase, Rutile and P25 in MB degradation

P25 is usually considered to be the most active catalyst due to the heterojunction enabling efficient charge separation. A heterojunction is the interface that occurs between two layers or regions of dissimilar crystalline semiconductors like heterojunction with TiO_2. These semiconducting materials have unequal band gaps as opposed to a homojunction. Both anatase and rutile increase the rate of reaction compared to the control. However neither have as good activity as P25. The reaction rate or the decay constant was higher in anatase phase more than rutile phase; this could be due to the relativity surface activity and stability of the respective materials. The hetrojunction TiO_2 under UV-vis irradiation is proposed in figure 6.53. Electrons flow from rutile to anatase and the holes move in the opposite direction. Thus, the separation of h^+ and e^- pairs is promoted. The photoactivity of P25 is mainly attributed to a synergistic effect between the two phases.

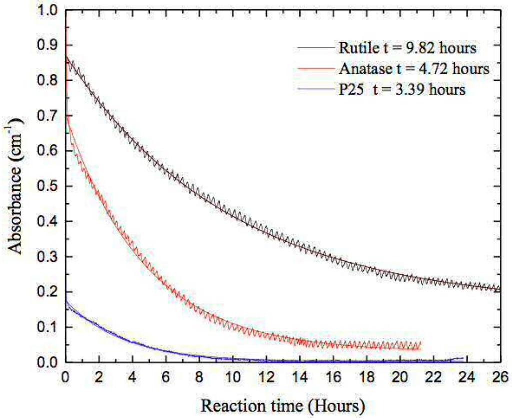

Figure 6.52: Time needed to decay the anatase and rutile phases, and also P25.

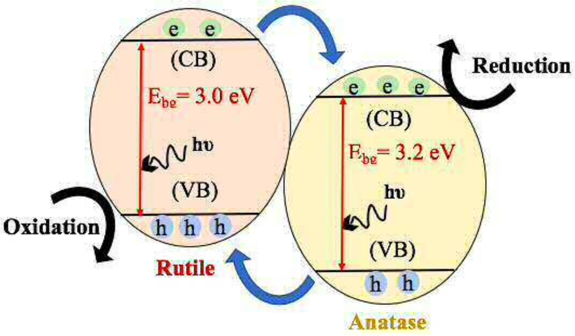

Figure 6.53: The heterojunction with TiO_2 nanoparticles is believed to enhance photocatalytic hydrogen evolution.

6.5.3 Doped TiO_2 and MB Decomposition

The photo degradation of MB indicated that the photocatalytic activity of pure TiO_2 nanoparticles increased with increasing Cr^{6+} ,Mo^{5+} ,Mo^{6+},W^{5+} and W^{6+} cations concentration. UV irradiation was performed for TiO_2 doped with several group 6 elements such as Mo, W and Cr. For each case, the support-catalyst was calcined to temperatures exceeding 800°C in order to observe the photocatalytic degradation of methylene blue for each sample as anatase and rutile phases were formed. Anatase was formed at 450°C whereas rutile was formed around 800°C. The trends observed in activities were as follows:

P25 > TiO_2(A) > Mo-A > Mo-R > TiO_2(R) > W-A > W-R > Cr-A > Cr-R > Control

The performance of Mo was observed to be better than that of W and Cr, while the performance of pure anatase titania was better than all others. This can be attributed to the fact that electrons are trapped more effectively on Mo and W cations as compared with Cr [113].

The performance of each components anatase phase was better than its rutile phase performance. While there is no general consensus about the better activity of anatase as compared with rutile, it can be explained that it is the bulk transport of excitons to the surface that contributes to the difference in activities of each phase. For anatase, the activity increases for films up to 5 nm thick, while rutile films reach their maximum activity for 2.5 nm films. This shows that charge carriers excited deeper in the bulk contribute to surface reactions in anatase than in rutile [114].

Furthermore, pure titania is seen to perform better than group 6 metals doped titania due to the activity that each metal brings when it is doped onto the titania support. Often, SMSI (strong metal-support interactions) are observed which lead to drastically altered properties of metal-support (titania as the support) versus the pure titania.

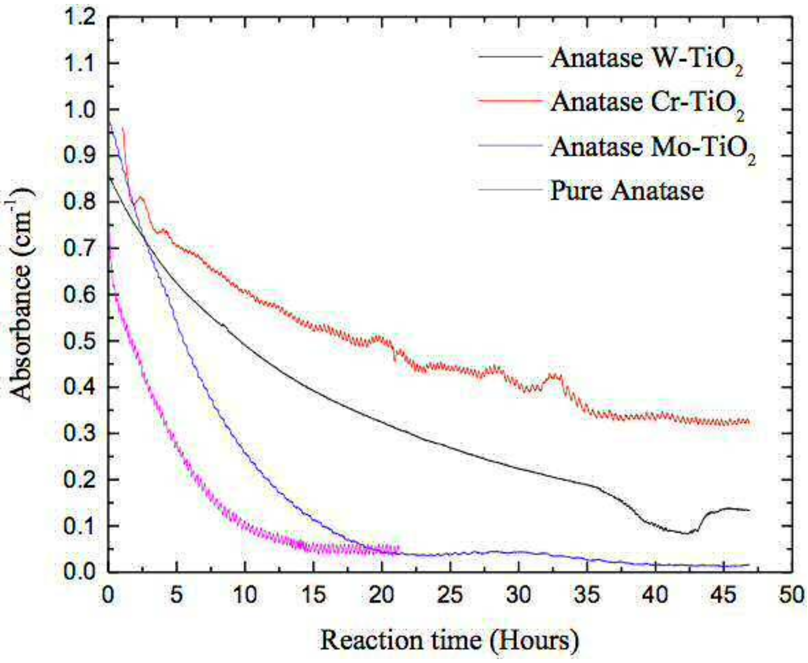

Figure 6.54: Methylene Blue decomposition by Cr, Mo and W doped into TiO_2, Anatase phase

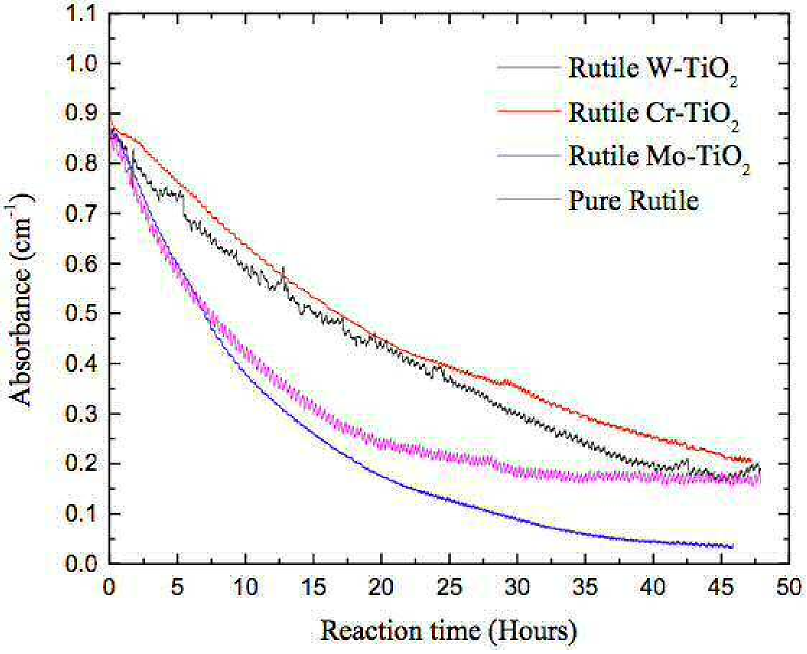

Figure 6.55: Methylene Blue decomposition by (VI) group doped intoTiO_2

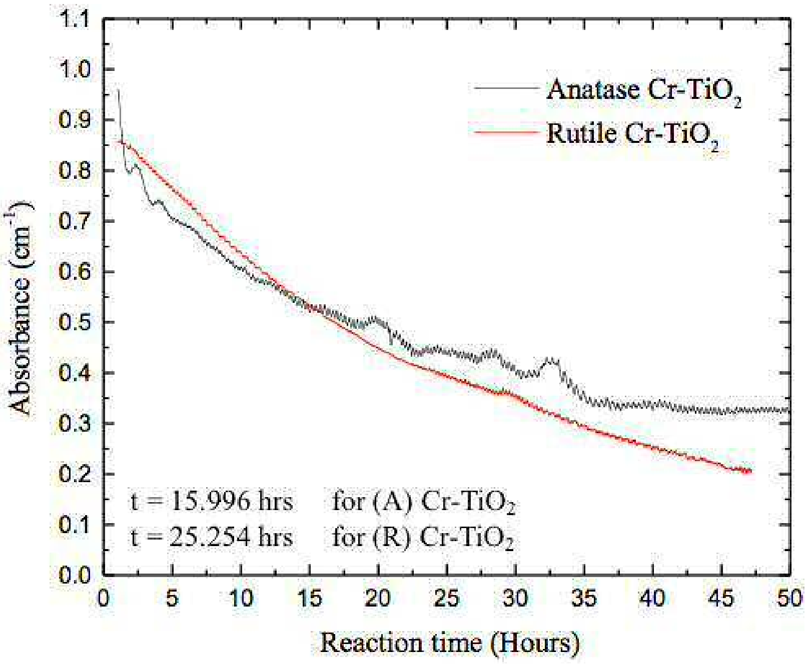

Figure 6.56: Methylene Blue decomposition by Cr-TiO_2 in both phases

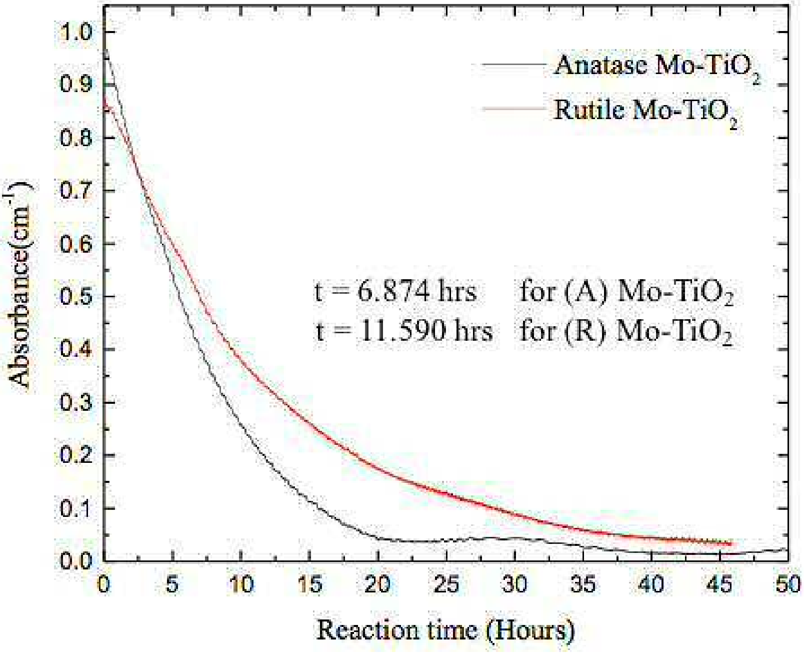

Figure 6.57: Methylene Blue decomposition by Mo-TiO_2 in both phases

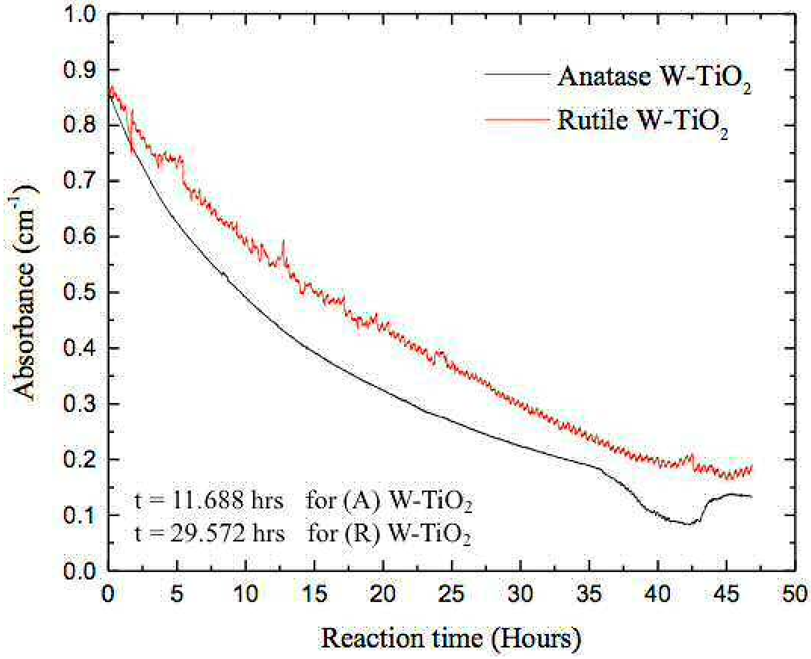

Figure 6.58: Methylene Blue decomposition by $W\text{-}TiO_2$ in both phases

6.5.4 MB Decomposition Under Visible Light Irradiation

I checked for photocatalytic activity under visible light rather than UV. This was one of the key aims of my work: to show that TiO_2 could be modified to be used for photocatalytic reactions at longer wavelengths. For these experiments a number of different wavelength LEDs were tried, 420 nm, 455 nm, 525 nm. The photocatalytic decays are shown in the following plots. The long time constants for many of the reactions meant they were particularly susceptible to gross changes in the environmental conditions. This made many to the plots hard to fit. Mo-TiO_2 seemed to display the highest photocatalytic activity toward the degradation of MB.

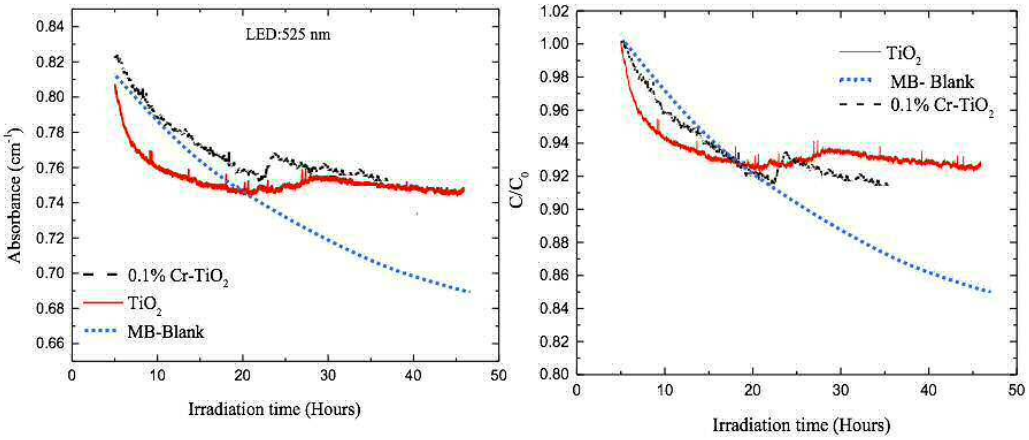

Figure 6.59: Blank, undoped TiO_2 and 0.1 wt.% Cr-doped TiO_2 under LED: 525 nm (left), Photocatalytic degradation of MB under visible light illumination in the presence of pure anatase, doped TiO_2 and blank (right).

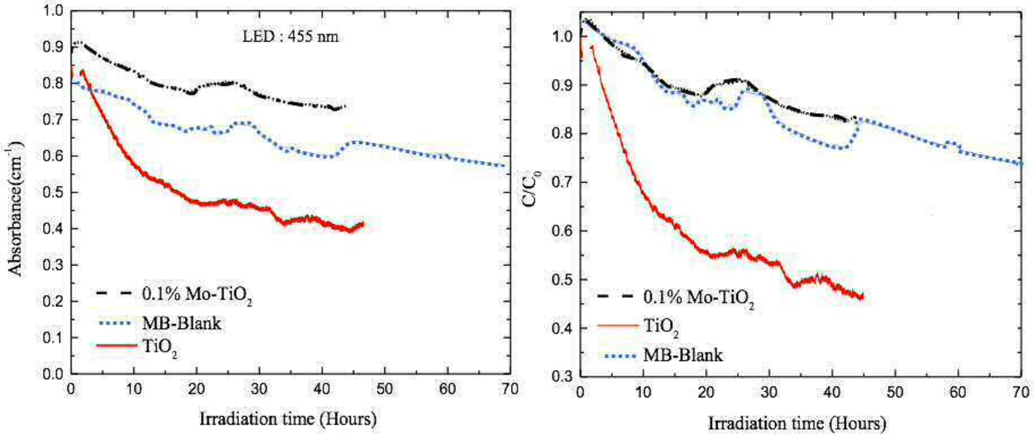

Figure 6.60: Blank, undoped TiO_2 and 0.1 wt.% Mo-doped TiO_2 under LED: 455 nm(left), Photocatalytic degradation of MB under visible light illumination in the presence of pure anatase, doped TiO_2 and blank (right).

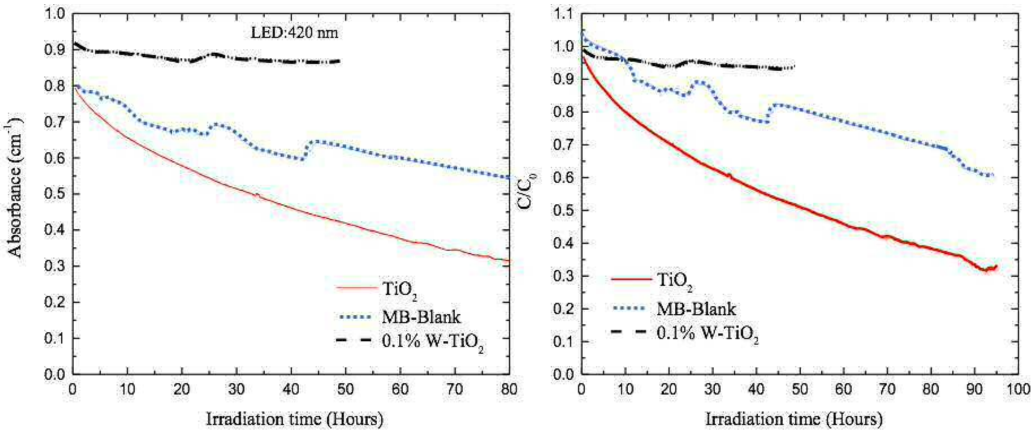

Figure 6.61: Blank, undoped TiO_2 and 0.1 wt.% W-doped TiO_2 under LED: 420 nm (left), Photocatalytic degradation of MB under visible light illumination in the presence of pure anatase, doped TiO_2 and blank (right).

6.5.5 UVA vs Visible light in MB Decomposition

Finally, I have made a comparison between the photocatalytic rates under UV and Visible light. The results are summarised in table 6.10 and the decay curves are presented after. While the materials do demonstrate some photocatalytic activity at longer wavelengths the reaction rates are much slower than under UV irradiation. Interestingly Cr-doped TiO$_2$ does show some photocatalytic activity for illumination with 525 nm light.

Degradation time (Hours)

Catalyst	**UVA**	**Visible light**
	365 nm	**LED: 525 nm**
Cr-TiO$_2$	t= 15.99 ± 0.01	t >> 48
	365 nm	**LED: 455 nm**
Mo-TiO$_2$	t= 6.87 ± 0.01	t >> 48
	365 nm	**LED: 420 nm**
W-TiO$_2$	t=11.68 ± 0.01	t >> 48

Table 6.10: Comparison of the decay time of Methylene blue in both cases UV and visible light.

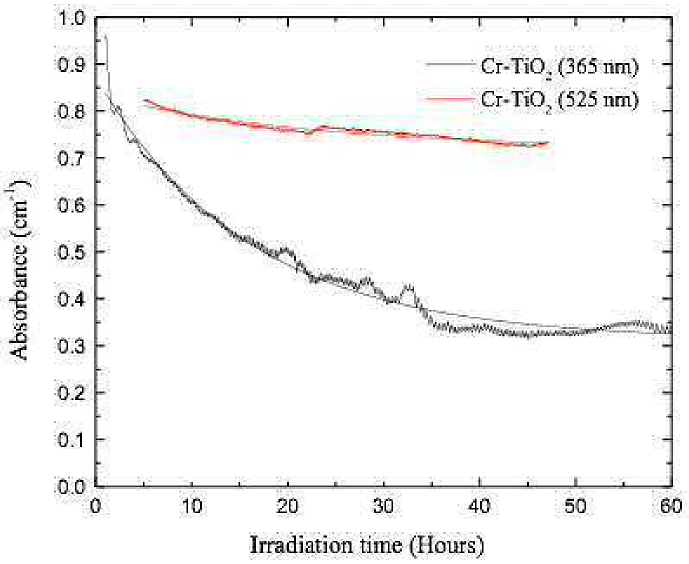

Figure 6.62: Cr-TiO$_2$ under UVA and visible light LED: 525nm

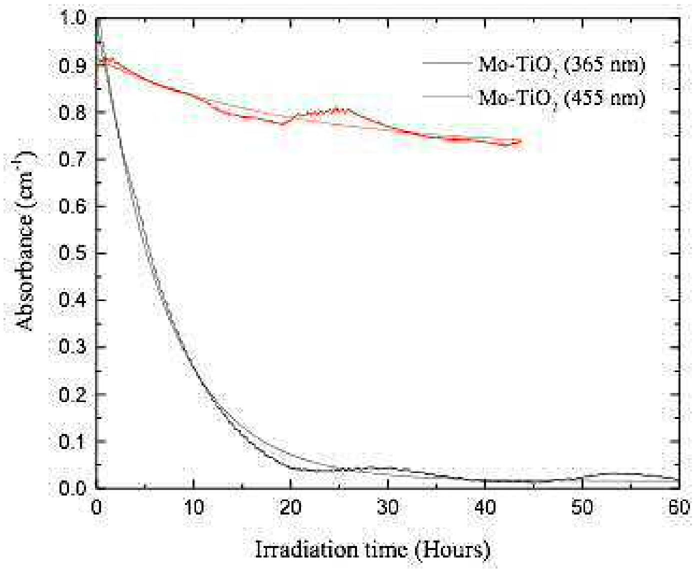

Figure 6.63: Mo-TiO_2 under UVA and visible light LED: 455nm

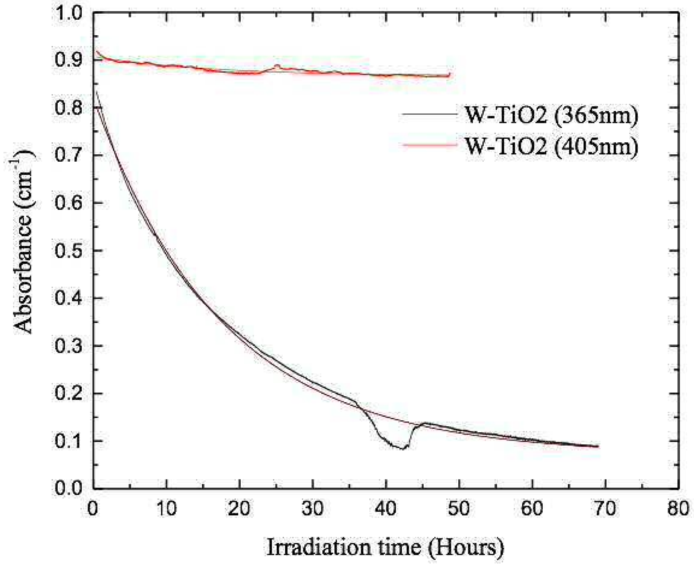

Figure 6.64: W-TiO_2 under UVA and visible light LED: 420nm

I was expecting that by using transition metal element Cr, Mo and W doped into TiO_2 in methylene blue decomposition experiment with longer wavelength > 365 nm, will give a better result than using UVA which mean that the reaction will be faster and take a shorter time to clean water from MB but, I was wrong. It take more than two days to clean the water from pollutant (MB).

I knew that modified TiO_2 by doping transition metal element into TiO_2 will reduce their band gap [Eg has been measured - see table: 6.5], then by using the wavelength required for each doping [as mentioned in table: 6.2], they show nearly a flat line not exponential curve compared to their activity in UVA light and they also take longer time than the UVA light to clean the water.

That results show that the transition metal element doped into TiO_2 work better in UVA light much more than longer wavelength (visible light).

6.5.6 Comparison of MB Decomposition w & w/o Anatase at Different Wavelengths.

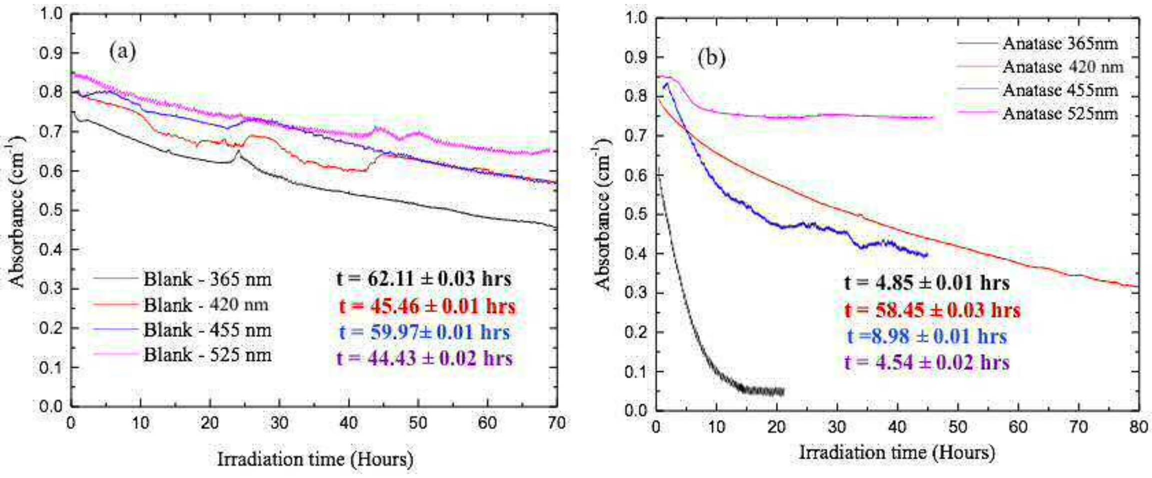

Figure 6.65: (a) The degradation of MB as a function of irradiation time under UV and visible light. (b) MB decomposition as a function of time in the presence of TiO_2 (anatase) nanoparticles under UV and visible light.

6.6 Conclusions

For the purpose of this study, methylene blue mimics a pollutant which is reacted with the catalyst. It took the place of a test pollutant to study the activity of photocatalysis such as Mo, W and Cr doped titania (TiO_2). TiO_2, a typical catalyst, has its band gap in the UV region of the electromagnetic spectrum. Since sunlight does not contain substantial UV, the material would need to be altered in order to increase its photonic efficiency under visible light.

I attempted to use group-VI dopants to alter the lattice structure of titania as well as its optical band gap. As mentioned previously, SMSI (Strong Metal-Support Interaction) explains the altered properties of doped titania which may make it more or less reactive than pure titania, depending on the dopant. I used a number of different material characterisation techniques, including XRD, XPS, and Raman to verify the incorporation of the transition metals into the crystal lattice. Unfortunately, for this study, doping with group-VI metals mainly served to decrease the activity of the sample upon exposure to UV irradiation. One theory which was put forward to explain this result, was that the dopants may trap electrons and therefore reduce likeliness to form hydroxyl radicals at the TiO_2 surface. These radicals are essential for the decomposition; in their absence, activity is reduced.

On the plus side, the new materials did show some increased activity in the visible light region of the spectrum, which may be attributed to the reduction in band gap energy and potentially provide an alternative pathway for hydroxyl radical formation. This showed that there was potential for modifying TiO_2 to work under visible light for photocatalytic applications.

Chapter 7

Conclusions and Future Work

7.1 Perspective

The steadily rising rate of water pollution due to the discharge of toxic chemicals has led to an increasing demand for uncontaminated and freshwater sources. Water pollution will eventually become one of the major global crises of the 21st Century. One solution to this problem would be to stop all pollution. However, since pollution is ultimately driven by the need to grow national economies, particularly in the developing world, this seems an entirely naive and unrealistic aspiration. Another way to fulfil this demand is to seek scientific mediation. This could be achieved through scientific innovation, particularly through the use of photocatalytic compounds such as titanium dioxide (TiO_2), which exhibits extraordinary water purification properties. The photocatalytic properties of TiO_2 mean that it is capable of facilitating the conversion of light energy to chemical energy, and through this ability has numerous applications including degrading organic compounds. The chemical energy produced by ultraviolet (UV) radiation in the presence of TiO_2 generates free radicals capable of degrading organic compounds. During the process, TiO_2 generates electron-hole pairs that facilitate RedOx reactions, which consequently generate hydroxyl radicals capable of oxidant organic pollutants such as industrial pharmaceuticals.

7.2 The Work Described in this Thesis

The aim of my PhD research was to investigate how TiO_2-based materials could be exploited for water purification. My project had several different components. The first task was to understand how to make repeatable thin-films, and this was the subject of chapter 3. To achieve thin film deposition, I used the spin coating method. However, given that different speeds during the spin affect thickness, I had to explore different techniques to estimate the film thickness. It proved distinctly challenging to find one technique that worked. Some techniques had the potential to be more reliable and accurate than others, but the selection process also depended factors such as the impact of the technique had on film. For example, stylus techniques such as Dektek and AFM damaged the film as they were measuring. Optical techniques didn't work well because of the inherent scattering properties of the films. I finally settled on a method of my own design. I encapsulated the wafers in resin, and then used a diamond cut-off machine to produce vertical sections through the wafer and TiO_2 layer. The sections were then viewed and digitally recorded using an optical microscope. The layer thickness was finally established by a statistical analysis of the number of pixels associated with the dimensions of the TiO_2 film. This finally confirmed that the spin coated films were 20-30 microns in thickness. It also allowed the packing fraction to be estimated.

The second component of my work involved building a test-rig to measure the photocatalytic reaction rate of the TiO_2 films in the presence of an artificial test pollutant. This is mainly described in chapter 4. Methylene blue and methyl orange were chosen as the test pollutants because they are non-toxic, yet still contain some of the molecular structures such as benzene rings that are found in more toxic pollutants. The experiment was based on a design by Nickels *et al.* and contained an open loop, with a recirculating pump, a glass reaction vessel, and an optical flow-cell for real-time monitoring. I exploited a property of the organic dyes, namely their colour, to follow the photocatalytic degradation over time on exposure to UV light. During the experiment, the dye degrades due to the activity of the photocatalyst, and the solution gradually became clearer. The progress is monitored by continuously measuring the absorption of the light passing through the flow cell. The experimental test-rig was the foundation for all further research performed during the rest of my PhD.

A chance observation proved the driver behind the research described in chapter 5. The activity of the TiO_2 seemed to wane over time in the presence of methylene blue, while it remained constant for reactions performed with methyl orange. The cause was traced to an accumulation of chloride ions poisoning the catalyst. Methylene blue contains chloride ions and methyl orange does not. This inhibited performance occurs through competitive adsorption, where the inorganic ions accumulate on the TiO_2 surface, hindering the target molecules from accessing the adsorption sites, and also through photo-generated hole scavenging, where the adsorbed inorganic ions consume the photo-generated holes. The attack on the photo-generated hole forms the basis of photocatalytic oxidation, and by crippling this mechanism, the chloride ions render the degradation process useless. Nonetheless, chloride ions also increase the solution pH, which has a compensating positive effect on the rate of degradation, as the presence of more hydroxyl radicles leads to more photo-induced holes that are trapped on the TiO_2 surface.

In the final experimental chapter of my thesis, I attempted to produce TiO_2 films with a modified band gap to access more of the solar spectrum. TiO_2 has a band gap of 3.2 eV which means the longest wavelength of photon capable of generating electron-hole pairs is 387 nm. The aim of the work was to extend the range of the TiO_2 by shrinking the effective band gap through doping with transition metals. As a first step I manufactured pristine TiO_2 as a control. This had the added benefit of allowing me to study how the crystal phases anatase and rutile effect photocatalytic reaction rates.

Considerable effort was expended to demonstrate incorporation of the transition metals into the TiO_2 lattice, and I learned a lot of material characterisation techniques while working closely with two colleagues in the Cardiff School of Chemistry. This work did not prove totally successful. Doping with group-VI metals mainly served to decrease the activity of the photocatalyst upon exposure to UV irradiation. One theory which was put forward to explain this result, was that the dopants may trap electrons and therefore reduce likeliness to form hydroxyl radicals at the TiO_2 surface. These radicals are essential for the pollutant decomposition and in their absence activity is reduced. On the plus side, the new materials did show some increased activity in the visible light region of the spectrum, which may be attributed to the reduction in band gap energy, and potentially provide an alternative pathway for hydroxyl radical formation. This showed that there was potential for modifying TiO_2 to work under visible light for photocatalytic applications.

7.3 Future Work

While transition metal doping showed some potential, it also showed several drawbacks: thermal instability of the doped TiO_2, electron trapping by the metal centres, introduction of electron-hole recombination centres [115]. Tamaki *et al.* investigated the reaction dynamics of the trapped holes by means of TAS (transient absorption spectroscopy) and found that in the presence of alcohols the transient absorption of the trapped holes decayed more rapidly, clearly indicating that trapped holes can react with these alcohols. The lifetime of the trapped holes in methanol, ethanol, and 2-propanol was found to be 300, 1000, and 3000 ps, respectively. The charge-transfer rate was also reported to be effected by the adsorption behaviour of the adsorbates at the TiO_2 surface. For example, it was found that methanol and ethanol adsorb predominately via a dissociative pathway on the rutile surface, resulting in the formation of surface alkoxide and hydroxyl groups, with the charge transfer from the alkoxide group to the surface causing an increase of the adsorption strength. This work shows that there may be other avenues for transition metal doped TiO_2 other than water purification, and that this could further be explored using the type of experiment I designed.

Bibliography

[1] (2012). [Online]. Available: http://blog.nus.edu.sg/me4105precisionengineering2012/types-of-metrology-equipments/interferometers/

[2] M. N. Chong, B. Jin, C. W. K. Chow, and C. Saint, "Recent developments in photocatalytic water treatment technology: a review," *Water Res*, vol. 44, no. 10, pp. 2997–3027, May 2010.

[3] Y. Dong, H. Yang, K. He, S. Song, and A. Zhang, "β-mno 2 nanowires: a novel ozonation catalyst for water treatment," *Applied Catalysis B: Environmental*, vol. 85, no. 3, pp. 155–161, 2009.

[4] S. A. Alrumman, A. F. El-kott, and S. M. Keshk, "Water pollution: source & treatment," *American Journal of Environmental Engineering*, vol. 6, no. 3, pp. 88–98, 2016.

[5] P. Goel, *Water pollution: causes, effects and control.* New Age International, 2006.

[6] (2018). [Online]. Available: https://www.thoughtco.com/how-much-of-your-body-is-water-609406

[7] Y. Wu and J. Chen, "Investigating the effects of point source and nonpoint source pollution on the water quality of the east river (dongjiang) in south china," *Ecological Indicators*, vol. 32, pp. 294 – 304, 2013.

[8] E. DeNicola, O. S. Aburizaiza, A. Siddique, H. Khwaja, and D. O. Carpenter, "Climate change and water scarcity: The case of saudi arabia," *Annals of Global Health*, vol. 81, no. 3, pp. 342 – 353, 2015.

[9] (2013, 5). [Online]. Available: dec.alaska.gov/water/opcert/docs/chapter4.pdf-2013-05-20

[10] D. Deng, M. G. Kim, J. Y. Lee, and J. Cho, "Green energy storage materials: nanostructured tio 2 and sn-based anodes for lithium-ion batteries," *Energy & Environmental Science*, vol. 2, no. 8, pp. 818–837, 2009.

[11] N. W. Brown and E. P. L. Roberts, “Electrochemical pre-treatment of effluents containing chlorinated compounds using an adsorbent,” *Journal of Applied Electrochemistry*, vol. 37, no. 11, pp. 1329–1335, Jul 2007. [Online]. Available: http://dx.doi.org/10.1007/s10800-007-9376-3

[12] M. K. Gibbons and G. A. Gagnon, “Adsorption of arsenic from a nova scotia groundwater onto water treatment residual solids,” *Water Research*, vol. 44, no. 19, pp. 5740 – 5749, 2010, groundwater Arsenic: From Genesis to Sustainable Remediation. [Online]. Available: http://www.sciencedirect.com/science/article/pii/S0043135410004379

[13] J. H. Al-Rifai, H. Khabbaz, and A. I. Schäfer, “Removal of pharmaceuticals and endocrine disrupting compounds in a water recycling process using reverse osmosis systems,” *Separation and Purification Technology*, vol. 77, no. 1, pp. 60 – 67, 2011. [Online]. Available: http://www.sciencedirect.com/science/article/pii/S1383586610004855

[14] S. G. Öner, N. Kabay, E. Güler, M. Kitis, and M. Yüksel, “A comparative study for the removal of boron and silica from geothermal water by cross-flow flat sheet reverse osmosis method,” *Desalination*, vol. 283, pp. 10 – 15, 2011, special issue in honour of Professor Tony Fane on his 70th Birthday. [Online]. Available: http://www.sciencedirect.com/science/article/pii/S0011916411001640

[15] M. Clever, F. Jordt, R. Knauf, N. Räbiger, M. Rüdebusch, and R. Hilker-Scheibel, “Process water production from river water by ultrafiltration and reverse osmosis,” *Desalination*, vol. 131, no. 1, pp. 325 – 336, 2000. [Online]. Available: http://www.sciencedirect.com/science/article/pii/S0011916400900316

[16] W. Fuchs, H. Binder, G. Mavrias, and R. Braun, “Anaerobic treatment of wastewater with high organic content using a stirred tank reactor coupled with a membrane filtration unit,” *Water Research*, vol. 37, no. 4, pp. 902 – 908, 2003. [Online]. Available: http://www.sciencedirect.com/science/article/pii/S0043135402002464

[17] M. D. Francesco and P. Costamagna, “On the design of electrochemical reactors for the treatment of polluted water,” *Journal of Cleaner Production*, vol. 12, no. 2, pp. 159 – 163, 2004, advances in cleaner production technologies. [Online]. Available: http://www.sciencedirect.com/science/article/pii/S0959652602001919

[18] I. Sirés, N. Oturan, and M. A. Oturan, “Electrochemical degradation of β-blockers. studies on single and multicomponent synthetic aqueous solutions,” *Water Research*, vol. 44, no. 10, pp. 3109 – 3120, 2010. [Online]. Available: http://www.sciencedirect.com/science/article/pii/S0043135410001788

[19] I. A. Katsoyiannis and A. I. Zouboulis, "Biological treatment of mn(ii) and fe(ii) containing groundwater: kinetic considerations and product characterization," *Water Research*, vol. 38, no. 7, pp. 1922 – 1932, 2004. [Online]. Available: http://www.sciencedirect.com/science/article/pii/S0043135404000314

[20] S. I. Abou-Elela, M. M. Kamel, and M. E. Fawzy, "Biological treatment of saline wastewater using a salt-tolerant microorganism," *Desalination*, vol. 250, no. 1, pp. 1 – 5, 2010. [Online]. Available: http://www.sciencedirect.com/science/article/pii/S0011916409009928

[21] I. Oller, S. Malato, and J. Sánchez-Pérez, "Combination of advanced oxidation processes and biological treatments for wastewater decontamination—a review," *Science of the total environment*, vol. 409, no. 20, 2011.

[22] K. Hashimoto, H. Irie, and A. Fujishima, "Tio2 photocatalysis: a historical overview and future prospects," *Japanese journal of applied physics*, vol. 44, no. 12R, p. 8269, 2005.

[23] A. T. Mecherikunnel and J. C. Richmond, "Spectral distribution of solar radiation," NASA, Technical Memorandum 82021, September 1980.

[24] Y. Gorlin and T. F. Jaramillo, "A bifunctional nonprecious metal catalyst for oxygen reduction and water oxidation," *J Am Chem Soc*, vol. 132, no. 39, pp. 13 612–4, Oct 2010.

[25] N. Helaili, Y. Bessekhouad, A. Bouguelia, and M. Trari, "Visible light degradation of orange ii using xcuyoz/tio2 heterojunctions," *Journal of hazardous materials*, vol. 168, no. 1, pp. 484–492, 2009.

[26] C. Han, M. Pelaez, V. Likodimos, A. G. Kontos, P. Falaras, K. O'Shea, and D. D. Dionysiou, "Innovative visible light-activated sulfur doped tio 2 films for water treatment," *Applied Catalysis B: Environmental*, vol. 107, no. 1, pp. 77–87, 2011.

[27] R. D. Ambashta and M. Sillanpää, "Water purification using magnetic assistance: a review," *J Hazard Mater*, vol. 180, no. 1-3, pp. 38–49, Aug 2010.

[28] [Online]. Available: http://images-of-elements.com/lead.php

[29] E. F. Schubert, *Doping in III-V semiconductors*. E. Fred Schubert, 2015.

[30] K. Rajeshwar, A. Thomas, and C. Janáky, "Photocatalytic activity of inorganic semiconductor surfaces: myths, hype, and reality," *ACS Publications*, 2015.

[31] (2012). [Online]. Available: http://www.eolss.net/sample-Chapters/c06/E6-190-16-00.pdf

[32] B. Cornils, W. A. Herrmann, M. Beller, and R. Paciello, *Applied Homogeneous Catalysis with Organometallic Compounds: A Comprehensive Handbook in Four Volumes*. John Wiley & Sons, 2018, vol. 4.

[33] T. B. Scott, I. C. Popescu, R. A. Crane, and C. Noubactep, "Nano-scale metallic iron for the treatment of solutions containing multiple inorganic contaminants," *J Hazard Mater*, vol. 186, no. 1, pp. 280–7, Feb 2011.

[34] J. Lee, "Synthesis and characterization of nanostructured metal oxide for water remediation and energy applications," Ph.D. dissertation, Stony Brook University, 2013. [Online]. Available: http://hdl.handle.net/11401/76317

[35] C. Seghetti, "Gold/ tio2 nanocomposites as photoactive materials for environmental remediation," *Tecnico Lisboa*, 2016.

[36] R. Asahi, T. Morikawa, H. Irie, and T. Ohwaki, "Nitrogen-doped titanium dioxide as visible-light-sensitive photocatalyst: designs, developments, and prospects," *Chemical reviews*, vol. 114, no. 19, pp. 9824–9852, 2014.

[37] O. Tonomura, T. Sekiguchi, N. Inada, T. Hamada, H. Miki, and K. Torii, "Band engineering of ru/rutile-tio2/ru capacitors by doping cobalt to suppress leakage current," *Journal of The Electrochemical Society*, vol. 159, no. 1, pp. G1–G5, 2011.

[38] J. Zhang, P. Zhou, J. Liu, and J. Yu, "New understanding of the difference of photocatalytic activity among anatase, rutile and brookite tio2," *Physical Chemistry Chemical Physics*, vol. 16, no. 38, pp. 20 382–20 386, 2014.

[39] B. Ohtani, O. Prieto-Mahaney, D. Li, and R. Abe, "What is degussa (evonik) p25? crystalline composition analysis, reconstruction from isolated pure particles and photocatalytic activity test," *Journal of Photochemistry and Photobiology A: Chemistry*, vol. 216, no. 2-3, pp. 179–182, 2010.

[40] Z. Pap, V. Danciu, Z. Cegléd, Á. Kukovecz, A. Oszkó, A. Dombi, and K. Mogyorósi, "The influence of rapid heat treatment in still air on the photocatalytic activity of titania photocatalysts for phenol and monuron degradation," *Applied Catalysis B: Environmental*, vol. 101, no. 3-4, pp. 461–470, 2011.

[41] Y. Ide, N. Inami, H. Hattori, K. Saito, M. Sohmiya, N. Tsunoji, K. Komaguchi, T. Sano, Y. Bando, D. Golberg *et al.*, "Remarkable charge separation and photocatalytic efficiency enhancement through interconnection of tio2 nanoparticles by hydrothermal treatment," *Angewandte Chemie International Edition*, vol. 55, no. 11, pp. 3600–3605, 2016.

[42] R. I. Bickley, T. Gonzalez-Carreno, J. S. Lees, L. Palmisano, and R. J. Tilley, "A structural investigation of titanium dioxide photocatalysts," *Journal of Solid State Chemistry*, vol. 92, no. 1, pp. 178–190, 1991.

[43] A. Houas, H. Lachheb, M. Ksibi, E. Elaloui, C. Guillard, and J.-M. Herrmann, "Photocatalytic degradation pathway of methylene blue in water," *Applied Catalysis B: Environmental*, vol. 31, no. 145-157, 2001.

[44] (2018). [Online]. Available: http://www.rsc.org/learn-chemistry/resource/res00001266/tio2-photocatalysis-the-future-of-water-treatment-with-tio2?cmpid=CMP00002616

[45] I. Levchuk *et al.*, "Titanium dioxide based nanomaterials for photocatalytic water treatment," *Acta Universitatis Lappeenrantaensis*, 2016.

[46] V. Binas, D. Venieri, D. Kotzias, and G. Kiriakidis, "Modified tio2 based photocatalysts for improved air and health quality," *Journal of Materiomics*, vol. 3, no. 1, pp. 3–16, 2017.

[47] [Online]. Available: https://medium.com/@phoebetyler127/what-are-the-representative-elements-2f2721fb6820

[48] A. Zhang, F. Gong, Y. Xiao, X. Guo, F. Li, L. Wang, Y. Zhang, and L. Zhang, "Electrochemical reductive doping and interfacial impedance of tio2 nanotube arrays in aqueous and aprotic solvents," *Journal of The Electrochemical Society*, vol. 164, no. 2, pp. H91–H96, 2017.

[49] J.-H. Kim, G. Kwon, H. Lim, C. Zhu, H. You, and Y.-T. Kim, "Effects of transition metal doping in pt/m-tio2 (m= v, cr, and nb) on oxygen reduction reaction activity," *Journal of Power Sources*, vol. 320, pp. 188–195, 2016.

[50] W. H. Mahmoud, R. G. Deghadi, and G. G. Mohamed, "Novel schiff base ligand and its metal complexes with some transition elements. synthesis, spectroscopic, thermal analysis, antimicrobial and in vitro anticancer activity," *Applied Organometallic Chemistry*, vol. 30, no. 4, pp. 221–230, 2016.

[51] R. Liang, "Tio2 nanomaterials: Photocatalysis and multifunctional water treatment applications," *UWSpace*, 2017.

[52] R. J. Klein, Ed., *Welding: Processes, Quality, and Applications.* Nova Science Publishers Inc, 2015.

[53] D. K. A. Robert H.Todd and L. Alting, *Manufacturing Processes Reference Guide.* Industrial Press Inc, 1994.

[54] K. Okamoto, *Fundamentals of optical waveguides.* Academic press, 2010.

[55] P. Nickels, H. Zhou, S. N. Basahel, A. Y. Obaid, T. T. Ali, A. A. Al-Ghamdi, E.-S. H. El-Mossalamy, A. O. Alyoubi, and S. A. Lynch, "Laboratory scale water circuit including a photocatalytic reactor and a portable in-stream sensor to monitor pollutant degradation," *Industrial & Engineering Chemistry Research*, vol. 51, no. 8, pp. 3301–3308, 2012.

[56] A. Rockett, *The Materials Science of Semiconductors.* Springer US, 2008.

[57] C. Sun, H. Li, and L. Chen, “Nanostructured ceria-based materials: synthesis, properties, and applications,” *Energy Environ. Sci.*, vol. 5, no. 9, pp. 8475–8505, 2012.

[58] A. TUROLLA, “Heterogeneous photocatalysis and electrophotocatalysis on nanostructured titanium dioxide for water and wastewater treatment: process assessment, modelling and optimization,” *Italy*, 2014.

[59] A. Cuevas and D. Macdonald, “Measuring and interpreting the lifetime of silicon wafers,” *Solar Energy*, vol. 76, no. 1-3, pp. 255–262, 2004.

[60] D. K. Schroder, *Semiconductor material and device characterization.* John Wiley & Sons, 2006.

[61] J. C. Colmenares, R. Luque, J. M. Campelo, F. Colmenares, Z. Karpiński, and A. A. Romero, “Nanostructured photocatalysts and their applications in the photocatalytic transformation of lignocellulosic biomass: an overview,” *Materials*, vol. 2, no. 4, pp. 2228–2258, 2009.

[62] [Online]. Available: https://upload.wikimedia.org/wikipedia/commons/e/ef/Atomic_force_microscope_block_diagram_v2.svg

[63] H. Tompkins. (2004) Spectroscopic ellipsometry: What it is, what it will do, and what it won’t do. [Online]. Available: https://www.aps.org/units/fiap/meetings/presentations/upload/tompkins.pdf

[64] (2018). [Online]. Available: https://www.jawoollam.com/resources/ellipsometry-tutorial/ellipsometry-data-analysis

[65] D. H. Park, J. Luo, A. K.-Y. Jen, and W. N. Herman, “Simplified reflection fabry-perot method for determination of electro-optic coefficients of poled polymer thin films,” *Polymers*, vol. 3, no. 3, pp. 1310–1324, 2011.

[66] P. Hajireza, K. Krause, M. Brett, and R. Zemp, “Glancing angle deposited nanostructured film fabry-perot etalons for optical detection of ultrasound,” *Opt Express*, vol. 21, no. 5, pp. 6391–400, Mar 2013.

[67] J. M. Hollas, *Modern spectroscopy.* John Wiley & Sons, 2004.

[68] H. W. Siesler, Y. Ozaki, S. Kawata, and H. M. Heise, *Near-infrared spectroscopy: principles, instruments, applications.* John Wiley & Sons, 2008.

[69] H. Meyers and H. Myers, *Introductory solid state physics.* CRC press, 1997.

[70] B. Van Driel, P. Kooyman, K. Van den Berg, A. Schmidt-Ott, and J. Dik, "A quick assessment of the photocatalytic activity of tio 2 pigments—from lab to conservation studio!" *Microchemical Journal*, vol. 126, pp. 162–171, 2016.

[71] A. O. Ibhadon and P. Fitzpatrick, "Heterogeneous photocatalysis: Recent advances and applications," *Catalysts*, vol. 3, no. 1, pp. 189–218, 2013.

[72] Methylene blue spectra. [Online]. Available: https://omlc.org/spectra/mb/index.html

[73] Methyl orange. [Online]. Available: https://www.photochemcad.com/compounds/J03_Methyl_Orange.htm

[74] R. A. Khaydarov, R. R. Khaydarov, and O. Gapurova, "Nano-photocatalysts for the destruction of chloro-organic compounds and bacteria in water," *Journal of colloid and interface science*, vol. 406, pp. 105–110, 2013.

[75] A. Piscopo, D. Robert, and J. V. Weber, "Influence of ph and chloride anion on the photocatalytic degradation of organic compounds: Part i. effect on the benzamide and para-hydroxybenzoic acid in tio2 aqueous solution," *Applied Catalysis B: Environmental*, vol. 35, no. 2, pp. 117–124, 2001.

[76] Q. Liu and J. H. Lunsford, "The roles of chloride ions in the direct formation of h2o2 from h2 and o2 over a pd/sio2 catalyst in a h2so4/ethanol system," *Journal of Catalysis*, vol. 239, no. 1, pp. 237–243, 2006.

[77] A.-G. Rincón and C. Pulgarin, "Effect of ph, inorganic ions, organic matter and h2o2 on e. coli k12 photocatalytic inactivation by tio2: Implications in solar water disinfection," *Applied Catalysis B: Environmental*, vol. 51, no. 4, pp. 283–302, August 2004.

[78] M. I. Litter, "Heterogeneous photocatalysis: transition metal ions in photocatalytic systems," *Applied Catalysis B: Environmental*, vol. 23, no. 2-3, pp. 89–114, 1999.

[79] C. S. Zalazar, C. A. Martin, and A. E. Cassano, "Photocatalytic intrinsic reaction kinetics. ii: Effects of oxygen concentration on the kinetics of the photocatalytic degradation of dichloroacetic acid," *Chemical Engineering Science*, vol. 60, no. 15, pp. 4311–4322, 2005.

[80] A. Dhanya and K. Aparna, "Synthesis and evaluation of tio2/chitosan based hydrogel for the adsorptional photocatalytic degradation of azo and anthraquinone dye under uv light irradiation," *Procedia Technology*, vol. 24, pp. 611–618, 2016.

[81] H. R. E. Afarani, "Preparation of metal catalysts on granule glass for degradation of textile dyes as environmental contaminants," *World Appl Sci J*, vol. 3, pp. 738–741, 2008.

[82] J.-S. Chang, C. Chou, Y.-C. Lin, P.-J. Lin, J.-Y. Ho, and T. L. Hu, "Kinetic characteristics of bacterial azo-dye decolorization by pseudomonas luteola," *Water Research*, vol. 35, no. 12, pp. 2841–2850, 2001.

[83] D. I. Enache, J. K. Edwards, P. Landon, B. Solsona-Espriu, A. F. Carley, A. A. Herzing, M. Watanabe, C. J. Kiely, D. W. Knight, and G. J. Hutchings, "Solvent-free oxidation of primary alcohols to aldehydes using au-pd/tio2 catalysts," *Science*, vol. 311, no. 5759, pp. 362–365, 2006.

[84] J. Lee, S. Divya, P. Shanmugasundaram, and P. I. Gouma, "Synthesis and characterization of visible-light activated cuo–tio2 nanofibrous mats," *Journal of Nanoengineering and Nanomanufacturing*, vol. 4, no. 2, pp. 140–145, 2014.

[85] [Online]. Available: https://uk.rs-online.com/web/p/visible-leds/9008918/

[86] [Online]. Available: https://uk.farnell.com/osram-opto-semiconductors/gd-cs8pm1-14-uovj-w4-1/led-hb-blue-455nm-smd/dp/2762589

[87] [Online]. Available: https://uk.farnell.com/lumileds/lhuv-0420-0650/led-hb-violet-420nm-smd/dp/2769110

[88] S. F. Sim, T. Y. Ling, L. Nyanti, N. Gerunsin, Y. E. Wong, and L. P. Kho, "Assessment of heavy metals in water, sediment, and fishes of a large tropical hydroelectric dam in sarawak, malaysia," *Journal of Chemistry*, vol. 2016, 2016.

[89] W. Wunderlich, T. Oekermann, L. Miao, N. T. Hue, S. Tanemura, and M. Tanemura, "Electronic properties of nano-porous tio 2- and zno thin films- comparison of simulations and experiments," *Journal of Ceramic Processing & Research*, vol. 5, no. 4, pp. 343–354, 2004.

[90] T. H. Jun, K.-S. Lee, and H. S. Song, "Hydrophilicity of anatase tio2/cr-doped tio2 thin films with different band gaps," *Thin Solid Films*, vol. 520, no. 7, pp. 2609–2612, 2012.

[91] J.-g. Huang, X.-t. Guo, B. Wang, L.-y. Li, M.-x. Zhao, L.-l. Dong, X.-j. Liu, and Y.-t. Huang, "Synthesis and photocatalytic activity of mo-doped tio2 nanoparticles," *Journal of Spectroscopy*, vol. 2015, 2015.

[92] I. Ullah, A. Haider, N. Khalid, S. Ali, S. Ahmed, Y. Khan, N. Ahmed, and M. Zubair, "Tuning the band gap of tio 2 by tungsten doping for efficient uv and visible photodegradation of congo red dye," *Spectrochimica Acta Part A: Molecular and Biomolecular Spectroscopy*, 2018.

[93] T. Aguilar, I. Carrillo-Berdugo, R. Gómez-Villarejo, J. Gallardo, P. Martínez-Merino, J. Piñero, R. Alcántara, C. Fernández-Lorenzo, and J. Navas, "A solvothermal synthesis of tio2 nanoparticles in a non-polar medium to prepare

highly stable nanofluids with improved thermal properties,” *Nanomaterials*, vol. 8, no. 10, p. 816, 2018.

[94] O. Avilés-García, J. Espino-Valencia, R. Romero, J. L. Rico-Cerda, M. Arroyo-Albiter, and R. Natividad, “W and mo doped tio2: Synthesis, characterization and photocatalytic activity,” *Fuel*, vol. 198, pp. 31–41, 2017.

[95] N. D. Abazović, L. Mirenghi, I. A. Janković, N. Bibić, D. V. Šojić, B. F. Abramović, and M. I. Čomor, “Synthesis and characterization of rutile tio2nanopowders doped with iron ions,” *Nanoscale Research Letters*, vol. 4, no. 6, p. 518, Feb 2009. [Online]. Available: https://doi.org/10.1007/s11671-009-9274-1

[96] M. M. Ba-Abbad, A. A. H. Kadhum, A. B. Mohamad, M. S. Takriff, and K. Sopian, “Synthesis and catalytic activity of tio2 nanoparticles for photochemical oxidation of concentrated chlorophenols under direct solar radiation,” *Int. J. Electrochem. Sci*, vol. 7, pp. 4871–4888, 2012.

[97] T. Theivasanthi and M. Alagar, “Titanium dioxide (tio2) nanoparticles xrd analyses: An insight,” *arXiv preprint arXiv:1307.1091*, 2013.

[98] Ž. Antić, R. M. Krsmanović, M. G. Nikolić, M. Marinović-Cincović, M. Mitrić, S. Polizzi, and M. D. Dramićanin, “Multisite luminescence of rare earth doped tio2 anatase nanoparticles,” *Materials Chemistry and Physics*, vol. 135, no. 2-3, pp. 1064–1069, 2012.

[99] D. Zacher, R. Schmid, C. Wöll, and R. A. Fischer, “Surface chemistry of metal–organic frameworks at the liquid–solid interface,” *Angewandte Chemie International Edition*, vol. 50, no. 1, pp. 176–199, 2011.

[100] R. Dubey and S. Singh, “Investigation of structural and optical properties of pure and chromium doped tio2 nanoparticles prepared by solvothermal method,” *Results in Physics*, vol. 7, pp. 1283–1288, 2017.

[101] A. Bellifa, A. Choukchou-Braham, C. Kappenstein, and L. Pirault-Roy, “Study of the effect of transition metals on titanium dioxide phase transformation,” in *International Congress on Energy Efficiency and Energy Related Materials (ENEFM2013)*. Springer, 2014, pp. 1–7.

[102] L. G. Devi and B. N. Murthy, “Characterization of mo doped tio 2 and its enhanced photo catalytic activity under visible light,” *Catalysis letters*, vol. 125, no. 3-4, pp. 320–330, 2008.

[103] Y. Zhang, “Flame synthesis of tungsten-doped titanium dioxide nanoparticles,” Ph.D. dissertation, Rutgers University-Graduate School-New Brunswick, 2016.

[104] M. J. Šćepanović, M. Grujić-Brojčin, Z. Dohčević-Mitrović, and Z. Popović, "Characterization of anatase tio2 nanopowder by variable-temperature raman spectroscopy," *Science of Sintering*, vol. 41, no. 1, pp. 67–73, 2009.

[105] S. Franssila, *Introduction to microfabrication.* John Wiley & Sons, 2010.

[106] P. Pichat, *Photocatalysis.* MDPI, 2018.

[107] T. Ohsaka, F. Izumi, and Y. Fujiki, "Raman spectrum of anatase, tio2," *Journal of Raman spectroscopy*, vol. 7, no. 6, pp. 321–324, 1978.

[108] J. Parker and R. Siegel, "Calibration of the raman spectrum to the oxygen stoichiometry of nanophase tio2," *Applied Physics Letters*, vol. 57, no. 9, pp. 943–945, 1990.

[109] P. R. Erickson, N. Walpen, J. J. Guerard, S. N. Eustis, J. S. Arey, and K. McNeill, "Controlling factors in the rates of oxidation of anilines and phenols by triplet methylene blue in aqueous solution," *The Journal of Physical Chemistry A*, vol. 119, no. 13, pp. 3233–3243, 2015.

[110] T. Nyokong and V. Ahsen, *Photosensitizers in medicine, environment, and security.* Springer Science & Business Media, 2012.

[111] M. Cesaria and B. Di Bartolo, "Nanophosphors: From rare earth activated multicolor-tuning to new efficient white light sources," in *Advanced Study Institute on NATO ASI on Quantum Nano-Photonics.* Springer, 2017, pp. 27–77.

[112] Y. Yamamoto, N. Imai, R. Mashima, R. Konaka, M. Inoue, and W. C. Dunlap, "[3] singlet oxygen from irradiated titanium dioxide and zinc oxide," in *Singlet Oxygen, UV-A, and Ozone*, ser. Methods in Enzymology. Academic Press, 2000, vol. 319, pp. 29 – 37. [Online]. Available: http://www.sciencedirect.com/science/article/pii/S0076687900190056

[113] R. Akbarzadeh and S. Javadpour, "W/mo-doped tio2 for photocatalytic degradation of methylene blue," *Int. J. Eng. Sci. Innovative Tech*, vol. 3, pp. 621–629, 2014.

[114] T. Luttrell, S. Halpegamage, J. Tao, A. Kramer, E. Sutter, and M. Batzill, "Why is anatase a better photocatalyst than rutile?-model studies on epitaxial tio 2 films," *Scientific reports*, vol. 4, p. 4043, 2014.

[115] J. Schneider, M. Matsuoka, M. Takeuchi, J. Zhang, Y. Horiuchi, M. Anpo, and D. W. Bahnemann, "Understanding tio2 photocatalysis: Mechanisms and materials," *Chemical Reviews*, vol. 114, no. 19, pp. 9919–9986, 2014.

Appendix A

Python Code

```
ï»¿
# -*- coding: utf-8 -*-
"""
Created on Tue Nov  3 13:30:44 2015

@author: user_2
"""

import visa
import time

rm = visa.ResourceManager()
#print rm.list_resources()
#First, set the parameters and check the file doesn't exist.
name = raw_input ('The degradation of M -- enter a filename: ')
print (name)
try:
    handle = open (name, 'r')
    text = handle.read()
    if len(text)>0:
       print('File exists and isnt empty')
       exit()
    handle.close()
except:
    pass

num_reading=int(raw_input('Enter number of readings to take: '))
measurement_delay=int(raw_input('Enter measurement delay: '))#seconds


#set up the multimeter
keithley_scope1 = rm.get_instrument("USB::0x05E6::0x2110::1415367::INSTR")
print(keithley_scope1.ask("*IDN?"))
keithley_scope1.write("HEADER OFF")
keithley_scope1.write("ACQUIRE:MODE AVERAGE")
keithley_scope1.write("ACQUIRE:NUMAVG 128")
```

```

num_read=0
#Main loop collects the data and stores it.
while num_read <num_reading:
    raw_voltage = float(keithley_scope1.ask("MEASURE:VOLTAGE:DC?"))
    print (num_read, time.strftime("%d/%m/%y %H:%M:%S"), raw_voltage)
    handle=open(name,'a')
    handle.write(str(num_read)+","+str(time.strftime("%d/%m/%y %H:%M:%S"))+","+str( raw_voltage)+"\n")
    handle.close()
    num_read = num_read +1
    time.sleep(measurement_delay)

#If num read == 10
#Print (num read)
    print (num_read, time.strftime("%d/%m/%y %H:%M:%S"), raw_voltage)
```

structure.py